micromachines

Special Issue Reprint

Magnetic and Spin Devices, Volume II

Edited by
Viktor Sverdlov and Seung-bok Choi

mdpi.com/journal/micromachines

MDPI

Magnetic and Spin Devices, Volume II

Magnetic and Spin Devices, Volume II

Editors

Viktor Sverdlov
Seung-bok Choi

MDPI

Basel • Beijing • Wuhan • Barcelona • Belgrade • Novi Sad • Cluj • Manchester

Editors

Viktor Sverdlov
Institute for Microelectronics,
CDL for NovoMemLog
TU Wien
Vienna
Austria

Seung-bok Choi
Department of Mechanical
Engineering
The State University of New
York at Korea (SUNY Korea)
Incheon
Korea, South

Editorial Office
MDPI
St. Alban-Anlage 66
4052 Basel, Switzerland

This is a reprint of articles from the Special Issue published online in the open access journal *Micromachines* (ISSN 2072-666X) (available at: www.mdpi.com/journal/micromachines/special_issues/Magnetic_Spin_Devices_Volume_II).

For citation purposes, cite each article independently as indicated on the article page online and as indicated below:

Lastname, A.A.; Lastname, B.B. Article Title. *Journal Name* **Year**, *Volume Number*, Page Range.

ISBN 978-3-0365-9892-5 (Hbk)
ISBN 978-3-0365-9891-8 (PDF)
doi.org/10.3390/books978-3-0365-9891-8

© 2023 by the authors. Articles in this book are Open Access and distributed under the Creative Commons Attribution (CC BY) license. The book as a whole is distributed by MDPI under the terms and conditions of the Creative Commons Attribution-NonCommercial-NoDerivs (CC BY-NC-ND) license.

Contents

micromachines

MDPI

Editorial

Editorial for the Special Issue on Magnetic and Spin Devices, Volume II

Viktor Sverdlov [1,*] and Seung-Bok Choi [2,3,*]

[1] Christian Doppler Laboratory for Nonvolatile Magnetoresistive Memory and Logic, Institute for Microelectronics, TU Wien, 1040 Vienna, Austria
[2] Department of Mechanical Engineering, The State University of New York at Korea (SUNY Korea), 119 Songdo Moonhwa-Ro, Yeonsu-Gu, Incheon 21985, Republic of Korea
[3] Department of Mechanical Engineering, Industrial University of Ho Chi Minh City, Ho Chi Minh City 7000, Vietnam
* Correspondence: sverdlov@iue.tuwien.ac.at (V.S.); seungbok.choi@sunykorea.ac.kr (S.-B.C.)

Citation: Sverdlov, V.; Choi, S.-B. Editorial for the Special Issue on Magnetic and Spin Devices, Volume II. *Micromachines* **2023**, *14*, 2131. https://doi.org/10.3390/mi14112131

Received: 16 November 2023
Accepted: 19 November 2023
Published: 20 November 2023

Copyright: © 2023 by the authors. Licensee MDPI, Basel, Switzerland. This article is an open access article distributed under the terms and conditions of the Creative Commons Attribution (CC BY) license (https://creativecommons.org/licenses/by/4.0/).

Although the miniaturization of metal–oxide–semiconductor field effect transistors (MOSFETs)—the main driver behind an outstanding increase in the speed, performance, density, and complexity of modern integrated circuits—is continuing, numerous outstanding technological challenges in complimentary metal–oxide–semiconductor (CMOS) device miniaturization are slowly bringing the downscaling to saturation. As the CMOS devices employed intrinsically rely on electron charge for their operation, to slow down the saturation of CMOS scaling, researchers are looking to an additional property of electrons: electron spin. Electron spin is attracting increasing attention as a suitable candidate for complementing or even replacing electron charge in future microelectronic devices [1–3].

Because of the success of the initial Special Issue on Magnetic and Spin Devices [4], we have decided to continue addressing the ever-advancing progress in spin-driven and magnetic devices with this second volume. There are 10 research articles published in this Special Issue, covering recent advances in research aspects ranging from manufacturing magnetic materials to modeling techniques for highly scaled magnetoresistive devices, design and optimization approaches, complex magnetic systems, and sensing applications.

Electron spin is characterized by two projections on a given axis. The axis is typically defined by a magnetic field or by a magnetization direction when the material is a ferromagnet. The magnetization in a ferromagnet itself can be used to store information when the ferromagnet possesses uniaxial magnetic anisotropy: its magnetization can be aligned along the anisotropy axis in either direction. In *Contribution 1*, a simple method to grow thin ferromagnetic films of permalloy (Py), an alloy of 80% Ni and 20% Fe, on a silicon wafer via electrochemical deposition [5] is explored. The effect of Py thickness on the magnetic properties of thin films was investigated by using field emission scanning electron microscopy, energy-dispersive X-ray spectroscopy, atomic force microscopy, ferromagnetic resonance, anisotropic magnetoresistance, and the magneto-optic Kerr effect. The magnetoresistance ratios of the deposited Py thin films were around 0.23%, while the damping constant was 1.36×10^{-2}; these characteristics are comparable to those of expensive sputtered layers.

At all stages of semiconductor device development, accurate technology computer-aided design (TCAD) tools are paramount to predict the device functionalities, to optimize the parameters, and to obtain the best performance. In particular, process and device TCAD has become indispensable in the design cycle of novel devices and technologies [6]. A comprehensive simulation approach capable of accurately describing the complex structures and behaviors of emerging ultra-scaled magnetoresistive random access memory (MRAM) devices [7] is proposed in *Contribution 2*. The approach is based on the finite element method solution of the Landau–Lifshitz–Gilbert equation coupled to the spin and charge transport through the device, and it allows for predicting the switching behavior of recently proposed structures with a double reference layer [8] and MRAM cells with

an elongated and composite free layer [9]. The modeling approach was extended in *Contribution 3* to investigate the role of temperature on the switching behavior in a spin-orbit torque (SOT) MRAM cell. It was demonstrated that the critical voltage for SOT switching is significantly reduced at elevated temperatures. The critical SOT voltage displayed a parabolic decrease as a function of the voltage applied across the magnetic tunnel junction (MTJ) of the SOT-MRAM cell, in agreement with recent experimental data [10].

Magnetic tunnel junctions switch stochastically [11], with their switching probabilities dependent on the applied current. *Contribution 4* proposes the use of electrically controlled MTJs to mimic Ising spins to build an Ising annealing machine [12]. Simulations with an Ising annealing system constructed using 64 such spins demonstrated factorization of n-bit integers up to 2^{64} with a temporal complexity proportional to $\sqrt{n}$.

Heat-assisted magnetic recording (HAMR) technology is a promising alternative to replace the current perpendicular magnetic recording, further increasing the areal density of hard disk drives; however, unwanted noise may affect the read-back signal. The transition jitter noise at ultrahigh areal density in $L1_0$-FePt-based [13] HAMR technology was explored by means of micromagnetic simulations in *Contribution 5*. The lowest transition jitter was obtained in an 8 nm track width at a 9 nm bit length, yielding a projected ultrahigh areal density of 8.9 Tb/in^2 for upcoming applications.

Regarding the design and optimization of a complex electromagnetic element, namely, a solenoid valve used to control the flow velocity and the flow direction in microfluidics [14], *Contribution 6* deals with a numerical determination of the magnetic isolation ring position in a solenoid valve for optimal dynamic response performance. The proposed model was verified experimentally, and optimally designed solenoid valves were realized.

In *Contribution 7*, a novel method for antenna miniaturization based on acoustic excitations and magnetoelectric coupling [15] is elaborated. A magnetoelectric antenna was designed and successfully fabricated and tested. The results demonstrate its potential to overcome the miniaturization limits and impedance mismatch of traditional antennas.

Composite multiferroic materials comprising piezoelectric and magnetostrictive properties [16] are also suitable for designing novel types of interconnects for efficient magnetic signal transmission. Internal magnetic signal amplification due to a portion of energy being transferred from electric to magnetic domains via stress-mediated coupling helps to efficiently compensate strong signal dumping so that the amplitude of the magnetic signal remains constant during the propagation. The model introduced in *Contribution 8* predicts the group velocity of a magnetic signal up to 10^5 m/s with an amazingly small energy dissipation of less than 10^{-18} J per bit per 100 nm.

Exploring magnetostrictive materials' properties has great potential for the development of advanced sensors. Magnetorheological elastomers (MREs) are a representative example of such sensors; these materials' mechanical properties can be controlled by the use of magnetic fields with enhanced magnetostriction magnitude and reaction force [17]. In *Contribution 9*, an approach based on exploring materials with storage modulus above 300 kPa was pursued by investigating various compositions of carbonyl iron particles. It was demonstrated that increments in both the magnetostriction percentage and normal force were achieved at a higher concentration of the particles. This behavior confirms the feasibility of sensor applications of magnetorheological elastomers.

A specially designed magnetic field gradiometer based on a single elliptical planar Hall effect sensor was fabricated and tested in *Contribution 10*. The gradiometer measured magnetic fields at nine different positions within a length scale of a few millimeters. It was demonstrated that this innovative device is able to detect magnetic field gradients with equivalent gradient magnetic noises of about 958, 192, 51, and 26 $pT/(mm\sqrt{Hz})$ at 0.1, 1, 10, and 50 Hz frequencies, respectively. The fabricated low-cost, high-resolution, and small-footprint gradiometer has great potential for portable and wearable applications, as well as for body implants [18].

We would like to sincerely thank all the authors for submitting exceptional research papers to this Special Issue. We would also like to thank all the reviewers who took

their precious time to carefully examine and help improve the quality of all submitted manuscripts. Last, but not least, we would like to thank Ms. Aria Zeng, the Section Managing Editor, for her outstanding continuous support.

Conflicts of Interest: The authors declare no conflict of interest.

List of Contributions

1. Khosravi, P.; Seyyed Ebrahimi, S.A.; Lalegani, Z.; Hamawandi, B. Anisotropic Magnetoresistance Evaluation of Electrodeposited $Ni_{80}Fe_{20}$ Thin Film on Silicon. *Micromachines* **2022**, *13*, 1804. https://doi.org/10.3390/mi13111804.
2. Fiorentini, S.; Jørstad, N.P.; Ender, J.; de Orio, R.L.; Selberherr, S.; Bendra, M.; Goes, W.; Sverdlov, V. Finite Element Approach for the Simulation of Modern MRAM Devices. *Micromachines* **2023**, *14*, 898. https://doi.org/10.3390/mi14050898.
3. Hadámek, T.; Jørstad, N.P.; de Orio, R.L.; Goes, W.; Selberherr, S.; Sverdlov, V. A Comprehensive Study of Temperature and Its Effects in SOT-MRAM Devices. *Micromachines* **2023**, *14*, 1581. https://doi.org/10.3390/mi14081581.
4. Chen, W.; Tang, H.; Wang, Y.; Hu, X.; Lin, Y.; Min, T.; Xie, Y. E-Spin: A Stochastic Ising Spin Based on Electrically-Controlled MTJ for Constructing Large-Scale Ising Annealing Systems. *Micromachines* **2023**, *14*, 258. https://doi.org/10.3390/mi14020258.
5. Jongjaihan, C.; Kaewrawang, A. Micromagnetic Simulation of $L1_0$-FePt-Based Transition Jitter of Heat-Assisted Magnetic Recording at Ultrahigh Areal Density. *Micromachines* **2022**, *13*, 1559. https://doi.org/10.3390/mi13101559.
6. Guo, J.; Li, L.; Qin, P.; Wang, J.; Ni, C.; Zhu, X.; Lu, D.; Tang, J. Optimization Design of Magnetic Isolation Ring Position in AC Solenoid Valves for Dynamic Response Performances. *Micromachines* **2022**, *13*, 1065. https://doi.org/10.3390/mi13071065.
7. Li, N.; Li, X.; Xu, B.; Zheng, B.; Zhao, P. Design and Optimization of a Micron-Scale Magnetoelectric Antenna Based on Acoustic Excitation. *Micromachines* **2022**, *13*, 1584. https://doi.org/10.3390/mi13101584.
8. Khitun, A. Magnetic Interconnects Based on Composite Multiferroics. *Micromachines* **2022**, *13*, 1991. https://doi.org/10.3390/mi13111991.
9. Tasin, M.A.; Aziz, S.A.A.; Mazlan, S.A.; Johari, M.A.F.; Nordin, N.A.; Yusuf, S.Y.M.; Choi, S.-B.; Bahiuddin, I. Magnetostriction Enhancement in Midrange Modulus Magnetorheological Elastomers for Sensor Applications. *Micromachines* **2023**, *14*, 767. https://doi.org/10.3390/mi14040767.
10. Nhalil, H.; Schultz, M.; Amrusi, S.; Grosz, A.; Klein, L. High Sensitivity Planar Hall Effect Magnetic Field Gradiometer for Measurements in Millimeter Scale Environments. *Micromachines* **2022**, *13*, 1898. https://doi.org/10.3390/mi13111898.

References

1. Johnson, M. *Magnetoelectronics*; Elsevier: Amsterdam, The Netherlands, 2004.
2. Fabian, J.; Matos-Abiague, A.; Ertler, C.; Stano, P.; Zutic, I. Semiconductor Spintronics. *Acta Phys. Slovaca* **2007**, *57*, 565–907. [CrossRef]
3. Jansen, R. Silicon Spintronics. *Nat. Mater.* **2012**, *11*, 400–408. [CrossRef] [PubMed]
4. Sverdlov, V.; Jittong, N. Editorial for the Special Issue on Magnetic and Spin Devices. *Micromachines* **2022**, *13*, 493. [CrossRef] [PubMed]
5. Nishino, J.; Chatani, S.; Uotani, Y.; Nosaka, Y. Electrodeposition Method for Controlled Formation of CdS Films from Aqueous Solutions. *J. Electroanal. Chem.* **1999**, *473*, 217–222. [CrossRef]
6. Selberherr, S. *Analysis and Simulation of Semiconductor Devices*; Springer: Berlin/Heidelberg, Germany, 1984.
7. Apalkov, D.; Dieny, B.; Slaughter, J.M. Magnetoresistive Random Access Memory. *Proc. IEEE* **2016**, *104*, 1796–1830. [CrossRef]
8. Hu, G.; Safranski, C.; Sun, J.Z.; Hashemi, P.; Brown, S.L.; Bruley, J.; Buzi, L.; D'Emic, C.P.; Galligan, E.; Gottwald, M.G.; et al. Double Spin-torque Magnetic Tunnel Junction Devices for Last-level Cache Applications. In Proceedings of the 2022 International Electron Devices Meeting (IEDM), San Francisco, CA, USA, 2–8 December 2022; pp. 10.2.1–10.2.4. [CrossRef]
9. Jinnai, B.; Igarashi, J.; Shinoda, T.; Watanabe, K.; Fukami, S.; Ohno, H. Fast Switching Down to 3.5 ns in Sub-5-nm Magnetic Tunnel Junctions Achieved by Engineering Relaxation Time. In Proceedings of the 2021 IEEE International Electron Devices Meeting (IEDM), San Francisco, CA, USA, 11–16 December 2021; pp. 1–4. [CrossRef]
10. Lu, J.; Li, W.; Liu, J.; Liu, Z.; Wang, Y.; Jiang, C.; Du, J.; Lu, S.; Lei, N.; Peng, S.; et al. Voltage-gated Spin-orbit Torque Switching in IrMn-based Perpendicular Magnetic Tunnel Junctions. *Appl. Phys. Lett.* **2023**, *122*, 012402. [CrossRef]
11. Thomas, L.; Jan, G.; Serrano-Guisan, S.; Liu, H.; Zhu, J.; Lee, Y.-J.; Le, S.; Iwata-Harms, J.; Tong, R.-Y.; Patel, S.; et al. STT-MRAM Devices with Low Damping and Moment Optimized for LLC Applications at Ox Nodes. In Proceedings of the 2018 IEEE International Electron Devices Meeting (IEDM), San Francisco, CA, USA, 1–5 December 2018; pp. 27.3.1–27.3.4.
12. Böhm, F.; Verschaffelt, G.; Van Der Sande, G. A Poor Man's Coherent Ising Machine Based on Opto-electronic Feedback Systems for Solving Optimization Problems. *Nat. Commun.* **2019**, *10*, 3538. [CrossRef]
13. Wei, D.-H.; Chen, S.-C.; Yang, C.-J.; Huang, R.-T.; Dong, C.-L.; Yao, Y.-D. Formation of FePt–MgO Nanocomposite Films at Reduced Temperature. *J. Compos. Sci.* **2022**, *6*, 158. [CrossRef]

14. Zhang, Q.; Zhang, P.-R.; Su, Y.-T.; Mou, C.-B.; Zhou, T.; Yang, M.-L.; Xu, J.; Ma, B. On-demand Control of Microfluidic Flow via Capillary-tuned Solenoid Microvalve Suction. *Lab. Chip.* **2014**, *14*, 4599–4603. [CrossRef] [PubMed]
15. Yao, Z.; Wang, Y.E.; Keller, S.; Carman, G.P. Bulk Acoustic Wave-Mediated Multiferroic Antennas: Architecture and Performance Bound. *IEEE Trans. Antennas Progag.* **2015**, *63*, 3335–3344. [CrossRef]
16. Balinskiy, M.; Chavez, A.C.; Barra, A.; Chiang, H.; Carman, G.P.; Khitun, A. Magnetoelectric Spin Wave Modulator Based On Synthetic Multiferroic Structure. *Sci. Rep.* **2018**, *8*, 10867. [CrossRef] [PubMed]
17. Ahn, J.; Gu, J.; Choi, J.; Han, C.; Jeong, Y.; Park, J.; Cho, S.; Oh, Y.S.; Jeong, J.H.; Amjadi, M.; et al. A Review of Recent Advances in Electrically Driven Polymer-Based Flexible Actuators: Smart Materials, Structures, and Their Applications. *Adv. Mater. Technol.* **2022**, *7*, 2200041. [CrossRef]
18. Feiner, R.; Dvir, T. Tissue–electronics Interfaces: From Implantable Devices to Engineered Tissues. *Nat. Rev. Mater.* **2017**, *3*, 17076. [CrossRef]

Disclaimer/Publisher's Note: The statements, opinions and data contained in all publications are solely those of the individual author(s) and contributor(s) and not of MDPI and/or the editor(s). MDPI and/or the editor(s) disclaim responsibility for any injury to people or property resulting from any ideas, methods, instructions or products referred to in the content.

micromachines

MDPI

Article

Anisotropic Magnetoresistance Evaluation of Electrodeposited $Ni_{80}Fe_{20}$ Thin Film on Silicon

Payam Khosravi [1], Seyyed Ali Seyyed Ebrahimi [1,*], Zahra Lalegani [1] and Bejan Hamawandi [2,*]

[1] Advanced Magnetic Materials Research Center, School of Metallurgy and Materials, College of Engineering, University of Tehran, Tehran 111554563, Iran
[2] Department of Applied Physics, KTH Royal Institute of Technology, SE-106 91 Stockholm, Sweden
* Correspondence: saseyyed@ut.ac.ir (S.A.S.E.); bejan@kth.se (B.H.)

Abstract: In this study, a simple growth of permalloy NiFe (Py) thin films on a semiconductive Si substrate using the electrochemical deposition method is presented. The electrodeposition was performed by applying a direct current of 2 mA/cm^2 during different times of 120 and 150 s and thin films with different thicknesses of 56 and 70 nm were obtained, respectively. The effect of Py thickness on the magnetic properties of thin films was investigated. Field emission scanning electron microscopy (FESEM), energy-dispersive X-ray spectroscopy (EDS), atomic force microscopy (AFM), ferromagnetic resonance (FMR), anisotropic magnetoresistance (AMR), and magneto-optic Kerr effect (MOKE) analyses were performed to characterize the Py thin films. It was observed that the coercivity of the Py thin film increases by increasing the thickness of the layer. Microscopic images of the layers indicated granular growth of the Py thin films with different roughness values leading to different magnetic properties. The magnetic resonance of the Py thin films was measured to fully describe the magnetic properties of the layers. The magnetoresistance ratios of deposited Py thin films at times of 120 and 150 s were obtained as 0.226% and 0.235%, respectively. Additionally, the damping constant for the deposited sample for 120 s was estimated as 1.36×10^{-2}, which is comparable to expensive sputtered layers' characteristics.

Keywords: electrodeposition; permalloy; magnetoresistance; MOKE; AMR; FMR

Citation: Khosravi, P.; Seyyed Ebrahimi, S.A.; Lalegani, Z.; Hamawandi, B. Anisotropic Magnetoresistance Evaluation of Electrodeposited $Ni_{80}Fe_{20}$ Thin Film on Silicon. *Micromachines* **2022**, *13*, 1804. https://doi.org/10.3390/mi13111804

Academic Editors: Viktor Sverdlov and Seung-bok Choi

Received: 6 October 2022
Accepted: 20 October 2022
Published: 22 October 2022

Copyright: © 2022 by the authors. Licensee MDPI, Basel, Switzerland. This article is an open access article distributed under the terms and conditions of the Creative Commons Attribution (CC BY) license (https://creativecommons.org/licenses/by/4.0/).

1. Introduction

Py thin films have played a very important role in the field of magnetism and spintronics due to their low magnetic anisotropy [1–7]. They have been used extensively in magneto-resistive devices with high efficiency [8–10]. Additionally, due to their very low damping parameter, they have been widely used for high-frequency spintronic devices which have a function based on the ferromagnetic resonance effect [11,12]. As electronic devices are still very dependent on semiconductor-based technology, coating Py on the surface of Si is of vital importance for magnetic device developments.

Today, physical methods such as molecular beam epitaxy [13], the ion-beam method [14], the vacuum evaporation technique [15], and sputtering [16] are commonly used for the fabrication of thin films. The advantages of these methods are obtaining pure materials, sharp interfaces, and high control of film growth but they require high vacuum so these techniques are complicated and expensive. However, electrodeposition is a fabrication technique that does not require a vacuum and is a relatively simple and inexpensive method [17,18]. To obtain high-quality deposits, the electrodeposition technique is a proper method to control the thickness, composition, and stoichiometry of alloys [19–21]. However, the deposition of thin films by electrodeposition requires special care. For example, contamination and fluctuations of the composition have an undesirable effect on the magnetic properties of the manufactured film [22].

There are many previous studies that have reported electrodeposited Py films onto metal substrates [23–27]. However, reports on the electrodeposition of Py on Si are not

reported often, especially regarding magnetic characteristic investigations [28–30]. Silicon is an appropriate case as a substrate because it conducts properly well to allow electrodeposition without the need for a seed layer, leading to the fabricating of thin magnetic films matched with silicon technology [31]. It is significant to optimize the electrochemical conditions for Py electrodeposition onto semiconductor substrates to get the desired microstructure. In order to obtain the optimal thickness of Py for better adhesion between Py and substrate, Py thin films of submicrometer thickness were electrodeposited onto Si (111) surfaces by Gao et al. [32]. They reported that Py films were able to have proper adhesion to the Si substrate when the thickness of the initial deposited Py was more than 20 nm. They also determined the coercivity of samples with 150 nm thickness to be about 6.8 Oe. The skewed shape of the hysteresis of the magnetization curve for a thin film of Fe_xNi_{1-x} electrodeposited on Si (100) was presented by Spada et al. [33]. Additionally, it is found that using surfactants in the electrodeposition electrolyte can enhance the quality and adhesion. For example, strong adhesion of Py on Si substrate by electrodeposition from a solution containing saccharin was observed by Sam et al. [34].

In the present research, Py was electrodeposited directly onto a Si substrate without a seed layer. Despite not using organic additives such as saccharin in the electrodeposition solution, it was found that electroplating thin films represented reasonably strong adhesion to the Si substrates. The properly prepared Py thin films on the Si have the capacity to be used in technological elements. In particular, in this work, the static and dynamic magnetic properties of the electrodeposited Py thin films on the Si substrate were investigated. The main purpose of investigating the magnetic properties of the electrodeposited Py layers was to observe the anisotropic magnetoresistance (AMR) effect. The AMR signal was successfully detected. For the first time, a relatively comprehensive study of the magnetic properties of such a magnetic thin film via magneto transport, magneto-optic, and magneto resonance measurements were presented.

2. Experimental

2.1. Materials and Instrumentation

N-type silicon wafers (D.M.S Co., Hwaseong, South Korea), nickel (II) sulfate ($NiSO_4.6H_2O$, Merck, Darmstadt, Germany), iron (II) sulfate ($FeSO_4.7H_2O$, Merck, Germany), and boric acid (H_3BO_3, Merck, Germany) were used as primary materials to make the solution for electrodeposition.

Atomic force microscopy (AFM, NT-MDT TS150 ENTEGRA) was used to investigate the surface topography of the samples. The magneto-optic characteristic of prepared samples was examined by the magneto-optic Kerr effect (MOKE) based on differential intensity using a He-Ne laser. The light passed through a polarizer, then reflected by the sample and passed through an analyzer, and was monitored by a detector. Optical lenses were used to focus and regulate the laser beam before and after reflection, respectively. The magnetic field was applied parallel to the plane of incident laser light. Ferromagnetic resonance (FMR) was analyzed using a subminiature version A (SMA) connector. For this purpose, a radiofrequency (RF) field with a fixed output power of 16 dBm was applied to a 50 Ω micro-stripe line (200 μm width). The microwave frequency range of the external DC magnetic field was up to 20 GHz (step of 1 GHz). Anisotropic magnetoresistance (AMR) measurement was performed using a four-point probe setup (Keithley 2450). The morphology of the samples was studied by field emission scanning electron microscopy (FESEM, MIRA3TESCAN-XMU). Additionally, energy-dispersive spectroscopy (EDS) was used to determine the film composition.

2.2. Sample Preparation

2.2.1. Solution

$NiSO_4.6H_2O$ (0.4 M) was added to deionized water under stirring. After nickel sulfate was dissolved in deionized water at room temperature, $FeSO_4.7H_2O$ (0.004 M) was added

and stirred until dissolved. Then, H_3BO_3 (0.4 M) was added to the solution and the solution remained under stirring until it was homogenized.

It should be noted that before each use of the solution, it was placed in an ultrasound for 10 min to ensure its homogeneity.

2.2.2. Electrochemical Deposition

The silicon wafer was cut out into 1.5 cm × 1.5 cm slices. In order to remove surface contamination such as surface oxide, the Si substrate was immersed in hydrofluoric acid (HF, 10% v/v) solution for 30 s, then washed with ethanol, acetone, and distilled water, respectively. After washing, the Si samples were instantly transferred to the electrodeposition cell to prevent oxidation of the silicon surface. A two-electrode cell system was utilized for the deposition of the Py layers with platinum as anode and Si substrate as a cathode. Two samples were electrodeposited at room temperature: the samples (S1 and S2) were electrodeposited by applying a direct current of 2 mA/cm^2 for 120 s and 150 s, respectively.

3. Result and Discussion

Figure 1 shows the FESEM images and element distribution (EDS) map analysis of sample S1. As can be seen in Figure 1, the surface of the sample shows the island growth of Py grains. Additionally, according to Figure 1, the distribution of Ni and Fe in the layer is uniform, which indicates the homogeneity of the layer and confirms the success of the coating using the electrochemical method. It should be noted that it is very difficult to obtain a homogeneous layer in the process of electrochemical deposition because different parameters such as deposition time, applied voltage, current, and substrate can affect the process and each of them can cause non-uniformity in the deposited layer. In this study, the appropriate parameters for the deposition were determined after much trial and error to obtain a uniform layer.

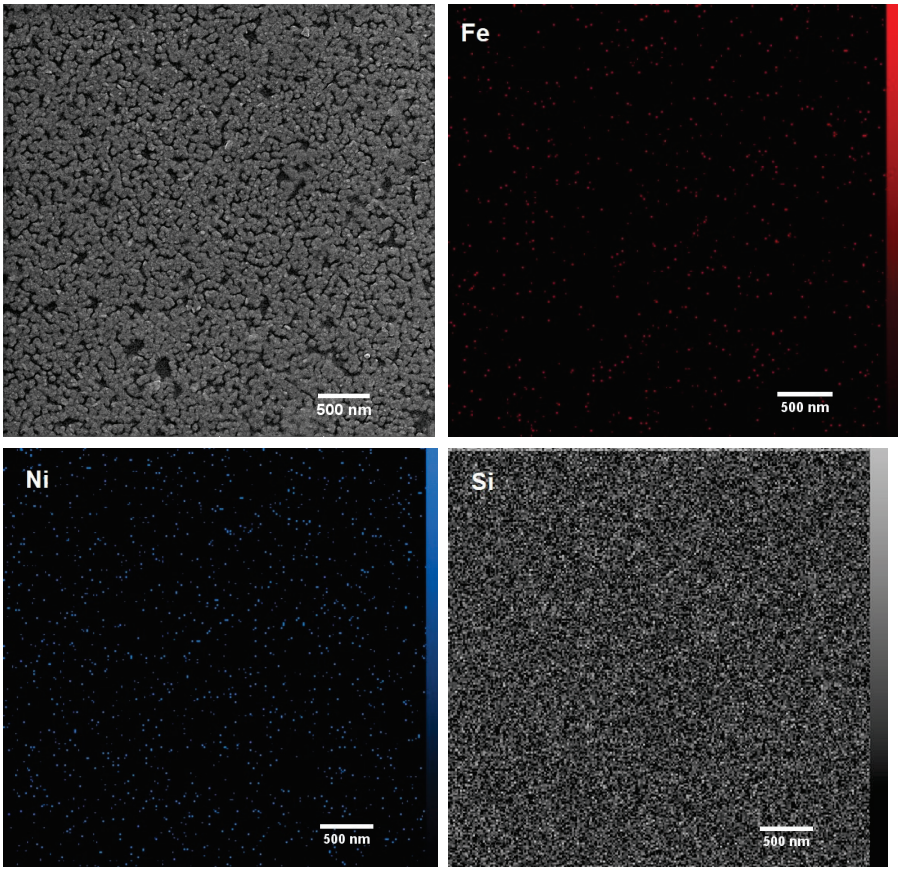

Figure 1. Morphology and element distribution map of sample S1.

Figure 2 shows the EDS analysis of sample S1. According to the EDS measurements, the Ni and Fe content of the layers were calculated and this shows that the ratio of the Ni to Fe is about 4:1, close to the composition of $Ni_{80}Fe_{20}$.

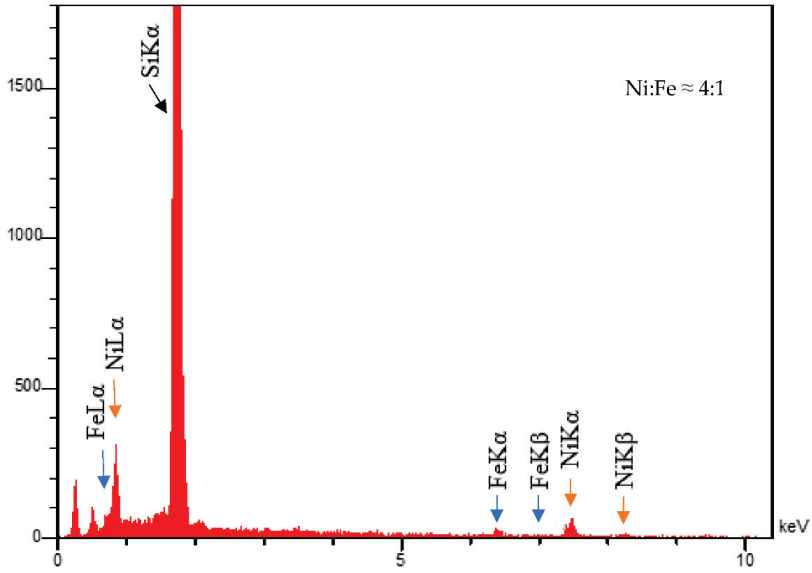

Figure 2. EDS analysis of sample S1.

The cross-sectional FESEM image of sample S1 is shown in Figure 3. According to Figure 3, the Py layer has an average thickness of about 56 nm, and it appears compact and fine in the structure. To estimate the thickness of the Py layer in sample S2, Faraday's law can be used [35]. According to Faraday's law, the thickness of coated layer with the electrochemical method can be determined by the following equation:

$$T = \frac{\alpha\, i\, M\, t}{10^{-7}\, F\, S\, n\, \rho} \tag{1}$$

where T is the thickness of the layer, t is time, i is the operating electric current, M is the molar mass of the substance, F is Faraday's constant, S is the area of electrodeposition, n is the number of electrons involved in an electrode reaction, ρ is the density of the substance, and α is the return coefficient which is equal to 1.516 here. The thickness of the S2 layer is estimated to be 70 nm by using Equation (1).

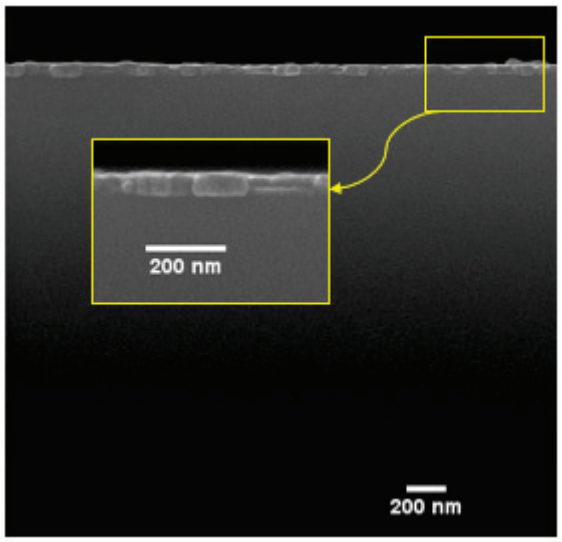

Figure 3. Cross-sectional FESEM image of sample S1.

AFM images analysis to investigate the surface morphologies (2D and 3D) of samples S1 and S2 are shown in Figure 4. AFM is a powerful technique to study the surface morphology at the nano- to micro-scale [36–39]. Topographical images from both samples were recorded over 5 µm × 5 µm scan areas. According to Figure 4, the grain size of both samples is in the nanometer range. It also shows that a rough surface was obtained by the electrodeposition method. According to the AFM results, a higher mean surface roughness (30 nm) is obtained for sample S2 deposited on Si in comparison with the mean surface roughness of sample S1 (22 nm). The AFM image of sample S1 shows regions with a typical rough shape and almost uniform grains. There are many sharp vertically aligned regions appearing in the topographical images of both samples S1 and S2. This vertical alignment can be the result of granular growth during the electroplating of the thin film. Electrodeposited samples in general give granular structure because the growth mode for electrochemical deposition of a metal (M) onto a substrate (S) follows the overall reaction [40]:

$$M^{+}_{solution} + e^{-} \xrightarrow{Substrate} M_{lattice} \quad (2)$$

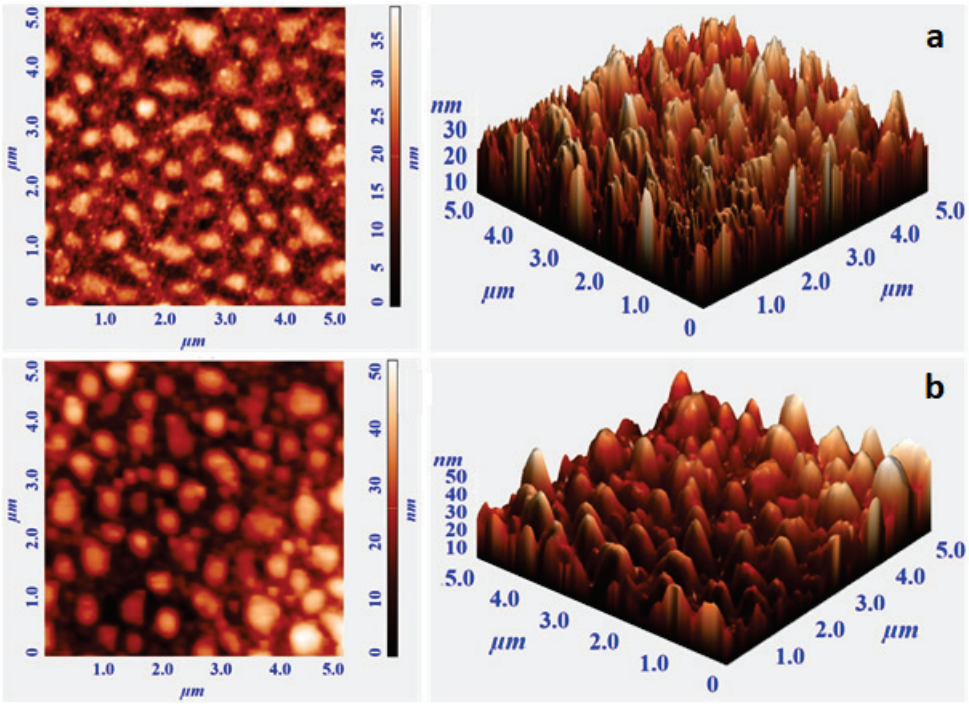

Figure 4. The 2D and 3D topographical images of (**a**) sample S1 and (**b**) sample S2.

Determinant parameters in this reaction are the interaction energy between the metal adatoms and the substrate (E_{M-S}), and the interaction energy or binding energy between the metal adatoms and the native substrate (E_{M-N}). In electrodeposition, $E_{M-S} < E_{M-N}$ and there is a driving force for the depositing material to segregate on the surface and deposition occurs according to the Volmer–Weber island growth mechanism [41,42].

The magnetic properties of the prepared samples are measured through MOKE, magnetoresistance (MR), and FMR measurements. According to the MOKE analysis, by increasing the Py thickness, coercivity is increased from 1.3 Oe for S1 to 3.9 Oe for S2. This could be due to alteration of thickness and also surface roughness. Some reports have discussed the increase of coercivity by increasing the thickness and attributed it to the existence of the out-of-plane anisotropy component at the thicker samples [43–46]. MOKE analysis showed that with an increase in Kerr intensity the saturation magnetization (M_s) is changed. Additionally, an increase in the thickness results in an increase in the interaction of light with the matter [47,48], hence both M_s and light–matter interaction are important.

The MR property was measured with two probe modes at room temperature by measuring the resistance of the samples as a function of the external magnetic field (H). The MR ratio was defined as [49]:

$$MR_{(H)} = \frac{\Delta\rho}{\rho_0} = \frac{\Delta R_{(H)}}{R_0} = \frac{R - R_0}{R_0} \quad (3)$$

where $\Delta\rho$ is the change in the sample resistivity, $\Delta R_{(H)}$ is the change of the sample resistance due to the magnetic applied field, ρ_0 is the zero-field resistivity, R_0 is the resistance of the sample, and R is the resistance in an external magnetic field H. Figure 5a shows the dependence of magnetoresistance and the angle between the electric field and the magnetic field. According to Figure 5a, for sample S1 the magnetoresistance increases by changing the angle between the electric field and magnetic field from 0 to 90. It can be due to the change in the angle between the magnetic easy-axis direction and the magnetic field [50]. According to Figure 5b, the MR ratios at the angle of 90 degrees are 0.226% and 0.235% for samples S1 and S2, respectively. According to previous studies [51,52], the magnitude of MR increases with the increase in thickness. AFM and FESEM studies showed that the thickness and roughness are larger in the case of sample S2 as compared to S1. A greater MR value in S2 compared to S1 could be due to the rough surface of S2. However, the effect of roughness and thickness has led to a negligible difference in the MR ratio. In comparison to other MR measurements of sputtered Py thin films, the MR ratios in this study are lower [53,54].

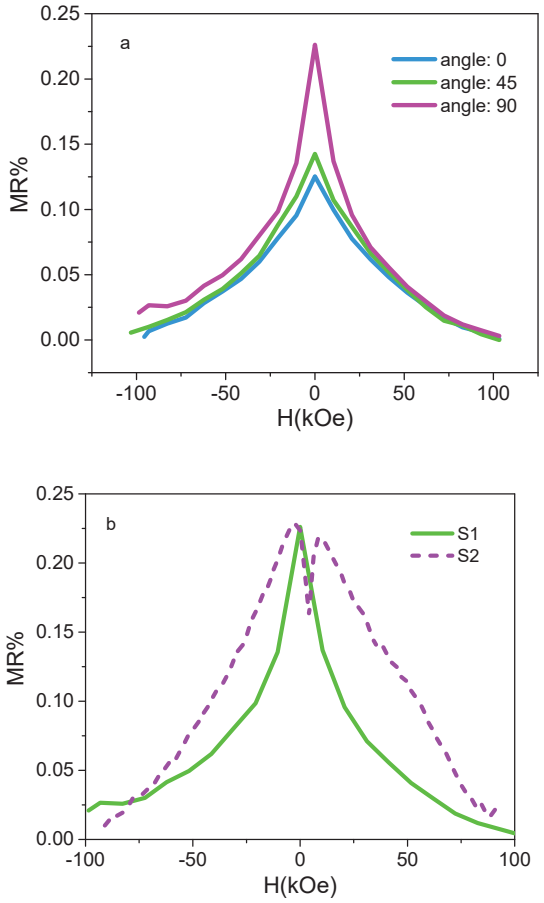

Figure 5. (**a**) AMR measurements for the S1 sample at different angles 0, 45, and 90° between H and current; (**b**) AMR measurements for S1 and S2 samples at the angle 90°.

FMR is a very powerful experimental technique in the study of ferromagnetic thin films. In the process of resonance, the energy is absorbed from the transverse magnetic

field, which occurred when the frequency matched the Larmor frequency. The Larmor frequency depends on the orientation of the material and the strength of the magnetic field. The dependence of FMR frequency on the external magnetic field for thin films can be described by the Kittel formula [55]:

$$f_r = \frac{\mu_0 \gamma}{2\pi} \sqrt{(H + H_k + M_s)(H + H_k)} \quad (4)$$

where μ_0 is the permeability of the free space, γ is the gyromagnetic ratio, H is the external magnetic field, M_s is the saturation magnetization, and H_k is the uniaxial anisotropy field, which is negligible for Py films with a thickness of 56 nm. FMR analysis was performed on sample S1 (with a thickness of 56 nm). The response of the sample to the FMR test is shown in Figure 6.

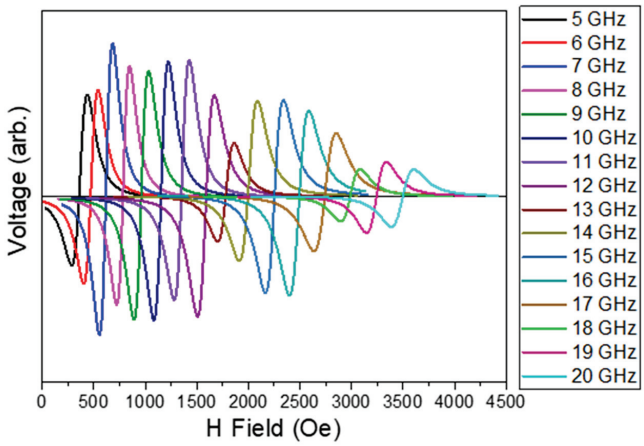

Figure 6. FMR analysis for sample S1.

Figure 7 shows the full width at half maximum (FWHM) of the resonance field peaks (ΔH) at each frequency. The damping constant can be derived from the FWHM [56]. According to Figure 7, the damping parameter was estimated as 1.36×10^{-2}. Several studies reported the value of the damping constant to be about 0.6×10^{-2} using the sputtering method for the deposition of thin films [57–59]. Additionally, some studies reported different damping constants for the deposition of permalloy onto a metal substrate such as Cu, Ag, and Ta [60]. One of the reasons for the increased damping constant in this study can be due to spin injection to Si substrate [61], which causes an increase in the damping constant.

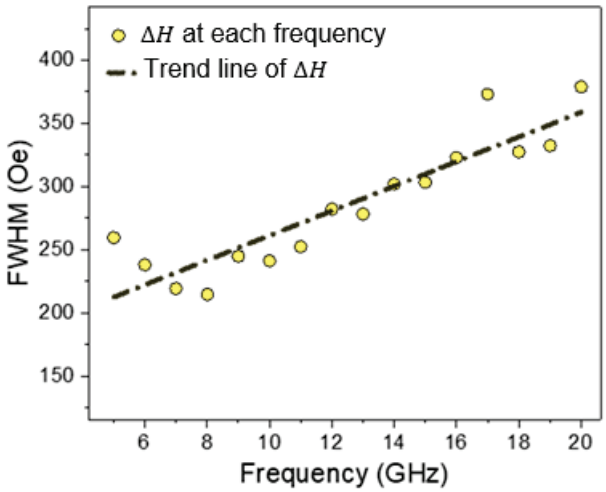

Figure 7. FMR analysis for sample S1 (FWHM vs. frequency).

4. Conclusions

In this research, the AMR effect was achieved with Py thin films prepared by a simple and inexpensive method. These layers were applied on inexpensive Si substrates which gives the layers great potential for use in Si-based electronics. The electrodeposited Py thin films represented good adhesion and uniformity on the Si surface. AFM and FESEM results showed that the thickness and morphology of the layers grown by electrodeposition can be tuned and, in turn, the MOKE, AMR, and FMR response of the layers can be controlled. The effect of electrodeposition time (120 s and 150 s) on the thickness of Py thin films was investigated and different thicknesses of 56 and 70 nm were obtained, respectively. The results showed that the increase in the thickness results in higher roughness, coercivity, MOKE signal, and AMR. The damping constant for Py thin film with 56 nm thickness was calculated as 1.36×10^{-2}, which is in the order of values achieved by sputtering. The proper magnetic characteristics along with the low-cost method and materials indicate that the growth method may be used for making industrial devices at a large scale with high functionality.

Author Contributions: Conceptualization, S.A.S.E.; Data curation, Z.L. and B.H.; Formal analysis, P.K. and Z.L.; Methodology, S.A.S.E.; Resources, S.A.S.E.; Supervision, S.A.S.E.; Validation, P.K. and Z.L.; Writing—original draft, P.K. and Z.L.; Writing—review and editing, S.A.S.E. and B.H. All authors have read and agreed to the published version of the manuscript.

Funding: This research did not receive any specific grant from funding agencies in the public, commercial, or not-for-profit sectors.

Conflicts of Interest: The authors declare that they have no conflict of interest.

References

1. Demand, M.; Encinas-Oropesa, A.; Kenane, S.; Ebels, U.; Huynen, I.; Piraux, L. Ferromagnetic resonance studies of nickel and permalloy nanowire arrays. *J. Magn. Magn. Mater.* **2002**, *249*, 228–233. [CrossRef]
2. Volmer, M.; Neamtu, J. Magnetic field sensors based on permalloy multilayers and nanogranular films. *J. Magn. Magn. Mater.* **2007**, *316*, e265–e268. [CrossRef]
3. Jiang, J.S.; Xiao, J.Q.; Chien, C.L. Magnetic properties and giant magnetoresistance of granular permalloy in silver. *Appl. Phys. Lett.* **1992**, *61*, 2362–2364. [CrossRef]
4. Manzin, A.; Nabaei, V.; Corte-León, H.; Kazakova, O.; Krzysteczko, P.; Schumacher, H.W. Modeling of anisotropic magnetoresistance properties of permalloy nanostructures. *IEEE Trans. Magn.* **2014**, *50*, 1–4. [CrossRef]
5. Zhang, B.; Fenineche, N.E.; Zhu, L.; Liao, H.; Coddet, C. Studies of magnetic properties of permalloy (Fe–30% Ni) prepared by SLM technology. *J. Magn. Magn. Mater.* **2012**, *324*, 495–500. [CrossRef]
6. Shi, Y.; Qian, P. Simulation Research of Magnetic Modulation Sensor Based on Permalloy. In Proceedings of the 2019 22nd International Conference on Electrical Machines and Systems (ICEMS), Harbin, China, 11–14 August 2019; pp. 1–5.
7. Greening, R.W.; Smith, D.A.; Lim, Y.; Jiang, Z.; Barber, J.; Dail, S.; Heremans, J.J.; Emori, S. Current-induced spin–orbit field in permalloy interfaced with ultrathin Ti and Cu. *Appl. Phys. Lett.* **2020**, *116*, 052402. [CrossRef]
8. Gong, M.; Dai, H. A mini review of NiFe-based materials as highly active oxygen evolution reaction electrocatalysts. *Nano Res.* **2015**, *8*, 23–39. [CrossRef]
9. Kwiatkowski, W.; Tumanski, S. The permalloy magnetoresistive sensors-properties and applications. *J. Phys. E Sci. Instrum.* **1986**, *19*, 502. [CrossRef]
10. Wang, S.; Gao, T.; Wang, C.; He, J. Studies of anisotropic magnetoresistance and magnetic property of Ni81Fe19 ultra-thin films with the lower base vacuum. *J. Alloy. Compd.* **2013**, *554*, 405–407. [CrossRef]
11. Bang, W.; Montoncello, F.; Kaffash, M.T.; Hoffmann, A.; Ketterson, J.B.; Jungfleisch, M.B. Ferromagnetic resonance spectra of permalloy nano-ellipses as building blocks for complex magnonic lattices. *J. Appl. Phys.* **2019**, *126*, 203902. [CrossRef]
12. Twisselmann, D.J.; McMichael, R.D. Intrinsic damping and intentional ferromagnetic resonance broadening in thin Permalloy films. *J. Appl. Phys.* **2003**, *93*, 6903–6905. [CrossRef]
13. Schreiber, N.; Nair, H.; Ruf, J.; Miao, L.; Goodge, B.; Shen, K.; Schlom, D. Growth and Characterization of Heterostructures of Ferromagnetic SrRuO 3 and Superconducting Sr 2 RuO 4 by Molecular-Beam Epitaxy. *Bull. Am. Phys. Soc.* **2020**, 65.
14. Nakatani, R.; Dei, T.; Kobayashi, T.; Sugita, Y. Giant magnetoresistance in Ni-Fe/Cu multilayers formed by ion beam sputtering. *IEEE Trans. Magn.* **1992**, *28*, 2668–2670. [CrossRef]
15. Neamtu, J.; Volmer, M. Magnetoresistance and magnetic properties of magnetic thin film multilayers. *Surf. Sci.* **2001**, *482*, 1010–1014. [CrossRef]

16. Meyer, D.C.; Paufler, P. Coherency and lattice spacings of textured permalloy/copper multilayers as revealed by X-ray diffraction. *J. Alloy. Compd.* **2000**, *298*, 42–46. [CrossRef]
17. Alper, M.; Schwarzacher, W.; Lane, S.J. The effect of pH changes on the giant magnetoresistance of electrodeposited superlattices. *J. Electrochem. Soc.* **1997**, *144*, 2346. [CrossRef]
18. Dulal, S.M.S.I.; Charles, E.A.; Roy, S. Characterisation of Co–Ni (Cu)/Cu multilayers deposited from a citrate electrolyte in a flow channel cell. *Electrochim. Acta* **2004**, *49*, 2041–2049. [CrossRef]
19. Ueda, Y.U.Y.; Ito, M.I.M. Magnetoresistance in Co–Cu alloy films formed by electrodeposition method. *Jpn. J. Appl. Phys.* **1994**, *33*, L1403. [CrossRef]
20. Yu, Z.; Jia, X.; Du, J.; Zhang, J. Electrochromic WO3 films prepared by a new electrodeposition method. *Sol. Energy Mater. Sol. Cells* **2000**, *64*, 55–63. [CrossRef]
21. Nishino, J.; Chatani, S.; Uotani, Y.; Nosaka, Y. Electrodeposition method for controlled formation of CdS films from aqueous solutions. *J. Electroanal. Chem.* **1999**, *473*, 217–222. [CrossRef]
22. Esmaili, S.; Bahrololoom, M.E. A new single bath for the electrodeposition of NiFe/Cu multilayers exhibiting giant magnetoresistance behavior. *Surface Eng. Appl. Electrochem.* **2012**, *48*, 35–41. [CrossRef]
23. Kockar, H.; Alper, M.; Kuru, H.; Meydan, T. Magnetic anisotropy and its thickness dependence for NiFe alloy films electrodeposited on polycrystalline Cu substrates. *J. Magn. Magn. Mater.* **2006**, *304*, e736–e738. [CrossRef]
24. Kok, K.Y.; Hangarter, C.M.; Goldsmith, B.; Ng, I.K.; Saidin, N.B.; Myung, N.V. Synthesis and characterization of electrodeposited permalloy (Ni80Fe20)/Cu multilayered nanowires. *J. Magn. Magn. Mater.* **2010**, *322*, 3876–3881. [CrossRef]
25. Kok, K.Y.; Hangarter, C.; Goldsmith, B.; Ng, I.K.; Saidin, N.U.; Myung, N.V. Template Assisted Growth and Characterization of Electrodeposited Permalloy (Ni80Fe20)/Cu Multilayered Nanowires. *ECS Trans.* **2010**, *25*, 97. [CrossRef]
26. Balachandran, R.; Yow, H.K.; Ong, B.H.; Tan, K.B.; Anuar, K.; Wong, H.Y. Surface morphology and electrical properties of pulse electrodeposition of NiFe films on copper substrates in ultrasonic field. *Int. J. Electrochem. Sci* **2011**, *6*, e3579.
27. Kuru, H.; Kockar, H.; Alper, M. Giant magnetoresistance (GMR) behavior of electrodeposited NiFe/Cu multilayers: Dependence of non-magnetic and magnetic layer thicknesses. *J. Magn. Magn. Mater.* **2017**, *444*, 132–139. [CrossRef]
28. Munford, M.L.; Seligman, L.; Sartorelli, M.L.; Voltolini, E.; Martins LF, O.; Schwarzacher, W.; Pasa, A.A. Electrodeposition of magnetic thin films of cobalt on silicon. *J. Magn. Magn. Mater.* **2001**, *226*, 1613–1615. [CrossRef]
29. Gómez, E.; Vallés, E. Electrodeposition of Co+ Ni alloys on modified silicon substrates. *J. Appl. Electrochem.* **1999**, *29*, 803–810. [CrossRef]
30. Pasa, A.A.; Schwarzacher, W. Electrodeposition of thin films and multilayers on silicon. *Phys. Status Solidi A* **1999**, *173*, 73–84. [CrossRef]
31. Rashkova, B.; Guel, B.; Pötzschke, R.T.; Staikov, G.; Lorenz, W.J. Electrodeposition of Pb on n-Si (111). *Electrochim. Acta* **1998**, *43*, 3021–3028. [CrossRef]
32. Gao, L.J.; Ma, P.; Novogradecz, K.M.; Norton, P.R. Characterization of Permalloy thin films electrodeposited on Si (111) surfaces. *J. Appl. Phys.* **1997**, *81*, 7595–7599. [CrossRef]
33. Spada, E.R.; De Oliveira, L.S.; Da Rocha, A.S.; Pasa, A.A.; Zangari, G.; Sartorelli, M.L. Thin films of FexNi1− x electroplated on silicon (1 0 0). *J. Magn. Magn. Mater.* **2004**, *272*, E891–E892. [CrossRef]
34. Sam, S.; Fortas, G.; Guittoum, A.; Gabouze, N.; Djebbar, S. Electrodeposition of NiFe films on Si (1 0 0) substrate. *Surf. Sci.* **2007**, *601*, 4270–4273. [CrossRef]
35. Barker, D.; Walsh, F.C. Applications of Faraday's laws of electrolysis in metal finishing. *Trans. IMF* **1991**, *69*, 158–162. [CrossRef]
36. Rugar, D.; Hansma, P. Atomic force microscopy. *Phys. Today* **1990**, *43*, 23–30. [CrossRef]
37. Albrecht, T.R.; Quate, C.F. Atomic resolution imaging of a nonconductor by atomic force microscopy. *J. Appl. Phys.* **1987**, *62*, 2599–2602. [CrossRef]
38. Meyer, E. Atomic force microscopy. *Prog. Surf. Sci.* **1992**, *41*, 3–49. [CrossRef]
39. Giessibl, F.J. Advances in atomic force microscopy. *Rev. Mod. Phys.* **2003**, *75*, 949. [CrossRef]
40. Tarditi, A.M.; Bosko, M.L.; Cornaglia, L.M. 3.1 Electroless Plating of Pd Binary and Ternary Alloys and Surface Characteristics for Application in Hydrogen Separation. In *Comprehensive Materials Finishing*; Elsevier: Oxford, UK, 2017; pp. 1–24.
41. Guo, L.; Oskam, G.; Radisic, A.; Hoffmann, P.M.; Searson, P.C. Island growth in electrodeposition. *J. Phys. D: Appl. Phys.* **2011**, *44*, 443001. [CrossRef]
42. Möller, F.A.; Magnussen, O.M.; Behm, R.J. Two-dimensional needle growth of electrodeposited Ni on reconstructed Au (111). *Phys. Rev. Lett.* **1996**, *77*, 3165. [CrossRef]
43. Miao, G.; Xiao, G.; Gupta, A. Variations in the magnetic anisotropy properties of epitaxial Cr O 2 films as a function of thickness. *Phys. Rev. B* **2005**, *71*, 094418. [CrossRef]
44. Poulopoulos, P.; Lindner, J.; Farle, M.; Baberschke, K. Changes of magnetic anisotropy due to roughness: A quantitative scanning tunneling microscopy study on Ni/Cu (001). *Surf. Sci.* **1999**, *437*, 277–284. [CrossRef]
45. Islam, J.; Yamamoto, Y.; Hori, H. Thickness-dependent coercivity and magnetization process of Co/GaAs (1 0 0). *J. Magn. Magn. Mater.* **2007**, *310*, 2234–2236. [CrossRef]
46. Camarero, J.; De Miguel, J.J.; Miranda, R.; Hernando, A. Thickness-dependent coercivity of ultrathin Co films grown on Cu (111). *J. Phys. Condens. Matter* **2000**, *12*, 7713. [CrossRef]

47. Arregi, J.A.; Riego, P.; Berger, A. What is the longitudinal magneto-optical Kerr effect? *J. Phys. D: Appl. Phys.* **2016**, *50*, 03LT01. [CrossRef]
48. Miyahara, T.; Takahashi, M. The dependence of the longitudinal Kerr magneto-optic effect on saturation magnetization in Ni-Fe films. *Jpn. J. Appl. Phys.* **1976**, *15*, 291. [CrossRef]
49. Tóth, B.G.; Péter, L.; Révész, Á.; Pádár, J.; Bakonyi, I. Temperature dependence of the electrical resistivity and the anisotropic magnetoresistance (AMR) of electrodeposited Ni-Co alloys. *Eur. Phys. J. B* **2010**, *75*, 167–177. [CrossRef]
50. Smith, D.O. Anisotropy in permalloy films. *J. Appl. Phys.* **1959**, *30*, S264–S265. [CrossRef]
51. Bakonyi, I.; Tóth, J.; Kiss, L.F.; Tóth-Kádár, E.; Péter, L.; Dinia, A. Origin of giant magnetoresistance contributions in electrodeposited Ni–Cu/Cu multilayers. *J. Magn. Magn. Mater.* **2004**, *269*, 156–167. [CrossRef]
52. Bakonyi, I.; Tóth, J.; Goualou, L.; Becsei, T.; Tóth-Kádár, E.; Schwarzacher, W.; Nabiyouni, G. Giant magnetoresistance of electrodeposited Ni81Cu19/Cu multilayers. *J. Electrochem. Soc.* **2002**, *149*, C195. [CrossRef]
53. Guanghua, Y.U.; Hongchen, Z.H.A.O.; Fengwu, Z.H.U. Ultrathin permalloy films. *Chin. Sci. Bull.* **2001**, *46*, 1681–1684. [CrossRef]
54. Kateb, M.; Ingvarsson, S. Thickness-dependent magnetic and magnetoresistance properties of permalloy prepared by field assisted tilt sputtering. In Proceedings of the 2017 IEEE Sensors Applications Symposium (SAS), Glassboro, NJ, USA, 13–15 March 2017; pp. 1–5.
55. Schmool, D.S.; Rocha, R.; Sousa, J.B.; Santos, J.A.M.; Kakazei, G.N.; Garitaonandia, J.S.; Rodriguez, D.M.; Lezama, L.; Barandiarán, J.M. Ferromagnetic resonance in nanometric magnetic systems. *J. Optoelectron. Adv. Mater.* **2004**, *6*, 541–550.
56. Landau, L.; Lifshitz, E. On the theory of the dispersion of magnetic permeability in ferromagnetic bodies. In *Perspectives in Theoretical Physics*; Pergamon: Oxford, UK, 1992; pp. 51–65.
57. Nahrwold, G.; Scholtyssek, J.M.; Motl-Ziegler, S.; Albrecht, O.; Merkt, U.; Meier, G. Structural, magnetic, and transport properties of Permalloy for spintronic experiments. *J. Appl. Phys.* **2010**, *108*, 013907. [CrossRef]
58. Urban, R.; Heinrich, B.; Woltersdorf, G.; Ajdari, K.; Myrtle, K.; Cochran, J.F.; Rozenberg, E. Nanosecond magnetic relaxation processes in ultrathin metallic films prepared by MBE. *Phys. Rev. B* **2001**, *65*, 020402. [CrossRef]
59. Celinski, Z.; Urquhart, K.B.; Heinrich, B. Using ferromagnetic resonance to measure the magnetic moments of ultrathin films. *J. Magn. Magn. Mater.* **1997**, *166*, 6–26. [CrossRef]
60. Rantschler, J.O.; Maranville, B.B.; Mallett, J.J.; Chen, P.; McMichael, R.D.; Egelhoff, W.F. Damping at normal metal/permalloy interfaces. *IEEE Trans. Magn.* **2005**, *41*, 3523–3525. [CrossRef]
61. Oestreich, M.; Hübner, J.; Hägele, D.; Klar, P.J.; Heimbrodt, W.; Rühle, W.W.; Ashenford, D.E.; Lunn, B. Spin injection into semiconductors. *Appl. Phys. Lett.* **1999**, *74*, 1251–1253. [CrossRef]

micromachines

MDPI

Article

Finite Element Approach for the Simulation of Modern MRAM Devices

Simone Fiorentini [1,2], Nils Petter Jørstad [1,2], Johannes Ender [1,2], Roberto Lacerda de Orio [2], Siegfried Selberherr [2], Mario Bendra [1,2], Wolfgang Goes [3] and Viktor Sverdlov [1,2,*]

[1] Christian Doppler Laboratory for Nonvolatile Magnetoresistive Memory and Logic at the Institute for Microelectronics, TU Wien, Gußhausstraße 27-29/E360, 1040 Vienna, Austria; fiorentini@iue.tuwien.ac.at (S.F.); jorstad@iue.tuwien.ac.at (N.P.J.); ender@iue.tuwien.ac.at (J.E.); bendra@iue.tuwien.ac.at (M.B.)
[2] Institute for Microelectronics, TU Wien, Gußhausstraße 27-29/E360, 1040 Vienna, Austria; orio@iue.tuwien.ac.at (R.L.d.O.); selberherr@tuwien.ac.at (S.S.)
[3] Silvaco Europe Ltd., Cambridge PE27 5JL, UK; wolfgang.goes@silvaco.com
* Correspondence: sverdlov@iue.tuwien.ac.at

Abstract: Because of their nonvolatile nature and simple structure, the interest in MRAM devices has been steadily growing in recent years. Reliable simulation tools, capable of handling complex geometries composed of multiple materials, provide valuable help in improving the design of MRAM cells. In this work, we describe a solver based on the finite element implementation of the Landau–Lifshitz–Gilbert equation coupled to the spin and charge drift-diffusion formalism. The torque acting in all layers from different contributions is computed from a unified expression. In consequence of the versatility of the finite element implementation, the solver is applied to switching simulations of recently proposed structures based on spin-transfer torque, with a double reference layer or an elongated and composite free layer, and of a structure combining spin-transfer and spin-orbit torques.

Keywords: finite element method; micromagnetics; spin and charge drift-diffusion; MRAM

Citation: Fiorentini, S.; Jørstad, N.P.; Ender, J.; de Orio, R.L.; Selberherr, S.; Bendra, M.; Goes, W.; Sverdlov, V. Finite Element Approach for the Simulation of Modern MRAM Devices. *Micromachines* **2023**, *14*, 898. https://doi.org/10.3390/mi14050898

Academic Editor: Zhongrui Wang

Received: 18 March 2023
Revised: 14 April 2023
Accepted: 20 April 2023
Published: 22 April 2023

Copyright: © 2023 by the authors. Licensee MDPI, Basel, Switzerland. This article is an open access article distributed under the terms and conditions of the Creative Commons Attribution (CC BY) license (https://creativecommons.org/licenses/by/4.0/).

1. Introduction

As the scaling of conventional CMOS technology shows signs of saturation, due to the increase in standby power consumption and leakage currents, the employment of nonvolatile memory components which do not require the memory bits to be refreshed becomes increasingly appealing [1]. One of the most promising candidates as a nonvolatile replacement is magnetoresistive random access memory (MRAM). It possesses a simple structure and is directly compatible with CMOS back-end of line processes. It has shown to be promising for several applications, for example in stand-alone memories and in the embedded automotive and Internet of Things fields, and is expected to replace charge-based devices in frame buffer memory and slow SRAM [2–5]. Moreover, MRAM devices have shown to be interesting for cryogenic applications, especially for employment in quantum computing systems [6–8].

The core of an MRAM cell is the magnetic tunnel junction (MTJ), a stack of two ferromagnetic (FM) layers separated by an oxide layer. The properties of the two FM layers are such that the magnetization in one of them, the reference layer (RL), is fixed, while in the other one, the free layer (FL), it can be switched between the two stable parallel (P) and anti-parallel (AP) states. The resistance of the stack can be employed to store the binary information, as it is higher in the AP state. The percentage difference between the resistance of the two stable states is labeled the tunneling magnetoresistance ratio (TMR).

The writing process in modern devices is performed by relying on spin-transfer torque (STT), spin-orbit torque (SOT), or a combination of both of them. In STT switching, the torque is generated by a current flowing through the MTJ. The electrons are polarized by the RL and

transfer their polarization to the FL magnetization, providing the torque [9–11]. Examples of structures based on STT are reported in Figure 1a–c. In SOT switching, the torque is generated by passing the current through a heavy metal line (HM) below the FL. The spin Hall effect (SHE) produces a spin current orthogonal to the charge one, which is absorbed by the FL magnetization, providing the torque [12,13]. An example of a three-terminal structure combining STT and SOT is shown in Figure 1d.

The design of modern MRAM cells can be supported by the development of reliable simulation tools. The magnetization dynamics are described by the Landau–Lifshitz–Gilbert (LLG) equation, which must be supplied with a term describing the spin torque. The drift-diffusion formalism offers a way of computing different torque contributions in all the ferromagnetic layers from a unified expression [14–16]. The finite element (FE) method, being able to handle structures with several domains of different materials and complex geometries, represents an optimal choice for computing a numerical solution to the micromagnetic equations in modern MRAM cells. In this work, we present an FE-based implementation of the LLG equation coupled with the drift-diffusion formalism, extended to include the charge and torque properties expected in MTJs. The solver was developed by employing the open-source C++ FE library MFEM [17,18], and is applied to the simulation of recently proposed structures based both on STT and SOT switching. The source code is available as an open-source repository [19].

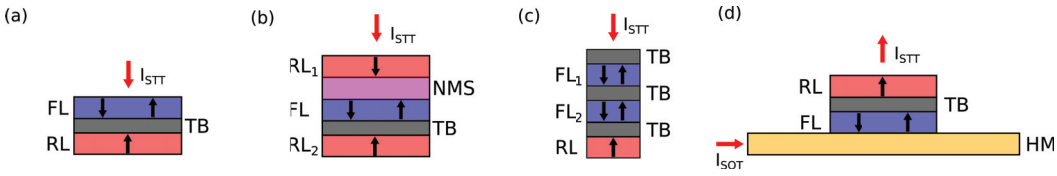

Figure 1. Four examples of multi-layer MRAM cell design: (**a**) standard STT-MRAM with single MTJ; (**b**) double RL STT-MRAM, where the second RL provides additional torque to reduce the critical voltage required for switching [20]; (**c**) ultra-scaled STT-MRAM, where the FM layers are elongated and additional oxide layers are added to improve scalability and benefit from the shape anisotropy [21]; (**d**) SOT-assisted STT-MRAM, where the switching process is kick-started by an initial current pulse in the HM [22].

2. Micromagnetic Modeling

The LLG equation for the description of the magnetization dynamics was first derived by Landau and Lifshitz in 1935 [23] and reworked by Gilbert in a more treatable form in 1955 [24]. With the inclusion of the spin torque $\mathbf{T}_S$, it takes the form

$$\frac{\partial \mathbf{m}}{\partial t} = -|\gamma|\mu_0\, \mathbf{m} \times \mathbf{H}_{\text{eff}} + \alpha\, \mathbf{m} \times \frac{\partial \mathbf{m}}{\partial t} + \frac{1}{M_S}\mathbf{T}_S \tag{1}$$

where $\mathbf{m} = \mathbf{M}/M_S$ is the unit vector in the direction of the local magnetization, M_S is the saturation magnetization, γ is the gyromagnetic ratio, and μ_0 is the vacuum permeability. $\mathbf{H}_{\text{eff}}$ is an effective magnetic field including the contributions of an externally applied field, the exchange coupling, the anisotropy field, and the demagnetizing field. The effects of temperature, which can be included by an additional effective field contribution describing thermal fluctuations [25], are not considered for the switching results presented in this work. The main effect of their inclusion would be to reduce the incubation time necessary for the switching process, while the behavior would remain qualitatively similar. While the external field $\mathbf{H}_{\text{ext}}$ can be simply added as an input parameter, the other contributions are intrinsic to the ferromagnets and must be computed from material parameters.

The exchange coupling can be modeled through a field which tends to keep the magnetization vectors aligned throughout the magnetic domain, described by the expression

$$\mathbf{H}_{\text{exc}} = \frac{2A_{\text{exc}}}{\mu_0 M_{\text{S}}} \nabla^2 \mathbf{m}\,, \tag{2}$$

where A_{exc} is the exchange coefficient.

Modern MRAM cells utilize MTJs with magnetization perpendicular to the stack, by virtue of both interface and shape anisotropy contributions [21]. While the latter is taken into account by the demagnetizing field, the former can be included as a uniaxial anisotropy field with the expression

$$\mathbf{H}_{\text{ani}} = \frac{2K_{\text{ani}}}{\mu_0 M_{\text{S}}} (\mathbf{a} \cdot \mathbf{m}) \mathbf{a}\,, \tag{3}$$

where **a** is a unit vector in the direction perpendicular to the stack and K_{ani} is the anisotropy coefficient, which can be computed from the interface anisotropy K_{int} as $K_{\text{ani}} = K_{\text{int}}/d_{\text{FM}}$, where d_{FM} is the thickness of the ferromagnetic layer under consideration.

The demagnetizing field can be computed from the scalar magnetic potential u_{m} as

$$\mathbf{H}_{\text{demag}} = -\boldsymbol{\nabla} u_{\text{m}} \tag{4}$$

u_{m} is obtained through the solution of the Poisson equation

$$-\nabla^2 u_{\text{m}} = -M_{\text{S}} \boldsymbol{\nabla} \cdot \mathbf{m}\,, \tag{5}$$

with the constraint of u_{m} decaying to zero as $\mathcal{O}(1/|\mathbf{x}|^2)$ outside the magnetic domain and the boundary condition $[\boldsymbol{\nabla} u_{\text{m}} \cdot \mathbf{n}] = -M_{\text{S}}\, \mathbf{m} \cdot \mathbf{n}$, where **n** is the unit vector normal to the boundary and $[\ldots]$ denotes a discontinuity across the boundary.

In the presence of a single thin FL, the torque acting on the magnetization can be described by simplified expressions [26–29], derived by Slonczewski [9,11]. A more general form of the torque term, which allows an arbitrary number of ferromagnetic and non-magnetic layers to be dealt with, can be obtained by computing the non-equilibrium spin accumulation in the structure under study through the solution of spin and charge transport equations.

Spin and Charge Transport

The torque term $\mathbf{T}_{\text{S}}$ entering (1) can be computed from the spin accumulation through the following expression [16,30–32]:

$$\mathbf{T}_{\text{S}} = -D_{\text{e}} \frac{\mathbf{m} \times \mathbf{S}}{\lambda_J^2} - D_{\text{e}} \frac{\mathbf{m} \times (\mathbf{m} \times \mathbf{S})}{\lambda_\varphi^2} \tag{6}$$

The first term describes the precession around the exchange field and is characterized by the exchange length λ_J, and the second term describes the dephasing process of the spins of the transiting electrons, and is characterized by the dephasing length λ_φ. D_{e} is the electron diffusion coefficient. The spin accumulation **S** describes the deviation of the polarization of the conducting electrons from the equilibrium configuration created by a charge current density $\mathbf{J}_{\text{C}}$, in units of the transported magnetic moment (A/m). Thus, by definition, **S** is non-zero only when an electric current is flowing through the system [33]. A solution for **S** in all non-magnetic and ferromagnetic layers of an MRAM cell can be obtained by means of the spin and charge drift-diffusion formalism.

Spin and charge drift-diffusion equations in multilayer structures with arbitrary magnetization orientation were reported by S. Zhang, P. Levy, and A. Fert [34], with both the precession and decay of the transverse spin accumulation components governed by the exchange length λ_{J}. Another possible mechanism for the absorption of the transverse components is the dephasing process [32,35]. The behavior of the spin accumulation with both precessional and dephasing terms was described in terms of the Continuous Random Matrix Theory (CRMT) in [35], and the equivalence of the CMRT and the spin and charge

drift-diffusion formalism was shown. The resulting equations for spin and charge currents are [14,16]:

$$\mathbf{J}_\mathrm{C} = \sigma\mathbf{E} + \frac{e}{\mu_\mathrm{B}}\beta_\mathrm{D} D_\mathrm{e}(\boldsymbol{\nabla}\mathbf{S})^\mathrm{T}\mathbf{m}\,, \tag{7}$$

$$\tilde{\mathbf{J}}_\mathrm{S} = -\frac{\mu_\mathrm{B}}{e}\beta_\sigma \mathbf{m}\otimes(\sigma\mathbf{E}) - D_\mathrm{e}\boldsymbol{\nabla}\mathbf{S}\,, \tag{8}$$

where $\tilde{\mathbf{J}}_\mathrm{S}$ is the spin current tensor, $\mathbf{J}_\mathrm{C}$ is the charge current density, μ_B is the Bohr magneton, e is the elementary charge, σ is the conductivity, and $\otimes$ is the outer product. $\beta_\sigma = \left(\sigma^\uparrow - \sigma^\downarrow\right)/\left(\sigma^\uparrow + \sigma^\downarrow\right)$ and $\beta_\mathrm{D} = \left(D_\mathrm{e}^\uparrow - D_\mathrm{e}^\downarrow\right)/\left(D_\mathrm{e}^\uparrow + D_\mathrm{e}^\downarrow\right)$ are the conductivity and diffusion polarization parameters, respectively, with $\sigma^\uparrow$, $D_\mathrm{e}^\uparrow$ ($\sigma^\downarrow$, $D_\mathrm{e}^\downarrow$) the conductivity and diffusion coefficient for the majority (minority) electrons. $\boldsymbol{\nabla}\mathbf{S}$ is the vector gradient of $\mathbf{S}$, with components $(\boldsymbol{\nabla}\mathbf{S})_\mathrm{ij} = \partial S_\mathrm{i}/\partial x_\mathrm{j}$, and the term $(\boldsymbol{\nabla}\mathbf{S})^\mathrm{T}\mathbf{m}$ is a vector with components $\left((\boldsymbol{\nabla}\mathbf{S})^\mathrm{T}\mathbf{m}\right)_\mathrm{i} = \sum_\mathrm{j}\left(\partial S_\mathrm{j}/\partial x_\mathrm{i}\right)m_j$. The spin current can be expressed in terms of the charge current by inserting (7) into (8):

$$\tilde{\mathbf{J}}_\mathrm{S} = -\frac{\mu_B}{e}\beta_\sigma \mathbf{m}\otimes\left(\mathbf{J}_\mathrm{C} - \frac{e}{\mu_B}\beta_D D_e(\boldsymbol{\nabla}\mathbf{S})^\mathrm{T}\mathbf{m}\right) - D_e\boldsymbol{\nabla}\mathbf{S} \tag{9}$$

The equation of motion for the spin accumulation is given by

$$\frac{\partial\mathbf{S}}{\partial t} = -\boldsymbol{\nabla}\cdot\tilde{\mathbf{J}}_\mathrm{S} - D_\mathrm{e}\frac{\mathbf{S}}{\lambda_{sf}^2} - \mathbf{T}_\mathrm{S}\,, \tag{10}$$

where λ_sf is the spin-flip length and $\nabla\cdot\tilde{\mathbf{J}}_\mathrm{S}$ is the divergence of $\tilde{\mathbf{J}}_\mathrm{S}$, with components $\left(\nabla\cdot\tilde{\mathbf{J}}_\mathrm{S}\right)_\mathrm{i} = \sum_\mathrm{j}\partial J_{\mathrm{S,ij}}/\partial x_\mathrm{j}$. As the typical time scale for the magnetization motion is three orders of magnitude larger than the spin accumulation one [34], it is sufficient to consider a steady-state expression for the spin accumulation. This assumption was numerically verified in [36]. With $\partial\mathbf{S}/\partial t = 0$, the equation describing the spin accumulation becomes

$$-\boldsymbol{\nabla}\cdot\tilde{\mathbf{J}}_\mathrm{S} - D_\mathrm{e}\frac{\mathbf{S}}{\lambda_{sf}^2} - \mathbf{T}_\mathrm{S} = 0 \tag{11}$$

3. Finite Element Implementation

The presented set of equations allows the magnetization dynamics of structures containing an arbitrary number of layers of different materials to be described. The FE method, a numerical approach for the computation of approximate solutions to partial differential equations, is naturally able to handle meshes with complex geometries and several domains of different materials [37,38], and was therefore employed for the implementation of a solver capable of handling charge, spin accumulation, and the magnetization dynamics. The implementation was carried out by employing the open-source C++ FE library MFEM [17,18].

The first schemes for a FE implementation of the LLG equation, which considered only the contribution of the exchange coupling, were proposed in [39,40]. A new FE algorithm, referred to as the tangent plane integrator scheme, was introduced in [41] and later generalized in [42,43] to include the contributions of the demagnetizing and anisotropy fields. The unconditional convergence of an algorithm coupling the LLG equation with a FE implementation of the spin and charge drift-diffusion formalism was proven in [44], and the scheme was later successfully applied to metallic spin valves in [14]. We report here an extension of the scheme to MTJs, which includes the spin dephasing contribution and allows both the TMR effect and the expected torque properties to be reproduced [45,46].

3.1. Charge Current Solution

For the computation of the charge current entering (9), the Laplace equation is solved:

$$-\boldsymbol{\nabla} \cdot (\sigma \boldsymbol{\nabla} V) = 0 \tag{12}$$

$$\mathbf{J}_{\mathrm{C}} = -\sigma \boldsymbol{\nabla} V \tag{13}$$

where V is the electric potential. Dirichlet conditions are applied to prescribe the voltage at the contacts, and the Neumann condition $\sigma \boldsymbol{\nabla} V \cdot \mathbf{n} = 0$ is assumed on external boundaries not containing an electrode, with $\mathbf{n}$ the unit vector normal to the boundary. In order to be able to reproduce the TMR effect, the tunnel barrier is treated as a poor conductor whose local conductivity depends on the relative magnetization orientation in the RL and FL [45,46]:

$$\sigma_{\mathrm{TB}} = \sigma_0 (1 + P_{\mathrm{FL}}\, P_{\mathrm{RL}} \mathbf{m}_{\mathrm{RL}} \cdot \mathbf{m}_{\mathrm{FL}}) \tag{14}$$

where P_{RL} and P_{FL} are the Slonczewski polarization parameters [11,47], $\sigma_0 = (\sigma_P + \sigma_{AP})/2$ is the angle independent portion of the conductivity, $\sigma_{P(AP)}$ is the conductivity in the parallel (anti-parallel) state, and $\mathbf{m}_{\mathrm{RL(FL)}}$ is the magnetization of the RL(FL) close to the interface. P_{RL} and P_{FL} are related to the TMR by Julliere's formula [48]:

$$\mathrm{TMR} = \frac{R_{\mathrm{AP}} - R_{\mathrm{P}}}{R_{\mathrm{P}}} = \frac{2\, P_{\mathrm{FL}} P_{\mathrm{RL}}}{1 - P_{\mathrm{FL}} P_{\mathrm{RL}}} \tag{15}$$

where $R_{\mathrm{P(AP)}}$ is the resistance in the parallel (anti-parallel) state.

In order to derive an FE representation, the equations must be written in the so-called weak formulation. For the presented Laplace equation, by using Gauss's theorem and applying the Neumann boundary conditions, the weak form reduces to

$$\int_{\Omega} \sigma \boldsymbol{\nabla} V \cdot \boldsymbol{\nabla} v \, \mathrm{d}\mathbf{x} = 0 \tag{16}$$

The test function v and the solution are both assumed to belong to the Sobolev space H^1, so that both they and their weak gradients are L^2-integrable [43].

In the FE approximation, in order to obtain a discretized version of (16), the original domain Ω is divided into smaller regular elements. The discrete solution V_{h} is defined by its values on the elements' nodes:

$$V_{\mathrm{h}}(\mathbf{x}) = \sum_{i=1}^{N} V_{\mathrm{i}} \varphi_{\mathrm{i}}(\mathbf{x}) \tag{17}$$

where N is the total number of nodes, $V_{\mathrm{i}} = V_{\mathrm{h}}(\mathbf{x}_{\mathrm{i}})$ are the values assumed by the approximate solution at the nodes, and $\mathbf{x}_{\mathrm{i}}$ is the coordinate vector of node i. φ_{i} is an affine function of the nodal basis of the mesh, characterized as

$$\varphi_{\mathrm{i}}(\mathbf{x}_{\mathrm{j}}) = \delta_{ij} \tag{18}$$

Figure 2 illustrates an example of the approximation of a function u through linear basis functions in a one-dimensional scenario.

With the given nodal basis decomposition, the original problem can thus be rewritten as the following system of linear equations:

$$\underline{A_{\mathrm{V}}}\, \underline{V_{\mathrm{h}}} = \underline{0} \tag{19}$$

where $\underline{A_{\mathrm{V}}} \in \mathbb{R}^N \times \mathbb{R}^N$ is the matrix representation of the left-hand side (LHS) of (16), and $\underline{V_{\mathrm{h}}}$ is a vector in $\mathbb{R}^N$ composed of the nodal values of V_{h}. As only neighboring nodes have overlapping basis functions, $\underline{A_{\mathrm{V}}}$ is a sparse matrix, with non-zero terms only around the diagonal.

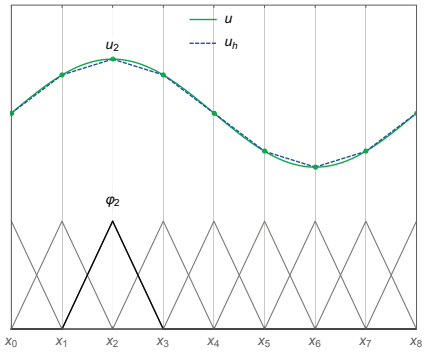

Figure 2. Representation of a continuous function u and its finite element approximation u_h in a one-dimensional setting. The basis functions for all the nodes are reported at the bottom of the graph. The basis function and solution value associated with the node x_2 are labeled φ_2 and u_2, respectively.

The weak formulation of (13) is

$$\int_\Omega \mathbf{J}_\mathrm{C} \cdot \boldsymbol{v}\, \mathrm{d}\mathbf{x} = -\int_\Omega \sigma \boldsymbol{\nabla} V \cdot \boldsymbol{v}\, \mathrm{d}\mathbf{x} \tag{20}$$

By choosing the test function $\boldsymbol{v}$ so that its components belong to H^1, noting the space containing $\boldsymbol{v}$ as $\mathbf{H}^1$, this equation allows a projection to be obtained of $\mathbf{J}_\mathrm{C}$ in the $\mathbf{H}^1$ function space [33] so that it can be readily employed for the computation of the spin accumulation. The resulting system of linear equations is

$$\underline{A_\mathrm{J}}\, \underline{\mathbf{J}_\mathrm{C,h}} = \underline{f_\mathrm{J}}\,, \tag{21}$$

where $\underline{A_\mathrm{J}} \in \mathbb{R}^{3N} \times \mathbb{R}^{3N}$ is the matrix coming from the LHS of (20) and $\underline{f_\mathrm{J}} \in \mathbb{R}^{3N}$ is the vector coming from the right-hand side (RHS).

The solution to both systems of equations is computed through a solver based on the conjugate gradient method [49], designed for the numerical solution of systems of linear equations whose matrices are positive definite, provided by the library MFEM.

In the scope of the MFEM library, only the data associated with a local element can be accessed during the assembly of the system matrices, while the computation of (14) in the TB requires knowledge of the magnetization vectors in the neighboring FM layers. In order to obtain access to the magnetization values, the coefficient describing the TB conductivity is initialized as follows:

- For each point inside the TB where the conductivity needs to be computed, referred to as an integration point, the solver loops through the integration points of the RL and FL elements closer to the interfaces.
- The RL and FL points near to or at the interface with coordinates closest to the TB point are selected.
- The integration point number and element number associated with the nearest RL and FL points are mapped to the coordinates of the TB points.

In a transient simulation, the search is carried out only during the initialization of the solver. At every time step, the data necessary for the computation of (14) can be accessed through the generated maps, without the need to repeat the search procedure. The computed charge current, consistent with the TMR effect, can then be employed to obtain a solution to the spin accumulation equation.

3.2. Spin Accumulation Solution

The weak form of Equation (11), with the spin current expressed as (9) and the spin torque as (6), takes the form

$$-D_{\mathrm{e}}\int_{\Omega}\left(\boldsymbol{\nabla}\cdot\left(\boldsymbol{\nabla}\mathbf{S}-\beta_{\sigma}\beta_{\mathrm{D}}\mathbf{m}\otimes\left(\left(\boldsymbol{\nabla}\mathbf{S}\right)^{\mathrm{T}}\mathbf{m}\right)\right)\right)\cdot\boldsymbol{v}\,\mathrm{d}\mathbf{x}+$$
$$+D_{\mathrm{e}}\int_{\Omega}\left(\frac{\mathbf{S}}{\lambda_{sf}^{2}}+\frac{\mathbf{S}\times\mathbf{m}}{\lambda_{J}^{2}}+\frac{\mathbf{m}\times(\mathbf{S}\times\mathbf{m})}{\lambda_{\varphi}^{2}}\right)\cdot\boldsymbol{v}\,\mathrm{d}\mathbf{x}=$$
$$\frac{\mu_{B}}{e}\beta_{\sigma}\int_{\omega}\left(\boldsymbol{\nabla}\cdot(\mathbf{m}\otimes\mathbf{J}_{\mathrm{C}})\right)\cdot\boldsymbol{v}\,\mathrm{d}\mathbf{x}\,, \tag{22}$$

where $\boldsymbol{v}$ represents again a test function belonging to $\mathbf{H}^1$, $\mathbf{S}$ also belongs to $\mathbf{H}^1$, and ω indicates a subdomain composed of only the ferromagnetic layers. By applying Gauss's theorem, the first term on the LHS of (22) becomes

$$D_{\mathrm{e}}\int_{\Omega}\left(\boldsymbol{\nabla}\mathbf{S}-\beta_{\sigma}\beta_{\mathrm{D}}\mathbf{m}\otimes\left(\left(\boldsymbol{\nabla}\mathbf{S}\right)^{\mathrm{T}}\mathbf{m}\right)\right):\boldsymbol{\nabla}\boldsymbol{v}\,\mathrm{d}\mathbf{x}+$$
$$-\int_{\partial\Omega}\left((\boldsymbol{\nabla}\mathbf{S})\mathbf{n}-\beta_{\sigma}\beta_{\mathrm{D}}(\mathbf{m}\otimes\mathbf{m})((\boldsymbol{\nabla}\mathbf{S})\mathbf{n})\right)\cdot\boldsymbol{v}\,\mathrm{d}\mathbf{x}\,, \tag{23}$$

where $\boldsymbol{\nabla}\mathbf{a}:\boldsymbol{\nabla}\mathbf{b}=\sum_{\mathrm{ij}}\left(\partial a_{\mathrm{i}}/\partial x_{\mathrm{j}}\right)\left(\partial b_{\mathrm{i}}/\partial x_{\mathrm{j}}\right)$ is the Frobenius inner product of two matrices. By assuming the natural Neumann condition $(\boldsymbol{\nabla}\mathbf{S})\mathbf{n}=\mathbf{0}$ on all external boundaries of the whole domain Ω, the integrals on $\partial\Omega$ are put to zero. If the contacts are longer than the spin-flip length, the condition is equivalent to an exponential decay of $\mathbf{S}$ towards the electrodes [14,16].

Gauss's theorem can also be applied to the RHS term of (22), obtaining

$$-\frac{\mu_{B}}{e}\beta_{\sigma}\int_{\omega}(\mathbf{m}\otimes\mathbf{J}_{\mathrm{C}}):\boldsymbol{\nabla}\boldsymbol{v}\,\mathrm{d}\mathbf{x}+\frac{\mu_{B}}{e}\beta_{\sigma}\int_{\partial\Omega\cap\partial\omega}((\mathbf{m}\otimes\mathbf{J}_{\mathrm{C}})\mathbf{n})\cdot\boldsymbol{v}\,\mathrm{d}\mathbf{x} \tag{24}$$

$\partial\omega$ indicates the external boundaries of the magnetic subdomains, and $\partial\Omega\cap\partial\omega$ indicates the shared external boundaries of the subdomain ω and the whole domain Ω.

3.2.1. Tunneling Spin Current

The inclusion of appropriate boundary conditions at the TB interface with the RL and FL, together with the employment of a low diffusion coefficient inside the TB, allows the expected properties of the torque acting in MTJs to be reproduced [46]. The additional boundary conditions to be added to the RHS of (22) read

$$\mathrm{RHS}_{\mathrm{TB}}=-\int_{RL|TB}\mathbf{J}_{\mathrm{S,TB}}\cdot\boldsymbol{v}\;\mathrm{d}\mathbf{x}+\int_{TB|FL}\mathbf{J}_{\mathrm{S,TB}}\cdot\boldsymbol{v}\;\mathrm{d}\mathbf{x}\,, \tag{25}$$

where $RL|TB(TB|FL)$ indicates the interface of the TB with the RL(FL). These internal boundary conditions prescribe the difference in spin current between the FM layers and the TB, according to the spin current polarization generated by the tunneling process. The tunneling spin current $\mathbf{J}_{\mathrm{S,TB}}$ can be expressed as [47,50]

$$\mathbf{J}_{\mathrm{S,TB}}=-\frac{\mu_{B}}{e}\frac{\mathbf{J}_{\mathrm{C,TB}}\cdot\mathbf{n}}{1+P_{\mathrm{RL}}\,P_{\mathrm{FL}}\,\mathbf{m}_{\mathrm{RL}}\cdot\mathbf{m}_{\mathrm{FL}}}\Big(a_{\mathrm{mx}}\,P_{\mathrm{RL}}\,\mathbf{m}_{\mathrm{RL}}+a_{\mathrm{mx}}\,P_{\mathrm{FL}}\,\mathbf{m}_{\mathrm{FL}}+$$
$$+1/2\left(P_{\mathrm{RL}}\,P_{\mathrm{RL}}^{\eta}-P_{\mathrm{FL}}\,P_{\mathrm{FL}}^{\eta}\right)\mathbf{m}_{\mathrm{RL}}\times\mathbf{m}_{\mathrm{FL}}\Big)\,, \tag{26}$$

where P_{RL}^{η} and P_{FL}^{η} are out-of-plane polarization parameters [47], a_{mx} describes the influence of the interface spin-mixing conductance on the transmitted in-plane spin current [50], $\mathbf{J}_{\mathrm{C,TB}}$ is the electric current density at the interface, $\mathbf{n}$ is the interface normal, and $\mathbf{m}_{\mathrm{RL(FL)}}$ is the local value of the RL(FL) magnetization at the interface.

3.2.2. Spin Hall Effect

When a charge current flows through an HM layer with strong spin–orbit coupling, it generates a spin current perpendicular to it, carrying a spin polarization perpendicular to the direction of both spin and charge currents [12]. This process is known as the spin Hall effect (SHE). If the FL is deposited right above the HM, this spin current can be employed to provide the torque necessary for switching.

In order to reproduce the SHE, the following term must be added to the spin current expression (9) [12,16]:

$$\tilde{\mathbf{J}}_{\mathrm{S,SHE}} = -\theta_{\mathrm{SHA}} \frac{\mu_{\mathrm{B}}}{e} \varepsilon \mathbf{J}_{\mathrm{C}} \tag{27}$$

where θ_{SHA} is the spin Hall angle, and ε is the rank-3 unit antisymmetric tensor [16]. With the boundary condition

$$(\boldsymbol{\nabla} \mathbf{S})\mathbf{n} = -\theta_{\mathrm{SHA}} \frac{D_{\mathrm{e}}}{\sigma} \frac{\mu_{\mathrm{B}}}{e} (\varepsilon \mathbf{J}_{\mathrm{C}})\mathbf{n} \tag{28}$$

the weak formulation with the updated spin current expression is the same as (22) with the addition of the following RHS term:

$$\mathrm{RHS}_{\mathrm{SHE}} = -\int_{\mathrm{HM}} \theta_{\mathrm{SHA}} \frac{\mu_{\mathrm{B}}}{e} (\varepsilon \mathbf{J}_{\mathrm{C}}) : \boldsymbol{\nabla} \boldsymbol{v} \, \mathrm{d}\mathbf{x} \tag{29}$$

The integral is performed only over the HM layer.

3.2.3. Complete Weak Formulation

The complete weak formulation of the spin accumulation equation takes the form

$$\begin{aligned}
&D_{\mathrm{e}} \int_{\Omega} \left(\boldsymbol{\nabla} \mathbf{S} - \beta_{\sigma} \beta_{\mathrm{D}} \mathbf{m} \otimes \left((\boldsymbol{\nabla} \mathbf{S})^{\mathrm{T}} \mathbf{m} \right) \right) : \boldsymbol{\nabla} \boldsymbol{v} \, \mathrm{d}\mathbf{x} + \\
&+ D_{\mathrm{e}} \int_{\Omega} \left(\frac{\mathbf{S}}{\lambda_{sf}^2} + \frac{\mathbf{S} \times \mathbf{m}}{\lambda_J^2} + \frac{\mathbf{m} \times (\mathbf{S} \times \mathbf{m})}{\lambda_{\varphi}^2} \right) \cdot \boldsymbol{v} \, \mathrm{d}\mathbf{x} = \\
&- \frac{\mu_B}{e} \beta_{\sigma} \int_{\omega} (\mathbf{m} \otimes \mathbf{J}_{\mathrm{C}}) : \boldsymbol{\nabla} \boldsymbol{v} \, \mathrm{d}\mathbf{x} + \frac{\mu_B}{e} \beta_{\sigma} \int_{\partial\Omega \cap \partial\omega} ((\mathbf{m} \otimes \mathbf{J}_{\mathrm{C}})\mathbf{n}) \cdot \boldsymbol{v} \, \mathrm{d}\mathbf{x} + \\
&- \int_{RL|TB} \mathbf{J}_{\mathrm{S,TB}} \cdot \boldsymbol{v} \, \mathrm{d}\mathbf{x} + \int_{TB|FL} \mathbf{J}_{\mathrm{S,TB}} \cdot \boldsymbol{v} - \int_{\mathrm{HM}} \theta_{\mathrm{SHA}} \frac{\mu_{\mathrm{B}}}{e} (\varepsilon \mathbf{J}_{\mathrm{C}}) : \boldsymbol{\nabla} \boldsymbol{v} \, \mathrm{d}\mathbf{x}
\end{aligned} \tag{30}$$

where $\mathbf{S}$ is the spin accumulation, $\mathbf{m}$ is the unit magnetization vector, $\mathbf{J}_{\mathrm{C}}$ is the charge current density, $\mathbf{J}_{\mathrm{S,TB}}$ is the tunneling spin current (26), D_{e} is the electron diffusion coefficient, β_{σ} and β_{D} are polarization parameters, λ_{sf} is the spin-flip length, λ_{J} is the exchange length, λ_{φ} is the dephasing length, and θ_{SHA} is the spin Hall angle. The system of linear equations to be solved in the FE implementation of (30) is

$$\underline{A_{\mathrm{S}}} \, \underline{\mathbf{S}_{\mathrm{h}}} = \underline{f_{\mathrm{S}}} \,, \tag{31}$$

where $\underline{A_{\mathrm{S}}} \in \mathbb{R}^{3N} \times \mathbb{R}^{3N}$ is the matrix coming from the LHS of (30) and $\underline{f_{\mathrm{S}}} \in \mathbb{R}^{3N}$ is the vector coming from the RHS. The solution of this system of equations is computed through a solver based on the generalized minimal residual (GMRES) method [51], provided by the library MFEM. The GMRES method is designed for indefinite non-symmetric systems of linear equations, as is the case for (31) due to the presence of the cross-product terms in (30). Material parameters that can change between the different subdomains are treated as piecewise constant coefficients.

As is the case for (14), the inclusion of the additional boundary conditions (25) in the MFEM implementation demands special care. The computation of the boundary terms requires knowledge of the magnetization vector on the opposite interfaces. In order to obtain access to these values, the coefficient describing the boundary integral is initialized as follows:

- For each integration point on the RL | TB interface requiring the computation of the tunneling spin current, the solver loops through the integration points of the TB | FL interface.
- The TB | FL point with coordinates closest to the RL | TB one is selected.
- The integration point number and the element number associated with the found TB | FL point are mapped to the coordinates of the RL | TB one.
- The mapping procedure is repeated for the TB | FL interface.

In a transient simulation, the search is carried out only during the initialization of the solver. At every time step, the data necessary for the computation of (26) can be accessed through the generated maps, without the need to repeat the search procedure.

3.3. Magnetization Dynamics Solution

In the tangent plane scheme, the quantity being solved for is the magnetization derivative $\partial\mathbf{m}/\partial t = \mathbf{v}$, with the constraint $\mathbf{m}\cdot\mathbf{v} = 0$. By cross-multiplying (1) with $\mathbf{m}$, using the product rule $\mathbf{a}\times(\mathbf{b}\times\mathbf{c}) = (\mathbf{c}\cdot\mathbf{a})\mathbf{b} - (\mathbf{a}\cdot\mathbf{b})\mathbf{c}$ and the constraint $|\mathbf{m}| = 1$, the LLG equation can be rewritten in a form employed to derive a weak formulation for the tangent plane scheme:

$$\alpha\frac{\partial\mathbf{m}}{\partial t} + \mathbf{m}\times\frac{\partial\mathbf{m}}{\partial t} = |\gamma|\mu_0\,\mathbf{H}_{\text{eff}} + \frac{D_{\text{e}}}{M_{\text{S}}\lambda_{\text{J}}^2}\mathbf{S} + \frac{D_{\text{e}}}{M_{\text{S}}\lambda_{\varphi}^2}\mathbf{m}\times\mathbf{S} + \\ -|\gamma|\mu_0(\mathbf{m}\cdot\mathbf{H}_{\text{eff}})\mathbf{m} - \frac{D_{\text{e}}}{M_{\text{S}}\lambda_{\text{J}}^2}(\mathbf{m}\cdot\mathbf{S})\mathbf{m} \tag{32}$$

The magnetization is taken to belong to $\mathbf{H}^1$, while the solution $\mathbf{v}$ and the test functions $\boldsymbol{w}$ are restricted to a space of vectors orthogonal to the magnetization, $U_{\text{T}} = \{\boldsymbol{w}\in\mathbf{H}^1 \mid \mathbf{m}\cdot\boldsymbol{w} = 0\}$. The weak formulation of (32) is then

$$\int_\omega(\alpha\mathbf{v} + \mathbf{m}\times\mathbf{v})\cdot\boldsymbol{w}\,\mathrm{d}\mathbf{x} = |\gamma|\mu_0\int_\omega\left(\mathbf{H}_{\text{ext}} + \mathbf{H}_{\text{exc}} + \mathbf{H}_{\text{ani}} + \mathbf{H}_{\text{demag}}\right)\cdot\boldsymbol{w}\mathrm{d}\mathbf{x} + \\ + \frac{D_{\text{e}}}{M_{\text{S}}}\int_\omega\left(\frac{\mathbf{S}}{\lambda_{\text{J}}^2} + \frac{\mathbf{m}\times\mathbf{S}}{\lambda_{\varphi}^2}\right)\cdot\boldsymbol{w}\;\mathrm{d}\mathbf{x}\,, \tag{33}$$

where the last two terms on the RHS of (32) are not present, as their scalar product with the test functions, belonging to the tangent space U_{T}, is zero. By using Gauss's theorem, the weak form of expression (2) for the exchange contribution can be written as

$$\frac{2A_{\text{exc}}}{\mu_0 M_{\text{S}}}\int_\omega\nabla^2\mathbf{m}\cdot\boldsymbol{w}\,\mathrm{d}\mathbf{x} = -\frac{2A_{\text{exc}}}{\mu_0 M_{\text{S}}}\int_\omega\boldsymbol{\nabla}\mathbf{m}:\boldsymbol{\nabla}\boldsymbol{w}\,\mathrm{d}\mathbf{x} + \frac{2A_{\text{exc}}}{\mu_0 M_{\text{S}}}\int_{\partial\omega}((\boldsymbol{\nabla}\mathbf{m})\mathbf{n})\cdot\boldsymbol{w}\,\mathrm{d}\mathbf{x} \tag{34}$$

The natural Neumann condition $(\boldsymbol{\nabla}\mathbf{m})\mathbf{n} = \mathbf{0}$ is assumed on $\partial\omega$, so that the boundary integral on the RHS is put to zero.

With the given weak formulation, the time derivative $\mathbf{v}$ at a certain time t^{k} is obtained by setting [33]

$$\mathbf{m}^{\text{k+1}} = \mathbf{m}^{\text{k}} + \theta\delta t\mathbf{v}\,, \tag{35}$$

where δt indicates the time step and θ is a parameter ranging from 0 to 1. A value of 0 leads to a fully explicit scheme, while a value of 1 gives a fully implicit one. The value of θ can differ between each effective field contribution. In the implementation reported here, only the exchange field contribution is treated implicitly with $\theta = 1$, as this leads to a better stability of the scheme [52]. The weak formulation employed by the FE solver to compute the magnetization dynamics is then expressed as

$$\int_\omega \left(\alpha \mathbf{v} + \mathbf{m}^{\mathrm{k}} \times \mathbf{v}\right) \cdot \boldsymbol{w}\, \mathrm{d}\mathbf{x} + \frac{2A_{\mathrm{exc}}|\gamma|}{M_S}\delta t \int_\omega \boldsymbol{\nabla}\mathbf{v} : \boldsymbol{\nabla}\boldsymbol{w}\mathrm{d}\mathbf{x} =$$
$$-\frac{2A_{\mathrm{exc}}|\gamma|}{M_S}\int_\omega \boldsymbol{\nabla}\mathbf{m}^{\mathrm{k}} : \boldsymbol{\nabla}\boldsymbol{w}\, \mathrm{d}\mathbf{x} + \gamma_0 \int_\omega \left(\mathbf{H}_{\mathrm{ext}} + \mathbf{H}_{\mathrm{ani}} + \mathbf{H}_{\mathrm{demag}}\right) \cdot \boldsymbol{w}\mathrm{d}\mathbf{x} +$$
$$+\frac{D_{\mathrm{e}}}{M_{\mathrm{S}}}\int_\omega \left(\frac{\mathbf{S}^{\mathrm{k}}}{\lambda_J^2} + \frac{\mathbf{m}^{\mathrm{k}} \times \mathbf{S}^{\mathrm{k}}}{\lambda_\varphi^2}\right) \cdot \boldsymbol{w}\, \mathrm{d}\mathbf{x}\,, \tag{36}$$

$$\mathbf{m}^{\mathrm{k+1}} = \frac{\mathbf{m}^{\mathrm{k}} + \delta t\, \mathbf{v}}{\left|\mathbf{m}^{\mathrm{k}} + \delta t\, \mathbf{v}\right|}\,, \tag{37}$$

with the initial condition $\mathbf{m}(0) = \mathbf{m}^0$. Equation (37) is evaluated nodewise. The additional tangent plane constraint $\mathbf{m} \cdot \boldsymbol{w} = 0$ leads to the following saddle point problem [53]:

$$\begin{pmatrix} \underline{A_{\mathrm{M}}} & \underline{C_{\mathrm{M}}^{\mathrm{T}}} \\ \underline{C_{\mathrm{M}}} & \underline{0} \end{pmatrix} \begin{pmatrix} \underline{\mathbf{v}_{\mathrm{h}}} \\ \underline{\lambda} \end{pmatrix} = \begin{pmatrix} \underline{f_{\mathrm{M}}} \\ \underline{0} \end{pmatrix} \tag{38}$$

where $\underline{A_{\mathrm{M}}} \in \mathbb{R}^{3N} \times \mathbb{R}^{3N}$ is the matrix coming from the LHS of (36), $\underline{f_{\mathrm{M}}} \in \mathbb{R}^{3N}$ is the vector coming from its RHS, $\underline{\lambda}$ is a scalar field, and $\underline{C_{\mathrm{M}}} \in \mathbb{R}^{N} \times \mathbb{R}^{3N}$ implements the constraint. A solution of (38) is computed at each time step through a solver based on the GMRES method.

3.4. Demagnetizing Field

The demagnetizing field contribution needs to be computed from the magnetic potential as (4), which in turn is obtained from (5). A direct FE implementation of the latter requires a large computational domain surrounding the magnetic material in order to ensure the proper decay properties of the computed potential. There have been various solutions proposed to solve this open-boundary problem [54–57], with the truncation of the external domain surrounding the magnetic one at a certain distance being the most straightforward. This approach, however, decreases computational efficiency, as it requires the inclusion of additional degrees of freedom.

High accuracy and reduced computational costs can be achieved by employing a hybrid approach, combining the FE method with the boundary element method (FEM-BEM), allowing u_{m} to be computed only in the magnetic subdomains [58]. The potential is first split into two parts:

$$u_{\mathrm{m}} = u_{\mathrm{m},1} + u_{\mathrm{m},2} \tag{39}$$

$u_{\mathrm{m},1}$ satisfies (5) inside the magnetic subdomain, with the boundary condition $\boldsymbol{\nabla} u_{\mathrm{m},1} \cdot \mathbf{n} = M_{\mathrm{S}}\, \mathbf{m} \cdot \mathbf{n}$, and is zero outside of it. $u_{\mathrm{m},2}$ satisfies the Laplace equation

$$\nabla^2 u_{\mathrm{m},2} = 0\,, \tag{40}$$

with the boundary conditions $[\boldsymbol{\nabla} u_{\mathrm{m},2} \cdot \mathbf{n}] = 0$ and $[u_{m,2}] = u_{m,1}$, where $[\ldots]$ denotes a discontinuity across the boundary. By having $u_{\mathrm{m},2} \to 0$ for $|\mathbf{x}| \to \infty$, potential theory leads to the following relation between $u_{\mathrm{m},1}$ and $u_{\mathrm{m},2}$ [59]:

$$u_{\mathrm{m},2} = \int_{\partial\omega} u_{\mathrm{m},1} \frac{\partial}{\partial \mathbf{n}} \frac{1}{|\mathbf{x}' - \mathbf{x}|}\, \mathrm{d}\mathbf{x}' \tag{41}$$

The decomposition allows $u_{\mathrm{m},1}$ to be computed by solving (5) only in the disconnected magnetic layers. The boundary value of $u_{\mathrm{m},2}$ is obtained by solving (41), and is then used as a Dirichlet condition for (40), which is also computed only inside the magnetized portions of the structure.

The weak formulation of (5), after applying Gauss's theorem and the boundary condition, results in

$$\int_\omega \nabla u_{\mathrm{m},1} \cdot \nabla v \, \mathrm{d}\mathbf{x} = M_\mathrm{S} \int_\omega \mathbf{m} \cdot \nabla v \, \mathrm{d}\mathbf{x} \,, \tag{42}$$

while that of (40) is

$$\int_\omega \nabla u_{\mathrm{m},2} \cdot \nabla v \, \mathrm{d}\mathbf{x} = 0 \tag{43}$$

Both the magnetic potential and the test functions belong to H^1. The FE implementation results in a system of equations analogous to the one employed for the charge potential.

A BEM approach is employed to discretize (41) on the magnetic boundary, resulting in the following matrix-vector multiplication:

$$\underline{u}_{\mathrm{m},2}^{\mathrm{bdr}} = \underline{B}_\mathrm{M} \, \underline{u}_{\mathrm{m},1}^{\mathrm{bdr}} \tag{44}$$

The matrix $\underline{B}_\mathrm{M}$ belongs to $\mathbb{R}^{N_\mathrm{bdr}} \times \mathbb{R}^{N_\mathrm{bdr}}$ and $\underline{u}_{\mathrm{m},1}^{\mathrm{bdr}}$, $\underline{u}_{\mathrm{m},2}^{\mathrm{bdr}}$ belong to $\mathbb{R}^{N_\mathrm{bdr}}$, with N_bdr being the number of boundary nodes of the magnetic subdomains. Even though $\underline{B}_\mathrm{M}$ is a dense matrix, the employment of matrix compression algorithms [60] can significantly reduce the memory demands [58]. The matrix compression algorithms and BEM functionalities are implemented by employing the H2Lib library [61]. The demagnetizing field is finally computed as the gradient of the magnetic potential u_m by using the same projection approach employed for the charge current in (20).

An example of the magnetic potential and field computed in a structure with three disconnected ferromagnetic layers is shown in Figure 3. Without interaction between the layers, the potential would only vary linearly along the magnetization direction. When applying the described FEM-BEM approach, the interactions are taken into account and the magnetic potential in each layer is shifted due to the stray field contributions of the neighboring ferromagnetic segments. The presented implementation allows the demagnetizing field acting in structures containing multiple ferromagnetic layers, as is typical of modern MRAM cells, to be readily computed.

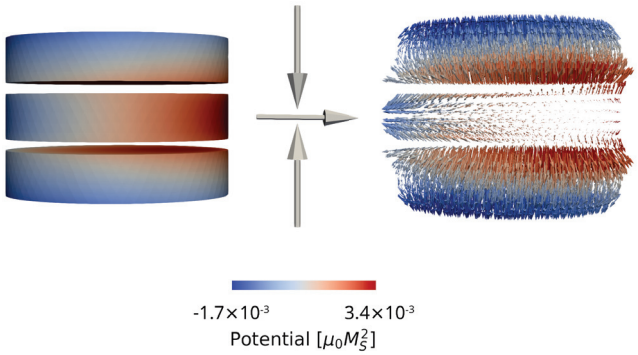

Figure 3. Magnetic potential (**left**) and demagnetizing field (**right**) computed in a structure with three disconnected ferromagnetic layers. The magnetization orientation in each layer is indicated by the arrows. The color coding indicates the value of the magnetic potential.

4. Device Simulation

Recently proposed devices are composed of several layers of ferromagnetic materials, non-magnetic spacers, and tunnel barriers, in order to reduce switching currents and cell size. Due to the capability of computing the torque acting in all layers from a unified expression, the presented FE solver is suitable for the simulation of such structures. The following sections report the results of switching simulations performed in the structures of Figure 1. The parameters employed are presented in Table 1. They are consistent with CoFeB and MgO for the FM layers and TB layers, respectively. The low values of λ_J and λ_φ are employed to have complete absorption of the transverse spin accumulation components

near the TB interface [46]. The results reported in this paper were obtained by employing tetrahedral elements.

Table 1. Material parameters.

LLG parameters	Value
Saturation magnetization (M_s)	0.81×10^6 A/m
Exchange constant (A_{exc})	2.0×10^{-11} J/m
Interface anisotropy (K_{int})	1.29×10^{-3} J/m^2
Gilbert damping constant (α)	0.02
Drift-diffusion parameters	**Value**
Conductivity polarization, β_σ	0.52
Diffusion polarization, β_D	0.7
FM diffusion coefficient, $D_{e,FM}$	10^{-3} m^2/s
NM diffusion coefficient, $D_{e,NM}$	10^{-2} m^2/s
HM diffusion coefficient, $D_{e,HM}$	1.1×10^{-3} m^2/s
TB diffusion coefficient, D_S	2.0×10^{-8} m^2/s
FM conductivity σ_{FM}	4.0×10^6 S/m
NM conductivity σ_{NM}	5.0×10^6 S/m
HM conductivity σ_{HM}	7.0×10^6 S/m
FM spin-flip length, $\lambda_{sf,FM}$	10 nm
NM spin-flip length, $\lambda_{sf,NM}$	10 nm
HM spin-flip length, $\lambda_{sf,HM}$	1.4 nm
Spin exchange length, λ_J	0.8 nm
Spin dephasing length, λ_φ	0.4 nm
Spin Hall angle, θ_{SHA}	0.19
TB resistance standard and double RL STT-MTJ	**Value**
Resistance parallel (R_P)	4.3×10^3 kΩ
Resistance anti-parallel (R_{AP})	9.1×10^3 kΩ
TB resistance ultra-scaled STT-MTJ	**Value**
Resistance parallel (R_P)	4.1×10^5 kΩ
Resistance anti-parallel (R_{AP})	7.5×10^5 kΩ
TB resistance SOT-assisted STT-MTJ	**Value**
Resistance parallel (R_P)	1.4×10^4 kΩ
Resistance anti-parallel (R_{AP})	4.2×10^4 kΩ

4.1. Double RL STT-MRAM

In order to reduce the critical current required for switching, an additional RL (RL_2) can be deposited on top of the FL [20] (cf. Figure 1b). When RL_2 is anti-parallel to the first RL (RL_1), the torque coming from the two becomes additive, and the switching is made faster [62]. To not compromise the TMR and data read, the second RL is separated from the FL by a non-magnetic metallic spacer (NMS).

We employed the presented solver to perform an AP to P switching simulation of both a regular MTJ with single RL (SMTJ) and the double RL MTJ (DSMTJ). The structure used for the DSMTJ simulation, with a diameter of 40 nm, is reported in Figure 4a. Long NM contacts were employed to allow the spin accumulation to completely decay inside them. The total number of nodes in the mesh was 7338. The magnetization reversal of the FL in both the SMTJ and DSMTJ is reported in Figure 4. A voltage of 1.0 V was applied. We note that the switching of the DSMTJ, presenting more oscillations in the z-component, is less smooth than the one of the SMTJ. This is due to the additional torque and stray field contributions from the second RL, which cause the magnetization to switch less uniformly and to produce the observed non-smooth trajectory of its average components. The results show a substantial reduction in switching time for the same applied voltage in the DSMTJ, in good agreement with the experimental results reported in [20].

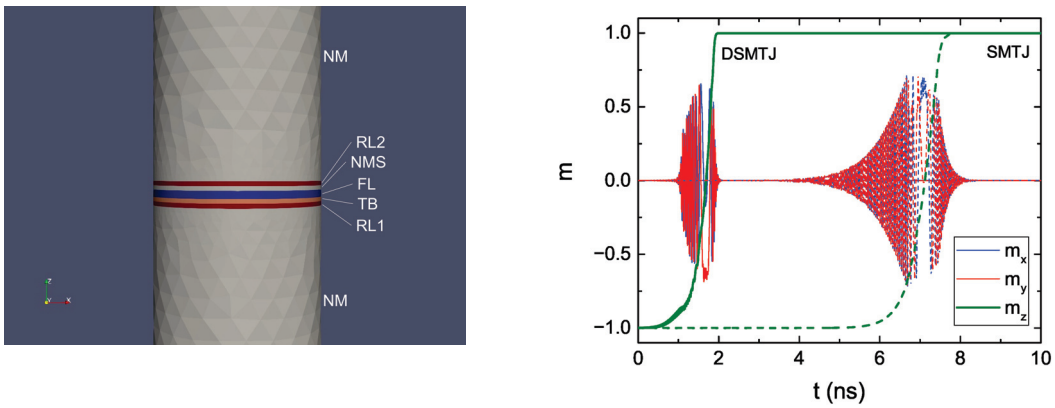

(**a**) (**b**)

Figure 4. (**a**) Structure for an MRAM cell with the addition of a second RL (RL2), separated from the FL by a non-magnetic metallic spacer (NMS). The RL_1, RL_2, and TB are 1 nm thick, the FL is 1.7 nm thick, and the NM contacts are 50 nm thick. (**b**) Magnetization reversal of the FL from AP to P for an MRAM cell with a single MTJ (SMTJ, dotted line) and the one with a double RL (DSMTJ, solid line).

4.2. Ultra-Scaled STT-MRAM

The stability of the FL can be increased by adding additional MgO tunneling layers, because of the perpendicular anisotropy provided by their interfaces with CoFeB. Moreover, employing elongated layers with small diameters allows additional stability to be gained from the contribution of the shape anisotropy [21] (cf. Figure 1c). Because of the reduced FL diameter, the scalability of this kind of device is also improved.

We employed the FE solver to investigate the switching behavior of such ultra-scaled MRAM cells. The structure used for the simulation is reported in Figure 5a. The cell had a diameter of 2.3 nm, and the total number of nodes was 9634. The FL was capped by a second TB, and further split into two sections, FL_1 and FL_2, by a third TB. The applied bias voltage was 1.5 V. The magnetization reversal from AP to P computed in this mesh is reported in Figure 5b, where clear steps in the trajectory can be observed. This is caused by the fact that while the static magnetic coupling between the two segments increases the overall stability of the FL and allows them to respond coherently to an applied external field, during STT switching the torque contributions coming from the different TBs make the segments switch one at a time. At the beginning of the process, the torques acting from RL and FL_2 on FL_1 are additive, causing it to switch first and fast. Then, the torque acting from FL_1 on FL_2 makes it switch as well, at a slower pace. The observed behavior can help explain the reduction in critical switching current observed for a quad-interface device in [63].

4.3. SOT Assisted STT-MRAM

Including the SHE in the model allows for the proper treatment of SOT. By interfacing the FL with an HM layer, and running a second current through it, it is possible to assist the STT switching by bringing the magnetization in-plane with SOTs in the starting phase [64] (cf. Figure 1d). With SOT, the incubation time needed for the FL to break its colinearity with the RL is avoided, reducing the overall switching time at the cost of a larger footprint.

We applied the presented solver to the switching simulation of an MRAM cell relying on both STT and SOT. The structure used for the simulation is reported in Figure 6a. The diameter of the MTJ is 40 nm, and the total number of nodes is 15,058. A bias voltage of 2.0 V was used for the STT current and one of 0.3 V for the SOT current. The parameters employed for the HM are consistent with Pt, with a spin Hall angle of 0.19 [65]. The SOT current is only applied for the first 0.2 ns of the simulation. As expected, the magnetization is quickly brought in-plane by the SOT contribution. When the SOT current is turned off, the switching is completed by the STT contribution.

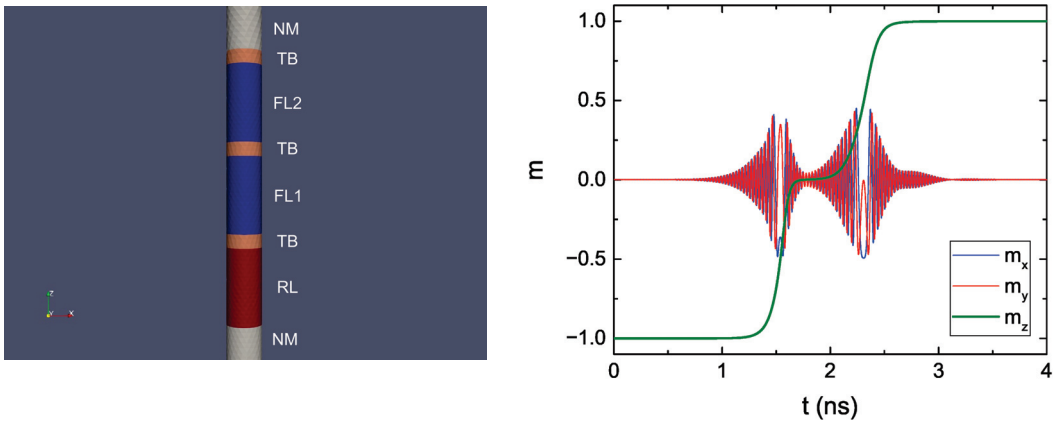

(**a**) (**b**)

Figure 5. (**a**) Structure for an elongated MRAM cell with FL composed of two sections (FL1 and FL2), separated by a TB. The RL, FL_1, and FL_2 are 5 nm thick, all the TBs are 0.9 nm thick, and the NM contacts are 50 thick. (**b**) Magnetization reversal of the FL from AP to P for the elongated cell.

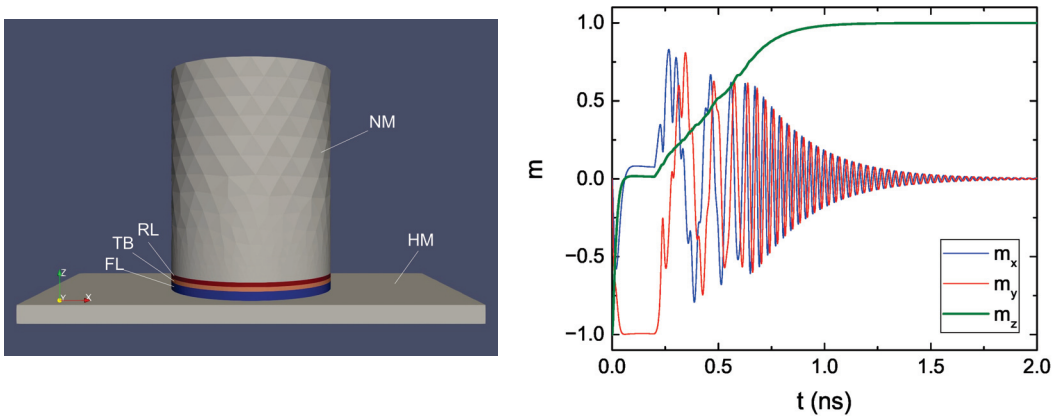

(**a**) (**b**)

Figure 6. (**a**) Structure reproducing an SOT + STT-based MRAM cell. The MTJ stack is deposited on top of a heavy metal line (HM). The RL and TB are 1 nm thick, the FL is 2 nm thick, the top NM contact is 50 nm thick, and the HM layer is 4 nm thick, 50 nm wide and 100 nm long. (**b**) Magnetization reversal of the FL from AP to P for the SOT + STT cell.

5. Conclusions

We presented the derivation of a finite element solution to the weak formulation of the LLG equation coupled with the spin and charge drift-diffusion formalism. The treatment of the tunneling layers as poor conductors, whose local conductivity depends on the relative magnetization orientation in the ferromagnetic layers, and the addition of appropriate boundary conditions at the tunnel barriers' interfaces, can account for the properties of both resistance and torque expected in MTJs. The addition of terms accounting for the SHE to the spin equation allows us to also reproduce the contribution of spin-orbit torques. The demagnetizing field is computed by employing a hybrid FEM-BEM approach. The presented solver was successfully used to perform switching simulations of recently proposed structures composed of several ferromagnetic, tunneling and non-magnetic layers, as well as heavy metal lines for the generation of spin-orbit torques, supporting its employment to help investigate and predict the switching performance of newly introduced devices.

Author Contributions: Conceptualization, S.F. and V.S.; software, S.F., N.P.J., J.E., M.B., R.L.d.O. and W.G.; investigation, S.F., N.P.J., J.E. and M.B.; resources, S.S. and W.G.; data curation, S.F., J.E. and N.P.J.; writing—original draft preparation, S.F.; writing—review and editing, S.F, N.P.J., J.E., R.L.d.O., S.S., M.B., W.G. and V.S.; supervision, V.S., S.S. and W.G.; project administration, V.S.; funding acquisition, V.S. and S.S. All authors have read and agreed to the published version of the manuscript.

Funding: This research was funded by the Christian Doppler Research Association, grant number 1558669. The APC was funded by the TU Wien Library through its Open Access Funding Program.

Data Availability Statement: The datasets generated during and/or analyzed during the current study are available from the corresponding author on reasonable request.

Acknowledgments: The financial support by the Austrian Federal Ministry for Digital and Economic Affairs, the National Foundation for Research, Technology and Development, and the Christian Doppler Research Association is gratefully acknowledged. The authors also acknowledge the TU Wien Library for financial support through its Open Access Funding Program.

Conflicts of Interest: The authors declare no conflict of interest.

Abbreviations

The following abbreviations are used in this manuscript:

MRAM	Magnetoresistive random access memory
CMOS	Complementary metal-oxide semiconductor
SRAM	Static random access memory
MTJ	Magnetic tunnel junction
FM	Ferromagnetic
NM	Non-magnetic
RL	Reference layer
FL	Free layer
TB	Tunnel barrier
NMS	Non-magnetic spacer
HM	Heavy metal
P	Parallel
AP	Anti-parallel
TMR	Tunneling magnetoresistance ratio
STT	Spin-transfer torque
SOT	Spin-orbit torque
SHE	Spin Hall effect
LLG	Landau–Lifshitz–Gilbert
FE	Finite element
CRMT	Continuous random matrix theory
BEM	Boundary element method
LHS	Left-hand side
RHS	Right-hand side
DSMTJ	Double spin torque MTJ

References

1. Hanyu, T.; Endoh, T.; Suzuki, D.; Koike, H.; Ma, Y.; Onizawa, N.; Natsui, M.; Ikeda, S.; Ohno, H. Standby-Power-Free Integrated Circuits Using MTJ-based VLSI Computing. *Proc. IEEE* **2016**, *104*, 1844–1863. [CrossRef]
2. Gallagher, W.J.; Chien, E.; Chiang, T.; Huang, J.; Shih, M.; Wang, C.Y.; Weng, C.; Chen, S.; Bair, C.; Lee, G.; et al. 22nm STT-MRAM for Reflow and Automotive Uses with High Yield, Reliability, and Magnetic Immunity and with Performance and Shielding Options. In Proceedings of the 2019 IEEE International Electron Devices Meeting (IEDM), San Francisco, CA, USA, 7–11 December 2019; pp. 2.7.1–2.7.4. [CrossRef]
3. Han, S.H.; Lee, J.M.; Shin, H.M.; Lee, J.H.; Suh, K.S.; Nam, K.T.; Kwon, B.S.; Cho, M.K.; Lee, J.; Jeong, J.H.; et al. 28-nm 0.08 mm^2/Mb Embedded MRAM for Frame Buffer Memory. In Proceedings of the IEDM Conference, San Francisco, CA, USA, 12–18 December 2020; pp. 11.2.1–11.2.4. [CrossRef]
4. Shih, Y.C.; Lee, C.F.; Chang, Y.A.; Lee, P.H.; Lin, H.J.; Chen, Y.L.; Lo, C.P.; Lin, K.F.; Chiang, T.W.; Lee, Y.J.; et al. A Reflow-Capable, Embedded 8Mb STT-MRAM Macro with 9ns Read Access Time in 16nm FinFET Logic CMOS Process. In Proceedings of the IEDM Conference, San Francisco, CA, USA, 12–18 December 2020; pp. 11.4.1–11.4.4. [CrossRef]

5. Naik, V.B.; Yamane, K.; Lee, T.; Kwon, J.; Chao, R.; Lim, J.; Chung, N.; Behin-Aein, B.; Hau, L.; Zeng, D.; et al. JEDEC-Qualified Highly Reliable 22nm FD-SOI Embedded MRAM For Low-Power Industrial-Grade, and Extended Performance Towards Automotive-Grade-1 Applications. In Proceedings of the IEDM Conference, San Francisco, CA, USA, 12–18 December 2020; pp. 11.3.1–11.3.4. [CrossRef]
6. Yau, J.B.; Fung, Y.K.K.; Gibson, G.W. Hybrid Cryogenic Memory Cells for Superconducting Computing Applications. In Proceedings of the ICRC Conference, Washington, DC, USA, 8–9 November 2017; pp. 1–3. [CrossRef]
7. Rowlands, G.E.; Ryan, C.A.; Ye, L.; Rehm, L.; Pinna, D.; Kent, A.D.; Ohki, T.A. A Cryogenic Spin-Torque Memory Element with Precessional Magnetization Dynamics. *Sci. Rep.* **2019**, *9*, 803. [CrossRef]
8. Lang, L.; Jiang, Y.; Lu, F.; Wang, C.; Chen, Y.; Kent, A.D.; Ye, L. A Low Temperature Functioning CoFeB/MgO-Based Perpendicular Magnetic Tunnel Junction for Cryogenic Nonvolatile Random Access Memory. *Appl. Phys. Lett.* **2020**, *116*, 022409. [CrossRef]
9. Slonczewski, J.C. Current-Driven Excitation of Magnetic Multilayers. *J. Magn. Magn. Mater.* **1996**, *159*, L1–L7. [CrossRef]
10. Berger, L. Emission of Spin Waves by a Magnetic Multilayer Traversed by a Current. *Phys. Rev. B* **1996**, *54*, 9353–9358. [CrossRef] [PubMed]
11. Slonczewski, J.C. Currents, Torques, and Polarization Factors in Magnetic Tunnel Junctions. *Phys. Rev. B* **2005**, *71*, 024411. [CrossRef]
12. Dyakonov, M.I.; Perel, V.I. Current-Induced Spin Orientation of Electrons in Semiconductors. *Phys. Lett. A* **1971**, *35*, 459–460. [CrossRef]
13. Ando, K.; Takahashi, S.; Harii, K.; Sasage, K.; Ieda, J.; Maekawa, S.; Saitoh, E. Electric Manipulation of Spin Relaxation Using the Spin Hall Effect. *Phys. Rev. Lett.* **2008**, *101*, 036601. [CrossRef]
14. Abert, C.; Ruggeri, M.; Bruckner, F.; Vogler, C.; Hrkac, G.; Praetorius, D.; Suess, D. A Three-Dimensional Spin-Diffusion Model for Micromagnetics. *Sci. Rep.* **2015**, *5*, 14855. [CrossRef]
15. Abert, C.; Ruggeri, M.; Bruckner, F.; Vogler, C.; Manchon, A.; Praetorius, D.; Suess, D. A Self-Consistent Spin-Diffusion Model for Micromagnetics. *Sci. Rep.* **2016**, *6*, 16. [CrossRef] [PubMed]
16. Lepadatu, S. Unified Treatment of Spin Torques Using a Coupled Magnetisation Dynamics and Three-Dimensional Spin Current Solver. *Sci. Rep.* **2017**, *7*, 12937. [CrossRef]
17. Anderson, R.; Andrej, J.; Barker, A.; Bramwell, J.; Camier, J.S.; Dobrev, J.C.V.; Dudouit, Y.; Fisher, A.; Kolev, T.; Pazner, W.; et al. MFEM: A Modular Finite Element Library. *Comp. Math. Appl.* **2020**, *81*, 42–74. [CrossRef]
18. MFEM: Modular Finite Element Methods [Software]. Available online: https://mfem.org (accessed on 19 April 2023). [CrossRef]
19. Ender, J.; Fiorentini, S.; de Orio, R.L.; Hadámek, T.; Bendra, M.; Jørstad, N.P.; Loch, W.J. ViennaSpinMag. 2023. Available online: https://www.iue.tuwien.ac.at/viennaspinmag (accessed on 19 April 2023).
20. Hu, G.; Lauer, G.; Sun, J.Z.; Hashemi, P.; Safranski, C.; Brown, S.L.; Buzi, L.; Edwards, E.R.J.; D'Emic, C.P.; Galligan, E.; et al. 2X Reduction of STT-MRAM Switching Current Using Double Spin-Torque Magnetic Tunnel Junction. In Proceedings of the IEDM Conference, San Francisco, CA, USA, 11–16 December 2021; pp. 2.5.1–2.5.4. [CrossRef]
21. Jinnai, B.; Igarashi, J.; Watanabe, K.; Funatsu, T.; Sato, H.; Fukami, S.; Ohno, H. High-Performance Shape-Anisotropy Magnetic Tunnel Junctions down to 2.3 nm. In Proceedings of the IEDM Conference, San Francisco, CA, USA, 12–18 December 2020; pp. 24.6.1–24.6.4. [CrossRef]
22. Wang, M.; Cai, W.; Zhu, D.; Wang, Z.; Kan, J.; Zhao, Z.; Cao, K.; Wang, Z.; Zhang, Y.; Zhang, T.; et al. Field-Free Switching of a Perpendicular Magnetic Tunnel Junction Through the Interplay of Spin–Orbit and Spin-Transfer Torques. *Nat. Electron.* **2018**, *1*, 582–588. [CrossRef]
23. Landau, L.D.; Lifshitz, E.M. On the Theory of the Dispersion of Magnetic Permeability in Ferromagnetic Bodies. *Phys. Z. Sowjetunion* **1935**, *8*, 153–164.
24. Gilbert, T.L. A Phenomenological Theory of Damping in Ferromagnetic Materials. *IEEE Trans. Magn.* **2004**, *40*, 3443–3449. [CrossRef]
25. Martinez, E.; Lopez-Diaz, L.; Torres, L.; Garcia-Cervera, C. Micromagnetic Simulations with Thermal Noise: Physical and Numerical Aspects. *J. Magn. Magn. Mater.* **2007**, *316*, 269–272. [CrossRef]
26. Torres, L.; Lopez-Diaz, L.; Martinez, E.; Carpentieri, M.; Finocchio, G. Micromagnetic Computations of Spin Polarized Current-Driven Magnetization Processes. *J. Magn. Magn. Mater.* **2005**, *286*, 381–385. [CrossRef]
27. Xiao, Z.H.; Ma, X.Q.; Wu, P.P.; Zhang, J.X.; Chen, L.Q.; Shi, S.Q. Micromagnetic Simulations of Current-Induced Magnetization Switching in Co/Cu/Co Nanopillars. *J. Appl. Phys.* **2007**, *102*, 093907. [CrossRef]
28. Finocchio, G.; Azzerboni, B.; Fuchs, G.D.; Buhrman, R.A.; Torres, L. Micromagnetic Modeling of Magnetization Switching Driven by Spin-Polarized Current in Magnetic Tunnel Junctions. *J. Appl. Phys.* **2007**, *101*, 063914. [CrossRef]
29. Carpentieri, M.; Finocchio, G.; Torres, L.; Azzerboni, B. Modeling of Fast Switching Processes in Nanoscale Spin Valves. *J. Appl. Phys.* **2008**, *103*, 07B117. [CrossRef]
30. Petitjean, C.; Luc, D.; Waintal, X. Unified Drift-Diffusion Theory for Transverse Spin Currents in Spin Valves, Domain Walls, and Other Textured Magnets. *Phys. Rev. Lett.* **2012**, *109*, 117204. [CrossRef] [PubMed]
31. Graczyk, P.; Krawczyk, M. Nonresonant Amplification of Spin Waves Through Interface Magnetoelectric Effect and Spin-Transfer Torque. *Sci. Rep.* **2021**, *11*, 15692. [CrossRef] [PubMed]
32. Haney, P.; Lee, H.W.; Lee, K.J.; Manchon, A.; Stiles, M. Current Induced Torques and Interfacial Spin-Orbit Coupling: Semiclassical Modeling. *Phys. Rev. B* **2013**, *87*, 174411. [CrossRef]
33. Abert, C. Micromagnetics and Spintronics: Models and Numerical Methods. *Eur. Phys. J. B* **2019**, *92*, 120. [CrossRef]

34. Zhang, S.; Levy, P.M.; Fert, A. Mechanisms of Spin-Polarized Current-Driven Magnetization Switching. *Phys. Rev. Lett.* **2002**, *88*, 236601. [CrossRef]
35. Luc, D. Théorie Unifiée du Transport de Spin, Charge et Chaleur. Ph.D. Thesis, Université Grenoble Alpes, Grenoble, France, 2016.
36. Ruggeri, M.; Abert, C.; Hrkac, G.; Suess, D.; Praetorius, D. Coupling of Dynamical Micromagnetism and a Stationary Spin Drift-Diffusion Equation: A Step Towards a Fully Self-Consistent Spintronics Framework. *Physica B* **2016**, *486*, 88–91. [CrossRef]
37. Braess, D. *Finite Elements: Theory, Fast Solvers, and Applications in Solid Mechanics*, 3rd ed.; Cambridge University Press: Cambridge, UK, 2007. [CrossRef]
38. Larson, M.G.; Bengzon, F. *The Finite Element Method: Theory, Implementation, and Applications*; Springer: Berlin/Heidelberg, Germany, 2013. [CrossRef]
39. Alouges, F.; Jaisson, P. Convergence of a Finite Element Discretization for the Landau-Lifshitz Equations in Micromagnetism. *Math. Models Methods Appl. Sci.* **2006**, *16*, 299–316. [CrossRef]
40. Bartels, S.; Ko, J.; Prohl, A. Numerical Analysis of an Explicit Approximation Scheme for the Landau-Lifshitz-Gilbert Equation. *Math. Comput.* **2008**, *77*, 773–788. [CrossRef]
41. Alouges, F. A New Finite Element Scheme for Landau-Lifchitz Equations. *Discrete Contin. Dyn. Syst. S* **2008**, *1*, 187–196. [CrossRef]
42. Alouges, F.; Kritsikis, E.; Toussaint, J.C. A Convergent Finite Element Approximation for Landau–Lifschitz–Gilbert Equation. *Physica B* **2012**, *407*, 1345–1349. [CrossRef]
43. Bruckner, F.; Suess, D.; Feischl, M.; Führer, T.; Goldenits, P.; Page, M.; Praetorius, D.; Ruggeri, M. Multiscale Modeling in Micromagnetics: Existence of Solutions and Numerical Integration. *Math. Models Methods Appl. Sci.* **2014**, *24*, 2627–2662. [CrossRef]
44. Abert, C.; Hrkac, G.; Page, M.; Praetorius, D.; Ruggeri, M.; Suess, D. Spin-Polarized Transport in Ferromagnetic Multilayers: An Unconditionally Convergent FEM Integrator. *Comp. Math. Appl.* **2014**, *68*, 639–654. [CrossRef]
45. Fiorentini, S.; Ender, J.; Selberherr, S.; de Orio, R.L.; Goes, W.; Sverdlov, V. Coupled Spin and Charge Drift-Diffusion Approach Applied to Magnetic Tunnel Junctions. *Solid-State Electron.* **2021**, *186*, 108103. [CrossRef]
46. Fiorentini, S.; Bendra, M.; Ender, J.; de Orio, R.L.; Goes, W.; Selberherr, S.; Sverdlov, V. Spin and Charge Drift-Diffusion in Ultra-Scaled MRAM Cells. *Sci. Rep.* **2022**, *12*, 20958. [CrossRef]
47. Chshiev, M.; Manchon, A.; Kalitsov, A.; Ryzhanova, N.; Vedyayev, A.; Strelkov, N.; Butler, W.; Dieny, B. Analytical Description of Ballistic Spin Currents and Torques in Magnetic Tunnel Junctions. *Phys. Rev. B* **2015**, *92*, 104422. [CrossRef]
48. Julliere, M. Tunneling Between Ferromagnetic Films. *Phys. Lett. A* **1975**, *54*, 225–226. [CrossRef]
49. Hestenes, M.R.; Stiefel, E. Methods of Conjugate Gradients for Solving Linear Systems. *J. Res. Natl. Bur. Stand.* **1952**, *49*, 409–436. [CrossRef]
50. Camsari, K.Y.; Ganguly, S.; Datta, D.; Datta, S. Physics-Based Factorization of Magnetic Tunnel Junctions for Modeling and Circuit Simulation. In Proceedings of the IEDM Conference, San Francisco, CA, USA, 15–17 December 2014; pp. 35.6.1–35.6.4. [CrossRef]
51. Saad, Y.; Schultz, M.H. GMRES: A Generalized Minimal Residual Algorithm for Solving Nonsymmetric Linear Systems. *SIAM J. Sci. Stat. Comput.* **1986**, *7*, 856–869. [CrossRef]
52. Hrkac, G.; Pfeiler, C.M.; Praetorius, D.; Ruggeri, M.; Segatti, A.; Stiftner, B. Convergent Tangent Plane Integrators for the Simulation of Chiral Magnetic Skyrmion Dynamics. *Adv. Comput. Math.* **2019**, *45*, 1329–1368. [CrossRef]
53. Abert, C.; Exl, L.; Bruckner, F.; Drews, A.; Suess, D. magnum.fe: A Micromagnetic Finite-Element Simulation Code Based on FEniCS. *J. Magn. Magn. Mater.* **2013**, *345*, 29–35. [CrossRef]
54. Imhoff, J.; Meunier, G.; Brunotte, X.; Sabonnadiere, J. An Original Solution for Unbounded Electromagnetic 2D- and 3D-Problems Throughout the Finite Element Method. *IEEE Trans. Magn.* **1990**, *26*, 1659–1661. [CrossRef]
55. Brunotte, X.; Meunier, G.; Imhoff, J. Finite Element Modeling of Unbounded Problems Using Transformations: A Rigorous, Powerful and Easy Solution. *IEEE Trans. Magn.* **1992**, *28*, 1663–1666. [CrossRef]
56. Henrotte, F.; Meys, B.; Hedia, H.; Dular, P.; Legros, W. Finite Element Modelling with Transformation Techniques. *IEEE Trans. Magn.* **1999**, *35*, 1434–1437. [CrossRef]
57. Leliaert, J.; Mulkers, J. Tomorrow's Micromagnetic Simulations. *J. Appl. Phys.* **2019**, *125*, 180901. [CrossRef]
58. Ender, J.; Mohamedou, M.; Fiorentini, S.; de Orio, R.L.; Selberherr, S.; Goes, W.; Sverdlov, V. Efficient Demagnetizing Field Calculation for Disconnected Complex Geometries in STT-MRAM Cells. In Proceedings of the SISPAD Conference, Kobe, Japan, 23 September–6 October 2020; pp. 213–216. [CrossRef]
59. Fredkin, D.; Koehler, T. Hybrid Method for Computing Demagnetizing Fields. *IEEE Trans. Magn.* **1990**, *26*, 415–417. [CrossRef]
60. Popović, N.; Praetorius, D. $\mathcal{H}$-Matrix Techniques for Stray-Field Computations in Computational Micromagnetics. In Proceedings of the Large-Scale Scientific Computing Conference, Sozopol, Bulgaria, 6–10 June 2005; Lirkov, I., Margenov, S., Waśniewski, J., Eds.; Springer: Berlin/Heidelberg, Germany, 2006; pp. 102–110. [CrossRef]
61. H2Lib [Software]. Available online: http://www.h2lib.org (accessed on 19 April 2023).
62. Loch, W.J.; Fiorentini, S.; Jørstad, N.P.; Goes, W.; Selberherr, S.; Sverdlov, V. Double Reference Layer STT-MRAM Structures with Improved Performance. *Solid-State Electron.* **2022**, *194*, 108335. [CrossRef]
63. Nishioka, K.; Honjo, H.; Ikeda, S.; Watanabe, T.; Miura, S.; Inoue, H.; Tanigawa, T.; Noguchi, Y.; Yasuhira, M.; Sato, H.; et al. Novel Quad-Interface MTJ Technology and its First Demonstration With High Thermal Stability Factor and Switching Efficiency for STT-MRAM Beyond 2X nm. *IEEE Trans. Electron Devices* **2020**, *67*, 995–1000. [CrossRef]

64. Grimaldi, E.; Krizakova, V.; Sala, G.; Yasin, F.; Couet, S.; Sankar Kar, G.; Garello, K.; Gambardella, P. Single-Shot Dynamics of Spin-Orbit Torque and Spin Transfer Torque Switching in Three-Terminal Magnetic Tunnel Junctions. *Nat. Nanotechnol.* **2020**, *15*, 111–117. [CrossRef]
65. Zhang, W.; Han, W.; Jiang, X.; Yang, S.-H.; Parkin, S.S.P. Role of Transparency of Platinum–Ferromagnet Interfaces in Determining the Intrinsic Magnitude of the Spin Hall Effect. *Nat. Phys.* **2015**, *11*, 496–502. [CrossRef]

Disclaimer/Publisher's Note: The statements, opinions and data contained in all publications are solely those of the individual author(s) and contributor(s) and not of MDPI and/or the editor(s). MDPI and/or the editor(s) disclaim responsibility for any injury to people or property resulting from any ideas, methods, instructions or products referred to in the content.

micromachines

MDPI

Article

A Comprehensive Study of Temperature and Its Effects in SOT-MRAM Devices

Tomáš Hadámek [1,*], Nils Petter Jørstad [1], Roberto Lacerda de Orio [2], Wolfgang Goes [3], Siegfried Selberherr [2] and Viktor Sverdlov [1]

[1] Christian Doppler Laboratory for Nonvolatile Magnetoresistive Memory and Logic, Institute for Microelectronics, TU Wien, Gußhausstraße 27-29, A-1040 Wien, Austria; sverdlov@iue.tuwien.ac.at (V.S.)
[2] Institute for Microelectronics, TU Wien, Gußhausstraße 27-29, A-1040 Wien, Austria
[3] Silvaco Europe Ltd., Cambridge PE27 5JL, UK
* Correspondence: hadamek@iue.tuwien.ac.at

Abstract: We employ a fully three-dimensional model coupling magnetization, charge, spin, and temperature dynamics to study temperature effects in spin-orbit torque (SOT) magnetoresistive random access memory (MRAM). SOTs are included by considering spin currents generated through the spin Hall effect. We scale the magnetization parameters with the temperature. Numerical experiments show several time scales for temperature dynamics. The relatively slow temperature increase, after a rapid initial temperature rise, introduces an incubation time to the switching. Such a behavior cannot be reproduced with a constant temperature model. Furthermore, the critical SOT switching voltage is significantly reduced by the increased temperature. We demonstrate this phenomenon for switching of field-free SOT-MRAM. In addition, with an external-field-assisted switching, the critical SOT voltage shows a parabolic decrease with respect to the voltage applied across the magnetic tunnel junction (MTJ) of the SOT-MRAM cell, in agreement with recent experimental data.

Keywords: micromagnetics; spintronics; SOT-MRAM; temperature scaling; temperature effects; incubation time

Citation: Hadámek, T.; Jørstad, N.P.; de Orio, R.L.; Goes, W.; Selberherr, S.; Sverdlov, V. A Comprehensive Study of Temperature and Its Effects in SOT-MRAM Devices. *Micromachines* **2023**, *14*, 1581. https://doi.org/10.3390/mi14081581

Academic Editor: Zhongrui Wang

Received: 18 June 2023
Revised: 30 July 2023
Accepted: 7 August 2023
Published: 11 August 2023

Copyright: © 2023 by the authors. Licensee MDPI, Basel, Switzerland. This article is an open access article distributed under the terms and conditions of the Creative Commons Attribution (CC BY) license (https://creativecommons.org/licenses/by/4.0/).

1. Introduction

Magnetoresistive random access memory (MRAM) has recently gained strong attention as a potential replacement for the existing charge-based memories, the static and dynamic random access memories (SRAM and DRAM). Due to the ultra-scaled transistor technology, the leakage currents have rapidly increased together with the static power consumption of the conventional memories. As the information in the MRAM is stored in a relative orientation of two magnetic layers, separated by a thin oxide tunnel barrier, the memory is intrinsically nonvolatile. Hence, the static power consumption is strongly reduced with respect to SRAM and DRAM [1,2]. Moreover, the MRAM is also complementary metal–oxide–semiconductor (CMOS) compatible. In recent years, the two-terminal spin-transfer torque MRAM (STT-MRAM), shown in Figure 1a, has become widely available in the segment of embedded systems. However, due to fairly slow writing times related to the nature of the STT, the writing speed cannot easily reach the sub-nanosecond regimes. Higher currents would partly diminish the problem; however, due to a dielectric breakdown, this would result in faster degradation of the memory cell [3,4].

In order to reach the desired sub-nanosecond switching times and increase the endurance of the MRAM cell, new ways of magnetization manipulation had to be found. In [5], a new method based on the spin Hall effect (SHE) was proposed. Due to the intrinsic characteristics of SOTs, the three-terminal SOT-MRAM, shown in Figure 1b, can operate in the sub-ns region. Moreover, the read and write current paths are separated, and therefore, the endurance is significantly increased. A problem with SOTs for memory application

is that, due to the symmetry of the SOTs, the free layer (FL) perpendicular magnetization can only be brought in-plane and another mechanism has to be utilized to complete the switching. These methods include shape symmetry breaking [6], the use of external magnetic fields and built-in magnetic layers [7–9], Cr doping to introduce an intrinsic magnetic field [10], two-pulse switching [11], magnetization anisotropy tilt [12], the inclusion of an exchange bias [13], interlayer exchange coupling [14], spin current gradient [15], FL composition gradient [16–18], lateral spin-orbit torques [19], competing spin currents [20], out-of-plane spin polarization [21–23], ion implantation [24,25], a combination of STT and SOT switching [26,27], or combinations of multiple methods [8,28].

During the writing process of the SOT-MRAM, a strong current passes through the heavy metal (HM). Due to the SHE, a spin accumulation is generated along the sides of the HM. This results in a spin current that is injected into the FL, affecting its magnetization. During the process, however, the current passing through the HM and the FL generates Joule heat and the temperature of the system rises. Consequently, the magnetic properties of the system change, which affects the whole switching process [8]. In [29], the effects of temperature on switching in an SOT system with an exchange bias were studied. Rahaman et al. [30] presented an investigation of the critical switching current with respect to the pulse length duration for an in-plane SOT for different wafer temperatures. In [31], a ferrimagnetic SOT structure is measured and an analysis of the critical switching current is shown. Arpaci et al. [32] then studied the switching of an antiferromagnetic SOT and estimated the device temperature during switching. Even though the mentioned articles discuss temperature and its effects on the switching behavior, none of the articles present a study of the temperature dynamics and its effects on the switching in the ns-regime. Moreover, the listed studies work with μm-sized devices that are several orders bigger than the industry-relevant nm-sized memory cells. In general, the temperature behavior is expected to be different when the size is reduced due to the reduced times scales of the system.

In this work, we focus on the modeling of temperature dynamics and its effects on the switching of the nm-sized SOT-MRAM. We investigate both field-free and field-assisted switching. In Section 2, the used method, implementation, and simulated structures are described. In the first subsection of Section 3, the temperature of an SOT-MRAM cell is analyzed and compared to previous work. The following subsections describe the effects of the increased temperature on the switching.

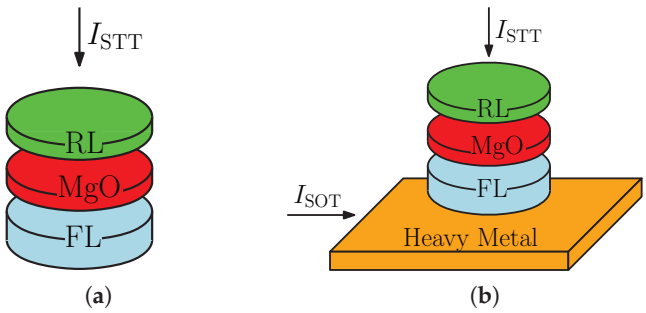

Figure 1. (**a**) A schematic illustration of STT- and (**b**) SOT-MRAM cells. Two separate current paths are present for the SOT-MRAM, where an HM layer is placed underneath the magnetic FL.

2. Method

In order to model the switching behavior of an SOT-MRAM cell, we fully couple magnetization, charge, spin, and temperature dynamics. We employ the Landau–Lifschitz–Gilbert (LLG) equation to describe the magnetization dynamics.

$$\frac{\partial \mathbf{m}}{\partial t} = -\gamma \mu_0 \mathbf{m} \times \mathbf{H}_{\text{eff}} + \alpha \mathbf{m} \times \frac{\partial \mathbf{m}}{\partial t} + \frac{1}{M_S} \mathbf{T}_S \tag{1}$$

where $\mathbf{m}$ stands for the normalized magnetization, and γ, μ_0, α, and M_S are the gyromagnetic ratio, the vacuum permeability, the Gilbert damping, and the saturation magnetization, respectively. $\mathbf{H}_{\text{eff}}$ represents the effective field consisting of several components, namely: the demagnetization field $\mathbf{H}_{\text{demag}}$, the anisotropy field $\mathbf{H}_{\text{aniso}}$, the exchange field $\mathbf{H}_{\text{exch}}$, and the external field $\mathbf{H}_{\text{ext}}$. $\mathbf{H}_{\text{demag}}$ is solved through a hybrid FEM-BEM method [33]. $\mathbf{H}_{\text{aniso}}$ is considered to be uniaxial.

$$\mathbf{H}_{\text{aniso}} = \frac{2K_a}{\mu_0 M_S}(\mathbf{n}\cdot\mathbf{m})\mathbf{n} \tag{2}$$

where K_a is the anisotropy energy density and $\mathbf{n}$ is a unit vector coinciding with the axis of the magnetic tunnel junction (MTJ) cylinder. The exchange field is determined using

$$\mathbf{H}_{\text{exch}} = \frac{2A_{\text{exch}}}{\mu_0 M_S}\nabla^2\mathbf{m}, \tag{3}$$

where A_{exch} is the exchange stiffness. $\mathbf{H}_{\text{ext}}$, when considered, points in the SOT current direction. The spin torque $\mathbf{T}_S$ represents the torque's action on the magnetization due to spin-relevant effects and is determined from the spin accumulation $\mathbf{S}$.

$$\mathbf{T}_S = -\frac{D_e}{\lambda_J^2}\mathbf{m}\times\mathbf{S} - \frac{D_e}{\lambda_\varphi^2}\mathbf{m}\times(\mathbf{m}\times\mathbf{S}) \tag{4}$$

where D_e stands for the electron diffusion constant, and λ_J and λ_φ are the spin exchange and dephasing lengths, respectively. Due to the spin dynamics being several orders of magnitude faster than the magnetization dynamics, $\mathbf{S}$ can be treated as a static problem [34,35].

$$\frac{\partial\mathbf{S}}{\partial t} = 0 = -\nabla\cdot\overline{\mathbf{J_S}} - D_e\left(\frac{\mathbf{S}}{\lambda_{sf}^2} + \frac{\mathbf{S}\times\mathbf{m}}{\lambda_J^2} + \frac{\mathbf{m}\times(\mathbf{S}\times\mathbf{m})}{\lambda_\varphi^2}\right) \tag{5}$$

$$\overline{\mathbf{J_S}} = -\frac{\mu_B}{e}\beta_\sigma\mathbf{m}\otimes\left(\mathbf{J_C} - \beta_D D_e\frac{e}{\mu_B}\left[(\nabla\mathbf{S})^{\mathbf{T}}\mathbf{m}\right]\right) - D_e\nabla\mathbf{S} - \theta_{SHA}\frac{\mu_B}{e}\varepsilon\mathbf{J_C} \tag{6}$$

where λ_{sf} is the spin-flip length, and $\mathbf{J_C}$ stands for the charge current, while μ_B, e, β_σ, and β_D are the atomic magnetic moment, the elementary charge, the conductivity spin polarization, and the diffusivity spin polarization, respectively. The last term in (6) represents the spin Hall effect with spin Hall angle θ_{SHA}. We consider the transverse spin currents to be fully absorbed at the FL/HM interface and we implement a boundary condition based on the real and imaginary part of the mixing conductance $G^{\uparrow\downarrow}$ [35,36].

$$\overline{\mathbf{J_S}}\cdot\mathbf{n}|_N = -\frac{2D_e}{\sigma}\left[\text{Re}(G^{\uparrow\downarrow})\mathbf{m}\times(\mathbf{m}\times\mathbf{S}|_N) + \text{Im}(G^{\uparrow\downarrow})\mathbf{m}\times\mathbf{S}|_N\right] \tag{7}$$

where σ stands for the electric conductivity and $|N$ indicates the HM side of the interface. Equation (7) is included as a contribution to the torque in the first layer of elements on the FM side of the interface. The charge current in (6) is determined from the potential V solving (8) and (9).

$$-\nabla\cdot(\sigma\nabla V) = 0 \tag{8}$$

$$\mathbf{J_C} = -\sigma\nabla V \tag{9}$$

where σ is assumed to be constant in the ferromagnetic and nonmagnetic layers, while in the tunneling layer, it is assumed to be dependent on the respective angle between the FL and the reference layer (RL) [37,38].

The dynamics of the temperature T is modeled using the heat transport equation.

$$c_V\rho_m\frac{\partial T}{\partial t} - \kappa\Delta T = \dot{q}_V \tag{10}$$

where c_V, ρ_m, and K are the heat capacity, the material density, and the thermal conductivity, respectively. $\dot{q}_V$ represents the heat sources, in this case, the Joule heating $\dot{q}_V = \sigma\mathbf{J_C^2}$. To

account for the change in magnetization dynamics, M_S, K_a, and A_{exch} in (1)–(3) are made temperature-dependent [8,39]. The M_S is scaled according to Bloch's power law.

$$M_S(T) = M_{S_0} m_S = M_{S_0} \left[1 - \left(\frac{T}{T_C} \right)^{\beta} \right] \tag{11}$$

where M_{S_0} is the saturation magnetization at 0 K, and the factor m_S represents the scaling with respect to the Curie temperature T_C and a temperature power parameter β. The anisotropy constant and the exchange constant also scales with m_S; however, with additional power coefficients p and q, and K_{a_0} and A_{exch_0}, the anisotropy and exchange constants at 0 K, respectively.

$$K_a(T) = K_{a_0} m_S^p \tag{12}$$

$$A_{exch}(T) = A_{exch_0} m_S^q \tag{13}$$

2.1. Implementation

To solve Equations (1)–(13), we use the finite element method. The equations are transferred into weak formulations and implemented within our MRAM simulation framework [40]. More details about the weak formulation of the equations can be found in [41].

2.2. Simulated Structures

We simulate two different structures. The first one, Structure I, is based on previous simulation work in [8] and is shown in Figure 1a. It consists of a $200 \times 230\,\text{nm}^2$ $\beta-$W layer (orange) with a 3.7 nm thickness. On top of the rectangle, an MTJ stack with an 80 nm diameter is placed, consisting of a 1.2 nm thick FeCoB FL (light blue), a 1 nm MgO (red), and a 1 nm FeCoB RL (green). A 12 nm Cu layer is placed on top of the MTJ stack. The whole structure is surrounded by an oxide (half opaque nonhomogeneous gray). Dirichlet conditions are applied (constant 300 K) to the sides of the oxide "box", which is large enough not to affect the temperature simulation results.

Structure II, depicted in Figure 2b, represents a realistic SOT-MRAM cell [8,42]. The FeCoB FL and the RL (green) are considered to be 1.2 nm and 1.0 nm thick, respectively, the MgO barrier thickness is 1.0 nm, and the MTJ diameter is 40 nm. The $\beta-$W heavy metal (depicted in orange) is considered to be 3.7 nm thick and 50 nm wide, the total length is 140 nm. The HM layer is connected through a Cu via to a doped Si substrate (pink). The other end is connected to a long Cu interconnect. The top 50 nm long Cu region is connected to another long Cu interconnect. The whole structure is surrounded by SiO (half opaque nonhomogeneous gray). Both the bottom of the substrate and the ends of the word and read lines are made sufficiently large so as not to have any significant effects on the final result. Dirichlet boundary conditions (constant 300 K) are applied at the ends of the contacts and the bottom of the substrate.

(**a**) (**b**)

Figure 2. Simulated SOT-MRAM structures. (**a**) Simple structure from [8]. (**b**) Realistic structure with contacts, current lines, and a Si buffer beneath.

2.3. Simulation Parameters

The parameters relevant for the magnetization, charge, and spin dynamics are listed in Tables A1 and A2, given in Appendix A. We choose the temperature-dependent Fe-CoB properties so that $M_S(300\,\mathrm{K}) = 0.81\,\mathrm{MAm}^{-1}$, $K_a(300\,\mathrm{K}) = 539\,\mathrm{kJm}^{-3}$ [43], and $A_{exch}(300\,\mathrm{K}) = 20\,\mathrm{pJm}^{-1}$ [44]. $T_C = 750\,\mathrm{K}$, $\beta = 1.7$, $p = 3$, and $q = 1.7$ [8,45]. The temperature-relevant parameters for different materials are listed in Table A3. We consider the parameters to be constant for the simulated temperature range.

3. Results

3.1. Temperature of the Structure

First, we simulate Structure I (Figure 2a). To analyze the heating of the structure and the time constants of the system, we consider a constant SOT current density of $1.1 \cdot 10^{12}\,\mathrm{Am}^{-2}$ in the HM layer, in agreement with [8]. The potential at the top of the contact is left floating. After the current pulse is turned on, the temperature of the structure rises. Figure 3 shows an FL temperature increase ΔT in time. The black dots indicate data extracted from [8]. Only the average FL temperatures are shown. In order to match the heating curves, the conductivity of the surrounding oxide layer is varied. The solid blue and orange curves represent the heating of the structure with the surrounding oxide conductivity of 2.4 and $2.6\,\mathrm{Wm}^{-1}\mathrm{K}^{-1}$, respectively. The data are fitted with a triple exponential (single and double exponentials do not provide a good match) and corresponding time constants τ_i-s are extracted and listed in Table 1. The longest time constant τ_3 is also plotted in Figure 3, for illustration.

Table 1. Time constants for different structures.

Structure	τ_1 (ns)	τ_2 (ns)	τ_3 (ns)
Structure I, $2.4\,\mathrm{Wm}^{-1}\mathrm{K}^{-1}$	0.073	0.746	5.013
Structure I, $2.6\,\mathrm{Wm}^{-1}\mathrm{K}^{-1}$	0.072	0.733	4.896
Structure I, [8]	0.152	1.216	5.796
Structure II	0.035	0.439	2.539

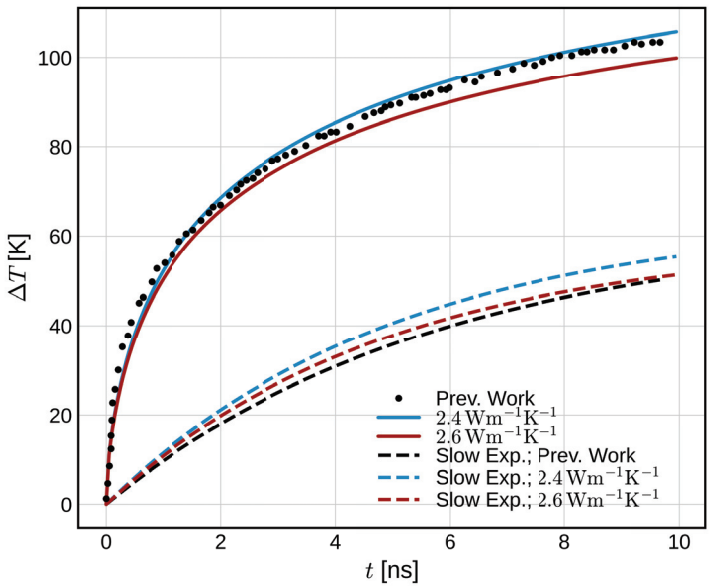

Figure 3. Temperature increase of Structure I [8]. Comparison between the data extracted from [8] (black dotted) and the presented model with two different conductivity of the surrounding oxide (solid). The slow exponential temperature increases are extracted (dashed). A constant current density of $1.1 \times 10^{12}\,\mathrm{Am}^{-2}$ in the HM is considered.

We observe a relatively good match of τ_3, whereas τ_1 and τ_2 show a bigger difference. We attribute the bigger difference for the fast time constants to the shape of the current pulse used (heavyside versus slower initial increase), although other differences are likely to be present due to parameter deviation from the original model (not listed in [8]). We note that the fast time constants mostly represent the heating of the structure, whereas a slow temperature increase is present due to a slow temperature increase of the surrounding oxide.

In order to fully understand the switching of the SOT-MRAM cell, we focus on the more complex Structure II, described in Section 2.2. We first apply only the SOT voltage U_{SOT} between the lower contact and the write line, which results in the SOT current I_{SOT} through the HM. In Figure 4a, the temperature of the structure at 0.2 ns for 0.4 V is illustrated. The temperature increases fast around the FL, mainly due to the heating in the HM. The sides of the HM are cooled down by heat transfer through the via and the current line. The heat transfer through the MgO layer is not significant and a strong temperature gradient across the layer exists due to its very low thermal conductivity. The FL temperature increase for different voltages is shown in Figure 4b. We observe a swift temperature increase in the beginning and a much slower increase towards the end. As the used model is linear, the temperature increase is proportional to the heating power in the system—proportional to the second power of U_{SOT}, or I_{SOT}. The linear dependence of the FL temperature increase ΔT with respect to U_{SOT}^2 is shown in the inset of Figure 4b, similar to [46]. In other words, if only the I_{SOT} is considered throughout the structure, it is sufficient to scale the temperature with its second power. This result is, however, not applicable if both I_{SOT} and I_{STT} are present, as shown in the following subsections. We notice the time constants of Structure II (last line in Table 1) are shorter than those of Structure I, mainly due to the structure geometry and different boundary (Structure I unrealistically floats in the oxide). As previously mentioned, the two short time constants are dominated by the smaller HM and MTJ sizes, whereas the long time constant is mainly determined by the heating of the contacts, substrate, and the surrounding oxide.

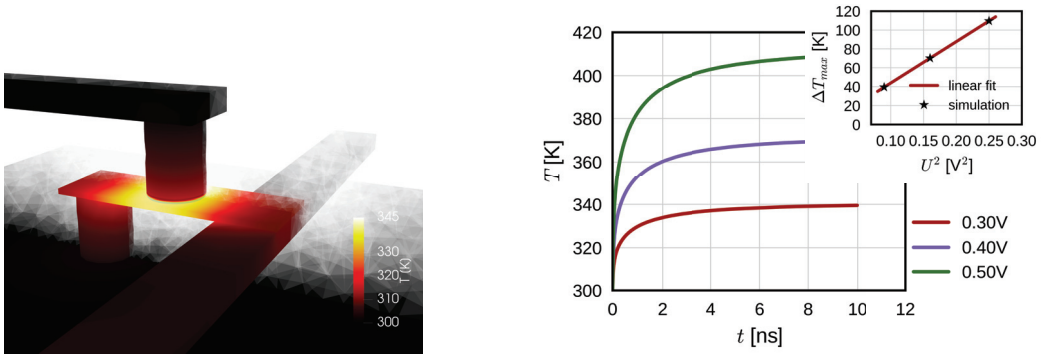

(**a**) (**b**)

Figure 4. (**a**) Structure temperature at 0.2 ns after a voltage pulse U_{SOT} = 0.4 V was applied between the contacts. In the beginning, the temperature increase is centralized around the MTJ stack. (**b**) Maximum temperature increase of the FL for different voltages. The inset shows the maximum temperature increase with respect to U_{SOT}^2.

3.2. Effect of Temperature on the Initial Switching Dynamics

In this section, we investigate how the increasing temperature affects the initial stage of the switching of Structure II (Figure 2b). First, we consider I_{SOT} only and no heating of the structure (no scaling applied). In Figure 5a, the initial dynamics for different U_{SOT} is shown. An average FL magnetization in the z-direction is shown.

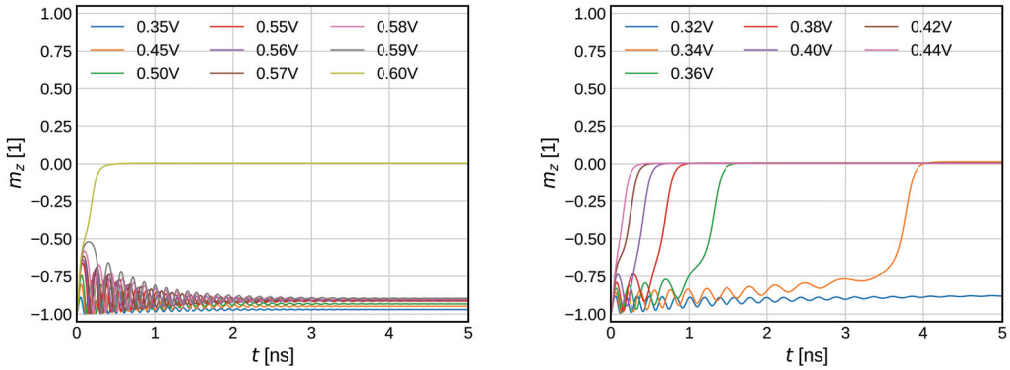

Figure 5. (**a**) Simulations of the FL magnetization in-plane flip with SOTs only. Temperature scaling is not included. (**b**) Simulations of the FL magnetization in-plane flip with SOTs only, with temperature scaling included. An incubation time due to the slow temperature rise can be observed. The critical SOT voltage that flips the FL magnetization in-plane is significantly reduced in comparison to the constant temperature model.

A sharp transition into a final state can be observed with respect to U_{SOT}. For the lower voltages, the FL magnetization starts to oscillate; however, it falls back close to the negative z-direction. When the $U_{\mathrm{SOT}} = 0.6\,\mathrm{V}$ is applied, the magnetization suddenly flips in-plane ($m_z = 0$). In order to understand this behavior, we employ a simpler macromagnetic model. The steady-state solutions of the explicit form of the LLG are shown in Figure 6. The black dots represent a stable solution, whereas the gray dots show an unstable solution. The colored markers represent the final magnetization states of the system and the magnitude of the first oscillation (the strongest one) for different damping and different pulse shapes. The crosses show a solution when a heavyside function is applied. The final solution falls on the lower branch, until the first oscillation comes close to the unstable one. When the oscillation is big enough, the final magnetization solution falls into the plane ($m_z = 0$)), thus causing the abrupt change in the final state of the system. When the damping is increased, the first oscillation is reduced and the jump is present for higher current densities. Lastly, if the voltage is changed slowly (1 ns for the full value), the initial oscillation is almost gone and the solution follows the lower stable solution, until it disappears for high enough current densities.

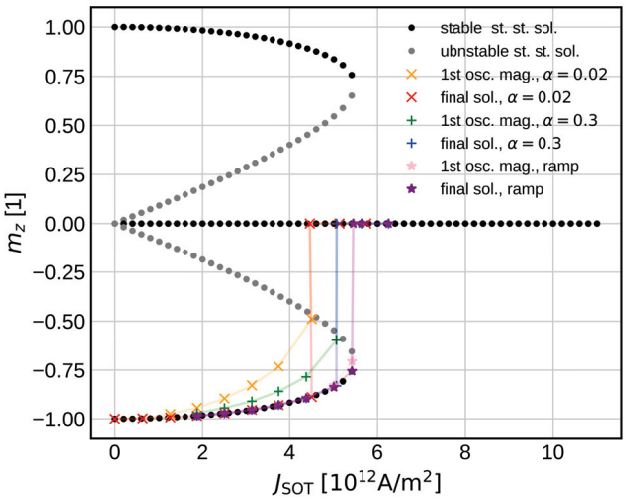

Figure 6. Steady-state solutions (gray, black) and real trajectories of the final magnetization state (orange, red, green). When the first oscillation amplitude (orange, green, pink) reaches the unstable solution (gray), an instant jump into the in-plane state appears.

When the full temperature simulation is included, the magnetization dynamics change significantly (Figure 5b). The sharp in-plane transition is not present anymore. For higher voltages, the magnetization flips immediately into the plane whereas, for the lower voltages, an incubation phase can be observed, in agreement with experimental data [8]. We observe significantly lower voltages required for the magnetization in-plane flip in comparison to the constant temperature model. For the full temperature model, a voltage of 0.34 V is able to bring magnetization in-plane versus the 0.6 V required in the constant temperature model. If one considers the shorter time scales, the reduction is less pronounced; however, even the 0.42 V means a significant reduction in the critical SOT current. The lower critical switching voltage is caused by reduced anisotropy energy and saturation magnetization, which moves the shoulder of the unstable solution lower. The lowered exchange stiffens then enables easier nucleation of the magnetization reversal and allows for a more domain-like switching.

Lastly, we compare the reduction in the critical switching voltages to the results of the highly damped macrospin model [47]. Within the macrospin approximation, the critical switching current is proportional to M_S and K_a in the absence of the external field H_{ext}.

$$J_C = \frac{2e\, M_S\, t_F}{\hbar\, \theta_{SHA}} \left(\frac{H_{aniso}}{2} - \frac{H_{ext}}{\sqrt{2}} \right) \tag{14}$$

where t_F stands for the thickness of the FL. First, we consider the switching at 0.42 V when no significant initial oscillation is present. Considering the FL temperature reached when the FL starts switching ($\sim$355 K), M_S and K_a drop to 91 and 76% of the initial value, respectively, and the critical switching current (voltage) is reduced to 69%. This is in good agreement with our simulation, with the critical voltage reduced to 0.42/0.6 = 70% of its initial value. Secondly, we look at the switching at 0.34 V. When the FL switches, the FL temperature reaches $\sim$345 K, which results in a critical voltage reduced to about 74% of its original value. The reduction is significantly lower than the simulated reduction of 0.34/0.6 = 56%. We attribute this discrepancy to the missing dynamics in the critical current calculation within the macrospin model. As we have already demonstrated, the initial oscillation can significantly reduce the critical current, and we conclude that any further reduction in the critical current is caused by the increase in the amplitude of the FL magnetization oscillation.

3.3. Field-Free Switching—Combined STT-SOT-MRAM

We now focus on the previously mentioned field-free switching, often referred to as a combined STT-SOT switching or SOT-assisted STT switching. In the first switching phase, both the SOT and STT currents are present, whereas in the later switching phase, the SOT current is turned off. We employ both of the pulses for the first 2 ns and investigate the difference between the constant temperature and full temperature models again. We vary U_{SOT}, whereas U_{STT} is kept at a constant 0.75 V.

In Figure 7, the switching simulations within the described SOT-STT switching scheme are shown. We observe that the behavior of both models looks very alike (constant temperature model shown in Figure 7a, full temperature model in Figure 7b). The initial oscillatory behavior is present in both systems. We attribute this to the additional STT torque, which acts on the FL only when nonzero magnetization components m_x and m_y are present. The STT torque is strongest when the FL magnetization is in-plane. An important difference between the two models is still the significantly reduced critical voltage, which flips the FL magnetization in the plane: 0.3 versus 0.5 V for the full 2 ns interval, or 0.4 versus 0.6 V if a shorter 0.5 ns SOT interval is considered. The reduced critical voltage can clearly be seen from Figure 8a, which shows the average magnetic parameter change in the FL for U_{SOT} = 0.31 V and U_{STT} = 0.75 V. The anisotropy energy density is significantly reduced and so is the energy barrier. In Figure 8b, the corresponding temperature increase in the FL is shown (in black). The maximum and minimum FL temperatures are also indicated (gray dotted and dashed lines, respectively). We observe a highly nontrivial temperature

development due to the STT heating and changing resistance of the MTJ. At 2 ns, a fast temperature decrease is observed due to the I_{SOT} being turned off.

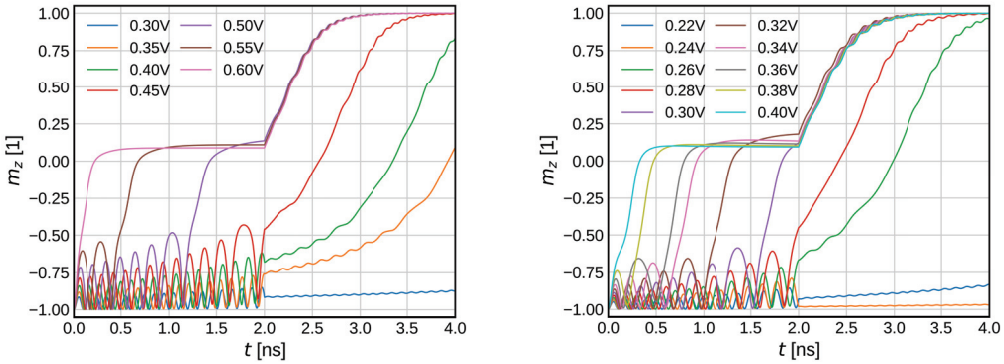

(**a**) (**b**)

Figure 7. (**a**) Simulations of the combined STT-SOT switching at constant 300 K, and (**b**) with the full temperature model. The different paths (colors) represent different U_{SOT}, U_{STT} = 0.75 V. The SOT current is only present during the first 2 ns, while the STT is kept for the whole simulation. Due to the additional presence of the STT field, the initial oscillatory behavior is amplified and acts as an additional field that amplifies the oscillations. Both of the switching simulations with a constant temperature and with the full temperature model look similar; however, the oscillations are modulated for the latter. The critical switching voltage is also significantly reduced.

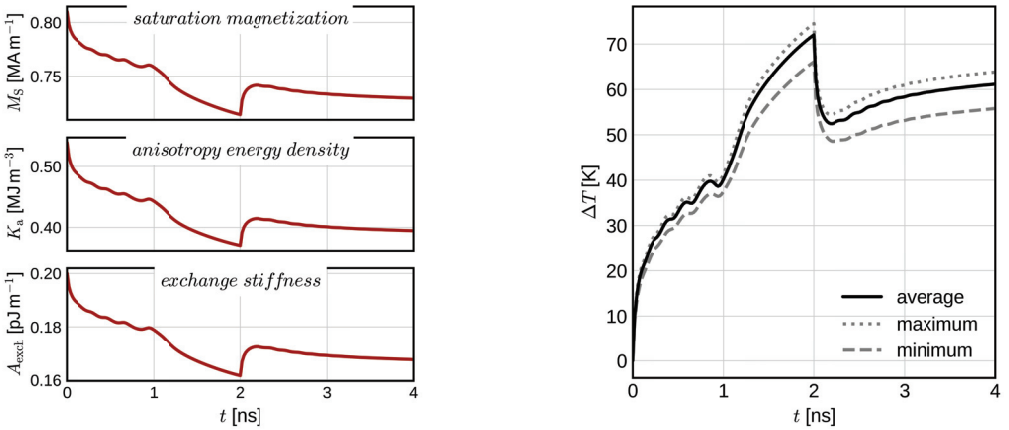

(**a**) (**b**)

Figure 8. (**a**) Parameter change due to the increased FL temperature, and (**b**) the corresponding FL temperature increase.

3.4. Switching with External Fields

In this last subsection, we focus on switching assisted by an external field. Such a field is of importance as it can represent different scenarios: the real external field, the stray fields induced by additional hard magnetic layers above [8] or below [7] the MTJ stack, or doping [10].

First, we simulate Structure II with a 50 mT external field in the I_{SOT} direction. We only apply the U_{SOT} voltage and vary its length. Unlike with SOT only, the magnetization does not stay in-plane ($m_z = 0$), but due to the presence of the magnetic field, it precesses around the field, which brings the magnetization closer to the reversed orientation. This can be understood from the first cross-product term in the LLG (1). The numerical experiment is as follows: (i) In the beginning, the system is left to relax for 1 ns. (ii) After the relaxation, U_{SOT} is switched on for a short period of time. (iii) U_{SOT} is switched off again and the system relaxes to the final state. We study two different U_{SOT} pulse durations, 1.5 and

3.0 ns. The results of such an experiment are shown in Figure 9. For the shorter 1.5 ns pulse, voltages 0.32 V and below do not switch. For 0.32 V, a short incubation is observed, the magnetization passes the in-plane configuration but is brought back to the initial state after the pulse is turned off. For the longer 3.0 ns pulse, both 0.32 V and 0.30 V switch due to the longer pulse length. We note that for the constant temperature model, voltages up to 0.4 V do not show any switching, and the switching simulations are therefore not shown.

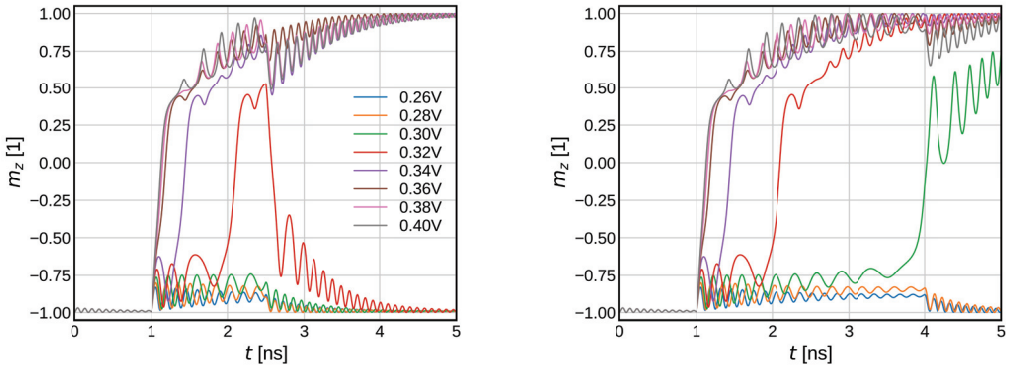

Figure 9. Switching simulations with an external field for different U_{SOT} and (**a**) 1.5 ns, (**b**) 3.0 ns pulse durations. The external field is 50 mT in the I_{SOT} direction. We let the system relax for 1 ns before the pulse is applied. The color coding is identical for both plots.

As a last experiment, we simulate SOT switching with an external field of 50 mT (identical direction to I_{SOT}) and with additional heating due to the STT. Such a system was reported in [28]. We keep both the U_{SOT} and U_{STT} for 4 ns and let the magnetization relax afterward. We then check the final magnetization state and see if the switching has been completed, and then we determine the lowest U_{SOT} for which the magnetization is switched, the critical SOT switching voltage U_{SOT}. We note that the temperature increase consists of both the smooth SOT temperature change shown in Figure 4b and the FL magnetization-dependent STT heating. The total temperature increase is similar to the one reported in Figure 8b but without the drop due to the SOT being turned off. In Figure 10, the dependence of U_{SOT} on U_{STT} is shown. We observe a parabolic dependence of U^C_{SOT} with the increasing absolute value of U_{STT}, in agreement with [28]. Note that our system always kept the same set of parameters. In comparison to [28], where an additional voltage-controlled magnetic anisotropy (VCMA) was considered, we have a stronger STT torque, and no VCMA. The qualitatively identical result shows the significance of the additional STT heating on the U^C_{SOT}. We observe a slight shift of the parabola due to the additional STT torques, in agreement with [28].

In all the previously presented experiments, the increased temperature, due to Joule heating, significantly reduces switching currents and/or switching times. In turn, the writing energy of the SOT-MRAM cell can be reduced if the pulse duration is kept short. In addition, the reduced switching currents and voltages allow for smaller switching transistors needed for memory operation, resulting in a reduced device footprint. On the other hand, all the generated heat is an irreversible energy loss that contributes to the total switching energy. Moreover, the increased temperatures can lead to a random bit flip just after the current pulse is turned off before the FL cools down, resulting in an increased write error rate. Finally, if the temperature increase is too high, the memory device can be damaged.

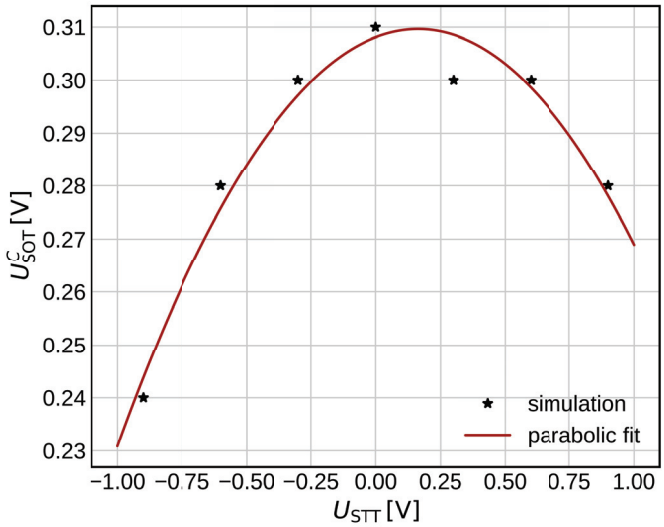

Figure 10. Dependence of the critical SOT switching voltage U^C_{SOT} on the applied STT heating voltage for the SOT switching with an external field. A parabolic reduction in U^C_{SOT} is observed due to the increased temperature of the FL. The parabola is shifted due to the additional STT torque.

4. Conclusions

We coupled magnetization, charge, spin, and temperature dynamics to study modern SOT-MRAM devices. In order to allow for the SOT switching, the spin Hall effect was added. To account for the elevated temperature, scaling of the magnetization parameters was implemented. We validated our model by comparing the temperature dynamics to the previously published data and obtained a good agreement. With the validated model, we showed that a significant incubation time is present when the SOT-generating current is applied to the MRAM cell and that such behavior cannot be reproduced by a constant temperature model. We then demonstrated a field-free switching combining both SOT and STT. The temperature shows a nontrivial behavior due to the change in MTJ resistance during switching. Due to the increased temperature, the critical switching voltage is significantly reduced in comparison to the constant temperature model. We also studied SOT-MRAM switching with an external field. We changed the SOT voltage duration and showed that the increasing temperature has significant effects on the switching dynamics. Finally, we showed that an additional STT voltage pulse reduces the critical SOT switching voltage due to the extra heating. This dependence is quadratic, in agreement with our experiments. We conclude that Joule heating significantly affects the switching behavior of SOT-MRAM cells and can considerably reduce the switching currents and switching times, resulting in reduced writing energy and total device size. However, special care should still be taken regarding the maximum temperature to prevent any damage to the device. In order to fully understand the switching of modern SOT-MRAM devices and to accurately predict and optimize the intended behavior, the full temperature dynamics have to be considered.

Author Contributions: Conceptualization, T.H., R.L.d.O. and V.S.; software, T.H., N.P.J., R.L.d.O. and W.G.; investigation, T.H.; resources, V.S. and W.G.; data curation, T.H. and N.P.J.; writing—original draft preparation, T.H.; writing—review and editing, T.H, N.P.J., R.L.d.O., W.G., S.S. and V.S.; supervision, V.S., S.S. and W.G.; project administration, V.S.; funding acquisition, V.S. All authors have read and agreed to the published version of the manuscript.

Funding: This research was funded by the Christian Doppler Research Association, grant number 1558669. The APC was funded by the TU Wien Bibliothek through its Open Access Funding Program.

Data Availability Statement: The datasets generated and/or analyzed during the current study are available from the corresponding author upon reasonable request.

Acknowledgments: The financial support by the Austrian Federal Ministry for Digital and Economic Affairs, the National Foundation for Research, Technology and Development, and the Christian Doppler Research Association is gratefully acknowledged. The authors also acknowledge the TU Wien Bibliothek for financial support through its Open Access Funding Program.

Conflicts of Interest: The authors declare no conflict of interest.

Appendix A

The parameters listed in Tables A1–A3 are mostly taken from the Boris Computational Spintronics material database [48]. The original parameter sources can be found on the linked website.

Table A1. Magnetization- and charge-relevant parameters.

Parameter	Value
MTJ Parameters	
Tunnel magnetoresistance ratio (TMR)	200%
Current spin polarization, β_σ	0.7
Diffusion spin polarization, β_D	1.0
Resistance parallel	$1.4 \cdot 10^4\,\Omega$
Resistance antiparallel	$4.2 \cdot 10^4\,\Omega$
Magnetic Parameters of FeCoB	
Gilbert damping, α	0.02
Gyromagnetic ratio, γ	$1.76 \cdot 10^{-11}\,\mathrm{rad \cdot s^{-1} T^{-1}}$
Saturation magnetization (300 K), M_S	$0.81 \cdot 10^6\,\mathrm{Am^{-1}}$
Exchange stiffness, A_{exch}	$2 \cdot 10^{-11}\,\mathrm{Jm^{-1}}$
Anisotropy energy density, K_a	$0.539 \cdot 10^6\,\mathrm{Jm^{-3}}$

Table A2. Drift diffusion-relevant parameters.

Material ↓ / Parameter →	D_e $(10^{-3}\mathrm{m^2/s})$	λ_sf (nm)	λ_φ (nm)	λ_J (nm)	θ_SHA
FeCoB	1	10	0.4	0.8	-
MgO	-	-	-	-	-
β-W	0.2	2.4	-	-	-0.3
Contacts, Vias	1.1	1.4	-	-	-
SiO	0.1	1.4	-	-	-
Substrate	0.2	1.4	-	-	-

Table A3. Temperature-relevant parameters.

Material ↓ / Parameter →	σ (Ωm)	$\rho_\mathrm{m}\,(\mathrm{kg\,m^{-3}})$	$c_\mathrm{V}\,(\mathrm{J\,kg^{-1}K^{-1}})$	$\kappa(\mathrm{W\,m^{-1}K^{-1}})$
FeCoB	$4{\cdot}10^6$	8800	612	36
MgO	-	3580	877	0.4 [49]
β-W	$0.6{\cdot}10^6$	19,300	134	173
Contacts, Vias	$7{\cdot}10^6$	8800	420	122
SiO	0	2200	730	1.4
Substrate	$1{\cdot}10^6$	2330	710	150

References

1. Chang, M.T.; Rosenfeld, P.; Lu, S.L.; Jacob, B. Technology comparison for large last-level caches (L3Cs): Low-leakage SRAM, low write-energy STT-RAM, and refresh-optimized eDRAM. In Proceedings of the International Symposium on High Performance Computer Architecture (HPCA), Shenzhen, China, 23–27 February 2013; pp. 143–154. [CrossRef]
2. Komalan, M.; Rock, O.H.; Hartmann, M.; Sakhare, S.; Tenllado, C.; Gomez, J.I.; Kar, G.S.; Furnemont, A.; Catthoor, F.; Senni, S.; et al. Main memory organization trade-offs with DRAM and STT-MRAM options based on gem5-NVMain simulation frameworks. In Proceedings of the Design, Automation and Test in Europe Conference and Exhibition (DATE), Dresden, Germany, 19–23 March 2018; pp. 103–108. [CrossRef]

3. Pey, K.L.; Lim, J.H.; Raghavan, N.; Mei, S.; Kwon, J.H.; Naik, V.B.; Yamane, K.; Yang, H.; Lee, K. New Insights into Dielectric Breakdown of MgO in STT-MRAM Devices. In Proceedings of the Electron Devices Technology and Manufacturing Conference (EDTM), Singapore, 12–15 March 2019; pp. 264–266. [CrossRef]
4. Panagopoulos, G.; Augustine, C.; Roy, K. Modeling of dielectric breakdown-induced time-dependent STT-MRAM performance degradation. In Proceedings of the Device Research Conference, Santa Barbara, CA, USA, 20–22 June 2011; pp. 125–126. [CrossRef]
5. Liu, L.; Pai, C.F.; Li, Y.; Tseng, H.W.; Ralph, D.C.; Buhrman, R.A. Spin-torque switching with the giant spin Hall effect of tantalum. *Science* **2012**, *336*, 555–558. [CrossRef] [PubMed]
6. Yu, G.; Upadhyaya, P.; Fan, Y.; Alzate, J.G.; Jiang, W.; Wong, K.L.; Takei, S.; Bender, S.A.; Chang, L.T.; Jiang, Y.; et al. Switching of perpendicular magnetization by spin–orbit torques in the absence of external magnetic fields. *Nat. Nanotechnol.* **2014**, *9*, 548–554. [CrossRef]
7. Cai, K.; Talmelli, G.; Fan, K.; Van Beek, S.; Kateel, V.; Gupta, M.; Monteiro, M.; Chroud, M.B.; Jayakumar, G.; Trovato, A.; et al. First demonstration of field-free perpendicular SOT-MRAM for ultrafast and high-density embedded memories. In Proceedings of the International Electron Devices Meeting (IEDM), San Francisco, CA, USA, 3–7 December 2022; pp. 36.2.1–36.2.4. [CrossRef]
8. Grimaldi, E.; Krizakova, V.; Sala, G.; Yasin, F.; Couet, S.; Kar, G.S.; Garello, K.; Gambardella, P. Single-shot dynamics of spin–orbit torque and spin transfer torque switching in three-terminal magnetic tunnel junctions. *Nat. Nanotechnol.* **2020**, *15*, 111–117. [CrossRef] [PubMed]
9. Garello, K.; Yasin, F.; Hody, H.; Couet, S.; Souriau, L.; Sharifi, S.H.; Swerts, J.; Carpenter, R.; Rao, S.; Kim, W.; et al. Manufacturable 300mm platform solution for field-free switching SOT-MRAM. In Proceedings of the Symposium on VLSI Technology and Circuits, Kyoto, Japan, 9–14 June 2019; pp. T194–T195. [CrossRef]
10. Lyu, H.; Zhao, Y.; Qi, J.; Huang, H.; Zhang, J.; Yang, G.; Guo, Y.; Shen, S.; Qin, W.; Sun, Y.; et al. Field-Free Magnetization Switching Driven by Spin-Orbit Torque in $L1_0$-FeCrPt Single Layer. *Adv. Funct. Mater.* **2022**, *32*, 2200660. [CrossRef]
11. Zeinali, B.; Madsen, J.K.; Raghavan, P.; Moradi, F. Ultra-fast SOT-MRAM cell with STT current for deterministic switching. In Proceedings of the International Conference on Computer Design (ICCD), Boston, MA, USA, 5–8 November 2017; pp. 463–468. [CrossRef]
12. Kim, H.J.; Moon, K.W.; Tran, B.X.; Yoon, S.; Kim, C.; Yang, S.; Ha, J.H.; An, K.; Ju, T.S.; Hong, J.I.; et al. Field-free switching of magnetization by tilting the perpendicular magnetic anisotropy of Gd/Co multilayers. *Adv. Funct. Mater.* **2022**, *32*, 2112561. [CrossRef]
13. Fukami, S.; Zhang, C.; DuttaGupta, S.; Kurenkov, A.; Ohno, H. Magnetization switching by spin–orbit torque in an antiferromagnet–ferromagnet bilayer system. *Nat. Mater.* **2016**, *15*, 535–541. [CrossRef] [PubMed]
14. Lau, Y.C.; Betto, D.; Rode, K.; Coey, J.M.D.; Stamenov, P. Spin–orbit torque switching without an external field using interlayer exchange coupling. *Nat. Nanotechnol.* **2016**, *11*, 758–762. [CrossRef]
15. Cai, K.; Yang, M.; Ju, H.; Wang, S.; Ji, Y.; Li, B.; Edmonds, K.W.; Sheng, Y.; Zhang, B.; Zhang, N.; et al. Electric field control of deterministic current-induced magnetization switching in a hybrid ferromagnetic/ferroelectric structure. *Nat. Mater.* **2017**, *16*, 712–716. [CrossRef]
16. Zheng, Z.; Zhang, Y.; Lopez-Dominguez, V.; Sánchez-Tejerina, L.; Shi, J.; Feng, X.; Chen, L.; Wang, Z.; Zhang, Z.; Zhang, K.; et al. Field-free spin-orbit torque-induced switching of perpendicular magnetization in a ferrimagnetic layer with a vertical composition gradient. *Nat. Commun.* **2021**, *12*, 4555. [CrossRef]
17. Wu, H.; Nance, J.; Razavi, S.A.; Lujan, D.; Dai, B.; Liu, Y.; He, H.; Cui, B.; Wu, D.; Wong, K.; et al. Chiral Symmetry Breaking for Deterministic Switching of Perpendicular Magnetization by Spin–Orbit Torque. *Nano Lett.* **2020**, *21*, 515–521. [CrossRef]
18. Liu, L.; Zhou, C.; Zhao, T.; Yao, B.; Zhou, J.; Shu, X.; Chen, S.; Shi, S.; Xi, S.; Lan, D.; et al. Current-induced self-switching of perpendicular magnetization in CoPt single layer. *Nat. Commun.* **2022**, *13*, 3539. [CrossRef] [PubMed]
19. Cao, Y.; Sheng, Y.; Edmonds, K.W.; Ji, Y.; Zheng, H.; Wang, K. Deterministic Magnetization Switching Using Lateral Spin–Orbit Torque. *Adv. Mater.* **2020**, *32*, 1907929. [CrossRef]
20. Ma, Q.; Li, Y.; Gopman, D.; Kabanov, Y.; Shull, R.; Chien, C. Switching a Perpendicular Ferromagnetic Layer by Competing Spin Currents. *Phys. Rev. Lett.* **2018**, *120*, 117703. [CrossRef] [PubMed]
21. Baek, S.-h.C.; Amin, V.P.; Oh, Y.W.; Go, G.; Lee, S.J.; Lee, G.H.; Kim, K.J.; Stiles, M.D.; Park, B.G.; Lee, K.J. Spin currents and spin–orbit torques in ferromagnetic trilayers. *Nat. Mater.* **2018**, *17*, 509–513. [CrossRef]
22. Liu, L.; Zhou, C.; Shu, X.; Li, C.; Zhao, T.; Lin, W.; Deng, J.; Xie, Q.; Chen, S.; Zhou, J.; et al. Symmetry-dependent field-free switching of perpendicular magnetization. *Nat. Nanotechnol.* **2021**, *16*, 277–282. [CrossRef]
23. Kao, I.H.; Muzzio, R.; Zhang, H.; Zhu, M.; Gobbo, J.; Yuan, S.; Weber, D.; Rao, R.; Li, J.; Edgar, J.H.; et al. Deterministic switching of a perpendicularly polarized magnet using unconventional spin–orbit torques in WTe2. *Nat. Mater.* **2022**, *21*, 1029–1034. [CrossRef]
24. Yang, M.; Li, Y.; Luo, J.; Deng, Y.; Zhang, N.; Zhang, X.; Li, S.; Cui, Y.; Yu, P.; Yang, T.; et al. All-Linear Multistate Magnetic Switching Induced by Electrical Current. *Phys. Rev. Appl.* **2021**, *15*, 054013. [CrossRef]
25. Li, Y.; Yang, M.; Yu, G.; Cui, B.; Luo, J. Current controlled non-hysteresis magnetic switching in the absence of magnetic field. *Appl. Phys. Lett.* **2022**, *120*, 062402. [CrossRef]
26. Pathak, S.; Youm, C.; Hong, J. Impact of Spin-Orbit Torque on Spin-Transfer Torque Switching in Magnetic Tunnel Junctions. *Sci. Rep.* **2020**, *10*, 2799. [CrossRef]

27. Meo, A.; Chureemart, J.; Chantrell, R.W.; Chureemart, P. Magnetisation switching dynamics induced by combination of spin transfer torque and spin orbit torque. *Sci. Rep.* **2022**, *12*, 3380. [CrossRef]
28. Lu, J.; Li, W.; Liu, J.; Liu, Z.; Wang, Y.; Jiang, C.; Du, J.; Lu, S.; Lei, N.; Peng, S.; et al. Voltage-gated spin-orbit torque switching in IrMn-based perpendicular magnetic tunnel junctions. *Appl. Phys. Lett.* **2023**, *122*, 012402. [CrossRef]
29. Razavi, S.A.; Wu, D.; Yu, G.; Lau, Y.C.; Wong, K.L.; Zhu, W.; He, C.; Zhang, Z.; Coey, J.; Stamenov, P.; et al. Joule Heating Effect on Field-Free Magnetization Switching by Spin-Orbit Torque in Exchange-Biased Systems. *Phys. Rev. Appl.* **2017**, *7*, 024023. [CrossRef]
30. Rahaman, S.Z.; Wang, I.J.; Chen, T.Y.; Pai, C.F.; Wang, D.Y.; Wei, J.H.; Lee, H.H.; Hsin, Y.C.; Chang, Y.J.; Yang, S.Y.; et al. Pulse-Width and Temperature Effect on the Switching Behavior of an Etch-Stop-on-MgO-Barrier Spin-Orbit Torque MRAM Cell. *IEEE Electron Device Lett.* **2018**, *39*, 1306–1309. [CrossRef]
31. Pham, T.H.; Je, S.G.; Vallobra, P.; Fache, T.; Lacour, D.; Malinowski, G.; Cyrille, M.; Gaudin, G.; Boulle, O.; Hehn, M.; et al. Thermal Contribution to the Spin-Orbit Torque in Metallic-Ferrimagnetic Systems. *Phys. Rev. Appl.* **2018**, *9*, 064032. [CrossRef]
32. Arpaci, S.; Lopez-Dominguez, V.; Shi, J.; Sánchez-Tejerina, L.; Garesci, F.; Wang, C.; Yan, X.; Sangwan, V.K.; Grayson, M.A.; Hersam, M.C.; et al. Observation of current-induced switching in non-collinear antiferromagnetic IrMn3 by differential voltage measurements. *Nat. Commun.* **2021**, *12*, 3828. [CrossRef]
33. Fredkin, D.R.; Koehler, T.R. Hybrid method for computing demagnetizing fields. *IEEE Trans. Magn.* **1990**, *26*, 415–417. [CrossRef]
34. Abert, C.; Ruggeri, M.; Bruckner, F.; Vogler, C.; Hrkac, G.; Praetorius, D.; Suess, D. A three-dimensional spin-diffusion model for micromagnetics. *Sci. Rep.* **2015**, *5*, 14855. [CrossRef]
35. Lepadatu, S. Unified treatment of spin torques using a coupled magnetisation dynamics and three-dimensional spin current solver. *Sci. Rep.* **2017**, *7*, 12937. [CrossRef]
36. Amin, V.P.; Stiles, M.D. Spin transport at interfaces with spin-orbit coupling: Phenomenology. *Phys. Rev. B* **2016**, *94*, 104420. [CrossRef]
37. Slonczewski, J.C. Currents, torques, and polarization factors in magnetic tunnel junctions. *Phys. Rev. B* **2005**, *71*, 024411. [CrossRef]
38. Zhu, J.G.; Park, C. Magnetic tunnel junctions. *Mater. Today* **2006**, *9*, 36–45. [CrossRef]
39. Alzate, J.G.; Khalili Amiri, P.; Yu, G.; Upadhyaya, P.; Katine, J.A.; Langer, J.; Ocker, B.; Krivorotov, I.N.; Wang, K.L. Temperature dependence of the voltage-controlled perpendicular anisotropy in nanoscale MgO|CoFeB|Ta magnetic tunnel junctions. *Appl. Phys. Lett.* **2014**, *104*, 112410. [CrossRef]
40. Christian Doppler Laboratory for Nonvolatile Memory and Logic, ViennaSpinMag. 2023. Available online: https://www.iue.tuwien.ac.at/viennaspinmag/ (accessed on 14 June 2023).
41. Fiorentini, S.; Jørstad, N.P.; Ender, J.; de Orio, R.L.; Selberherr, S.; Bendra, M.; Goes, W.; Sverdlov, V. Finite element approach for the simulation of modern MRAM devices. *Micromachines* **2023**, *14*, 898. [CrossRef]
42. Honjo, H.; Nguyen, T.V.A.; Watanabe, T.; Nasuno, T.; Zhang, C.; Tanigawa, T.; Miura, S.; Inoue, H.; Niwa, M.; Yoshiduka, T.; et al. First demonstration of field-free SOT-MRAM with 0.35 ns write speed and 70 thermal stability under 400 °C thermal tolerance by canted SOT structure and its advanced patterning/SOT channel technology. In Proceedings of the IEEE International Electron Devices Meeting (IEDM), San Francisco, CA, USA, 7–11 December 2019; pp. 28.5.1–28.5.4. [CrossRef]
43. Litzius, K.; Leliaert, J.; Bassirian, P.; Rodrigues, D.; Kromin, S.; Lemesh, I.; Zazvorka, J.; Lee, K.J.; Mulkers, J.; Kerber, N.; et al. The role of temperature and drive current in skyrmion dynamics. *Nat. Electron.* **2020**, *3*, 30–36. [CrossRef]
44. Devolder, T.; Kim, J.V.; Nistor, L.; Sousa, R.; Rodmacq, B.; Diény, B. Exchange stiffness in ultrathin perpendicularly magnetized CoFeB layers determined using the spectroscopy of electrically excited spin waves. *J. Appl. Phys.* **2016**, *120*, 183902. [CrossRef]
45. Lee, K.M.; Choi, J.W.; Sok, J.; Min, B.C. Temperature dependence of the interfacial magnetic anisotropy in W/CoFeB/MgO. *AIP Adv.* **2017**, *7*, 065107. [CrossRef]
46. Hadámek, T.; Fiorentini, S.; Bendra, M.; Ender, J.; de Orio, R.; Goes, W.; Selberherr, S.; Sverdlov, V. Temperature increase in STT-MRAM at writing: A fully three-dimensional finite element approach. *Solid-State Electron.* **2022**, *193*, 108269. [CrossRef]
47. Lee, K.S.; Lee, S.W.; Min, B.C.; Lee, K.J. Threshold current for switching of a perpendicular magnetic layer induced by spin Hall effect. *Appl. Phys. Lett.* **2013**, *102*, 112410. [CrossRef]
48. Lepadatu, S. Boris Computational Spintronics. 2023. Available online: https://www.boris-spintronics.uk/ (accessed on 14 June 2023).
49. Zhang, J.; Bachman, M.; Czerner, M.; Heiliger, C. Thermal transport and nonequilibrium temperature drop across a magnetic tunnel junction. *Phys. Rev. Lett.* **2015**, *115*, 037203. [CrossRef]

Disclaimer/Publisher's Note: The statements, opinions and data contained in all publications are solely those of the individual author(s) and contributor(s) and not of MDPI and/or the editor(s). MDPI and/or the editor(s) disclaim responsibility for any injury to people or property resulting from any ideas, methods, instructions or products referred to in the content.

micromachines

MDPI

Article

E-Spin: A Stochastic Ising Spin Based on Electrically-Controlled MTJ for Constructing Large-Scale Ising Annealing Systems

Wenhan Chen [1], Haodi Tang [1], Yu Wang [1], Xianwu Hu [1], Yuming Lin [1], Tai Min [2,*] and Yufeng Xie [1,*]

[1] State Key Laboratory of ASIC & System, School of Microelectronics, Fudan University, Shanghai 201203, China
[2] Center for Spintronics and Quantum Systems, State Key Laboratory for Mechanical Behavior of Materials, Department of Materials Science and Engineering, Xi'an Jiaotong University, Xi'an 710049, China
* Correspondence: tai.min@mail.xjtu.edu.cn (T.M.); xieyf@fudan.edu.cn (Y.X.)

Abstract: With its unique computer paradigm, the Ising annealing machine has become an emerging research direction. The Ising annealing system is highly effective at addressing combinatorial optimization (CO) problems that are difficult for conventional computers to tackle. However, Ising spins, which comprise the Ising system, are difficult to implement in high-performance physical circuits. We propose a novel type of Ising spin based on an electrically-controlled magnetic tunnel junction (MTJ). Electrical operation imparts true randomness, great stability, precise control, compact size, and easy integration to the MTJ-based spin. In addition, simulations demonstrate that the frequency of electrically-controlled stochastic Ising spin (E-spin) is 50 times that of the thermal disturbance MTJ-based spin (p-bit). To develop a large-scale Ising annealing system, up to 64 E-spins are implemented. Our Ising annealing system demonstrates factorization of integers up to 2^{64} with a temporal complexity of around $O(\sqrt{n})$. The proposed E-spin shows superiority in constructing large-scale Ising annealing systems and solving CO problems.

Keywords: spintronics; spin-transfer torque magnetic tunnel junctions (STT-MTJ); Ising annealing system; combinatorial optimization problem

Citation: Chen, W.; Tang, H.; Wang, Y.; Hu, X.; Lin, Y.; Min, T.; Xie, Y. E-Spin: A Stochastic Ising Spin Based on Electrically-Controlled MTJ for Constructing Large-Scale Ising Annealing Systems. *Micromachines* **2023**, *14*, 258. https://doi.org/10.3390/mi14020258

Academic Editors: Mehmet Remzi Dokmeci and Viktor Sverdlov

Received: 19 October 2022
Revised: 1 January 2023
Accepted: 14 January 2023
Published: 19 January 2023

Copyright: © 2023 by the authors. Licensee MDPI, Basel, Switzerland. This article is an open access article distributed under the terms and conditions of the Creative Commons Attribution (CC BY) license (https://creativecommons.org/licenses/by/4.0/).

1. Introduction

Combinatorial optimization problems have long been a tangled mess for conventional computers. With the scale of the problem increasing, the consumption of time and hardware resources increases exponentially. Heuristic search techniques, such as the simulated annealing algorithm, have been utilized to search for a solution within a limited time. However, their search effectiveness remains unsatisfactory. It is anticipated that quantum annealing [1,2] would surpass the calculating limit of conventional computers. However, the quantity of Q-bits, the requisite cryogenic environment, and the decoherence generated by the environment's interface severely restrict the system's scalability.

Ising annealing was offered as an alternative scenario between classical computing and quantum computing. Ising annealing is a novel non-von Neumann computing architecture that specializes in CO problems [3–6]. There have been numerous proposals to construct Ising systems with physical entities, including superconductive qubits [7] and degenerate optical parametric oscillators (DOPOs) [3,8–11]. However, the above methods are hampered by their integration complexity and stringent working conditions. Other methods, such as complementary metal–oxide–semiconductor (CMOS) circuits [12–14] and LC oscillators [5], are constrained by circuit area. New devices such as insulator-to-metal phase transition nano oscillators (IMT-NOs) [15] and nano-magnet (p-bit) [16] have been investigated as Ising spins. When manufactured on a wide scale, discrepancies caused by device instability and process variation remain a hurdle. Due to the low computer capability, only 10-bit integer factorization was supported [16]. Therefore, a novel type of Ising spins that are easy to integrate and an efficient Ising annealing algorithm is urgently required.

This paper proposes an electrically-controlled stochastic-MTJ-based Ising spin (E-spin) and an E-spin-based probabilistic Ising annealing algorithm (QFactor). The E-spin has good thermal stability, compact size, true randomness, and high controllability. In addition, the E-spin significantly achieves a 92.2% smaller area and 2% power consumption reduction compared to LFSR [17] based digital Ising spins [16]. Based on the electrically-controlled stochastic MTJ, we introduced a new stochastic Ising annealing algorithm named QFactor. The QFactor outperforms various stochastic or heuristic techniques, including the simulated annealing algorithm and the Ising annealing algorithm, when factoring up to 64-bit integers as a demonstration. The proposed approach is easily extensible to numerous additional CO problems.

2. Spin-Transfer Torque Magnetic Tunnel Junctions and E-Spin

2.1. Mechanism of the Spin-Transfer Torque Magnetic Tunnel Junctions

The spin-transfer torque magnetic tunnel junctions (STT-MTJs) possess the property of stochastic switching [18–20], and their switching probability is dependent on the applied current. According to prior research [21–23], the switching characteristics of STT-MRAM can be roughly seen as a sigmoidal function of the current magnitude. The schematic diagram of MTJ's switching probability is depicted in Figure 1b, and it is written as follows:

$$p_{sw} = 1 - exp\left\{-\frac{t}{\tau_0} exp\left[-\Delta\left(1 - \frac{I}{I_{c0}}\right)^2\right]\right\} \quad (1)$$

where τ_0, t, Δ, I, and I_{c0} are respectively the attempt time, the duration time of the current pulse, the thermal stability parameter, the applied current, and the critical switching current at 0 K. While t and I are variables that can be changed after fabrication, parameter τ_0, Δ, and I_{c0} are process-related parameters and cannot be altered. Applying various current pulses of suitable amplitude and length allows us to change the switching probability [22,24].

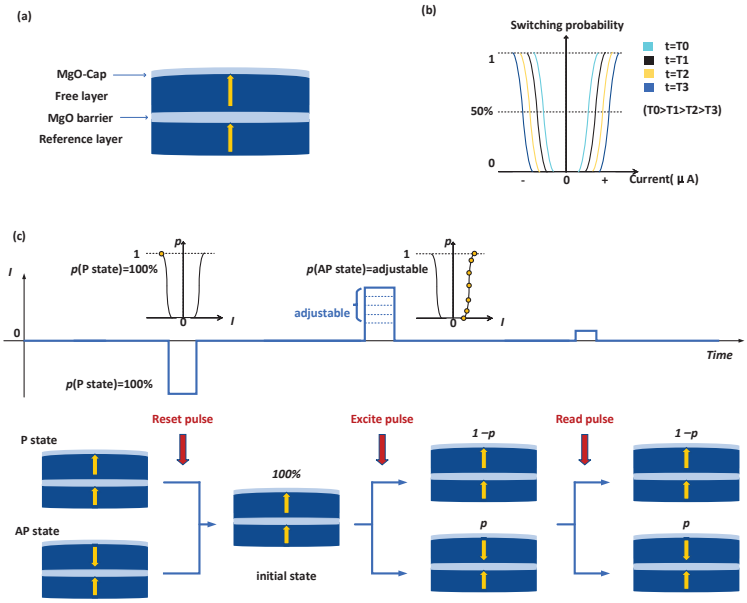

Figure 1. (**a**) Diagrammatic representation of the Double-MTJ employed in this investigation. (**b**) Switching probability of Double-MTJ under various current and pulse duration conditions. (**c**) Process of operation. Pulses for reset, excite, and read are applied in that order.

The construction of the Double-MTJ employed in this work is depicted in Figure 1a. MgO makes up the tunnel barrier and the cap layer, while CoFeB makes up the free layer. The additional CoFeB/MgO interface raises the energy barrier of STT-MTJ [25].

The process of operation is shown in Figure 1c. First, we must perform the "reset" operation, which involves forcing the MTJ into a low resistance state by applying a strong reverse pulse. We call this state the 'initial state'. After that, to set the probability of MTJ in a high resistance state as the desired probability p, we must deliver the proper pulse according to (1). This process is called the 'excite' operation. A probability sequence with a p probability of a high voltage level is created by carrying out the reset and excite operations in order, then reading the resistance of the MTJ after each excite operation. The pulse given to the MTJ during excite operation determines the probability of a high voltage level in the probability sequence.

2.2. Schematic Diagram, Operation Paradigm, and Simulation of the E-Spin

The proposed E-spin was constructed based on the stochastic STT-MTJ, shown in Figure 2a.

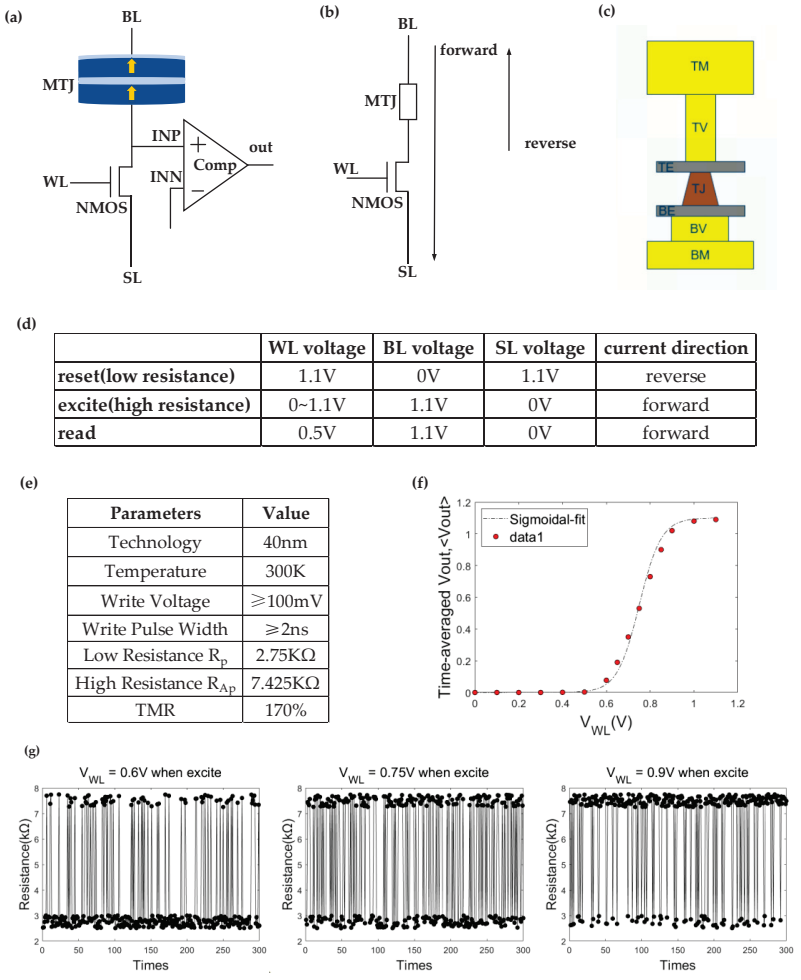

(d)

	WL voltage	BL voltage	SL voltage	current direction
reset(low resistance)	1.1V	0V	1.1V	reverse
excite(high resistance)	0~1.1V	1.1V	0V	forward
read	0.5V	1.1V	0V	forward

(e)

Parameters	Value
Technology	40nm
Temperature	300K
Write Voltage	⩾100mV
Write Pulse Width	⩾2ns
Low Resistance R_p	2.75KΩ
High Resistance R_{Ap}	7.425KΩ
TMR	170%

Figure 2. (**a**) Schematic diagram of the E-spin. (**b**) Operation paradigm of the E-spin. (**c**) The layout of the MTJ's film stack. The technology node of our logic circuit was 40 nm. The MTJ was fabricated on the top layer of the logic circuit. (**d**) The applied voltage for the reset, excite, and read operations. (**e**) The parameters of MTJ were measured at 300 K. The low resistance was 2.75 KΩ and the high resistance was 7.425 KΩ. The TMR (Tunnel Magneto Resistance) was 170%. The switch error rate of the MTJ was correlated with the write voltage and pulse width. The minimum write voltage and pulse width were 100 mV and 2 ns, respectively. (**f**) Time-averaged V_{out}, <V_{out}>. <V_{out}> is the function of the applied input voltage V_{WL} and pulse width. The pulse width is 5 ns in this illustration. The function is fitted to the sigmoidal function. Each data point shown in this figure was averaged for 300 sampling points. (**g**) Time snapshots of the MTJ's resistance after each excite operation for various input voltage V_{WL} (0.6 V, 0.75 V, and 0.9 V). The MTJ's resistance was sampled 300 times for each V_{WL}.

The n-type metal–oxide–semiconductor (NMOS) transistor is a current source that supplies the electrically-controlled stochastic STT-MTJ with an appropriate amount of current. Depending on the direction and amount of current passing through it, the STT-MTJ may change its state (high or low resistance), altering the voltage of INP. Assuming that the high-resistance MTJ corresponds to $V_{INP} = V_{INP-low}$ and the low-resistance MTJ corresponds to $V_{INP} = V_{INP-high}$, then the voltage of reference INN is set to $(V_{INP-low} + V_{INP-high})/2$. The comparator compares the difference between INN and reference INP and output 1 (0) to distinguish the high (low) resistance state of stochastic MTJ.

The circuit's current direction is depicted in Figure 2b. The top metal (TM), top via (TV), top electrode (TE), MTJ, bottom electrode (BE), bottom via (BV), and bottom metal (BM) are shown in Figure 2c as the stack structure of the MTJ's arrangement.

Figure 2d shows the operation paradigm applied to the E-spin. In a single cycle, there are three operational modes: reset, excite, and read. The input of the E-spin (V_{WL}) is sufficiently large during the reset period to supply enough current to reset the MTJ to a low resistance state. The direction of the current flowing through the MTJ is reversed during the excite period. As illustrated in Figure 2e,f, a larger V_{WL} corresponds to a higher probability of switching to a high resistance state, in accordance with (1). The comparator, which senses the voltage variation caused by the fluctuation of the MTJ state during the read period, reads out the probability of E-spin.

The output of the ith stochastic MTJ (m_i) is refreshed during the read period according to:

$$m_i = \vartheta[\delta(I_i) - r] \tag{2}$$

where input I_i and output m_i can be represented as:

$$m_i = V_{out,i}/V_{DD} \tag{3}$$

$$I_i = V_{WL,i}/V_{DD} \tag{4}$$

r is a random number with range [0, 1]. $\delta(x)$ is the sigmoidal function, and $\vartheta(x)$ is the unit step function. As a result, the time-averaged output of the E-spin coincides with the sigmoidal curve, as shown in Figure 2f.

2.3. Advantages of the E-Spin

Table 1 shows the characteristics of three MTJ-based random sources, including the spin dice, thermal disturbance MTJ-based spin (p-bit) [16], and our E-spin.

Table 1. Characteristics of the three random sources.

Indicators	Spin Dice [26]	p-bit [16]	E-Spin (This Work)
probability	Fixed	adjustable	adjustable
randomness	TRNG	TRNG	TRNG
operation mode	electric	thermal	electric
reliability	good	poor	good
large-scale integration	easy	hard	easy

For the spin dice, P_{sw} was set to the fixed value of 50%, while we used the entire domain of the sigmoidal function (see Figure 1) in our design, which broadens the range of its applications.

The temperature, which is determined by the surroundings and operating conditions, has a direct impact on the switching frequency for thermal disturbance MTJ (p-bit) [16]. However, the E-spin, based on Double-MTJ and having a greater thermal stability factor Δ [25], could counteract the probability skew brought on by temperature variation. Because of this, our proposed electrical operation to adjust probability has better stability. By precisely controlling the current, the dependability and accuracy of the E-spin are

considerably enhanced. Additionally, Double-MTJ arrays can be incorporated thanks to the scalability of spin-torque switching, offering significant prospects for novel spintronics-based large-scale integrated circuits [25].

2.4. Endurance of the E-Spin

According to the spin operation modes mentioned in Figure 2, repetitive reset, excite, and read operations are required during work. Consequently, the endurance analysis of the spin is required.

In the existing non-volatile memories, the endurance of MRAM is an obvious advantage compared to RRAM and PCRAM. The endurance of STT-MTJ with multiple CoFeB/MgO interfaces could theoretically reach up to $10^{15} \sim 10^{16}$, which is higher than traditional MTJ [25]. Constructing spins using such STT-MTJ could reach over three years of lifetime at the working frequency of 10 MHz~100 MHz, satisfying the needs of most usage scenarios. Figure 3 shows the lifetime of such an STT-MTJ at various working frequencies. If the MTJ has an endurance of 1×10^{15}, it can operate at the frequency of 10 MHz for 3.17 years. The endurance can be increased even more if the SOT-MRAM is included [27]. Because the current is not passed directly through the MTJ in SOT-MRAM, the MTJ is clearly protected, increasing the endurance to almost infinite levels.

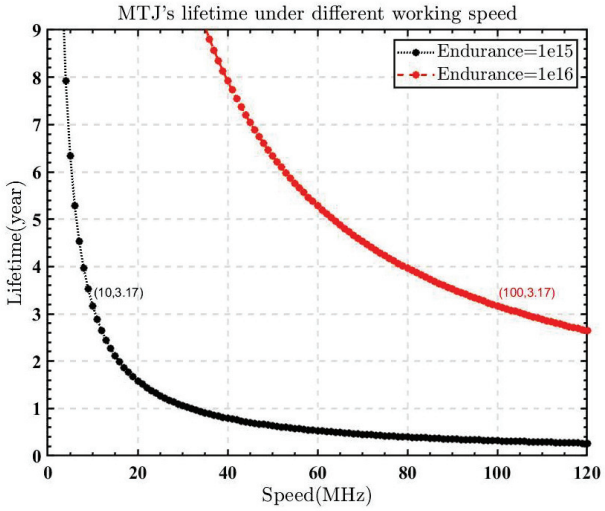

Figure 3. MTJ's lifetime at various operating frequencies. Under a clock frequency of 10 MHz, MTJ with 1×10^{15} endurance can operate for 3.17 years.

3. Large-Scale Ising Annealing System for Solving CO Problems Using E-Spins

3.1. Steps of Ising Annealing System Solving CO Problems

The Ising system is composed of Ising spins and their interconnections. The Hamiltonian of the Ising system is:

$$H = -\sum_{\langle i,j \rangle} J_{ij}\sigma_i\sigma_j - \mu\sum_j h_j\sigma_j \tag{5}$$

where spin $\sigma_{i,j} \in \{+1, -1\}$, and J_{ij}, h_j, μ are the coupling parameter between spins i and j, the magnitude of the external magnetic field, and the Bohr magneton, respectively.

By mapping the task function into the Ising Hamiltonian and mapping the best answer to the lowest value of the acquired Ising Hamiltonian, the task can be transformed into searching for the lowest energy state of the Ising system. After the annealing procedure, the system energy will gradually descend and reach the low energy state. At this point, a workable solution is discovered.

3.2. Mapping Integer Factorization Problem to Ising Annealing System

An illustration of the combinatorial optimization problem is the integer factorization problem. The integer factorization problem, which is still challenging for traditional computers, is now widely used in the RSA (Rivest–Shamir–Adleman) encryption technique.

According to [28], the Ising Hamiltonian (or system energy, cost function) of the integer factorization problem is:

$$H = (X \times Y - F)^2 \tag{6}$$

where X, Y, and F are odd integers. X and Y can be represented in binary form as:

$$X = \sum_{p=0}^{P-1} 2^p x_p \tag{7}$$

$$Y = \sum_{q=0}^{Q-1} 2^q y_q \tag{8}$$

with $x_0 = y_0 = 1$. P and Q donate the number of bits needed to represent X and Y. Suppose F is an N-bit integer. Then we have:

$$N = P + Q \tag{9}$$

We use E-spins to represent each bit of X and Y. The LSBs (least significant bits) of X and Y are fixed to '1'; then, only $P-1$ and $Q-1$ E-spins are needed to represent X and Y, respectively. Then we have:

$$X = \sum_{n=1}^{P-1} 2^n m_n + 1 \tag{10}$$

$$Y = \sum_{n=P}^{N-2} 2^{n-P+1} m_n + 1 \tag{11}$$

Since the two variables X and Y are discrete, H is a discontinuous function. Figure 4 demonstrates an example of the energy distribution of the system $H = (X \times Y - F_i)^2$. Here, F_i = 45,431. It can be inferred from the picture that there are lots of local minimums along the hyperbola $\ell: (X \times Y - F)^2 = 0$.

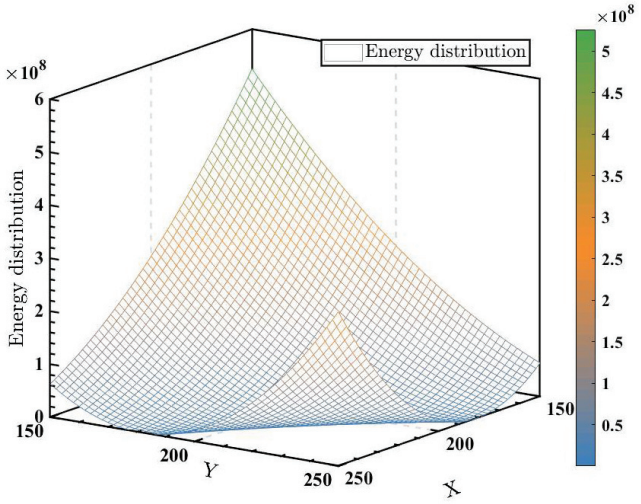

Figure 4. Energy distribution of the system $H = (X \times Y - 45431)^2$.

The integer factorization problem differs from other combinational problems in that the former requires the optimal solution, whilst the latter just requires a good enough response. In other words, the output answer must meet higher standards because it will not be legitimate if the product of two factors does not exactly equal the number F.

3.3. Stochastic Ising Annealing Algorithm Based on E-Spin

Figure 5 demonstrates the flowchart of the proposed QFactor, a stochastic Ising annealing algorithm. The first step is problem mapping. Section 3.2 has shown the procedure of mapping the integer factorization problem to the problem of finding out the minimum value of the discrete function $H = (X \times Y - F)^2$.

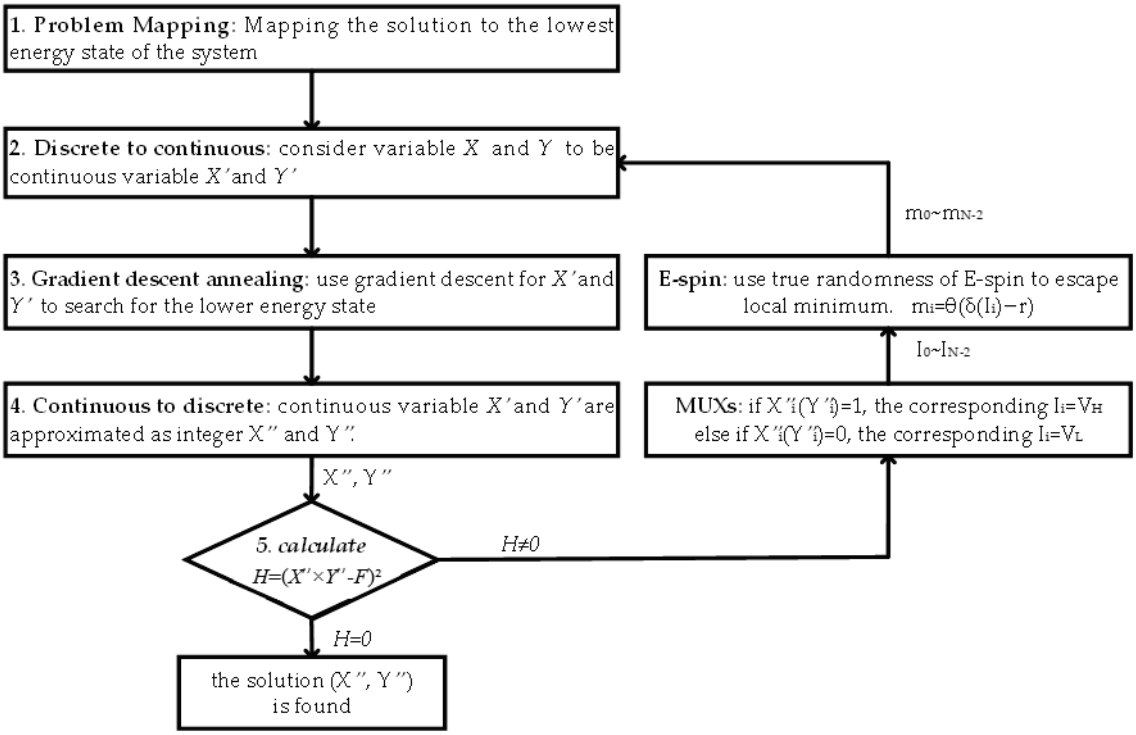

Figure 5. The framework of the proposed Ising annealing algorithm QFactor. $H = (X'' \times Y'' - F)^2$.

Making the non-continuous function into a continuous function is one of the effective ways to address discrete optimization problems since it speeds up the process of convergence to the local minimum. Therefore, in the second step, the discrete function H was transformed into its continuous function form $H' = (X' \times Y' - F)^2$, where X' and Y' are continuous variables. The problem was converted to obtaining the minimum value of the continuous function H'.

In the third step, gradient descent was employed to reach the local minimum, as deep learning algorithms do in neural networks. Variable X' and Y' are updated by $X' = X' + \lambda \cdot \frac{\partial H'}{\partial X'}$ and $Y' = Y' + \lambda \cdot \frac{\partial H'}{\partial Y'}$, where parameter λ is the stride length.

Fourthly, the continuous variable X' and Y' are approximated as integers X'' and Y''.

Lastly, verify that H is equal to 0. $H = 0$ indicates that we have arrived at the right answer.

If $H \neq 0$, then we must use the subsequent stages to discover a different solution:

- Map X and Y to the corresponding spin x_i and y_i using Equations (7) and (8).
- If the calculated x_i or y_i equals value "1", the MUX outputs V_H to the corresponding I_i. Then, the E-spin provides a strong likelihood of an output value "1". The V_H is the parameter that can be adjusted. In this experiment, we set V_H to be around 0.95 V and V_L to be 0.55 V. The random flips of E-spin do not frequently occur, so the gradient descent procedure is dominant in most cases.
- Accordingly, if x_i or y_i equals '0', the MUX outputs V_L to the corresponding E-spin I_i. Then the E-spin provides a high probability of output value "0".

Repeat step 2 to step 5 until the correct solution is found.

3.4. The Overall Diagram of the Proposed Ising Annealing System

The overall diagram of the proposed Ising annealing system is shown in Figure 6. The gradient-descent-based Ising annealing algorithm (QFactor) supplies an input signal for the E-spins through multiplexers (MUXs). If x_i (or y_i) equals '1', then the input of E-spin equals V_H. Otherwise, if x_i (or y_i) equals '0', then the input of E-spin equals V_L. Stochastic E-spins generate the sequenced stochastic bit streams according to the MUXs' output voltage (V_H or V_L).

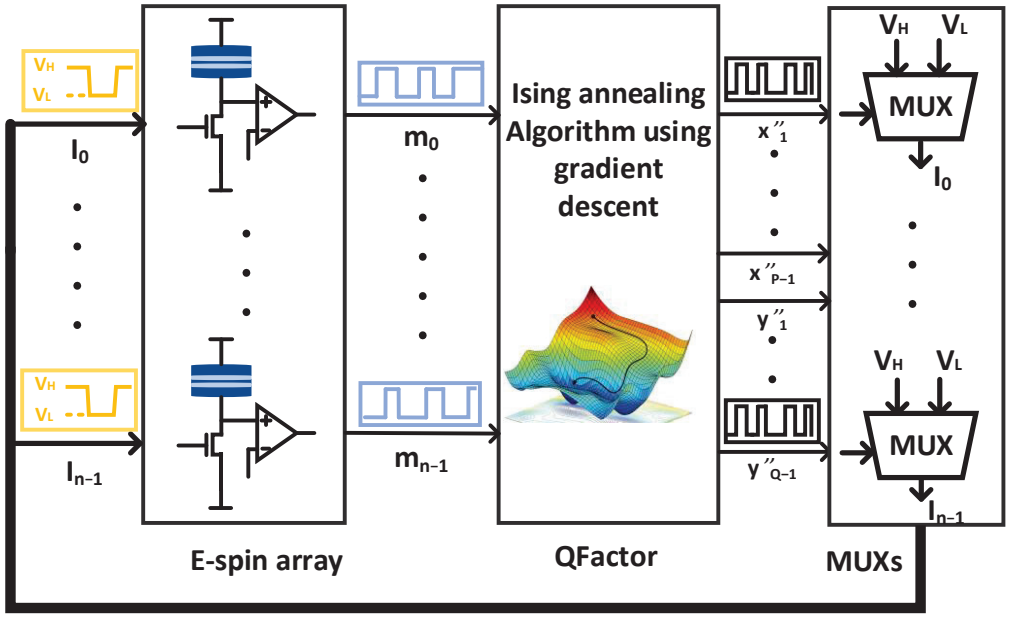

Figure 6. The overall diagram of the proposed Ising annealing system (QFactor). It comprises an E-spin array with 64 E-spins, a digital circuit to implement the QFactor annealing algorithm, and analog MUXs.

The key to obtaining a better solution for an Ising annealing system is jumping out of the local optimal solution. Therefore, randomness is required in the annealing procedure to escape the local minimum. A significant difference between QFactor and other Ising annealing algorithms is the production of randomness. The QFactor algorithm fully utilizes the stochastic nature of E-spin, negating the need to use another randomness as the motivation of the annealing procedure.

In addition, QFactor employs randomness differently than traditional heuristic search algorithms, such as simulated annealing, which selects a random number of X and Y for the following annealing cycle. While X and Y are denoted in QFactor as $X = \sum_{n=1}^{P-1} 2^n m_n + 1$ and $Y = \sum_{n=P}^{N-2} 2^{n-P+1} m_n + 1$, which means that any random flip of x_i will deviate X by the length of $2^i x_i$.

Except for Ising annealing algorithms and heuristic search algorithms, there are other traditional methods to solve integer factorization problems, such as numerical calculation algorithms. The General Number Field Sieve (GNFS) method is the most effective numerical computation algorithm for solving the integer factorization problem at present. However, because of the operation's complexity, hardware optimization is challenging. Nevertheless, GNFS is a specific algorithm for a single purpose. The QFactor algorithm provides an easy-to-implement way to solve more general discrete optimization problems.

4. Results

4.1. Integer Factorization Results

4.1.1. Examples of Factoring Integers

Figure 7a,b show the hardware simulation waveform of factoring 24-bit integers 14019841 and 14166761 using Vivado circuit simulator software. The entire system is simulated using all-digital circuitry for the convenience of larger-scale simulation. The behavior of the E-spin is simulated by the CMOS-based stochastic Ising spin. The 2-way digital MUXs, instead of the analog MUXs in Figure 6, select the input of E-spins.

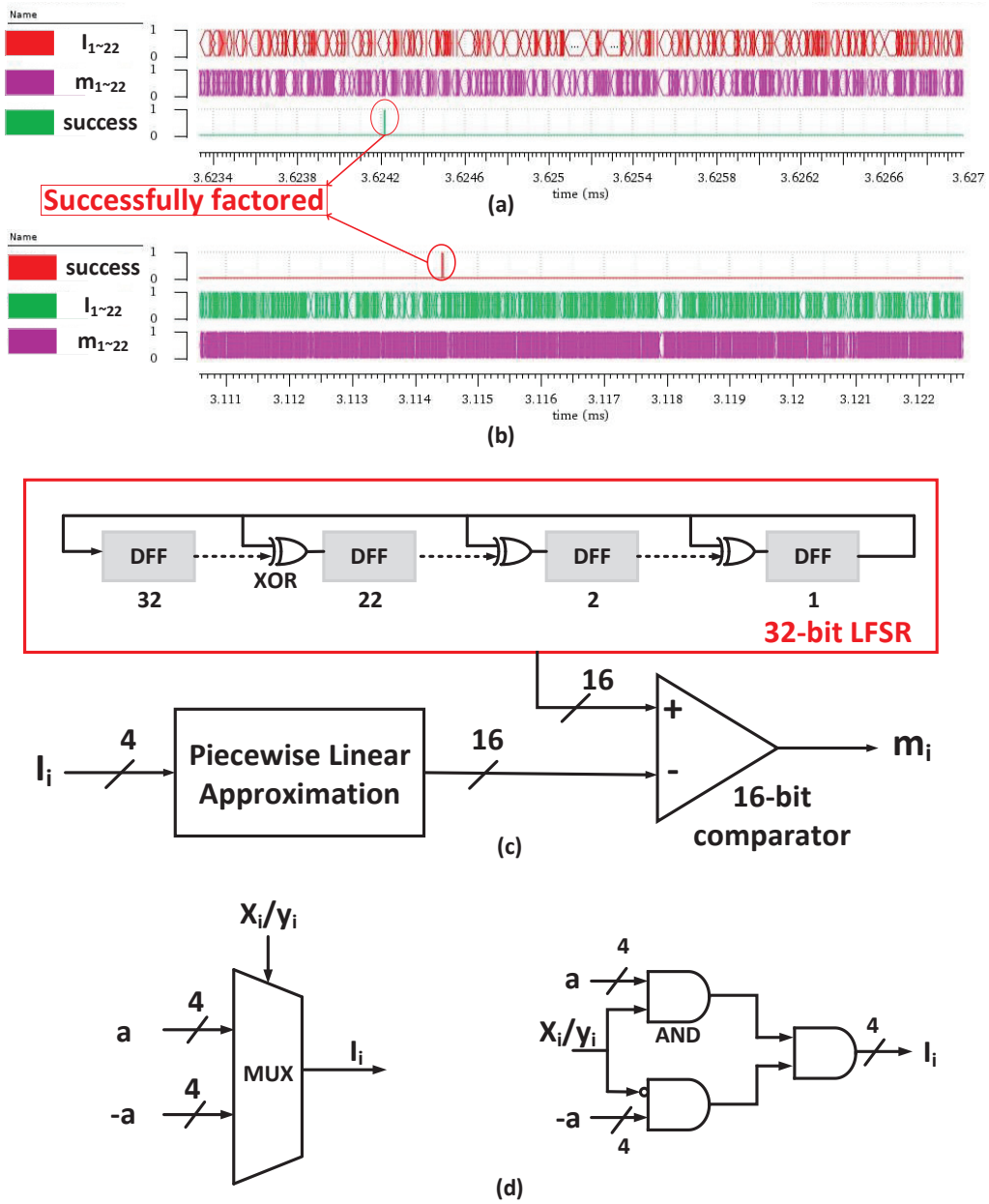

Figure 7. Examples of factoring 24-bit integers 14019841 (**a**) and 14166761 (**b**) using Vivado. $m_{10\sim1}$ and $m_{22\sim11}$ represent $\{x_{10}, \ldots, x_1\}$ and $\{y_{10}, \ldots, y_1\}$, respectively. The clock period in this front-end circuit simulation is 500 ns. (**c**) Schematic view of CMOS-based stochastic Ising spin. It comprises a 32-bit LFSR, a piecewise linear approximation module, and a 16-bit comparator. The behavior of the CMOS-based stochastic Ising spin is the same as described in Equation (2). (**d**) Schematic view (left) and circuitry (right) of a digital MUX.

The schematic view of the CMOS-based stochastic Ising spin is shown in Figure 7c. To better simulate the true-randomness property of the E-spin, we use 32-bit LFSR in our simulation because the 32-bit LFSR counter has a repetition time of up to $(2^{32}-1)$ clock periods. We used the high 16 bits of the 32-bit LFSR, which helps to reduce the overall hardware complexity and simulation time. The piecewise linear approximation module approximates the sigmoidal function using 16-segment polylines. The behavior of the MTJ-based E-spin described in Equation (2) is the same as the CMOS-based stochastic Ising spin. Figure 7d shows the schematic view and circuitry of 2-way digital MUXs. During the annealing process, it is proper to reach a balance between gradient descent and random exploration. Therefore, the value of the 4-bit parameter a in Figure 7d is 4 to 6. Suppose that a equals 5, the probability that an E-spin changes its state is $\frac{1}{1+e^5} = 0.0067$. The probability that at least one E-spin changes its state in the 22 E-spin system is $1-(1-0.0067)^{22} = 0.1373$, which indicates that there is a 13.7 percent chance that the E-spins will randomly choose another solution. The value of λ is the other hyperparameter to determine the appropriate stride length for X' and Y', which is closely related to the bit width n. In this experiment, λ is roughly 6.5×10^{-16} when n equals 24. a and λ are the only two hyperparameters used in the QFactor, and there is no need to adjust them when factoring different integers with the same n.

Since the LSB of the two factors X and Y is 1, only 22 E-spins are needed. Whenever the system energy $H = (X \times Y - F)^2$ equals 0, the 'success' signal is high. At this time, a successful factorization is reached.

4.1.2. Comparations for Simulated Annealing, Trial Division, and Ising Annealing Algorithm

Figure 8 shows the averaged cycles needed by the simulated annealing algorithm [12], Ising annealing algorithm [16], trial division [29], and the QFactor to factor integers with n bit widths. The performance of the simulated annealing algorithm was evaluated by mapping the factorization optimization problem into the minimum energy state, carrying out the pseudo-annealing procedure, and selecting the optimal sets of parameters in our trial. Accordingly, the performance of the Ising annealing algorithm was evaluated through our recurrence of the code. The trial division algorithm traverses all numbers from 2 to $\sqrt{n}$ until a factor is discovered. The four algorithms were tested using the exact integers. All values on the graph were tested more than five times.

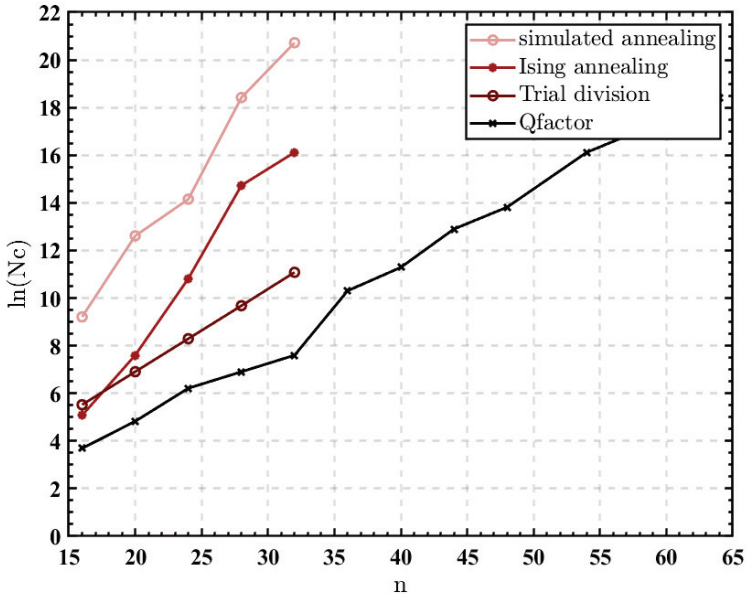

Figure 8. The required cycles to factor n-bit integers. Nc in the Y axis represents the number of required cycles. The four algorithms are simulated using MATLAB software.

For instance, the averaged number of cycles needed to factor 32-bit integers using the simulated annealing, Ising annealing, and trial division methods, respectively, is 5×10^5, 5×10^3, and 33 times greater than the QFactor. Additionally, the QFactor further extended its advantage as the integer bit width increased, remarkably outperforming other stochastic algorithms.

As the integer bit width (n) increases linearly, the size of the search space expands at the rate of 2^n. However, Figure 8 shows that the required cycles of the QFactor only grow at the rate of $2^{\sqrt{n}}$, which not only shortens annealing cycles but also remarkably outperforms other stochastic algorithms. The required cycles of trial division increase at the rate of $2^{\sqrt{n}}$ as well. The QFactor only employs the multiply operation, in contrast to the trial division method's use of divide operations. The hardware complexity of the divide operation is much higher than the multiply operation, especially as the problem's size increases. Therefore, implementing the trial division method in hardware is much more complicated than implementing the QFactor.

4.2. Analysis Results of the E-Spin

There are several technology roadmaps to implement the stochastic Ising spin. The CMOS-based stochastic Ising spin uses LFSR to build a pseudo-random-number-generator (PRNG). The thermal disturbance MTJ-based spin (p-bit) utilizes thermal-controlled unstable MTJ to realize a true-random-number-generator (TRNG).

Figure 9 shows the layout view of a single CMOS-based stochastic Ising spin and a single MTJ-based E-spin. The area of the CMOS-based stochastic Ising spin is 3546 μm^2. The CMOS-based stochastic Ising spin's power is 142.6 μW at the frequency of 333 MHz, according to the results provided by the Design Compiler.

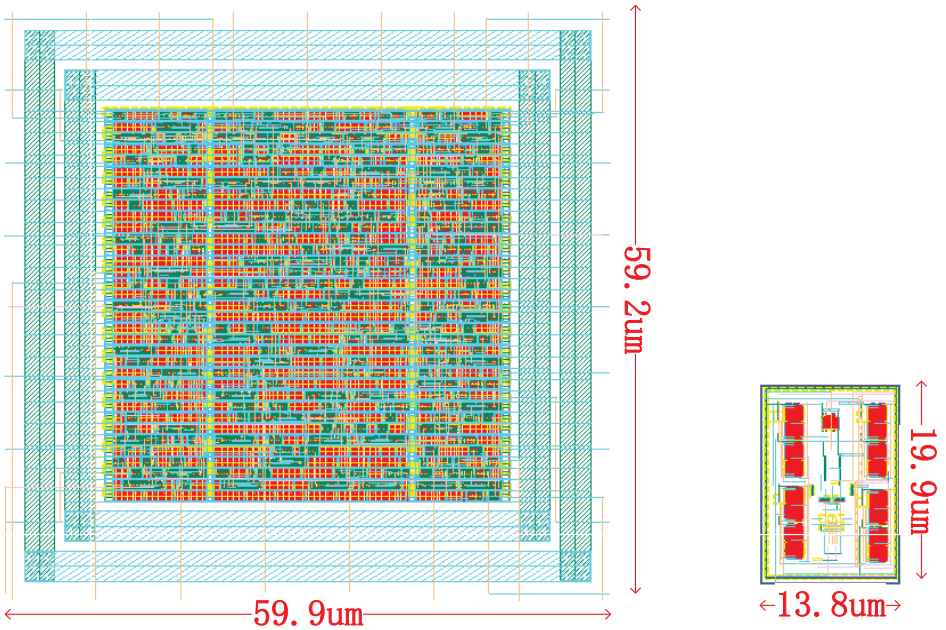

Figure 9. Layout view of a single CMOS-based stochastic Ising spin (left) and a single MTJ-based E-spin (right). The layout of the CMOS-based stochastic Ising spin is automatically generated by EDA (electronic design automation) software DC (Design Compiler) and ICC (IC Compiler). The layout of the MTJ-based E-spin is a customized design using Virtuoso.

The MTJ is simulated by a Verilog-A model with 7.425 KΩ high resistance and 2.75 KΩ low resistance. The Verilog-A model is used to simulate the behavior of MTJ under various voltages, which is shown in Table 2.

Table 2. The relationship between the voltage drop of the MTJ and the probability of switching from a low-resistance state to a high-resistance state.

Voltage Drop (mV) [1]	Switching Probability
[0,144)	0%
[144,171)	7%
[171,212)	20%
[212,275)	32%
[275,342)	48%
[342,428)	66%
[428,584)	81%
[584,718)	93%
[718,731)	98%
[731,1100]	100%

[1] In this table, the voltage pulse widths are 5 ns.

The current-time simulation of the E-spin is shown in Figure 10. The applied WL, BL, and SL voltages are shown in Figure 2d. In this illustration, $V_{WL,excite}$ = 0.75 V. Reference voltage V_{INN} is 250 mV. VSS2, VSS3, and VSS1 are the total current under reset, excite, and read operation modes. The reset, excite, and read operations of the stochastic MTJ last 5 ns, 5 ns, and 10 ns, respectively, with currents of 323.55 µA, 131.60 µA, 51.86 µA. Power consumption data (see Table 2) are calculated by multiplying the time-averaged current and VDD (1.1 V).

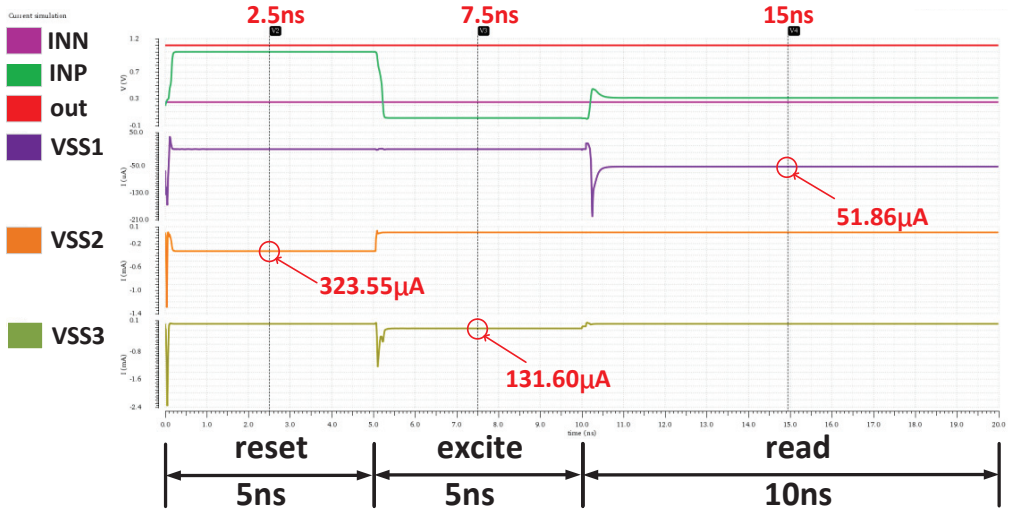

Figure 10. MTJ's current simulation under reset, excite, and read operation modes.

Table 3 lists the critical indicators of the three stochastic Ising spins.

Table 3. Critical indicators of three stochastic Ising spins.

Indicators	CMOS-Based Stochastic Ising Spin	Thermal Disturbance MTJ-Based Spin (p-bit) [16]	E-Spin (This Work)
Area (µm^2)	1600	NA	280
Speed (MHz)	333	<1	50
Power (µW)	142.6	20	139.7
Technology node	40 nm	NA (discrete)	40 nm
Randomness	PRNG	TRNG	TRNG

The primary shortage of LFSR is that it is not a truly random source. The random number generated by an n-bit LFSR will loop for a maximum of 2^n cycles. That means

the size of LFSR must be sufficient to simulate the characteristics of a truly random source. There are some applications that LFSR is incapable of, such as encrypted communication and Monte Carlo simulation.

The primary defect of thermal disturbance MTJ is the intricate voltage offset operation requirement for each bit, which restricts the application in large-scale issues.

The proposed E-spin outperforms the p-bits in stability, speed, and large-scale integration. Firstly, the E-spin adapts the electrical operation, which helps in precise control. Meanwhile, the p-bit uses the thermal-disturbance-controlled MTJ, the frequency of which is influenced by the operating temperature. As a result, the frequency of p-bit is unpredictable, which could cause problems if interconnected with other modules. Additionally, the p-bit is in demand of the voltage offset for each bit. As a result, building an array out of p-bits is challenging.

Secondly, the electrical operation also permits the E-spin to operate with a high frequency. The minimum pulse width of the read/write operation is 2 ns. The frequency of the E-spin could reach higher than 50 MHz. In comparison, the frequency of p-bit is less than 1 MHz. The working frequency of the E-spin is considerably higher.

Lastly, the E-spin could easily integrate with logic circuits. We demonstrate the fabrication of 64 E-spins with logic circuits under the 40 nm technology node, which shows great potential in large-scale integration. Nevertheless, ref [16] only demonstrates eight p-bits, which are selectively chosen from discrete devices. Additionally, the working conditions of each p-bit have to be carefully adjusted. The peripheral circuits for adjusting p-bit working conditions are a considerable expense when manufactured on a large scale.

5. Conclusions

This paper proposes a stochastic Ising spin (E-spin) based on the electrically-controlled STT-MTJ. The probabilistic Ising annealing algorithm (QFactor) is based on the E-spins. The E-spin has true randomness, excellent stability, fine control, high frequency, compact size, and is simple to integrate thanks to its electrical operation. Using the gradient descent algorithm and E-spins to escape the local minimum is a novel approach to solving optimization problems. The E-spin achieved 50 times the frequency of p-bit. Up to 64 E-spins are implemented to construct a large-scale Ising annealing system. Factorization of integers up to 2^{64} is demonstrated using our Ising annealing system, with a time complexity of roughly $O(\sqrt{n})$. This work shows the enormous application potential of the electrically-controlled STT-MTJ, which is also instructive for further research on new computing paradigms.

Author Contributions: Conceptualization, Y.X., T.M., W.C., H.T. and Y.W.; methodology, Y.X., W.C., H.T., X.H. and Y.W.; software, W.C. and H.T.; validation, W.C., H.T., X.H. and Y.L.; formal analysis, W.C., H.T. and Y.W.; investigation, W.C., H.T., X.H. and Y.W.; resources, T.M.; writing—original draft preparation, W.C.; writing—review and editing, Y.X., T.M., W.C., H.T. and Y.L.; visualization, W.C.; supervision, Y.X., T.M., X.H. and Y.W.; project administration, Y.X.; funding acquisition, Y.X. All authors have read and agreed to the published version of the manuscript.

Funding: This research was funded by [National Natural Science Foundation of China] grant number [61874031].

Data Availability Statement: No new data were created or analyzed in this study. Data sharing is not applicable to this article.

Conflicts of Interest: The authors declare no conflict of interest.

References

1. Arute, F.; Arya, K.; Babbush, R.; Bacon, D.; Bardin, J.C.; Barends, R.; Biswas, R.; Boixo, S.; Brandao, F.G.S.L.; Buell, D.A.; et al. Quantum supremacy using a programmable superconducting processor. *Nature* **2019**, *574*, 505–510. [CrossRef] [PubMed]
2. Jiang, S.; Britt, K.A.; McCaskey, A.J.; Humble, T.S.; Kais, S. Quantum Annealing for Prime Factorization. *Sci. Rep.* **2018**, *8*, 17667. [CrossRef]

3. Takata, K.; Marandi, A.; Hamerly, R.; Haribara, Y.; Maruo, D.; Tamate, S.; Sakaguchi, H.; Utsunomiya, S.; Yamamoto, Y. A 16-bit Coherent Ising Machine for One-Dimensional Ring and Cubic Graph Problems. *Sci. Rep.* **2016**, *6*, 34089. [CrossRef] [PubMed]
4. Böhm, F.; Verschaffelt, G.; Van Der Sande, G. A poor man's coherent Ising machine based on opto-electronic feedback systems for solving optimization problems. *Nat. Commun.* **2019**, *10*, 3538. [CrossRef]
5. Chou, J.; Bramhavar, S.; Ghosh, S.; Herzog, W. Analog Coupled Oscillator Based Weighted Ising Machine. *Sci. Rep.* **2019**, *9*, 14786. [CrossRef]
6. Böhm, F.; Verschaffelt, G.; Sande, G.V. Solving MAXCUT Optimization Problems with a Coherent Ising Machine Based on Opto-Electronic Oscillators. In Proceedings of the 2019 Conference on Lasers and Electro-Optics Europe & European Quantum Electronics Conference (CLEO/Europe-EQEC), Munich, Germany, 23–27 June 2019; p. 1.
7. Ayanzadeh, R.; Halem, M.; Finin, T. Reinforcement Quantum Annealing: A Hybrid Quantum Learning Automata. *Sci. Rep.* **2020**, *10*, 7592. [CrossRef] [PubMed]
8. Inagaki, T.; Inaba, K.; Hamerly, R.; Inoue, K.; Yamamoto, R.H.Y.; Takesue, T.I.K.I.H. Large-scale Ising spin network based on degenerate optical parametric oscillators. *Nat. Photon.* **2016**, *10*, 415–419. [CrossRef]
9. Inagaki, T.; Haribara, Y.; Igarashi, K.; Sonobe, T.; Tamate, S.; Honjo, T.; Marandi, A.; McMahon, P.L.; Umeki, T.; Enbutsu, K.; et al. A coherent Ising machine for 2000-node optimization problems. *Science* **2016**, *354*, 603. [CrossRef]
10. McMahon, P.L.; Marandi, A.; Haribara, Y.; Hamerly, R.; Langrock, C.; Tamate, S.; Inagaki, T.; Takesue, H.; Utsunomiya, S.; Aihara, K.; et al. A fully programmable 100-spin coherent Ising machine with all-to-all connections. *Science* **2016**, *354*, 614. [CrossRef]
11. Böhm, F.; Inagaki, T.; Inaba, K.; Honjo, T.; Enbutsu, K.; Umeki, T.; Kasahara, R.; Takesue, H. Understanding dynamics of coherent Ising machines through simulation of large-scale 2D Ising models. *Nat. Commun.* **2018**, *9*, 5020. [CrossRef]
12. Takemoto, T.; Hayashi, M.; Yoshimura, C.; Yamaoka, M. A 2 $\times$ 30k-Spin Multi-Chip Scalable CMOS Annealing Processor Based on a Processing-in-Memory Approach for Solving Large-Scale Combinatorial Optimization Problems. *IEEE J. Solid-State Circuits* **2019**, *55*, 145–156. (In English) [CrossRef]
13. Yamaoka, M.; Yoshimura, C.; Hayashi, M.; Okuyama, T.; Aoki, H.; Mizuno, H. A 20k-Spin Ising Chip to Solve Combinatorial Optimization Problems with CMOS Annealing. *IEEE J. Solid-State Circuits* **2015**, *51*, 303–309. [CrossRef]
14. Takemoto, T.; Yamamoto, K.; Yoshimura, C.; Hayashi, M.; Tada, M.; Saito, H.; Mashimo, M.; Yamaoka, M. 4.6 A 144Kb Annealing System Composed of 9$\times$16Kb Annealing Processor Chips with Scalable Chip-to-Chip Connections for Large-Scale Combinatorial Optimization Problems. In Proceedings of the 2021 IEEE International Solid- State Circuits Conference (ISSCC), San Francisco, CA, USA, 13–22 February 2021.
15. Dutta, S.; Khanna, A.; Gomez, J.; Ni, K.; Toroczkai, Z.; Datta, S. Experimental Demonstration of Phase Transition Nano-Oscillator Based Ising Machine. In Proceedings of the 2019 IEEE International Electron Devices Meeting (IEDM), San Francisco, CA, USA, 7–11 December 2019; pp. 37.8.1–37.8.4.
16. Borders, W.A.; Pervaiz, A.Z.; Fukami, S.; Camsari, K.Y.; Ohno, H.; Datta, S. Integer factorization using stochastic magnetic tunnel junctions. *Nature* **2019**, *573*, 390–393. [CrossRef] [PubMed]
17. Alfke, P. Efficient Shift RegistersLFSR Counters and Long Pesudo-Random Sequence Generators. *Xlilinx Appl. Note XAPP 052* **1996**, 1–6.
18. Vincent, A.F.; Larroque, J.; Locatelli, N.; Ben Romdhane, N.; Bichler, O.; Gamrat, C.; Zhao, W.S.; Klein, J.-O.; Galdin-Retailleau, S.; Querlioz, D. Spin-Transfer Torque Magnetic Memory as a Stochastic Memristive Synapse for Neuromorphic Systems. *IEEE Trans. Biomed. Circuits Syst.* **2015**, *9*, 166–174. [CrossRef]
19. Diao, Z.; Li, Z.; Wang, S.; Ding, Y.; Panchula, A.; Chen, E.; Wang, L.-C.; Huai, Y. Spin-transfer torque switching in magnetic tunnel junctions and spin-transfer torque random access memory. *J. Phys. Condens. Matter* **2007**, *19*, 165209. [CrossRef]
20. Zhang, Y.; Zhao, W.; Prenat, G.; Devolder, T.; Klein, J.-O.; Chappert, C.; Dieny, B.; Ravelosona, D. Electrical Modeling of Stochastic Spin Transfer Torque Writing in Magnetic Tunnel Junctions for Memory and Logic Applications. *IEEE Trans. Magn.* **2013**, *49*, 4375–4378. [CrossRef]
21. Jan, G.; Thomas, L.; Le, S.; Lee, Y.-J.; Liu, H.; Zhu, J.; Iwata-Harms, J.; Patel, S.; Tong, R.-Y.; Sundar, V.; et al. Demonstration of Ultra-Low Voltage and Ultra Low Power STT-MRAM designed for compatibility with 0x node embedded LLC applications. In Proceedings of the 2018 IEEE Symposium on VLSI Technology, Honolulu, HI, USA, 18–22 June 2018; pp. 65–66. [CrossRef]
22. Thomas, L.; Jan, G.; Serrano-Guisan, S.; Liu, H.; Zhu, J.; Lee, Y.-J.; Le, S.; Iwata-Harms, J.; Tong, R.-Y.; Patel, S.; et al. STT-MRAM devices with low damping and moment optimized for LLC applications at Ox nodes. In Proceedings of the 2018 IEEE International Electron Devices Meeting (IEDM), San Francisco, CA, USA, 1–5 December 2018; pp. 27.3.1–27.3.4. [CrossRef]
23. Jan, G.; Thomas, L.; Le, S.; Lee, Y.-J.; Liu, H.; Zhu, J.; Iwata-Harms, J.; Patel, S.; Tong, R.-Y.; Serrano-Guisan, S.; et al. Achieving Sub-ns switching of STT-MRAM for future embedded LLC applications through improvement of nucleation and propagation switching mechanisms. In Proceedings of the 2016 IEEE Symposium on VLSI Technology, Honolulu, HI, USA, 14–16 June 2016; pp. 1–2. [CrossRef]
24. Kar, G.S.; Kim, W.; Tahmasebi, T.; Swerts, J.; Mertens, S.; Heylen, N.; Min, T. Co/Ni based p-MTJ stack for sub-20nm high density stand alone and high performance embedded memory application. In Proceedings of the 2014 IEEE International Electron Devices Meeting, San Francisco, CA, USA, 15–17 December 2014; pp. 19.1.1–19.1.4. [CrossRef]

25. Miura, S.; Nishioka, K.; Naganuma, H.; Nguyen, T.V.A.; Honjo, H.; Ikeda, S.; Watanabe, T.; Inoue, H.; Niwa, M.; Tanigawa, T.; et al. Scalability of Quad Interface p-MTJ for 1X nm STT-MRAM With 10-ns Low Power Write Operation, 10 Years Retention and Endurance > 10^{11}. *IEEE Trans. Electron Devices* **2020**, *67*, 5368–5373. [CrossRef]
26. Fukushima, A.; Seki, T.; Yakushiji, K.; Kubota, H.; Imamura, H.; Yuasa, S.; Ando, K. Spin dice: A scalable truly random number generator based on spintronics. *Appl. Phys. Express* **2014**, *7*, 083001. [CrossRef]
27. Endoh, T.; Honjo, H.; Nishioka, K.; Ikeda, S. Recent Progresses in STT-MRAM and SOT-MRAM for Next Generation MRAM. In Proceedings of the 2020 IEEE Symposium on VLSI Technology, Honolulu, HI, USA, 16–19 June 2020; pp. 1–2. [CrossRef]
28. Peng, X.; Liao, Z.; Xu, N.; Qin, G.; Zhou, X.; Suter, D.; Du, J. Quantum Adiabatic Algorithm for Factorization and Its Experimental Implementation. *Phys. Rev. Lett.* **2008**, *101*, 220405. [CrossRef]
29. SAHIN, M. Generalized Trial Division. *Int. J. Contemp. Math. Sci.* **2011**, *6*, 59–64.

Disclaimer/Publisher's Note: The statements, opinions and data contained in all publications are solely those of the individual author(s) and contributor(s) and not of MDPI and/or the editor(s). MDPI and/or the editor(s) disclaim responsibility for any injury to people or property resulting from any ideas, methods, instructions or products referred to in the content.

micromachines

MDPI

Article

Micromagnetic Simulation of $L1_0$-FePt-Based Transition Jitter of Heat-Assisted Magnetic Recording at Ultrahigh Areal Density

Chavakon Jongjaihan and Arkom Kaewrawang *

Magnetic Materials and Applications Research Laboratory, Department of Electrical Engineering, Faculty of Engineering, Khon Kaen University, Khon Kaen 40002, Thailand
* Correspondence: arkom@kku.ac.th

Abstract: The areal density of hard disk drives increases every year. Increasing the areal density has limitations. Therefore, heat-assisted magnetic recording (HAMR) technology has been the candidate for increasing the areal density. At ultrahigh areal density, the main problem of the magnetic recording process is noise. Transition jitter is noise that affects the read-back signal. Hence, the performance of the magnetic recording process depends on the transition jitter. In this paper, the transition jitter of $L1_0$-FePt-based HAMR technology was simulated at the ultrahigh areal density. The micromagnetic simulation was used in the magnetic recording process. The average grain size was 5.1 nm, and the standard deviation was 0.08 nm. The recording simulation format was five tracks in a medium. It was found that a bit length of 9 nm with a track width of 16.5 nm at the areal density of 4.1 Tb/in^2 had the lowest transition jitter average of 1.547 nm. In addition, the transition jitter average decreased when increasing the areal density from 4.1 to 8.9 Tb/in^2. It was found that the lowest transition jitter average was 1.270 nm at an 8 nm track width and a 9 nm bit length, which achieved an ultrahigh areal density of 8.9 Tb/in^2.

Keywords: transition jitter; heat-assisted magnetic recording; magnetic footprints

Citation: Jongjaihan, C.; Kaewrawang, A. Micromagnetic Simulation of $L1_0$-FePt-Based Transition Jitter of Heat-Assisted Magnetic Recording at Ultrahigh Areal Density. *Micromachines* **2022**, *13*, 1559. https://doi.org/10.3390/mi13101559

Academic Editors: Seung-bok Choi and Viktor Sverdlov

Received: 13 July 2022
Accepted: 19 September 2022
Published: 20 September 2022

Copyright: © 2022 by the authors. Licensee MDPI, Basel, Switzerland. This article is an open access article distributed under the terms and conditions of the Creative Commons Attribution (CC BY) license (https://creativecommons.org/licenses/by/4.0/).

1. Introduction

The trend of the areal density (AD) in magnetic recording technology increases every year [1]. It can increase with increased bit density, increased track density, and reduced grain size [2,3]. However, the effects of reducing grain size decrease the thermal stability, which causes superparamagnetic effects. The thermal stability can increase by increasing the magnetocrystalline anisotropy constant, K_u. Magnetic materials are modified to accommodate increasing the areal density for the magnetic recording technology. The $L1_0$-FePt medium is currently selected as a candidate because of the suitability of the magnetic properties [4–8]. The high K_u, the high saturation magnetization, M_s, and the low curie temperature, T_c, are the magnetic properties of $L1_0$-FePt that have been optimized for the new technology of hard disks, such as MAMR [9] and HAMR [4,10–15].

Heat-assisted magnetic recording (HAMR) technology is chosen to assist magnetic recording at high AD [8,16,17] due to the high K_u of the magnetic materials. In addition, one of the main problems that occurs in the magnetic recording process is the noise that decreases the signal-to-noise ratio (SNR) or increases the error of the read-back signal. The noise mainly consists of DC noise and jitter noise; consequently, they cause irregular amplitude and make the read-back signal transition less sharp, respectively. The correlation of the noise and the transition jitter, σ_{jitter}, is strong [18–20]. Therefore, the performance of the magnetic recording process is indicated by the σ_{jitter}. The main causes of the σ_{jitter} are the grain size, grain size distribution, grain shape, read width, heat spot geometry, and thermal gradient [10–12,19,21,22].

Many publications have simulated magnetic recording to achieve high areal density and high performance. The transition jitter has been used to indicate the performance of

the magnetic recording process [12–15,22]. Valcu and Yeh [22] have improved Voronoi-pattern media for very close to the microtrack model prediction. The transition jitter is used to indicate the efficiency of Voronoi-pattern media and that the detection positions are the zero crossings. It was found that the read width is inversely proportional to the jitter. Niranjan and Victora [12] have shown that these analytical calculations work well for estimating the jitter when comparisons are made with simulation results under different recording conditions and media variations. One of the simulations showed that the grain pitch has a greater effect on the transition jitter than on the read width. Pituso et al. [13,14] have simulated the magnetic recording process in a two-dimensional (2-D) format. The simulation demonstrates magnetic footprints of HAMR technology where heating is based on the relationship of magnetic properties with temperature. The behavior of magnetic properties with temperature is used to identify the hotspot for the simulation. Hernandez et al. [15] proposed parameters that can achieve the high areal density in HAMR technology.

From many studies [10–12,19,21,22], the transition jitter can be obtained by the standard deviation from a read-back signal at the zero-crossing position. In this paper, the transition jitter was shown in another form of the transition jitter by indicating the position of the transition bits in a 2-D format. Since the magnetic footprint simulation was analyzed for the transition jitter simulation in a 2-D format, this simulation was analyzed to resemble the magnetic footprint experimental analysis imaging shown in the 2-D format of spin-stand microscopy. The spin-stand is a machine that can characterize of the magnetic footprints for analysis, such as transition curvature analysis [23–25]. Therefore, this paper aimed to maintain a reasonable level of performance from increasing both the linear density and the track density. We also proposed that the magnetic footprint simulation was simulated for the transition jitter simulation in a 2-D format. The $L1_0$-FePt magnetic material's properties depend on the temperature used to identify the hotspot area for the heating simulation in the Voronoi medium. The micromagnetic modeling is based on the Landau–Lifshitz–Gilbert (LLG) equation. The lowest transition jitter average simulation was investigated at the areal density of 4.1 Tb/in^2. In addition, the lowest transition jitter average was investigated at ultrahigh areal densities from 4.1 to 8.9 Tb/in^2 in HAMR technology.

2. Materials and Methods

In this work, the micromagnetic simulation was based on the LLG equation, as shown in Equation (1) [13,26,27]:

$$\frac{d\vec{M}}{dt} = -\gamma\vec{M} \times \vec{H}_{eff} - \frac{\gamma\alpha}{M_s}\vec{M} \times \left(\vec{M} \times \vec{H}_{\text{eff}}\right) \quad (1)$$

where $\vec{M}$ is the magnetization vector, γ is the gyromagnetic ratio, α is the damping constant, and M_s is the saturation magnetization. The effective field, $\vec{H}_{\text{eff}}$, includes the exchange, demagnetizing, anisotropy, and Zeeman fields. The simulation was implemented by the object-oriented micromagnetic framework (OOMMF) software [28].

The magnetic recording simulation process of HAMR technology used the correlation between the temperature and the properties of the magnetic materials to create the hotspot area. Therefore, the hotspot area model used the Brillouin function equation, as shown in Equations (2)–(4) [13,14]:

$$M_s(T) = M_s(0)\left[\frac{2J+1}{2\text{J}}\coth\left(\frac{2J+1}{2\text{J}}\beta\right) - \frac{1}{2J}\coth\left(\frac{\beta}{2J}\right)\right] \quad (2)$$

and

$$\frac{K_u(T)}{K_u(0)} = \left(\frac{M_s(T)}{M_s(0)}\right)^n \quad (3)$$

where

$$\beta = 3(1 - \frac{T}{T_C}) \tag{4}$$

where J is the total angular momentum quantum number, n is a medium film series factor, T is the temperature, T_C is the Curie temperature, H_k is the anisotropy field, and K_u is the magnetocrystalline anisotropy constant.

The shape of the hotspot area was a squircle, the shape of the applied field was rectangular, and they were the same width. The writing model was five tracks in a medium of each bit length, and a single-tone sequence was written on a track of 31 bits and 30 boundaries. The Voronoi grain medium had dimensions of 1000 nm × 1500 nm and a thickness of 6 nm. The medium model had a resolution of 0.25 pixels per 1 nm in the x–y plane. The average grain size was 5.1 nm [15] with the standard deviation of 0.08 nm, and the grain boundary width was about 1–2 nm. The mesh cell size of the micromagnetic simulation in the x–y plane was 1 nm × 1 nm, and in the Z-axis it was 3 nm. The magnetic properties at room temperature of the $L1_0$-FePt medium were as follows: M_s (300 K) = 1.100 MA/m and K_u (300 K) = 7 MJ/m^3. The T for heating in the HAMR process was 700 K, and the T_C was 710 K. The write head field was 10 kOe along the z-direction, and J was 0.85 at a medium film series factor, n, of 2.15 for the $L1_0$-FePt magnetic material [14,15]. The intragrain exchange stiffness constant was 12 pJ/m, and the intergrain exchange stiffness was 0 J/m [13]. MATLAB [29] was used for the Voronoi medium modeling and the σ_{jitter} that could be obtained from the zig-zag boundary procedure flow chart for the transition jitter simulation, as shown in Figure 1.

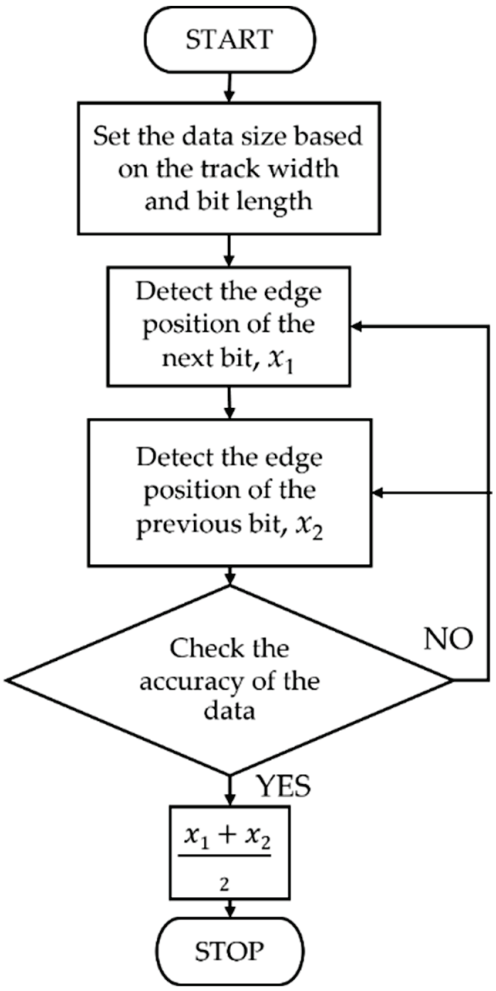

Figure 1. The zig-zag boundary procedure flow chart.

The σ_{jitter} was the standard deviation of each zero-crossing position, as shown in Equation (5) [10–12,19,21,22]:

$$\sigma_{jitter} = \sqrt{\frac{1}{N-1}\sum_{i=1}^{N}(x_i - \overline{x}_m)^2} \quad (5)$$

where x_i is zero-crossing position, $\overline{x}_m$ is an average position, and N is a total number of transitions.

The transition jitter average, $\overline{\sigma}_{jitter}$, was calculated by the summation of σ_{jitter} of each track in a medium divided by the total number of tracks, N_t, as shown in Equation (6).

$$\overline{\sigma}_{jitter} = \frac{1}{N_t}\sum_{i=1}^{N_t}\sigma_{jitter\,i} \quad (6)$$

2.1. Minimum Transition Jitter at the Areal Density of 4.1 Tb/in²

The simulation parameters were determined under the scope of the AD at 4.1 Tb/in^2 for finding the lowest $\overline{\sigma}_{jitter}$, as shown in Table 1.

Table 1. Bit length, track width, and hotspot size use in the simulation at the areal density of 4.1 Tb/in^2.

Areal Density (Tb/in^2)	Bit Length (nm)	Track Width (nm)	Hotspot Size (nm)
4.1 [15]	7 [15]	22.5 [15]	28
	7.5	21	26.5
	8 [15]	19.5 [15]	25 [15]
	8.5	18	23.5
	9	16.5	22
	9.5	15	20.5
	10	13.5	19

2.2. Transition Jitter at Ultrahigh Areal Density of 4.1–8.9 Tb/in²

In Table 2, the bit length of 9 nm was selected to investigate the $\overline{\sigma}_{jitter}$ at ultrahigh areal densities from 4.1 to 8.9 Tb/in^2 by decreasing the track width.

Table 2. Track width and hotspot size at ultrahigh areal density from 4.1 to 8.9 Tb/in^2.

Bit Length (nm)	Track Width (nm)	Hotspot Size (nm)	Areal Density (Tb/in^2)
9	16.5	22	4.1
	14	19.5	5.1
	12	17.5	6.1
	10	15.5	7.1
	8	13.5	8.9

3. Results and Discussions

3.1. Minimum Transition Jitter at the Areal Density of 4.1 Tb/in²

Figure 2 shows the magnetic footprint simulation result of 31 bits per track (between the yellow lines) at the areal density of 4.1 Tb/in^2 (9 nm bit length and 16.5 nm track width). The magnetic footprints of each track were analyzed to show the transition boundaries in a 2-D format, as shown in Figure 3.

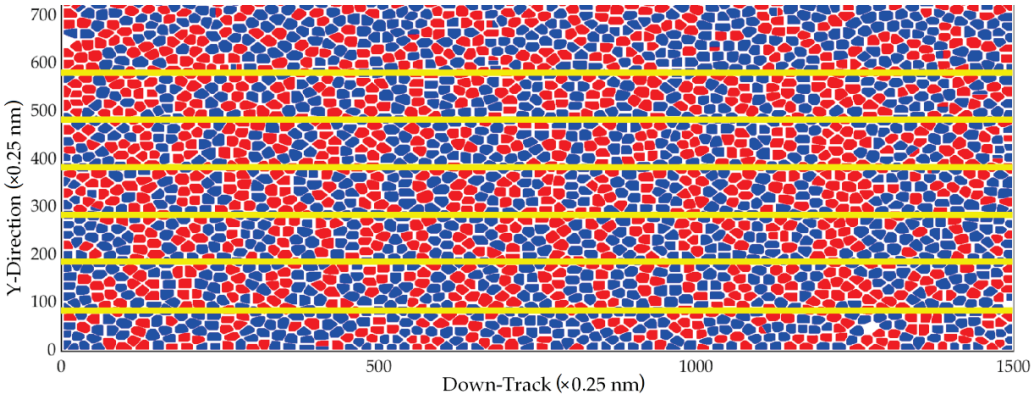

Figure 2. Magnetic footprints of 9 nm bit lengths with a track width of 16.5 nm.

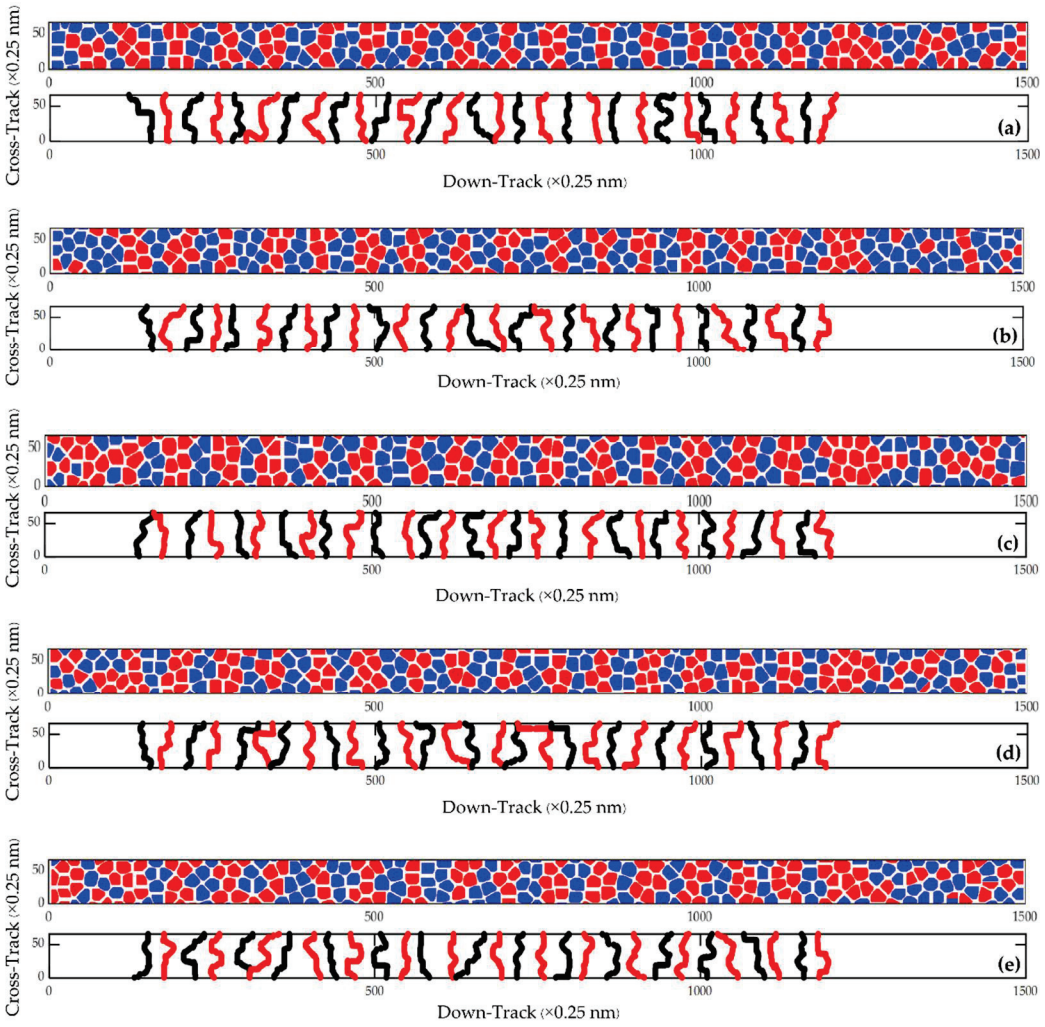

Figure 3. The magnetic footprints (**upper**) at a bit length of 9 nm with a track width of 16.5 nm and the boundary between bits (**lower**) of the (**a**) 1st, (**b**) 2nd, (**c**) 3rd, (**d**) 4th, and (**e**) 5th tracks.

Figure 4 shows the results of the $\overline{\sigma}_{jitter}$ at the areal density of 4.1 Tb/in^2. It was found that the $\overline{\sigma}_{jitter}$ values of bit lengths of 7, 7.5, 8, 8.5, 9, 9.5, and 10 nm were 1.703, 1.635, 1.661, 1.649, 1.547, 1.629, and 1.655 nm, respectively. The lowest $\overline{\sigma}_{jitter}$ was 1.547 nm at a bit length of 9 nm and a track width of 16.5 nm. The results in Figure 4 also show that the fluctuations in the $\overline{\sigma}_{jitter}$ at bit lengths of 7 to 10 nm are probably from the grain shape or the grain size distribution. The $\overline{\sigma}_{jitter}$ of the 7 nm bit length increased when the reducing bit length approached the grain size because the bit length of 6 nm cannot be simulated.

The results of the micromagnetic simulations also found that some of the bits did not have the magnetization switching in the grain because some parts of the grain were not in the hotspot area. Therefore, the broad zig-zag boundary was the effect of reducing bit length approaches to the grain size.

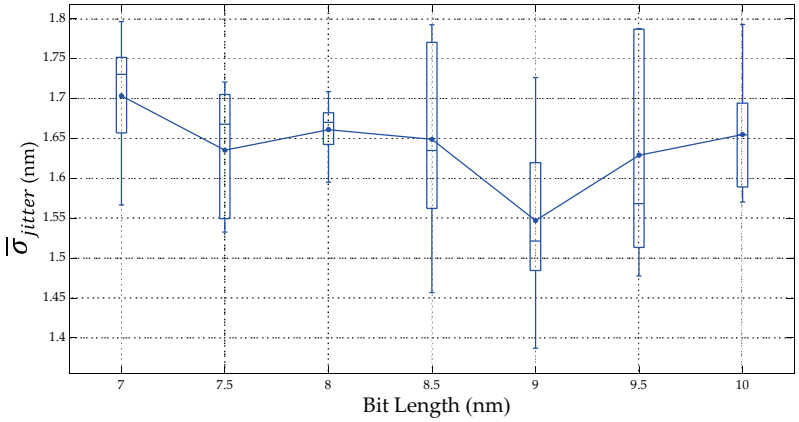

Figure 4. Relationship between the $\overline{\sigma}_{jitter}$ and bit length.

3.2. Transition Jitter at Ultrahigh Areal Densities of 4.1–8.9 Tb/in^2

Figure 5 shows the magnetic footprint simulation result that was investigated from the areal density of 4.1 Tb/in^2, and this is the magnetic footprint simulation result of 31 bits per track (between the yellow lines) at the ultrahigh areal densities from 4.1 to 8.9 Tb/in^2. The magnetic footprints of each track in Figure 5 were analyzed to show the transition boundaries in a 2-D format, as shown in Figure 6.

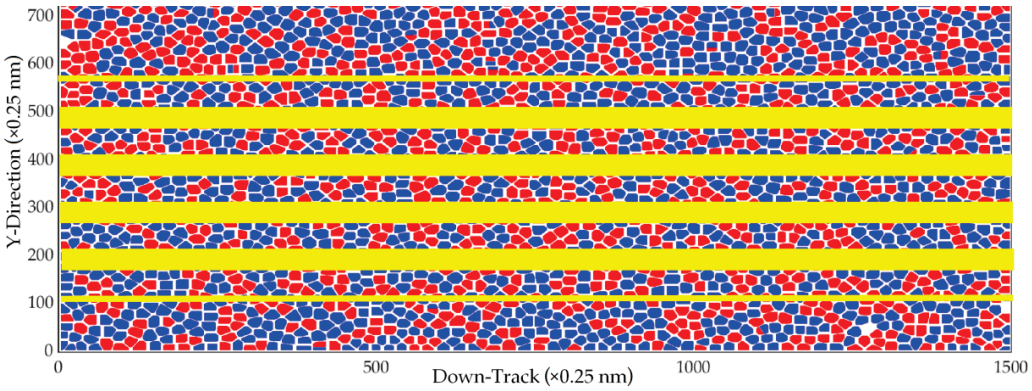

Figure 5. Magnetic footprints at AD of 8.9 Tb/in^2.

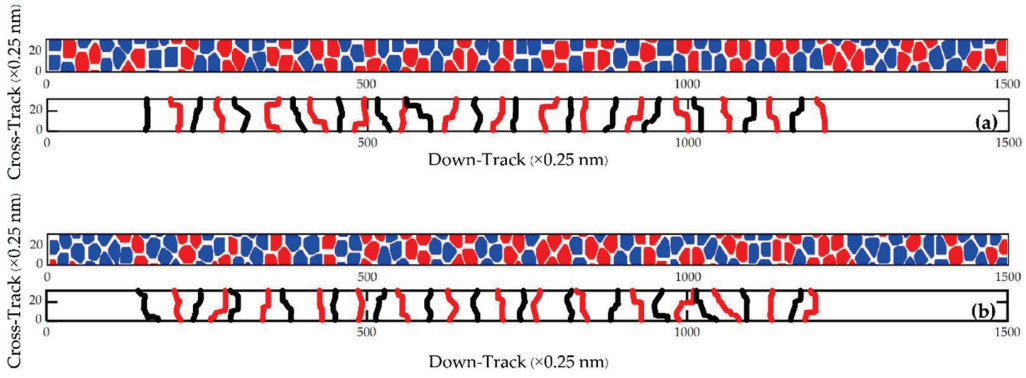

Figure 6. *Cont.*

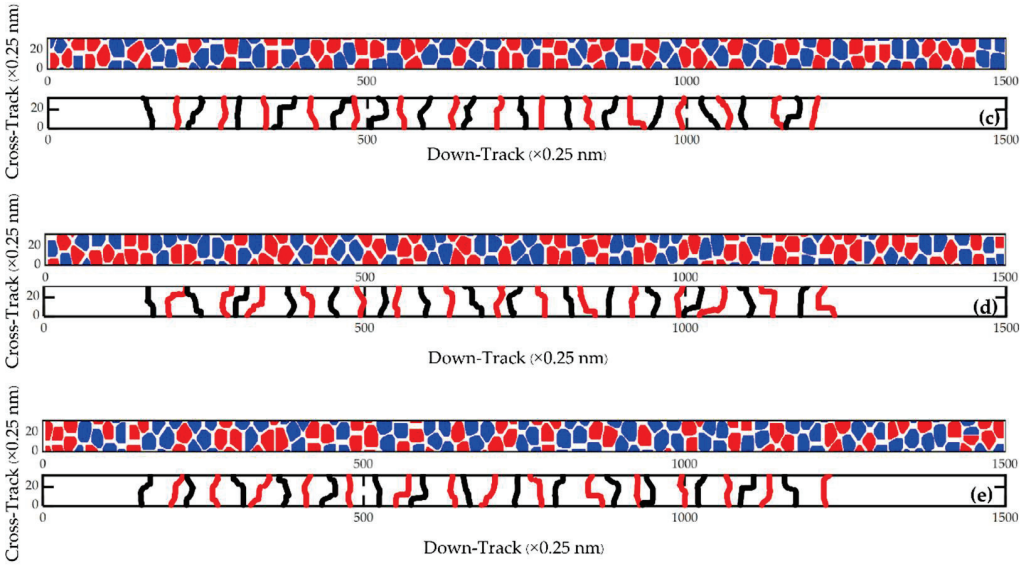

Figure 6. The magnetic footprints (**upper**) at a bit length of 9 nm with a track width 8 nm and the boundary between bits (**lower**) of the (**a**) 1st, (**b**) 2nd, (**c**) 3rd, (**d**) 4th, and (**e**) 5th tracks.

The results in Section 3.1 show that the bit length of 9 nm had the lowest $\overline{\sigma}_{jitter}$. In this section, the track width of the 9 nm bit length was selected to investigate the $\overline{\sigma}_{jitter}$ at ultrahigh areal densities from 4.1 to 8.9 Tb/in^2, and Figure 7 shows the $\overline{\sigma}_{jitter}$ for track width and areal density variation. It was found that the $\overline{\sigma}_{jitter}$ values of each track width at 9 nm bit lengths of 8, 10, 12, 14, and 16.5 nm were 1.270, 1.490, 1.493, 1.60, and 1.547 nm, respectively. The lowest $\overline{\sigma}_{jitter}$ was 1.270 nm at an 8 nm track width. The trend of $\overline{\sigma}_{jitter}$ reduced with increases in the areal density from 4.1 to 8.9 Tb/in^2 (or decreasing track width from 16.5 to 8 nm.). The trend of $\overline{\sigma}_{jitter}$ reduced with decreasing track width. It was likely due to the zero-crossing position being outside the track area, and this trend is consistent with those in the literature [12,30].

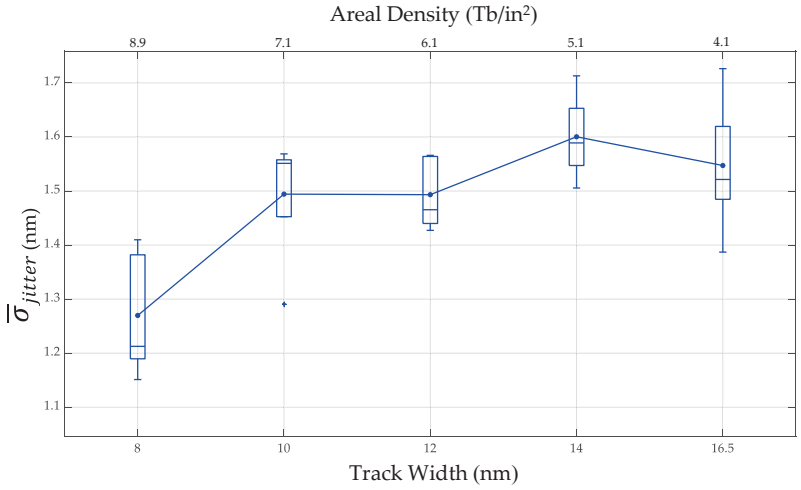

Figure 7. The $\overline{\sigma}_{jitter}$ for track width and areal density variation.

4. Conclusions

In this paper, we present the transition jitter simulation in the 2-D format of HAMR technology at ultrahigh areal densities from 4.1 to 8.9 Tb/in^2. The $L1_0$-FePt magnetic material was used as the magnetic medium for future magnetic recording. The OOMMF was used for recording process simulation, and the MATLAB program was used to simulate the transition jitter in a 2-D format. The areal density of 4.1 Tb/in^2 has the lowest $\overline{\sigma}_{jitter}$ of 1.547 nm (9 nm bit length and 16.5 nm track width). The areal densities from 4.1 to

8.9 Tb/in^2 had the lowest $\overline{\sigma}_{jitter}$ of 1.270 nm (9 nm bit length and 8 nm track width). These results can be the guidelines for future magnetic recording technology development.

Author Contributions: Conceptualization, C.J. and A.K.; methodology, C.J. and A.K.; software, C.J.; validation, C.J. and A.K.; formal analysis, C.J. and A.K.; investigation, C.J. and A.K.; data curation, C.J. and A.K.; writing—original draft preparation, C.J.; writing—review and editing, C.J. and A.K.; visualization, C.J.; supervision, A.K.; project administration, A.K.; funding acquisition, A.K. All authors have read and agreed to the published version of the manuscript.

Funding: This research was funded by funding for thesis, dissertation, or independent study for graduate students from the Faculty of Engineering, Khon Kaen University, Thailand (Grant No. Mas. Ee-2565/6).

Data Availability Statement: Not applicable.

Acknowledgments: We would like to thank Kotchakorn Pituso for the simulation code and the Magnetic Materials and Applications Research Laboratory at the Department of Electrical Engineering, Faculty of Engineering, Khon Kaen University. We would like to thank MATLAB and the OOMMF User's Guide, Version 1.0, M.J. Donahue, and D.G. Porter, Interagency Report NISTIR 6376, National Institute of Standards and Technology, Gaithersburg, MD, USA (September 1999), for the simulations. We would like to thank Wanitcha Wannasook for helping to edit and improve on English writing.

Conflicts of Interest: The authors declare no conflict of interest.

References

1. Coughlin, T. Developments in HDD Technology Provide Consumer Services [The Art of Storage]. *IEEE Consum. Electron. Mag.* **2016**, *5*, 122–133. [CrossRef]
2. Furrer, S.; Pantazi, A.; Cherubini, G.; Lantz, M.F. Compressional Wave Disturbance Suppression for Nanoscale Track-Following on Flexible Tape Media. Annual American Control Conference (ACC), Milwaukee, WI, USA, 27–29 June 2018.
3. Wood, R. Future hard disk driver system. *J. Magn. Mater.* **2009**, *321*, 555–561. [CrossRef]
4. Weller, D.; Mosendz, O.; Parker, G.; Pisana, S.; Santos, T.S. L10 FePtX–Y media for heat-assisted magnetic recording. *Phys. Status Solidi A.* **2013**, *210*, 1245–1260. [CrossRef]
5. Tsai, J.-L.; Chen, Y.-R.; Chen, J.-Y.; Hsu, T.-W.; Dai, C.; Hsu, C.-J. Magnetic Properties and Microstructure of FePt(BN, Ag, C) Films. *Coatings* **2018**, *8*, 358. [CrossRef]
6. Tsai, J.-L.; Dai, C.; Chen, J.-y.; Hsu, T.-W.; Weng, S.-M.; Huang, L.-C. Influence of an MgTiTaON Inserted Layer on Magnetic Properties and Microstructure of FePtAgC Films. *Coatings* **2019**, *9*, 238. [CrossRef]
7. Zhang, L.; Du, X.; Lu, H.; Gao, D.; Liu, H.; Lin, Q.; Cao, Y.; Xie, J.; Hu, W. Influence of Cu on the Improvement of Magnetic Properties and Structure of L10 FePt Nanoparticles. *Nanomaterials* **2021**, *11*, 1097. [CrossRef]
8. Wei, D.-H.; Chen, S.-C.; Yang, C.-J.; Huang, R.-T.; Dong, C.-L.; Yao, Y.-D. Formation of FePt–MgO Nanocomposite Films at Reduced Temperature. *J. Compos. Sci.* **2022**, *6*, 158. [CrossRef]
9. Khunkitti, P.; Wannawong, N.; Jongjaihan, C.; Siritaratiwat, A.; Kruesubthaworn, A.; Kaewrawang, A. Micromagnetic Simulation of $L1_0$-FePt-Based Exchange-Coupled-Composite-Bit-Patterned Media with Microwave-Assisted Magnetic Recording at Ultrahigh Areal Density. *Micromachines* **2021**, *12*, 1264. [CrossRef]
10. Victora, R.H.; Huang, P.W. Simulation of heat-assisted magnetic recording using renormalized media cells. *IEEE Trans. Magn.* **2013**, *49*, 751–757. [CrossRef]
11. Oezelt, H.; Kovacs, A.; Fischbacher, J.; Bance, S.; Gubbins, M.; Schrefl, T. Transition Jitter in Heat-Assisted Magnetic Recording by Micromagnetic Simulation. *IEEE Trans. Magn.* **2017**, *53*, 1–5. [CrossRef]
12. Natekar, N.A.; Victora, R.H. Analytical Estimation of Transition Jitter for the Heat-Assisted Magnetic Recording Process. *IEEE Magn. Lett.* **2020**, *11*, 1–4. [CrossRef]
13. Pituso, K.; Kaewrawang, A.; Tongsomporn, D.; Chooruang, K. The Simulation of Stationary Magnetic Footprints for Perpendicular Magnetic Recording in Granular Magnetic Media. In Proceedings of the 29th International Technical Conference on Circuit/Systems Computers and Communications (ITC-CSCC), Phuket, Thailand, 1–4 July 2014.
14. Pituso, K.; Khunkitti, P.; Tongsomporn, D.; Kruesubthaworn, A.; Chooruang, K.; Siritaratiwat, A.; Kaewrawang, A. Simulation of magnetic footprints for heat assisted magnetic recording. *Eur. Phys. J. Appl. Phys.* **2017**, *78*, 20301. [CrossRef]
15. Hernandez, S.; Liu, Z.; Jin, P.; Granz, S.D.; Krivosik, P.; Venkataramani, R.; Radich, W.; Rausch, T.; Dykes, J.; Gage, E.C. Geometrical Scaling Limits of Heat-Assisted Magnetic Recording. *IEEE Trans. Magn.* **2021**, *57*, 1–5. [CrossRef]
16. Granz, S.; Jury, J.; Rea, C.; Ju, G.; Thiele, J.U.; Rausch, T.; Gage, E.C. Areal Density Comparison Between Conventional, Shingled, and Interlaced Heat-Assisted Magnetic Recording with Multiple Sensor Magnetic Recording. *IEEE Trans. Magn.* **2019**, *55*, 1–3. [CrossRef]
17. Kryder, M.H.; Gage, E.C.; McDaniel, T.W.; Challener, W.A.; Rottmayer, R.E.; Ju, G.; Hsia, Y.T.; Erden, M.F. Heat Assisted Magnetic Recording. *Proc. IEEE* **2008**, *96*, 1810–1835. [CrossRef]

18. Zhu, J.G.; Li, H. Understanding Signal and Noise in Heat Assisted Magnetic Recording. *IEEE Trans. Magn.* **2013**, *49*, 765–772. [CrossRef]
19. Wang, X.; Gao, K.; Zhou, H.; Itagi, A.; Seigler, M.; Gage, E. HAMR Recording Limitations and Extendibility. *IEEE Trans. Magn.* **2013**, *49*, 686–692. [CrossRef]
20. Weller, D.; Parker, G.; Mosendz, O.; Champion, E.; Stipe, B.; Wang, X.; Klemmer, T.; Ju, G.; Ajan, A. A HAMR Media Technology Roadmap to an Areal Density of 4 Tb/in^2. *IEEE Trans. Magn.* **2014**, *50*, 1–8. [CrossRef]
21. Sohn, H.; Victora, R.H. Recording Comparison of ECC versus Conventional Media at Equal Grain Size. *IEEE Trans. Magn.* **2011**, *47*, 4073–4076. [CrossRef]
22. Valcu, F.B.; Yeh, N. Jitter in a Voronoi Pattern Media-Effect of Grain Size Distribution and Reader Width. *IEEE Trans. Magn.* **2010**, *46*, 2160–2162. [CrossRef]
23. Liu, Z.; Gilbert, I.; Hernandez, S.; Rea, C.; Granz, S.; Zhou, H.; Blaber, M.; Huang, P.W.; Peng, C.; Ju, G.; et al. Curvature and Skew in Heat-Assisted Magnetic. *IEEE Trans. Magn.* **2019**, *55*, 1–8. [CrossRef]
24. Gilbert, I.; Liu, Z.; Saunders, D.A.; Eppler, W.R.; Rea, C.; Rausch, T. Characterizing Curvature in Heat-Assisted Magnetic Recording Using Spin-Stand Imaging. *IEEE Trans. Magn.* **2019**, *55*, 1–4. [CrossRef]
25. Hernández, S.; Lu, P.L.; Granz, S.; Krivosik, P.; Huang, P.W.; Eppler, W.; Rausch, T.; Gage, E. Using Ensemble Waveform Analysis to Compare Heat Assisted Magnetic Recording Characteristics of Modeled and Measured Signals. *IEEE Trans. Magn.* **2017**, *53*, 1–6. [CrossRef]
26. Tipcharoen, W.; Warisarn, C.; Tongsomporn, D.; Karns, D.; Kovintavewat, P. Investigation of writing error in staggered heated-dot magnetic recording systems. *AIP Adv.* **2017**, *7*, 056511. [CrossRef]
27. Kaewrawang, A. *Magnetism and Magnetic Materials*; Khon Kaen University Press: Khon Kaen, Thailand, 2018. (In Thai)
28. Donahue, M.J.; Porter, D.G. OOMMF User's Guide, Release 1.2a3. Available online: https://math.nist.gov/oommf/ftp-archive/doc/userguide12a3_20021030.pdf (accessed on 15 October 2021).
29. The Math Works, Inc. *MATLAB*; Version 2022a; The Math Works, Inc.: Natick, MA, USA, 2022; Computer Software. Available online: www.mathworks.com/ (accessed on 1 April 2022).
30. Jiao, Y.; Victora, R.H. Dependence of Predicted Areal Density on Common Optimization Strategies for Heat-Assisted Magnetic Recording. *IEEE Magn. Lett.* **2017**, *8*, 1–4. [CrossRef]

micromachines

MDPI

Article

Optimization Design of Magnetic Isolation Ring Position in AC Solenoid Valves for Dynamic Response Performances

Jiang Guo [1,2], Linguang Li [1], Pu Qin [1], Jinghao Wang [1], Chao Ni [1], Xu Zhu [2], Dingyao Lu [3] and Jiwu Tang [4,*]

[1] Key Laboratory for Precision and Non-Traditional Machining Technology of Ministry of Education, Dalian University of Technology, Dalian 116024, China; guojiang@dlut.edu.cn (J.G.); lilinguang@mail.dlut.edu.cn (L.L.); qinpu@mail.dlut.edu.cn (P.Q.); 534657972@mail.dlut.cn (J.W.); nichao@mail.dlut.edu.cn (C.N.)
[2] Ningbo Institute of Dalian University of Technology, Ningbo 315000, China; zhux_nbi@dlut.edu.cn
[3] Jiayin Electromechanical Technology Co., Ltd., Ningbo 315400, China; ldy@jiayin.biz
[4] College of Applied Technology, Dalian Ocean University, Dalian 116300, China
* Correspondence: tangjiwu@dlou.edu.cn

Abstract: Dynamic response characteristics of solenoid valves directly determined their performances. Among numerous parameters, the influence of magnetic isolation ring (MIR) on solenoid valve performance is crucial. Previous optimization studies have not conducted a systematic exploration and analysis of MIR. In this paper, a model of an AC solenoid valve considering the position of the MIR is proposed, and the model's accuracy was verified by simulation and experiments. The electromagnetic force, response time, and magnetic field distribution at different positions of the MIR were analyzed, and the effect of the position of MIR on dynamic response characteristics of the solenoid valve was clarified. The results show that the MIR affects the dynamic response characteristics of the solenoid valve by changing the magnetic circuit. With the positive translation of the position of the MIR along the Z-axis, the electromagnetic force first increases and then decreases, and the response time first decreases and then increases. The position range of MIR with excellent dynamic response performance was obtained from the comprehensive consideration of response time and electromagnetic force. Finally, the optimization design for the dynamic response performance of the solenoid valves is realized.

Keywords: optimization design; magnetic isolation ring; dynamic response characteristics; simulation

Citation: Guo, J.; Li, L.; Qin, P.; Wang, J.; Ni, C.; Zhu, X.; Lu, D.; Tang, J. Optimization Design of Magnetic Isolation Ring Position in AC Solenoid Valves for Dynamic Response Performances. *Micromachines* **2022**, *13*, 1065. https://doi.org/10.3390/mi13071065

Academic Editors: Seung-bok Choi and Viktor Sverdlov

Received: 17 June 2022
Accepted: 30 June 2022
Published: 2 July 2022

Copyright: © 2022 by the authors. Licensee MDPI, Basel, Switzerland. This article is an open access article distributed under the terms and conditions of the Creative Commons Attribution (CC BY) license (https://creativecommons.org/licenses/by/4.0/).

1. Introduction

Solenoid valves are electromagnetic control elements used to control the flow, velocity, and direction of various media. They have many significant advantages, such as simple structure, low cost, rapid response, and high reliability. Therefore, solenoid valves play an essential role in aerospace, oil and gas transportation, industrial refrigeration, and other fields [1–4]. With the development of the industrial level, the requirements of miniaturization and high performance of solenoid valves in production are more urgent. Dynamic response characteristics of solenoid valves (i.e., response time, electromagnetic force, and magnetic induction intensity) are the most direct indicators to measure their operating performance, and it determines the comprehensive performance of the solenoid valve [5,6]. In order to obtain better solenoid valve performance, its structure needs to be optimized. The traditional design method is to determine the performance parameters of the valve through an empirical formula and analytical calculation. Then, the valve performance is verified through the prototype test. Finally, the design level is improved according to the feedback of the experimental results. This technical scheme based on theoretical calculation and experimental verification have the problems of a longer product development cycle, higher cost, and lower efficiency, which is gradually tricky to implement in meeting the needs of industrial development [7,8].

The finite element simulation technology is widely used in various optimization design links [9–11]. This technology is also combined with the optimized design of the solenoid valve. The optimization design method of solenoid valve based on finite element simulation is formed, which can overcome the limitations of traditional design. In recent years, researchers have done a great deal of simulation work for the optimization design of the structural parameters for the solenoid valve. Shukla et al. [12] verified the relationship between the external magnetic field strength and the movement of the moving iron core through simulation and experiments. Subic et al. [13] used the simulation method to explore reducing the solenoid valve's structural size while maintaining the solenoid valve's performance. Hung et al. [14] explored the influence of the solenoid spring stiffness, plunger mass and other structural parameters on the working characteristics. Grekhov et al. [15] found that the complete demagnetization of the iron core can achieve a faster response. Liu et al. [16] analyzed the core structure, coil structure, armature structure, and the effect of changes in the working air gap and drove current on the electromagnetic force of the solenoid valve. Hung et al. [17] found that the thickness of the solenoid valve cut-off sleeve, the cross-sectional shape of the coil, and the relative position of the coil and the plunger in the fuel injector have a significant influence on the electromagnetic force of the fuel injector. Yang et al. [18] found that the smaller the number of coils turns in the miniature digital valve, the more excellent the resistance and the faster the response of the electromagnet. Zhao et al. [19] studied the effect of eddy current on the dynamic response of high-speed solenoid valve of common rail injector and found that eddy current always hinders the change of magnetic field, which makes the dynamic response of high-speed solenoid valve worse. Slotting the yoke significantly reduces opening response time. Liao et al. [20] determined that the length of the casing, the length of the valve seat, and the height of the boss do not have a linear relationship with the electromagnetic force, but there is an optimal solution, and the study obtained the point with the largest electromagnetic force through simulation. At present, the research on the dynamic characteristics of solenoid valves mainly focuses on material optimization, external circuit optimization, and structure optimization. Among them, the main direction is the research on the coil structure and the shape of the armature in the structural part.

The concept of high-performance manufacturing is widely recognized and applied in modern manufacturing [21]. Performance-oriented manufacturing is a top-down reverse manufacturing process. Among them, performance-oriented design is an important core of high-performance manufacturing. However, the current research on solenoid valves does not fully meet the optimization requirements for dynamic response performance. At the same time, the magnetic isolation ring (MIR) is a critical component that affects the dynamic response characteristics of the solenoid valve. According to theoretical analysis, the position of the MIR significantly impacts the solenoid valve's response time and the armature's pull-in force [22]. The research on its influence law is still not systematic and in-depth.

In the present study, we incorporated the idea of high-performance manufacturing into the optimized design of solenoid valves and emphasized the optimization design of AC solenoid valves for dynamic response performances. The position of the MIR, which was more critical and rarely mentioned in previous studies, was taken as the research object. A model of an AC solenoid valve considering the position of the MIR was proposed and established. In order to verify the simulation results, a series of innovative solenoid valve dynamic response characteristic measurement devices were developed. The influence law of the position of the MIR on its dynamic response characteristics was deeply explored and analyzed. The research results can provide important references for developing high-performance optimization of solenoid valves.

2. Modeling of the AC Solenoid Valve

The experimental research is oriented to the standard AC normally closed solenoid valve. The structural diagram and optical image of the solenoid valve is shown in Figure 1.

The size of the solenoid valve is 60.8 mm (length) × 34.0 mm (width) × 53.8 mm (height). When the solenoid valve is not in operation, the coil is powered off, and the magnetic induction intensity in the air gap is zero. At this time, the movable iron core is not subjected to the electromagnetic force and moves downward to close the pilot valve port under the action of the spring force. The cavity pressure on the diaphragm increases, and the diaphragm is down under the action of spring force and differential pressure force to close the main valve port.

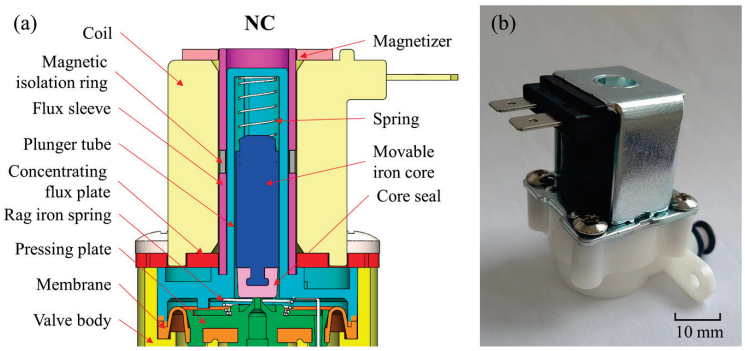

Figure 1. (**a**) Structural diagram and (**b**) optical image of the solenoid valve; the initial working air gap of the model is 12.16 mm, and the working stroke of the movable iron core is 5 mm.

In the experiment, the AC solenoid valve with a voltage of 36V was selected as the simulation object. The voltage input is sinusoidal AC voltage. Because the form of current excitation will directly determine the magnitude, direction, and variation trend of the electromagnetic force, the accuracy of the established current excitation model has an essential impact on the final calculation results. In Maxwell's default excitation form, only constant current excitation cannot restore the commutation behavior of sinusoidal alternating current in the excitation process. Therefore, this experiment uses the external circuit field to build a bridge rectifier circuit to construct the excitation source to simulate the actual working state of the solenoid valve more accurately. The mathematical circuit model of the electromagnetic coil can be expressed as

$$V(t) = V_0 + V_a \cdot e^{-Df(t-T_d)} \cdot \sin[2 \cdot \pi \cdot IFreq \cdot (t - T_d) - Phase] \quad (1)$$

where V_0 is the offset voltage in volts, V_a is the peak amplitude in volts, $IFreq$ is the signal frequency, T_d is the delay time in seconds, $Phase$ is the signal phase delay, and Df is the damping factor in 1/seconds.

The material properties of the main structure are defined as Table 1. MIR needs to be defined as a solid conductor with a voltage source. Definition of properties can be expressed as

$$\iint_{\Omega_c} \left(\sigma \frac{d\boldsymbol{A}}{dt} + \boldsymbol{j_t} \right) d\Omega = \iint_{\Omega_C} \frac{\sigma}{l} V_b d\Omega \quad (2)$$

where Ω_c is the width cross-section of the nth conductor, V_b is the known voltage source between the two conductors, $\boldsymbol{j_t}$ is the total current density to be solved for, σ is the conductivity, l is the thickness of the model, and $\boldsymbol{A}$ is the magnetic vector potential.

The motion domain is set as shown in Figure 2a. The motion direction of the movable iron core is set to be along the positive Z-axis. Motion types fall within the range of transient motions. The equation of motion for translational motion can be expressed as

$$ma + \lambda v = F_{em} + F_{load} \quad (3)$$

where m is the mass of the object, a is the acceleration of the object, v is the velocity, F_{em} is the computed electromagnetic force, F_{load} is the external load force, and λ is the damping.

Table 1. Part material setting.

Item	Setting
Moving iron core	Steel-1008
Magnetic isolation tube	Polyester
Coil	Copper
Magnetic isolation ring	Copper
Concentrating flux sleeve	Iron
Concentrating flux plate	Steel-1008
Solution region	Vacuum
Motion domain	Vacuum

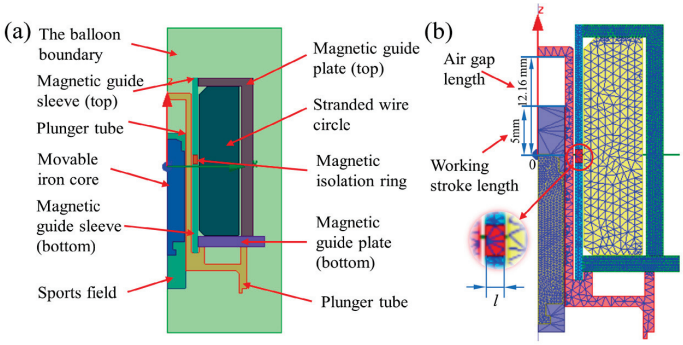

Figure 2. (**a**) Solution settings and (**b**) the meshing length of the magnetic conductive material is set to 0.5 mm, and the rest are set to 1.5 mm.

The electromagnetic force realizes the opening and closing behavior of the solenoid valve on the movable iron core overcoming the spring load force. Thus, the accurate definition of the spring load force directly determines the calculation results of the dynamic response characteristics of the solenoid valve. Since the spring load force change is not a monotonic linear relationship, the pwlx function defines the spring load force in this experiment. The Hooke coefficient is defined as 0.024 N/mm, the initial position is set to 0 mm, and the maximum displacement is set to 5 mm along the positive Z-axis, which is equal to the working stroke of the movable iron core. The iron core weight is set to 0.005 kg, and the damping coefficient is 1×10^{-5}. The specific value is obtained by experimental measurement.

The established solenoid valve simulation model is a 2D model. The model is of solenoids and insulators with rotational symmetry axis. The coordinate system adopts the cylindrical coordinate system ($r\varphi z$), the z-direction is the axial direction, and the r direction is the radial direction. Since any symmetry plane is the rz plane, there is no displacement in the φ direction. The electric or magnetic field in the calculation results must also be rotationally symmetric. Because $\boldsymbol{F}$ has a ϕ-component only, these operators are defined as

$$\nabla \times \boldsymbol{F} = (\frac{1}{r})[-\frac{\hat{\partial}(rF_\phi)}{\partial z}\hat{\boldsymbol{r}} + \frac{\partial(rF_\phi)}{\partial r}\hat{z} \tag{4}$$

where F is a scalar quantity, and $\boldsymbol{F}$ is a vector quantity.

Since the model is axisymmetric, the boundary condition of the solution domain is set to the balloon boundary. The balloon boundary simulates the outer region as near infinity. This boundary condition effectively isolates the model from other electrical current or magnetic fields sources.

The coil is set to add heat form, and the number of turns is set to 2700. A winding is defined as an external circuit with an initial voltage of 0. The external circuit setting form is shown in the figure. The internal division based on length is selected as the meshing form. The movable iron core and the magnetic conductor are our key observation objects for the magnetic ring. The meshing of the model is shown in Figure 2b. The free meshing method

is adopted to mesh the solenoid valve. The meshing density of magnetically conductive material should be larger to improve the simulation accuracy, which is set to 0.5 mm. The meshing division of other non-magnetic materials, such as the solution domain, can reduce the accuracy to improve the simulation efficiency, which is set to the system calculation value of 1.5 mm.

In modeling of magnetic induction intensity, the excitation source, material permeability, coercive force of the permanent magnet, and motion parameters of fixed components in the model are considered core factors. The vectors have only one component in the Z-direction. The v needs to be set to 0 in the transient solution. Because the moving components have now been fixed to their own coordinate system, the partial time derivative becomes the total time derivative of $\boldsymbol{A}$. The time-dependent magnetic equation is expressed as

$$\nabla \times v\nabla \times \boldsymbol{A} = \boldsymbol{J_s} - \sigma\frac{d\boldsymbol{A}}{dt} - \sigma\nabla\boldsymbol{V} + \nabla \times H_C \tag{5}$$

where H_c is the coercivity of the permanent magnet, v is the velocity of the moving parts, $\boldsymbol{A}$ is the magnetic vector potential, $\boldsymbol{V}$ is the electric potential, σ is the reluctance, and $\boldsymbol{J_s}$ is the current source density.

Then, the electromagnetic force is solved by using the Maxwell stress tensor, and the equation is expressed as

$$T_{ij} \equiv \varepsilon_0(E_iE_j - \frac{1}{2}\delta_{ij}E^2) + \frac{1}{\mu_0}(B_iB_j - \frac{1}{2}\delta_{ij}B^2) \tag{6}$$

where $\boldsymbol{T}$ is the stress tensor, $\boldsymbol{E}$ is the electric field, $\boldsymbol{B}$ is the magnetic field, ε_0 is the electric constant, μ_0 is the magnetic constant, and δ_{ij} is the Kronecker function.

The force density flow is obtained by calculating the inner product of $\boldsymbol{T}$ and ∇. The equation is expressed as

$$(\nabla \cdot \overleftrightarrow{\boldsymbol{T}})_j = \varepsilon_0[(\nabla \cdot \boldsymbol{E})E_j + (\boldsymbol{E} \cdot \nabla)E_j - \frac{1}{2}\nabla_j E^2] + \frac{1}{\mu_0}[(\nabla \cdot \boldsymbol{B})B_j + (\boldsymbol{B} \cdot \nabla)B_j - \frac{1}{2}\nabla_j B^2] \tag{7}$$

Equation (8) integrates over the full space. The electromagnetic force calculation equation is expressed as

$$\boldsymbol{F} = \iint_S \overleftrightarrow{\boldsymbol{T}} d\boldsymbol{a} \tag{8}$$

where $\boldsymbol{F}$ is the electromagnetic force on the moving iron core.

3. Design and Development of Measurement Platform

The leading indicators to measure dynamic response characteristics of solenoid valve include electromagnetic force, response time, and magnetic field strength. There are many solenoid valves with different functional types and structural dimensions in the industrial field. It is difficult for the existing detection devices to meet the current requirements for the universal measurement of solenoid valves. In order to meet the detection requirements of micro-miniature solenoid valves, a detection platform for the dynamic response characteristics of solenoid valves was designed and developed based on the principle of highly universal measurements. The platform is shown in Figure 3.

Figure 3a shows the schematic diagram of the electromagnetic force measurement platform. The electromagnetic force measurement is mainly based on the resistance strain gauge sensor. The strain effect reflects the electromagnetic force. It has the advantages of high resolution and tiny errors. It is suitable for static and fast alternating stress measurement. At the same time, the centering adjustment structure of the solenoid valve and the dynamometer are set to reduce the measurement error, which can realize the center alignment of the moving iron core and the dynamometer. The connector wire selects high-performance fibers with low elastic modulus to reduce the influence of the deformation of the connecting line on the measuring force. The moving iron core is connected with

the digital display force-measuring instrument through the connector wire in the actual measurement. The electromagnetic force on the moving iron core is transmitted to the digital display force-measuring instrument through the thin wire during the pull-in process. Finally, data collection and processing will be carried out through a special electromagnetic force acquisition software. The electromagnetic force-measurement device designed can obtain the force curve of the moving iron core in the whole process of moving, and the measurement resolution reaches 0.01 N.

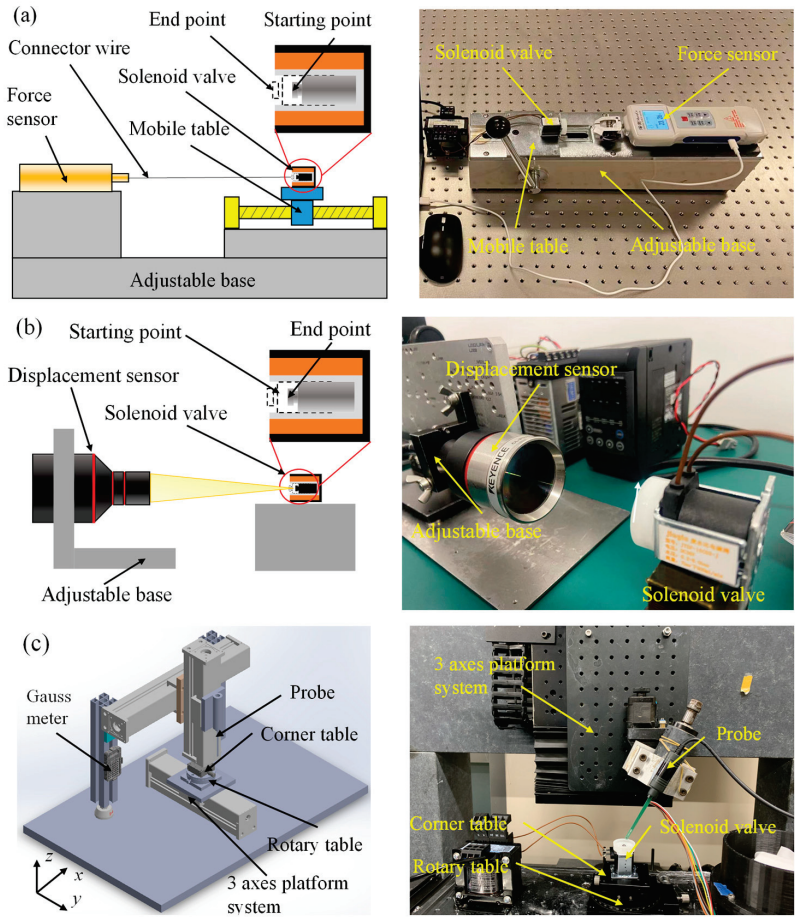

Figure 3. Experimental schematic diagram of measurement platform. (**a**) Electromagnetic force measurement with a measurement accuracy of 0.01 N, (**b**) response time measurement with a resolution of not less than 0.025 μm, and (**c**) magnetic field strength measurement with a measurement accuracy of 0.01 mT.

Currently, the measurement methods of response time mainly include the eddy current method, current-voltage analysis method, and displacement detection method, etc. [19,23]. Nevertheless, there is still a lack of equipment that is easy to implement and reliable in performance. Using the displacement detection method to realize the measurement of response time has high reliability by analyzing technically. The laser-based coaxial displacement sensor has the technical advantages of high sampling frequency and wide measurement range among the high-speed cameras and displacement sensors currently used in displacement measurement. Based on the preliminary design analysis and the design concept of high measurement accuracy and easy operation, the detection platform is settled to base on the coaxial laser displacement detection scheme. Figure 3b shows the response time detection platform designed and developed. The platform uses the Keyence CL-P070 laser color coaxial displacement sensor with good accuracy and an extensive measurement range. The displacement measurement range is ±10 mm, and the resolution is not less than 0.025 μm. It is also equipped with a self-aligning structure to reduce errors.

The response time of the solenoid valve is measured by collecting the displacement-time curve between the moving iron core and the laser displacement sensor.

The magnetic field strength is mainly measured by using a Gauss meter. In measuring the magnetic field strength of the solenoid valve, it is difficult for the Gauss meter probe to accurately approach the measurement position since the pipeline where the moving iron core is located is relatively narrow, with the aperture usually narrower than 1 cm. For this reason, a rigid and precise measuring platform must be developed. In order to measure the magnetic field strength of the solenoid valve, a detection platform for the magnetic induction strength of the solenoid valve is developed, as shown in Figure 3c. The detection platform mainly has manual and automatic control functions. The motion accuracy is less than or equal to 0.05 mm. Furthermore, a C-axis precision turntable and an angle stage are designed on the worktable, which can flexibly and accurately adjust the position of the solenoid valve and expand the measurement range of the Gauss meter. The gaussmeter probe is used to perform fixed-point detection on the solenoid valve in the state of power in the actual measurement. The magnetic field strength of the measurement position is output through the measurement software.

4. Results and Discussion

4.1. Simulation Results

In order to better explore the influence of the position of the MIR on the electromagnetic force curve and response time, a single-term rectifier circuit in the simulation work was added based on the constant model. The internal circuit resistance was reduced. The influence law of the MIR's position on the solenoid valve's dynamic response characteristics is revealed more intuitively. As shown in Figure 2b, the red part is the MIR. The position of the MIR in Figure 2b is set as the zero-point x_0 (x_z = 0 mm), and the position of the MIR is adjusted along the direction of the *Z*-axis. The effects of different MIR positions on the solenoid valve's response time t and the electromagnetic force are investigated by simulation.

The moving distance of the MIR relative to the initial position is defined as x_z, the time from turning on the power supply to the moving iron core reaching the working position is defined as the response time t, and the electromagnetic force received by the moving iron core after the suction is defined as f. The relationship between the position of the MIR, the response time, and the electromagnetic force are shown in Table 2. With the positive change in the position of the MIR, the response time of the solenoid valves, the electromagnetic force, and the displacement of the MIR do not have a linear relationship. However, there is an optimal position interval that takes both into account. With the positive increase of x_z, the electromagnetic force increases and then decreases, and the maximum value is 1.416 N. The response time gradually increases. The response time decreases first and then increases, and the minimum value is 13.0 ms.

Table 2. Electromagnetic force and response time at different MIR positions.

x_z/mm	t/ms	f/N
−3.0	14.0	0.503
−2.5	13.6	0.614
−2.0	13.2	0.747
−1.5	13.0	0.925
−1.0	13.6	1.023
−0.5	14.4	1.077
0	15.2	1.115
0.5	16.6	1.293
1.0	18.2	1.368
1.5	21.4	1.416
2.0	24.4	1.294
2.5	28.2	1.292
3.0	32.0	1.203

When the position of the MIR is within 1.5 mm, the electromagnetic force when the armature is pulled in reaches the highest level, and then, the magnitude of the electromagnetic force begins to decrease gradually. When the position of the MIR is within −1.5 mm, the valve has the shortest response time. The MIR continued to be moved down, increasing the response time slowly.

4.2. Experimental Verification

In order to verify the accuracy of the simulation model, a model verification study was carried out using the existing AC solenoid valve models based on the measurement platforms mentioned in Section 3. The AC solenoid valve with the MIR located at 0.5 mm was measured. The measured resistance value of the solenoid valve coil is 1378 Ω. The circuit in the experiment uses a simplified circuit without diodes. According to the requirements of the experimental conditions, an additional simulation of the solenoid valve selected in the experiment is carried out to verify the validity of the simulation model.

The measurement results show that when the moving iron core stroke reaches the end position, the electromagnetic force is 0.37 N, and the error compared with the simulation results is only 14.10%. The simulation results are in good agreement with the experimental results, and the simulation error is kept within 10%. The experimental results of the response time are shown in Figure 4. The test results record the displacement process of the moving iron core from the initial position to the end position as well as the start time and end time. The calculated response time is 63 ms. Compared with the simulation result of 59 ms, the error is only 6.35%. The magnetic induction intensity is measured on the top right corner of the magnetic guide plate, and the measurement result is 1.64 mT. The simulation results show that the magnetic induction intensity is 1.52 mT, and the simulation error is only 7.31%.

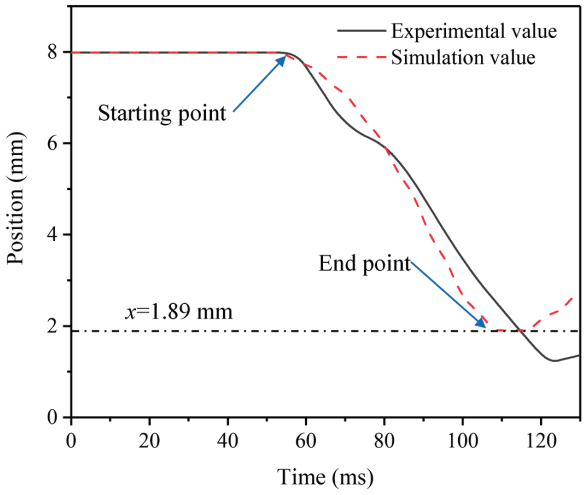

Figure 4. Measurement results of response time.

The dynamic response performances of the AC solenoid valve were measured by using the corresponding measurement platforms. The experimental results are in good agreement with the simulation results. The simulation error is generally stable at about 10%, which verifies the accuracy of the simulation model. On the other hand, the experimental verification further proves that the developed dynamic response characteristic measurement platforms have the excellent capability.

4.3. Effect of MIR Position on Electromagnetic Force and Response Time

In order to clarify the dynamic response performance of the solenoid valves, it is necessary to explore the dynamic change process of the electromagnetic force and the position of the movable iron core during the pull-in process of the movable iron core.

Therefore, the simulation method is used to analyze the dynamic response process of the solenoid valves.

Figure 5 shows the electromagnetic force dynamic change curves of the AC solenoid valve at different MIR positions. The fluctuation of the electromagnetic force comes from the excitation of the AC power supply. The electromagnetic force's magnitude and trend remain stable after 25 ms. The changing trend of the solenoid valve is essentially caused by the regulation of the magnetic circuit in the air gap by the spacer ring. When the MIR position $x_z < 0$ mm, a large electromagnetic force response is obtained in the initial stage, but the average electromagnetic force is low. At $x_z = -3$ mm, the subsequent electromagnetic force is even significantly lower than the initial response electromagnetic force. Conversely, the initial response electromagnetic force becomes weaker and weaker as x_z increases positively. Especially at $x_z = 3$ mm, the electromagnetic force basically has no obvious response in the first 25 ms. It is obvious that x_z has better performance in the (-1 mm, 1 mm) interval, the electromagnetic force response is faster, and the value of the force is also larger.

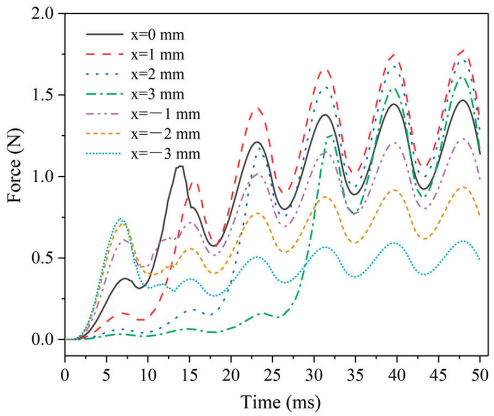

Figure 5. Electromagnetic force dynamic change curves at different positions of MIR.

Figure 6 shows the dynamic displacement curves of moving iron core at different MIR positions. When the MIR position $x_z < 0$ mm, the moving iron core displacement curve has little change, and the response performance is better. The response dynamic process and time are basically unchanged, and the experimental results can also be confirmed from the data in Table 2. Subsequently, with the increase of x_z, the time required for displacement becomes larger and larger, and the moving speed of the moving iron core becomes more slowly. Even at $x_z = -3$ mm, the time required for displacement reaches 32 s, and the displacement time is higher than two times the shortest. The electromagnetic force mainly limits the displacement time on the moving iron core.

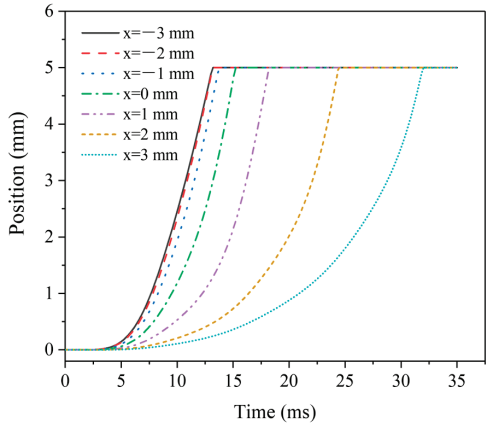

Figure 6. Dynamic displacement curves of MIR at different positions.

4.4. Effect of MIR on Magnetic Field Intensity and Distribution of Magnetic Force Lines

In order to explore the effect of MIR's position on electromagnetic force and response time, the size and distribution of the magnetic induction intensity of this model were studied. The simulation results are shown in Figure 7. There is no doubt that the position of the MIR has a significant effect on the magnetic field distribution inside the solenoid valve.

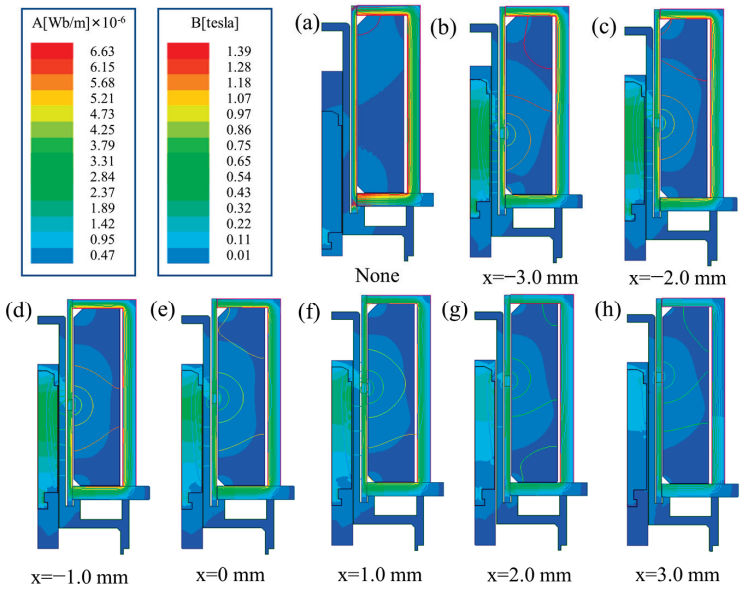

Figure 7. The distribution of the magnetic induction intensity at (**a**) without MIR and MIR's position at (**b**) −3 mm, (**c**) −2 mm, (**d**) −1 mm, (**e**) 0 mm, (**f**) 1 mm, (**g**) 2 mm, (**h**) 3 mm.

As the position of the MIR moves from bottom to top, the maximum magnetic induction intensity area gradually changes from the upper section of the magnetic guide sleeve to the lower end, and the peak value of the magnetic induction intensity generally shows a downward trend. The change of the MIR's position can affect the change of the magnetic induction intensity in the valve body. It affects the response time of the solenoid valve, and the electromagnetic force after the moving iron core is attracted.

During the design process, the solenoid force of the solenoid valve is calculated according to the following Formula (9):

$$F = \frac{1}{2\mu_0} B_0^2 S_0 \times 10^6 \tag{9}$$

where F is the electromagnetic force, μ_0 is the air permeability, B_0 is the magnetic field intensity in the air gap, and S_0 is the gap area. It is evident that under the structure of the solenoid valve is unchanged, the size of the magnetic force is proportional to the square of the magnetic induction strength in the air gap. The role of the MIR is mainly manifested in the change of the magnetic path.

As shown in Figure 7a, in the absence of the MIR, the magnetic field forms a loop in the conductive sleeve and cannot produce an excellent magnetic field effect in the air gap. As shown in Figure 7b–h, the magnetic line near the MIR is the strongest. The magnetic field strength is higher where the magnetic lines are dense. With the positive movement of the position of the MIR, the dense area of magnetic field lines gradually approaches the air gap position. The strength of the magnetic field in the air gap increases, and the electromagnetic force on the moving iron core also increases. However, when the moving iron core exceeds a specific limit, the effect on the moving iron core is weakened to a certain extent, and the strength of the air gap magnetic field is relatively weakened. Therefore, it can be obtained from the simulation results that MIR's position is affected by changing the magnetic circuit to affect the dynamic response characteristics of the solenoid valves.

4.5. Optimized Design for Dynamic Response Performances

As shown in Figure 8, the electromagnetic force is the largest when x_z is 1.5 mm. However, the optimal response time value occurs when x_z is −1.5 mm. When x_z is greater than this position, the response time gradually increases, and the rate increases continuously. Finally, the two gradually tend to be linear. Through analysis, a reasonable selection interval is obtained. This position interval is (−1.5 mm, 1.5 mm). Within this interval, the two performance parameters have the same trend with the increase of MIR position. The ability of the solenoid valve to respond quickly to overcome the electromagnetic force is worse when the electromagnetic force increases.

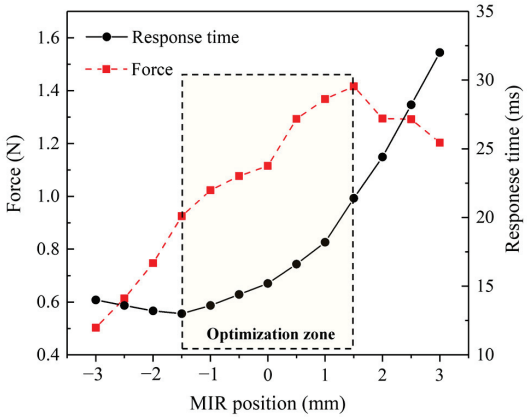

Figure 8. Variation curve of electromagnetic force and response time with MIR.

The position of the MIR can affect the magnitude of the electromagnetic force and the response time of the armature at the same time. The effects on the two aspects are conflicting. In general, too high an electromagnetic force can seriously inhibit the optimization of response time. It is always expected to obtain a larger electromagnetic force and a faster response time in practical production applications. A reasonable trade-off between the two is required when the two cannot be satisfied simultaneously. In the case where the application environment of the solenoid valve requires a faster response time, and the electromagnetic force is not strictly required, the optimization design parameter is where the MIR position x_z is −1.5 mm. The response time can reach 13 ms. In contrast, the maximum electromagnetic force can be obtained at the MIR position of 1.5 mm; i.e., the electromagnetic force can be greater than 1.4 N. This method can provide certain theoretical guiding significance for the optimization of the solenoid valves.

5. Conclusions

In this paper, the optimization design of MIR position in AC solenoid valves for the dynamic response performance based on a performance-oriented design idea is emphasized. A model of an AC solenoid valve considering the MIR is proposed and established. A series of innovative measurement platforms were developed to detect dynamic response characteristics. The electromagnetic force, response time, and magnetic field strength of the AC solenoid valve are measured by using the developed platform. The influence law of the dynamic response characteristics of the AC solenoid valve is explored and clarified. Finally, the performance-oriented solenoid valve optimization design is realized. The results obtained are summarized as follows:

(1) Through the experimental verification of the developed detection platform, the error rate of the proposed AC solenoid valve simulation model is generally stable at about 10%, which meets the accuracy requirements of the solenoid valve structure optimization.
(2) The electromagnetic force affected after armature absorption increases first and then decreases with the increase of x_z position and reaches the maximum value

at x_z = 1.5 mm and F_{max} = 1.416 N. Response time decreased first and then increased and reached a minimum at $x_z = -1.5$ mm, with t_{min} = 13.0 ms.

(3) The position of the magnetic partition ring changes the distribution of the magnetic path in the solenoid valve and then changes the magnetic flux in the air gap, thus affecting the dynamic response characteristics.

(4) The solenoid valve used in this study is an example, the optimal interval of the magnetic ring position is (−1.5 mm, +1.5 mm), in which the solenoid valve has a relatively balanced dynamic response characteristic.

In the subsequent research work, based on the proposed solenoid valve simulation model, the multi-objective parameter optimization of the solenoid valve combined with intelligent algorithms will better realize the high-performance design and manufacture.

Author Contributions: Conceptualization, J.G. and J.T.; methodology, J.G.; writing original draft, formal analysis, L.L. and P.Q.; validation, J.W., C.N. and X.Z.; writing—review and editing, J.G.; supervision, J.T.; funding acquisition, D.L. All authors have read and agreed to the published version of the manuscript.

Funding: This research was funded by the National Natural Science Foundation of China, grant number 51975096.

Conflicts of Interest: The authors declare no conflict of interest.

References

1. Murakami, T.; Kuwajima, Y.; Wiranata, A.; Minaminosono, A.; Shigemune, H.; Mao, Z.-B.; Maeda, S. A DIY fabrication approach for ultra-thin focus-tunable liquid lens using electrohydrodynamic pump. *Micromachines* **2021**, *12*, 1452. [CrossRef] [PubMed]
2. Bammesberger, S.B.; Kartmann, S.; Tanguy, L.; Liang, D.; Mutschler, K.; Ernst, A.; Zengerle, R.; Koltay, P. A low-cost, normally closed, solenoid valve for non-contact dispensing in the sub-µl range. *Micromachines* **2013**, *4*, 9–21. [CrossRef]
3. Kartmann, S.; Koltay, P.; Zengerle, R.; Ernst, A. A disposable dispensing valve for non-contact microliter applications in a 96-well plate format. *Micromachines* **2015**, *6*, 423–436. [CrossRef]
4. Zhang, Q.; Zhang, P.-R.; Su, Y.-T.; Mou, C.-B.; Zhou, T.; Yang, M.-L.; Xu, J.; Ma, B. On-demand control of microfluidic flow via capillary-tuned solenoid microvalve suction. *Lab. Chip.* **2014**, *14*, 4599–4603. [CrossRef] [PubMed]
5. Yang, M.-S. Study on dynamic and static performance of a micro digital hydraulic valve. *Micromachines* **2022**, *13*, 741. [CrossRef]
6. Wang, S.-M.; Miyano, T.; Hubbard, M. Electromagnetic field analysis and dynamic simulation of a two-valve solenoid actuator. *IEEE Trans. Magn.* **1993**, *29*, 1741–1746. [CrossRef]
7. Cai, B.-P.; Liu, Y.-H.; Tian, X.-J.; Wang, Z.-L.; Wang, F.; Li, H.; Ji, R.-J. Optimization of Submersible Solenoid Valves for Subsea Blowout Preventers. *IEEE Trans. Magn.* **2011**, *47*, 451–458. [CrossRef]
8. Liu, Q.-F.; Bo, H.-L.; Qin, B.-K. Optimization of direct-action solenoid valve based on CloudPSO. *Ann. Nucl. Energy.* **2013**, *53*, 299–308. [CrossRef]
9. Diao, K.; Sun, X.; Lei, G.; Guo, Y.; Zhu, J. Multi-objective system level optimization method for switched reluctance motor drive systems using finite-element model. *IEEE Trans. Ind. Electron.* **2020**, *67*, 10055–10064. [CrossRef]
10. Santos, G.D.; Sass, F.; Sotelo, G.G.; Fajoni, F.; Baldan, C.A.; Ruppert, E. Multi-objective optimization for the superconducting bias coil of a saturated iron core fault current limiter using the t-a formulation. *Supercond. Sci. Technol.* **2021**, *34*, 025012. [CrossRef]
11. Xu, B.; Shen, J.; Liu, S.-H.; Su, Q.; Zhang, J.-H. Research and development of electro-hydraulic control valves oriented to Industry 4.0: A review. *Chin. J. Mech. Eng.* **2020**, *33*, 13–32. [CrossRef]
12. Shukla, V.; Vaghela, H.; Madeenavalli, S.; Dash, B.R.; Garg, A. Effect of magnetic field environment on the performance of 3/2 solenoid valve. *Fusion. Eng. Des.* **2020**, *156*, 111618. [CrossRef]
13. Subic, A.; Cvetkovic, D. Virtual design and development of compact fast-acting fuel injector solenoid actuator. *Int. J. Veh. Des.* **2008**, *46*, 309–327. [CrossRef]
14. Hung, N.B.; Lim, O.; Yoon, S. Effects of Structural Parameters on Operating Characteristics of a Solenoid Injector. *Energy Procedia* **2017**, *105*, 1771–1775. [CrossRef]
15. Grekhov, L.; Zhao, J.; Ma, X. Fast-Response solenoid actuator computational dimulation for engine fuel systems. In Proceedings of the 2017 International Conference on Industrial Engineering, Applications and Manufacturing (ICIEAM), Nagoya, Japan, 21 April 2017.
16. Liu, P.; Fan, L.-Y.; Hayat, Q.; Xu, D.; Ma, X.-Z.; Song, E.-Z. Research on key factors and their interaction effects of electromagnetic force of high-speed solenoid valve. *Sci. World J.* **2014**, *8*, 567242. [CrossRef] [PubMed]
17. Hung, N.B.; Lim, O. Improvement of electromagnetic force and dynamic response of a solenoid injector based on the effects of key parameters. *Int. J. Automot. Technol.* **2019**, *20*, 949–960. [CrossRef]
18. Yang, M.; Zhang, J.; Xu, B. Experimental study and simulation analysis on electromagnetic characteristics and dynamic response of a new miniature digital valve. *Adv. Mater. Sci. Eng.* **2018**, *2018*, 2378576. [CrossRef]

19. Zhao, J.; Yue, P.; Wei, K. Eddy current effects on the dynamic response of high-speed solenoid valve for common rail injector. *Int. J. Appl. Electromagn. Mech.* **2020**, *62*, 607–618. [CrossRef]
20. Liao, Y.-Y.; Lian, Z.-S.; Yuan, H.-B.; Feng, J.-L.; Cui, H.-W. Optimization of an intrinsically safe solenoid valve and the static and dynamic characteristics. *Int. J. Appl. Electromagn. Mech.* **2019**, *61*, 111–122. [CrossRef]
21. Guo, D.-M. High-performance precision manufacturing. *China Mech. Eng.* **2018**, *29*, 757–765.
22. Cao, J.-N.; Liu, J.; Yang, Y. Impact characteristics study on electromagnet magnetic isolation ring to electromagnetic force. *Appl. Mech. Mater.* **2012**, *201–202*, 635–639. [CrossRef]
23. Zhang, X.; Lu, Y.; Li, Y.; Zhang, C.; Wang, R. Numerical calculation and experimental study on response characteristics of pneumatic solenoid valves. *Meas. Control* **2019**, *52*, 1382–1393. [CrossRef]

micromachines

MDPI

Article

Design and Optimization of a Micron-Scale Magnetoelectric Antenna Based on Acoustic Excitation

Na Li *, Xiangyang Li, Bonan Xu, Bin Zheng and Pengchao Zhao

Key Laboratory of Electronic Equipment Structure Design, Ministry of Education, Xidian University, Xi'an 710071, China

* Correspondence: lina@mail.xidian.edu.cn

Abstract: The development of antenna miniaturization technology is limited by the principle of electromagnetic radiation. In this paper, the structure size of the antenna is reduced by nearly two orders of magnitude by using Acoustic excitation instead of electromagnetic radiation. For this magnetoelectric (ME) antenna, the design, simulation and experiment were introduced. Firstly, the basic design theory of magnetoelectric antennas has been refined on a Maxwell's equations basis, and the structure of the ME antenna is designed by using the Mason equivalent circuit model. The influence mechanism of structure on antenna performance is studied by model simulation. In order to verify the correctness of the proposed design scheme, an antenna sample operating at 2.45 GHz was fabricated and tested. The gain measured is −15.59 dB, which is better than the latest research that has been reported so far. Therefore, the ME antenna is expected to provide an effective new scheme for antenna miniaturization technology.

Keywords: antenna miniaturization; ME antenna; mason equivalent circuit model; finite element simulation; high gain

Citation: Li, N.; Li, X.; Xu, B.; Zheng, B.; Zhao, P. Design and Optimization of a Micron-Scale Magnetoelectric Antenna Based on Acoustic Excitation. *Micromachines* **2022**, *13*, 1584. https://doi.org/10.3390/mi13101584

Academic Editors: Seung-bok Choi and Viktor Sverdlov

Received: 27 July 2022
Accepted: 15 September 2022
Published: 23 September 2022

Copyright: © 2022 by the authors. Licensee MDPI, Basel, Switzerland. This article is an open access article distributed under the terms and conditions of the Creative Commons Attribution (CC BY) license (https://creativecommons.org/licenses/by/4.0/).

1. Introduction

In recent years, with the rapid development of communication equipment miniaturization, most electronic components have achieved miniaturization. However, the size of an electrically small antenna is still larger than 1/10 of the working wavelength [1–3]. What is worse, the impedance matching is difficult, and the radiation efficiency is very low. The core reason is that the traditional small antenna is based on the working principle of the conduction current. Therefore, the inherent ohmic loss of the conduction current results in a reduction in the radiation efficiency. It suffers the platform effect when it is close to the conductive plane, the radiation Q value will increase and the antenna is difficult to match with the impedance [4,5]. Different from the traditional small antenna, the radiation time-varying field of the ME antenna is generated by rotating or oscillating an electric/magnetic dipole moment [6–8]. It not only overcomes the ohmic loss but also has a very high-quality factor. It converts the magnetic component of an electromagnetic wave into an acoustic wave and outputs it as a voltage. In turn, the piezoelectric material is voltage-driven to produce strain, which is then transmitted to the magnetic material, triggering it to magnetize and oscillate, and eventually radiates electromagnetic waves [9–11]. Based on the working principle of acoustic excitation, the advantages of the ME antenna are: (1) the size of the ME antenna can be reduced to 1/10 or even 1/100 of the size of the traditional small antenna, because the speed of sound waves compared to the speed of electromagnetic waves about five orders of magnitude slower. (2) It radiates without the conduction of an electric current; thus, it solves the problem of low radiation efficiency. (3) Its impedance can be adjusted by changing the sizes of the magnetic and the piezoelectric layers. There is no need to add an external matching network, which solves the problem of impedance matching.

Research of the ME antenna originated from the thin-film composite ME materials [8,12–16]. Greve used MEMS technology to fabricate a cantilever structure by integrating alnfecosib

magneto-electromechanical composite thin films onto a silicon substrate and obtained a ME coupling coefficient of up to 737 V/cm·Oe at a resonant frequency that was 200 times higher than that under non-resonant conditions [17]. However, the further improvement of the magnetoelectric coupling coefficient is limited by the influence of air damping, and the higher the resonant frequency of the antenna, the more significant the damping effect is. Subsequently, the introduction of acoustic resonators solved this problem. On the one hand, the dynamic magnetization of magnetic materials can be excited and controlled by elastic waves based on the magnetoelastic coupling effect. On the other hand, the mechanical energy can be confined in the piezoelectric layer and the magnetostrictive layer through the design of acoustic impedance. Surface and bulk acoustic resonators have very high-quality factors, which creates the basic conditions for improving the magnetoelectric coupling coefficient and enhancing the practicability of magnetoelectric composites [18,19]. In recent years, Yao et al. systematically studied the (bulk acoustic wave) BAW ME antenna by using the finite difference time domain (FDTD) method and, firstly, coupled the Maxwell's equation and Newton's equation by using the constitutive relationship of ME materials and constructed a complete mathematical model of the energy, average radiated power and radiated quality factor of the ME antenna [6]. Later, Yao generalized it to the 3D case but only in a simulation [20,21]. Domann et al. further proposed the concept of a strain-powered (SP) antenna and established an electrodynamic analytical model to describe the mechanical coupling of EM radiation of the SP antenna [7]. Nan et al. of Northeastern University (NEU) proposed a nanoelectromechanical system (NEMS) ME antenna excited by acoustic waves [8]. There are two structures: a nanoplate resonator (NPR) and thin-film bulk acoustic resonator (FBAR). However, both of them have the problems of low gain and a narrow bandwidth. Lin further proposed a ME antenna with high magnetic field sensitivity and high gain based on Nan [22]. Schneider et al. further experimentally demonstrated the working principle of near-field multiferroic antennas, and they mainly studied the near field of ME antennas and were not involved the far field [23]. Zaeimbashi proposed a novel ultra-miniaturized wireless implantable device, Nano Neuro RFID (Radio Frequency Identification) [24]. The core of this device is a NPR ME antenna array. They just put forward this design concept and did not really manufacture it, let alone carry out test experiments. Dong et al. applied ME antenna to VLF (Very Low Frequency, 3–30 KHz) [25], and they conducted the near-field testing, not far-field testing. Niu et al. studied a miniaturized low-frequency ME receiving antenna with integrated DC bias, which can achieve a higher performance than existing antennas without a DC bias [26], but they only studied the reception of the antenna, not the transmission of the antenna. Kevin used the Landau–Lifshitz–Gilbert (LLG) equation to accurately analyze the magnetoelastic coupling problem in the ME antenna [27], but they did not consider the spatially dependent electrodynamics governed by Maxwell's equation. Ren et al. demonstrated the possibility of using only one BAW-actuated ME transducer antenna for communication; however, the simulation method in this work cannot be used for modeling the far field of radiation [28]. Aiming at the problem of low gain and narrow bandwidth of the ME antenna, a new design scheme of the ME antenna is proposed in this paper based on the above works. In this paper, we design and test that, similar to the traditional antenna, the receiving and transmitting processes of the ME antenna are reciprocal. We first reviewed the working principle of the ME antenna and deduce the radiation power formula. For the structural design of the ME antenna, the equivalent circuit method was used to design the thickness of the ME antenna at 2.45 GHz. Based on the coupling of electric field, magnetic field and stress field, we used the finite element method (FEM) to simulate and obtain the far-field radiation pattern of the ME antenna. We tested the gain of the ME antenna to be −15.59 dB, which was better than the gain reported recently.

2. The Basic Principle of ME Antenna

The basic principle of the ME antenna is the ME coupling effect, which is the product effect of the piezoelectric effect of piezoelectric materials and the piezomagnetic effect of magnetostrictive materials [29,30].

The working principle is shown in Figure 1. When the antenna transmits EM waves, it applies the RF electric field to the upper and lower sides of the piezoelectric layer of the resonant cavity. The mechanical resonance will generate alternating strain waves, which will then be transmitted to the magnetostrictive layer above.

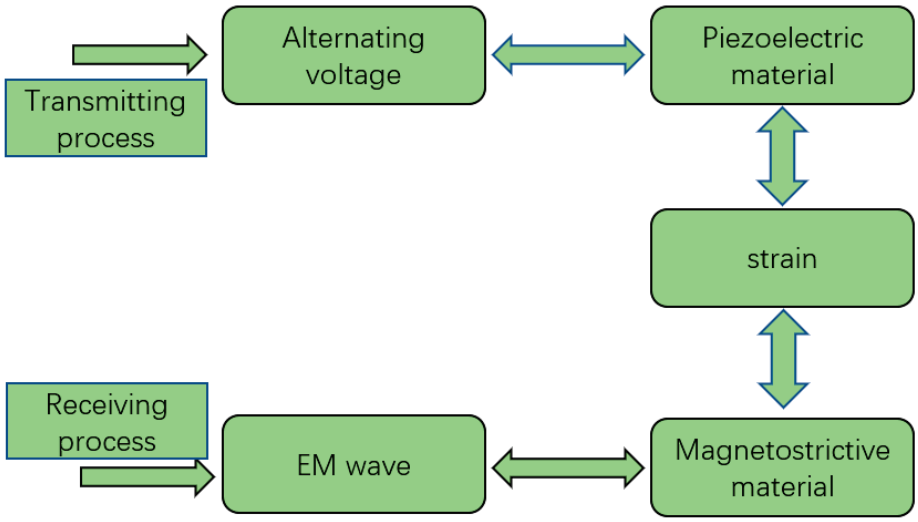

Figure 1. The working principle of the ME antenna.

In the case of the ME antenna, the bulk acoustic resonator utilizes the p-wave mode in the body, and the sound wave propagates along the *Z*-axis. Therefore, under the one-dimensional conditions, the piezoelectric constitutive equation can be rewritten as

$$\begin{aligned} S_E &= s_E T_E + \frac{d_E}{\varepsilon_T} D \\ E &= -\frac{d_E}{\varepsilon_T} T_E + \frac{1}{\varepsilon_T} D \end{aligned} \tag{1}$$

Accordingly, the piezomagnetic constitutive equation can be written as

$$\begin{aligned} S_H &= s_H T_H + \frac{d_H}{\mu_T} B \\ H &= -\frac{d_H}{\mu_T} T_H + \frac{1}{\mu_T} B \end{aligned} \tag{2}$$

where E and H are the electric and magnetic field intensity vectors, respectively, D and B are the electric and magnetic flux density vectors, ε_T and μ_T are the stress-free permittivity of the piezoelectric layer and stress-free permeability of the magnetostrictive layer, respectively, s_E and s_H are the mechanical compliance constants of piezoelectric layer and magnetostrictive layer, respectively and d_E and d_H are the strain constants of the piezoelectric layer and magnetostrictive layer, respectively. S_E and S_H are the strain field in the piezoelectric layer and magnetostrictive layer, respectively. T_E and T_H are the stress field in the piezoelectric layer and magnetostrictive layer, respectively.

The potential energy in the ME antenna is equal to the sum of the potential energy in the piezoelectric and the piezomagnetic layers. The potential energy in the piezoelectric layer mainly includes mechanical energy in the form of mechanical stress and electrical energy in the form of the electric field:

$$\begin{aligned} W_{PE} &= \tfrac{1}{2}\iiint S \cdot T dv + \tfrac{1}{2}\iiint D \cdot E dv \\ W_{PM} &= \tfrac{1}{2}\iiint S \cdot T dv + \tfrac{1}{2}\iiint B \cdot H dv \end{aligned} \tag{3}$$

Due to the open-circuit excitation of the piezoelectric layer ($D = 0$) after the initial current pulse drive and the weak magnetic field condition in the magnetostrictive layer ($H \approx 0$), it can be derived from the second equations in Equations (1) and (2):

$$\begin{array}{c} E = -\frac{d_E}{\varepsilon_T} T_E \\ B = d_H T_H \end{array} \tag{4}$$

The electromechanical and magnetomechanical coupling figures of merit are given by:

$$k_E^2 = \frac{d_E^2}{s_E \varepsilon_T}, \qquad k_H^2 = \frac{d_H^2}{s_H \mu_T} \tag{5}$$

The mechanical compliance in the magnetic layer and piezoelectric layer are:

$$\begin{array}{c} s_B = (1 - k_H^2) s_H \\ s_D = (1 - k_E^2) s_E \end{array} \tag{6}$$

The total energy in the magnetic layer and piezoelectric layer are simplified according to the following:

$$\begin{array}{c} W_{PM} = \frac{1}{2} \iiint S_H \cdot T_H dv + \frac{1}{2} \iiint B \cdot H dv = \frac{1}{2} \iiint s_H {T_H}^2 dv \\ W_{PE} = \frac{1}{2} \iiint S_E \cdot T_E dv + \frac{1}{2} \iiint D \cdot E dv = \frac{1}{2} \iiint s_E \cdot {T_E}^2 dv \end{array} \tag{7}$$

It is assumed that both materials deform at the same time, the strain is equal and the stress is different. The stress in the piezoelectric layer is assumed to be T_1 and the stress in the piezoelectric layer to be T_2, so the potential energy stored in the antenna can be expressed as the total potential stored in the form of mechanical stress:

$$\begin{array}{l} W_P = W_{PE} + W_{PM} = \frac{1}{2} \underset{v_1}{\iiint} s_E T_1^2 dv + \frac{1}{2} \underset{v_2}{\iiint} s_H T_2^2 dv \\ = \frac{A}{2} s_E \underset{z_1}{\int} T_1^2 dz + \frac{A}{2} s_H \underset{z_2}{\int} T_2^2 dz \end{array} \tag{8}$$

The stress field in the piezoelectric layer is $T_1 = nT_0 \sin\left(\frac{2\pi}{\lambda_{ac}} z\right)$, $T_2 = T_0 \sin\left(\frac{2\pi}{\lambda_{ac}} z\right)$, T_0 is the amplitude of the stress field and n is the proportional constant of the stiffness coefficient of the piezoelectric layer and magnetostrictive layer. The device thickness is $d = \frac{\lambda_{ac}}{2}$, and λ_{ac} is the wavelength of the sound waves.

By introducing the known stress field function into the potential energy formula, the total potential energy of the stacked structure magnetoelectric antenna can be calculated. In the process of the ME antenna radiating outward, the piezoelectric layer is the driving source of the stress, while the piezomagnetic layer is the radiation region of the antenna, which is mainly responsible for the radiation of the magnetic field coupled by the stress field. Therefore, the expression of the radiated power of a ME antenna is introduced:

$$P = \frac{1}{2\eta_0} \iint E_0^2 ds \tag{9}$$

In which E_0 is the aperture electric field formed on the surface of the magnetosphere, and η_0 is the free-space wave impedance.

The radiation power formula of the ME antenna is:

$$\begin{array}{l} P = \frac{1}{2\eta_0} \iint E_0^2 ds = \frac{\omega^2 h^2}{2\eta_0} \iint B^2 ds = \frac{\omega^2 h^2 d_H^2}{2\eta_0} \iint T_2^2 ds \\ = \frac{A\omega^2 h^2 d_H^2 T_0}{2\eta_0} \sin^2\left(\frac{2\pi}{\lambda_{ac}} z\right) \end{array} \tag{10}$$

3. Design and Impedance Analysis of ME Antenna

The main structure of the ME antenna designed in this paper is based on a cavity-backed FBAR. The substrate is Si, the bottom electrode material is Mo, the piezoelectric material layer is AlN and the magnetostrictive layer is FeGa (also known as the upper electrode). There is an AlN seed layer between the substrate and the lower electrode, and the specific structure and thickness are shown in Figure 2:

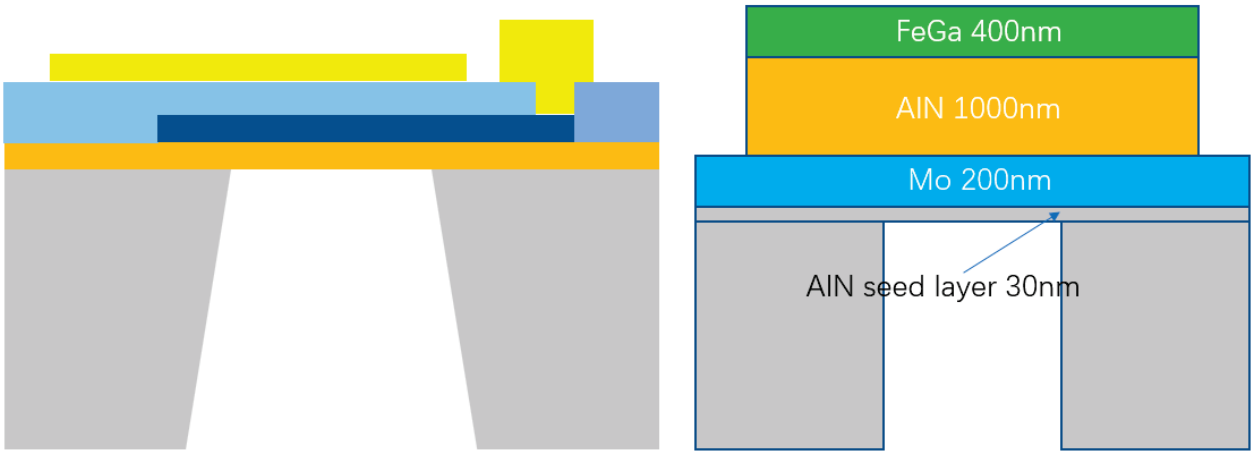

Figure 2. The left is the cavity-backed FBAR; the right is the structure and materials of the ME antenna.

In order to determine the resonant frequency and analyze the impedance characteristics of the ME antenna, the Mason equivalent circuit model is used to design the antenna circuit. At first, the structure size and material properties are equivalent to the circuit parameters, and the Mason equivalent circuit models of the piezoelectric layer, magnetostrictive layer and electrode layer are established, respectively, and then, the actual antenna structure is constructed, as shown in Figure 3.

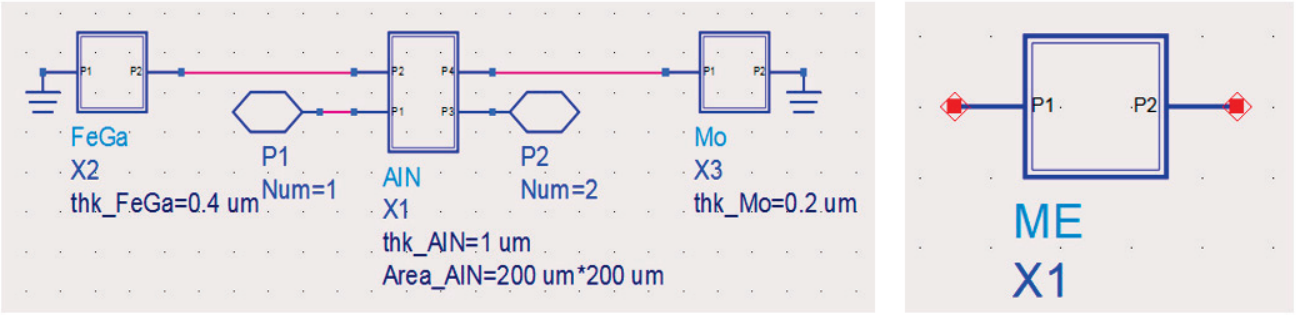

(**a**) (**b**)

Figure 3. (**a**) The cascade diagram of the ME antenna, and (**b**) the ME antenna encapsulation.

The electrical impedance of the antenna can be simulated by the circuit diagram shown in Figure 4, and the results shown in Figure 4a are the amplitude–frequency characteristic curve of the antenna, and Figure 4b is the phase–frequency characteristic of the antenna impedance curve. It can be seen from the simulation results that the ME antenna has two resonance frequencies—namely, the series resonance frequency is 2.305 GHz, and the parallel resonance frequency is 2.36 GHz.

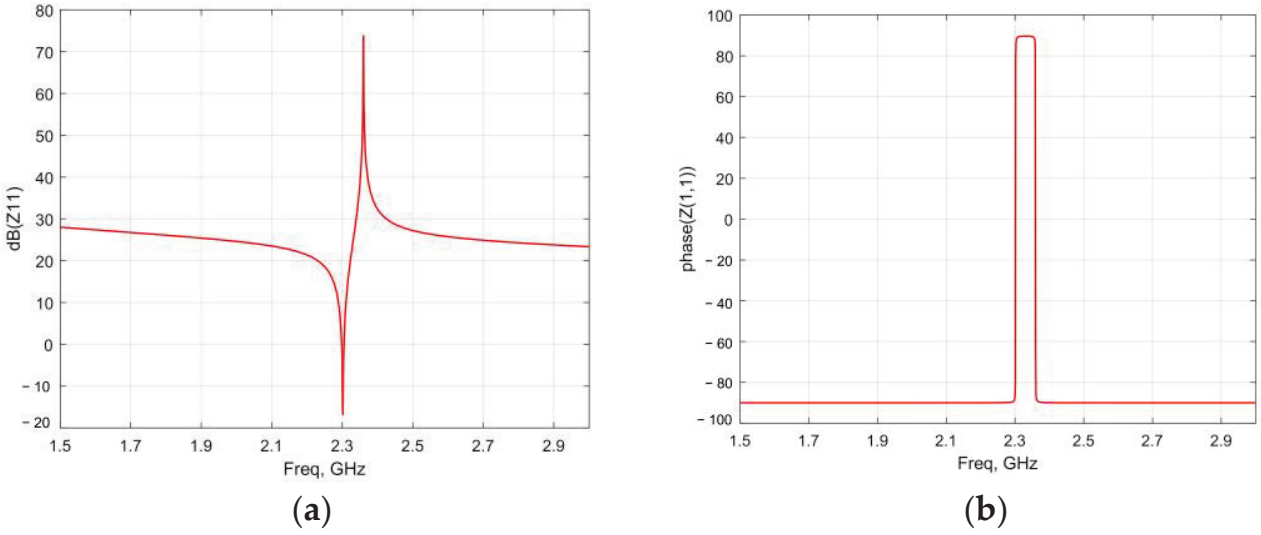

Figure 4. Amplitude (**a**) and phase (**b**) of the antenna impedance.

4. Finite Element Simulation and Performance Analysis of ME Antenna

In the previous section, the effect of the antenna structure size and material properties on the electrical characteristics was simulated by using the Mason equivalent circuit model. In order to further analyze the electromagnetic radiation characteristics of the ME antenna, it is necessary to establish an accurate finite element model. As shown in Figure 5, the radius of the resonance region is 100 um, AlN is used as the piezoelectric material and FeGa is used as the magnetostrictive material.

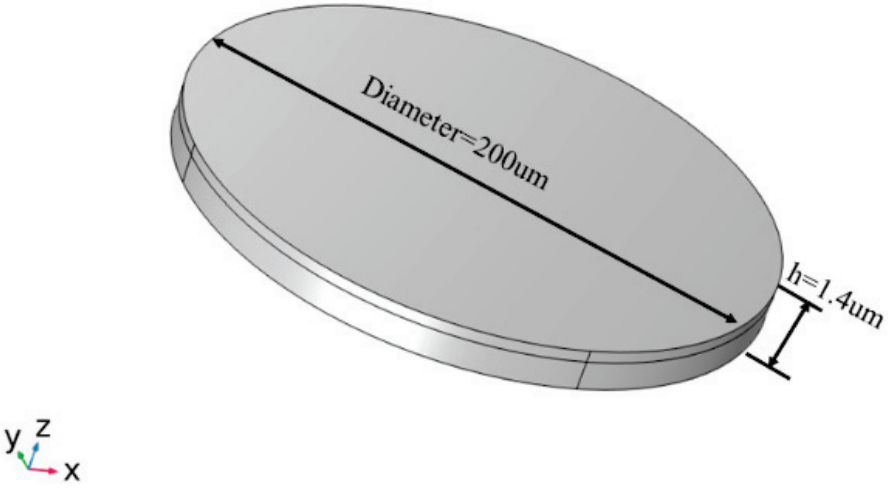

Figure 5. Antenna model.

Firstly, the static approximation method is used to study the spatial distribution of stress, strain, displacement and potential, as shown in Figure 6. It can be seen that the maximum stress and strain occur at the interface between the piezoelectric and the magnetostrictive layers. It can be found that the antenna is greatly deformed in the thickness direction, and the maximum displacement can reach 0.25 μm in Figure 6c. From Figure 6d, it can be found that the voltage amplitude at the boundary is significantly higher than that at the middle position.

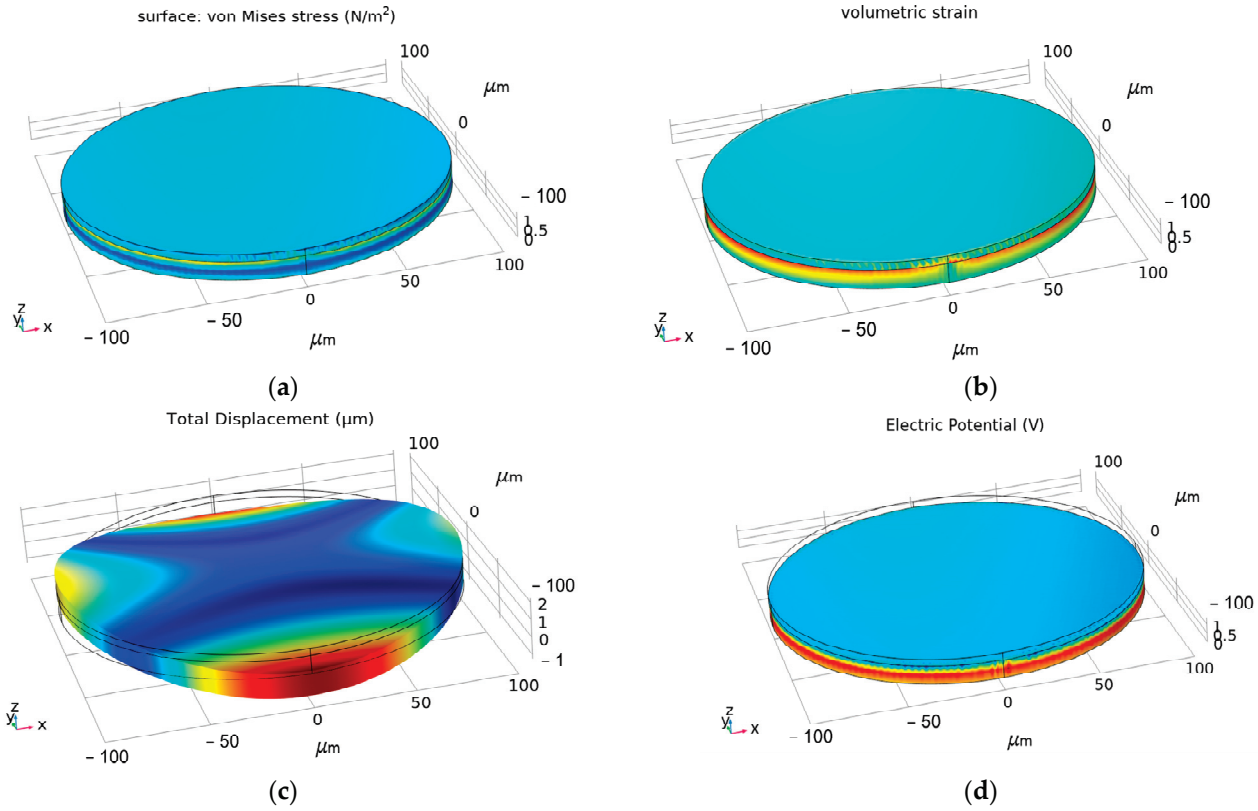

Figure 6. Distribution of the structure and electrical parameters of the ME antenna under a magnetic field. (**a**) Stress, (**b**) strain, (**c**) displacement and (**d**) electric potential.

In order to determine the optimum structural parameters of the antenna, the influence of the structural parameters on the resonant characteristics is analyzed [31].

1. Influence of substrate

For the cavity-backed FBAR structure, the backing is difficult to etch completely during practical machining. Therefore, the influence of the residual substrate thickness on the antenna performance is analyzed. As shown in Figure 7, the resonant frequency of the antenna decreases with the increase of the substrate thickness, because the increase of the substrate thickness directly results in the path of sound wave propagation along the longitudinal direction.

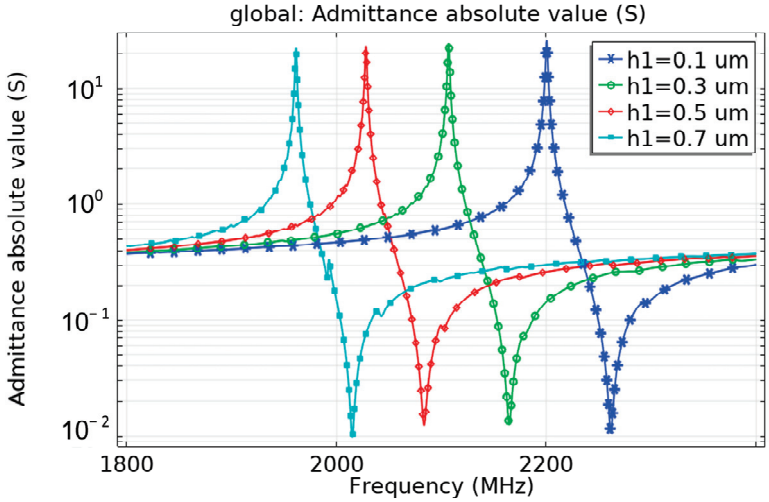

Figure 7. Influence of substrate thickness h on the admittance curve.

When the antenna substrate thickness H1 is increased from 0.1 μM to 0.7 μM, the real part of the information of admittance is analyzed based on the absolute value of admittance. It can be found that, with the increase of the substrate, more parasitic resonances are generated, the performance of the antenna is deteriorated. Therefore the substrate should be etched as cleanly as possible during actual processing to eliminate the clamping effect of the substrate.

2. Influence of electrode size

As shown in Figure 8, the electrode width has no effect on the operating frequency of the ME antenna, while the larger the electrode width is, the larger the admittance value will be. The increase in area results in an increase in the capacitance of the antenna and reduces the overall impedance of the antenna. Therefore, impedance matching can be performed by adjusting the electrode area. In the meantime, increasing the area of the electrode can reduce the parasitic mode, which can reduce the impact of the energy loss of the acoustic leakage on the antenna efficiency.

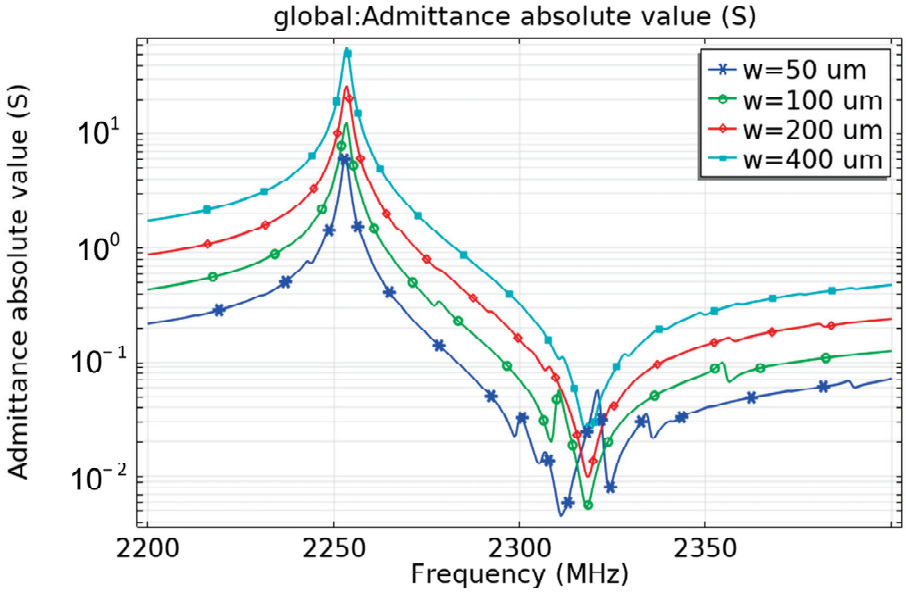

Figure 8. Influence of electrode width on the admittance curve.

3. Influence of electrode shape

In addition to longitudinal resonance, the ME antenna also has transverse parasitic resonance, which can disperse the energy of the main resonance. Therefore, it should be avoided as much as possible. The influence of the electrode shape on parasitic resonance is analyzed in this section. Figure 9 shows a square and a pentagonal electrode. Both of them have the same electrode area, and their admittance curves are shown in Figure 10. It can be seen that the parasitic resonance of the pentagonal electrode is obviously smaller than that of the square electrode. Therefore, the electrode shape of this design is optimized as a pentagonal shape.

Based on the above analysis results, the optimum structural parameters of the magnetoelectric antenna are determined, and the structural model of the magnetoelectric antenna is established. The solid mechanics and low-frequency Maxwell equation are used to calculate the inverse ME effect, and the near-field radiation is obtained. The far-field distribution is shown in Figure 11. In the COMSOL simulation, the input power is set as Pin = 1 W, and it can be calculated that the real gain Greal = 1.93×10^{-13}. Since impedance matching is not considered in the 3D model, the S11 of the resonance point is −0.0183 dB. Excluding the mismatch factor, the radiation efficiency can be calculated to be about 2.55×10^{-11}.

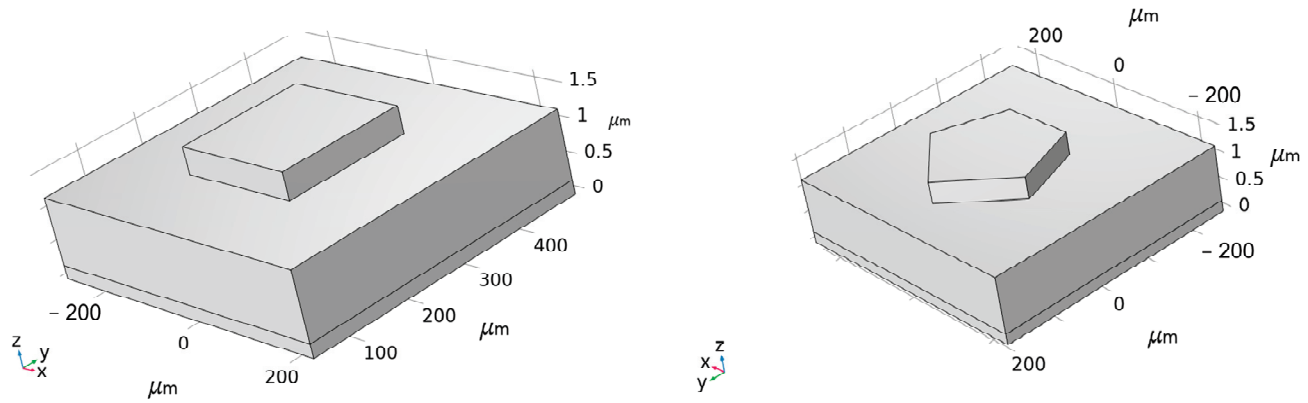

(**a**) (**b**)

Figure 9. Three-dimensional models of different electrode shapes: (**a**) square electrode and (**b**) pentagonal electrode.

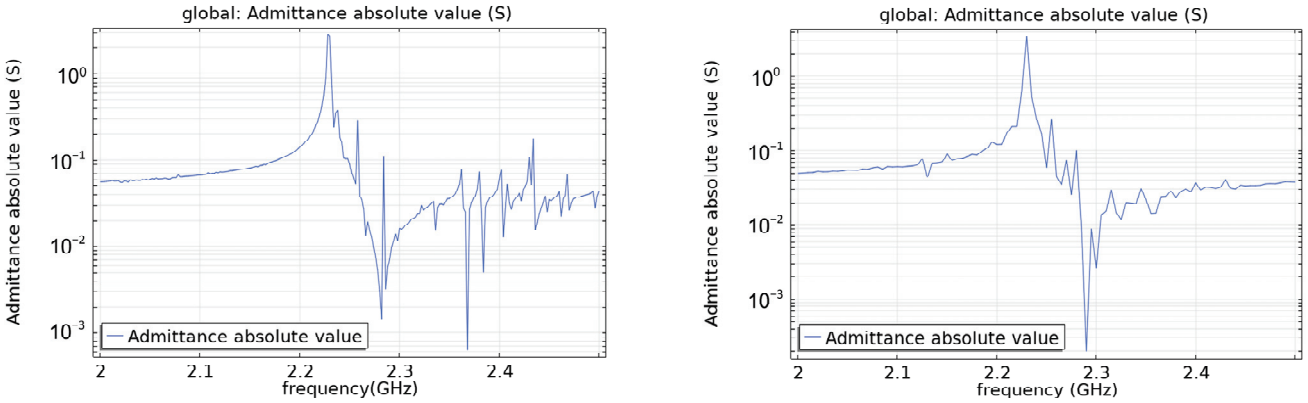

(**a**) (**b**)

Figure 10. Absolute values of admittance for different electrode shapes: (**a**) square electrode and (**b**) pentagonal electrode.

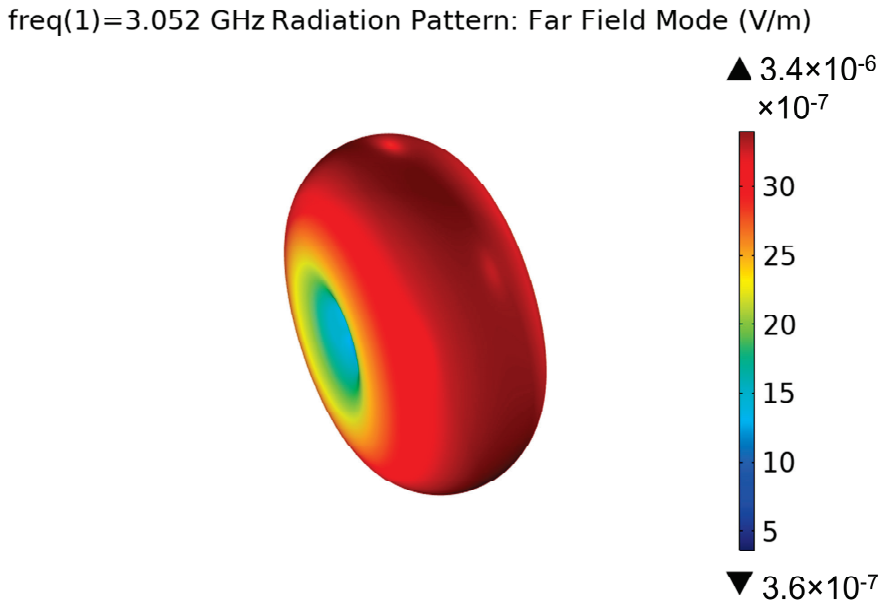

Figure 11. Far-field 3D pattern of the antenna.

5. Fabrication and Testing of Antenna Samples

In order to verify the superiority of the proposed design scheme, a 2.45-GHz antenna sample is fabricated, and its radiation performance is tested. The processing flow is shown in Figure 12.

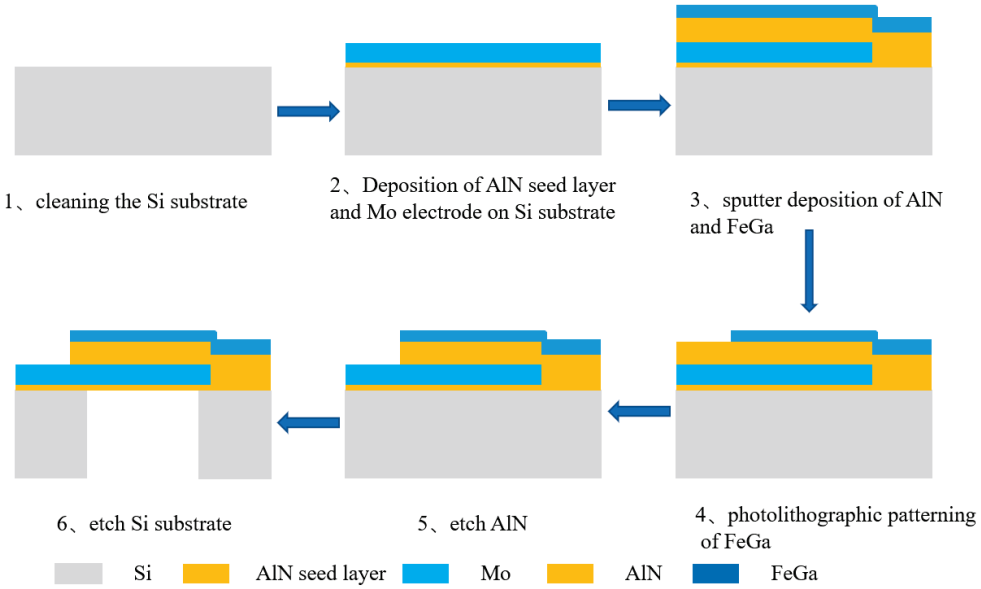

Figure 12. ME antenna preparation process.

The optical image of the ME antenna is shown in Figure 13.

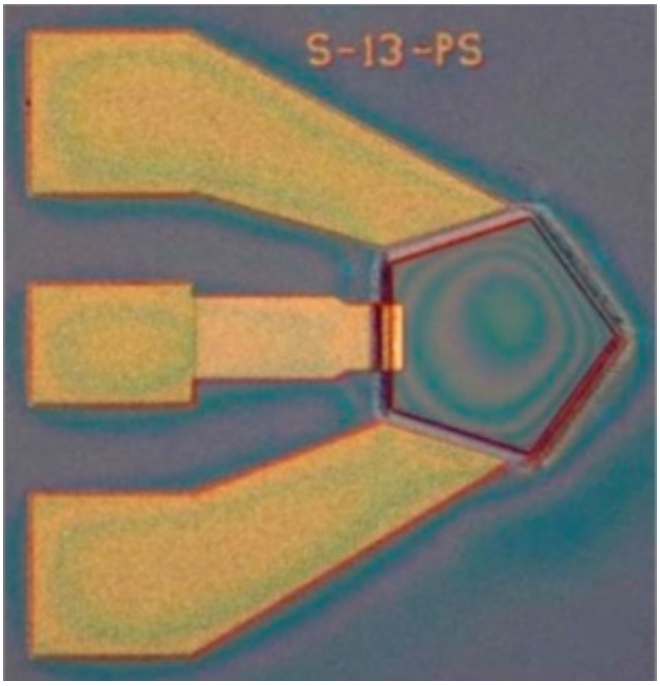

Figure 13. Optical image of the ME antenna.

The test platform is shown in Figure 14.

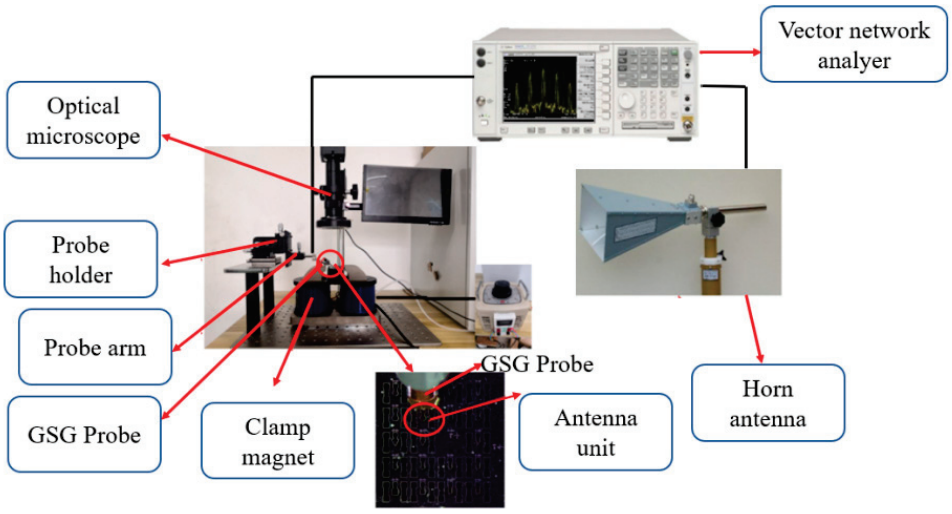

Figure 14. Testing platform.

The reflection coefficient (S11) of the antenna is measured as shown in Figure 15. It can be obtained that the resonant frequency of the antenna is about 2.49 GHz, and the peak return loss is −17.3 dB.

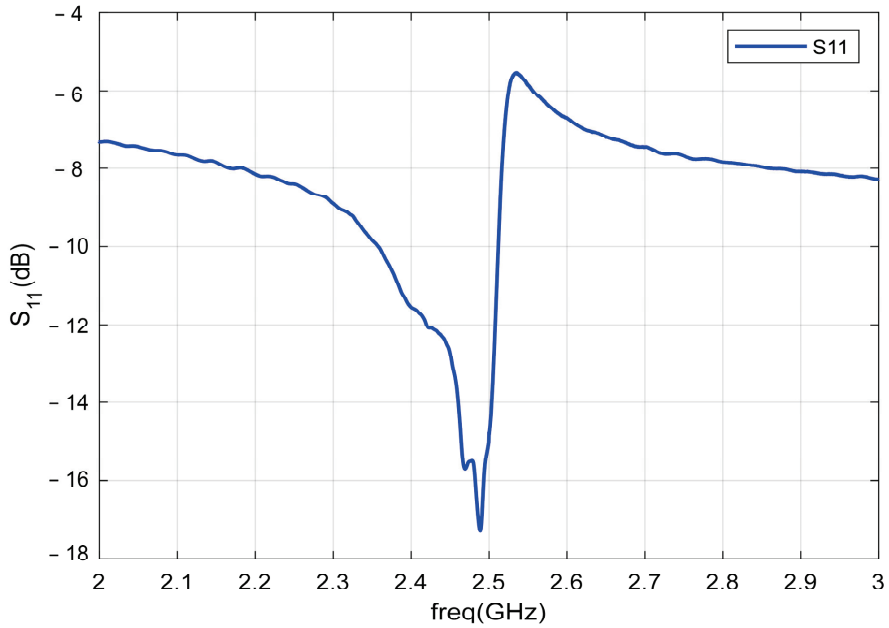

Figure 15. S11 curve of the ME antenna.

Then, the S11 and S21 curves are tested in the anechoic chamber environment, where S21 indicates that the ME antenna transmits the signal, and the horn antenna receives the signal. The S11 curve is converted into the Z11 curve and put together with the S21 curve, as shown in Figure 16. The test results show that the antenna has an obvious radiation enhancement at the parallel resonance point. It indicates that the ME antenna produces obvious radiation at the mechanical resonance frequency, which verifies that the radiation of the ME antenna comes from the ME coupling of the mechanical resonance.

The S12 and S21 parameter curves in Figure 17 are basically the same, indicating that the ME antenna has reciprocity under the action of the external magnetic field of small signals. The ME antenna meets the reciprocity principle of traditional antenna.

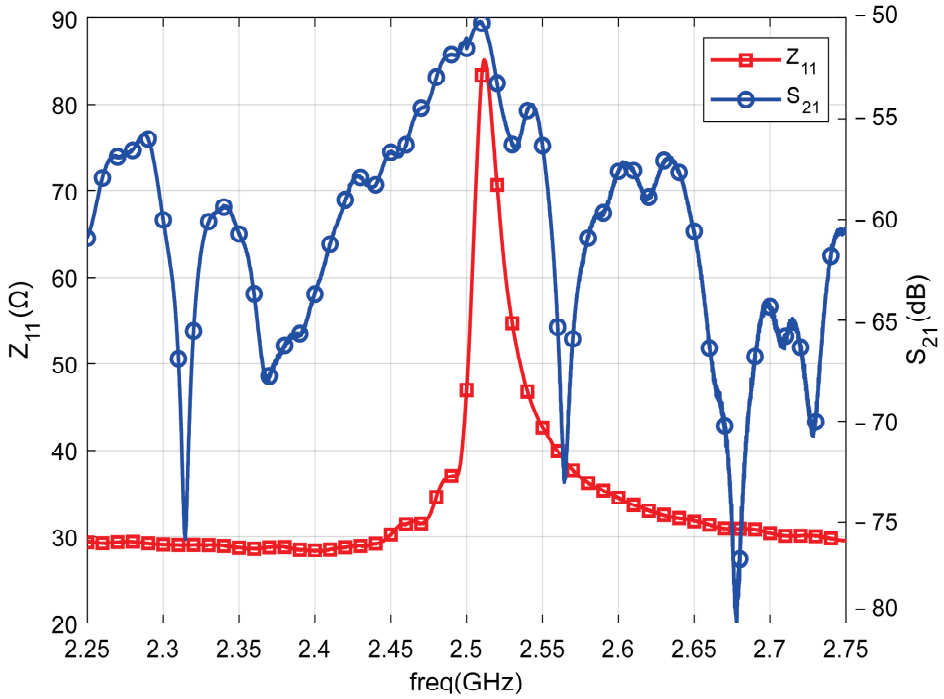

Figure 16. Z11 and S21 parameters of the antenna.

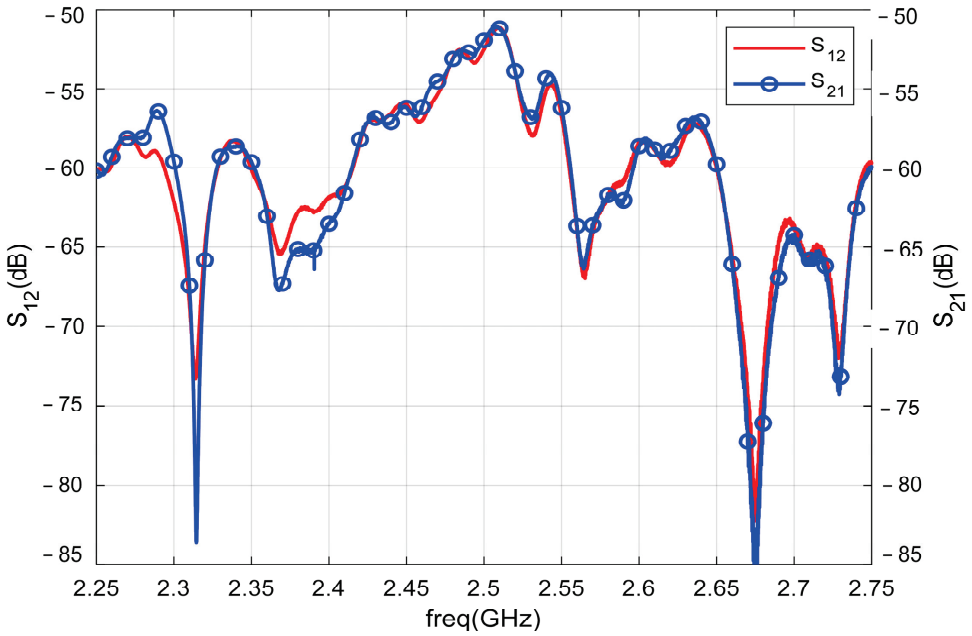

Figure 17. S12 and S21 parameters of the ME antenna.

1. Calculation of Antenna Gain

Measured against the antenna in an anechoic chamber at the resonant frequency of 2.49 GHz, the $S_{21,a}$ is −50.42 dB, and the $S_{21,r}$ is −18.03 dB, wherein the gain G_r of the reference standard horn antenna is 16.8 dB, and $S_{21,a}$ and $S_{21,r}$ represent the S21 peak value of the ME antenna to be tested and the reference horn antenna test, respectively. According to the comparison method, the antenna gain is calculated to be −15.59 dB.

2. Antenna pattern

In order to fully analyze the radiation characteristics of the ME antenna, its pattern is tested. Verified by the literature, the radiation of the ME antenna can be equivalent to

a model of a magnetic dipole. Using the MATLAB simulation, the radiation pattern of the equivalent magnetic dipole of the ME antenna can be obtained, as shown in Figure 18. Further radiation power P is calculated as:$2.61 \times 10^{-8} W$.

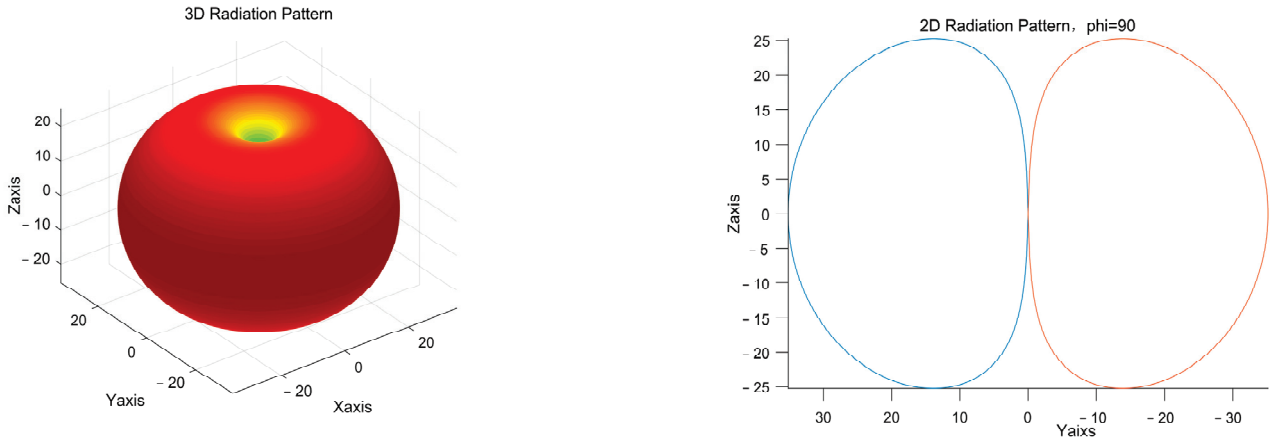

Figure 18. Pattern of the ME antenna: (**a**) 3D radiation pattern and (**b**) principal gain (phi = 90) pattern.

6. Conclusions

The proposed ME antenna provided a new method for antenna miniaturization. In this paper, a ME antenna structure was designed, the finite element simulation was carried out on it and the sample was prepared and tested. The results showed that the radiation of the ME antenna originates from the mechanical resonance. It also shows that the ME antenna has the potential to solve the problems of difficult miniaturization and impedance matching of traditional antennas. It can be equivalent to a dipole antenna, its radiation signal comes from the ME coupling and its gain is measured to be −15.59 dB.

Author Contributions: N.L. and X.L. are responsible for the design of the ME antenna, the simulation in this paper, the test of the ME antenna and the writing of the paper; N.L. is responsible for supervising and suggesting the revisions; P.Z. and B.Z. is responsible for data processing and B.X. is responsible for part of the simulation and thesis revision. All authors have read and agreed to the published version of the manuscript.

Funding: This work was funded by the National Natural Science Foundation of China (Grant No. 51775402 and U1931139).

Conflicts of Interest: The authors declare no conflict of interest.

References

1. Hansen, R.C. Fundamental limitations in antennas. *Proc. IEEE* **1981**, *69*, 170–182. [CrossRef]
2. McLean, J.S. A re-examination of the fundamental limits on the radiation Q of electrically small antennas. *IEEE Trans. Antennas Progag.* **1996**, *44*, 672. [CrossRef]
3. Wheeler, H.A. Fundamental limitations of small antennas. *Proc. IEEE* **1947**, *35*, 1479–1484. [CrossRef]
4. Sten, J.-E.; Hujanen, A.; Koivisto, P.K. Quality factor of an electrically small antenna radiating close to a conducting plane. *IEEE Trans. Antennas Progag.* **2001**, *49*, 829–837. [CrossRef]
5. Pozar, D.M. Microstrip antennas. *Proc. IEEE* **1992**, *80*, 79–81. [CrossRef]
6. Yao, Z.; Wang, Y.E.; Keller, S.; Carman, G.P. Bulk Acoustic Wave-Mediated Multiferroic Antennas: Architecture and Performance Bound. *IEEE Trans. Antennas Progag.* **2015**, *63*, 3335–3344. [CrossRef]
7. Domann, J.P.; Carman, G.P. Strain powered antennas. *J. Appl. Phys. Lett.* **2017**, *121*, 044905. [CrossRef]
8. Nan, T.; Lin, H.; Gao, Y.; Matyushov, A.; Yu, G.; Chen, H.; Sun, N.; Wei, S.; Wang, Z.; Li, M. Acoustically actuated ultra-compact NEMS magnetoelectric antennas. *Nat. Commun.* **2017**, *8*, 296. [CrossRef]
9. Hassanien, A.E.; Breen, M.; Li, M.-H.; Gong, S. A theoretical study of acoustically driven antennas. *J. Appl. Phys.* **2020**, *127*, 14903. [CrossRef]
10. Bickford, J.A.; Duwel, A.E.; Weinberg, M.S.; McNabb, R.S.; Freeman, D.K.; Ward, P.A. Performance of Electrically Small Conventional and Mechanical Antennas. *IEEE Trans. Antennas Progag.* **2019**, *67*, 2209–2223. [CrossRef]

11. Hassanien, A.E.; Breen, M.; Li, M.-H.; Gong, S. Acoustically driven electromagnetic radiating elements. *Sci. Rep.* **2020**, *10*, 17006. [CrossRef]
12. Liang, X.; Dong, C.; Chen, H.; Wang, J.; Wei, Y.; Zaeimbashi, M.; He, Y.; Matyushov, A.; Sun, C.; Sun, N. A Review of Thin-Film Magnetoelastic Materials for Magnetoelectric Applications. *Sensors* **2020**, *20*, 1532. [CrossRef]
13. Rowen, J.H.; Eggers, F.G.; Strauss, W. Generation of Microwave Electromagnetic Radiation in Magnetic Materials. *J. Appl. Phys.* **1961**, *32*, 313–315. [CrossRef]
14. Mindlin, R.D. Electromagnetic radiation from a vibrating quartz plate. *Int. J. Solids Struct.* **1973**, *9*, 697–702. [CrossRef]
15. Lee, P.C. Electromagnetic radiation from an AT-cut quartz plate under lateral-field excitation. *J. Appl. Phys.* **1989**, *65*, 1395–1399. [CrossRef]
16. Lee, P.C.; Kim, Y.G.; Prevost, J.H. Electromagnetic radiation from doubly rotated piezoelectric crystal plates vibrating at thickness frequencies. *J. Appl. Phys.* **1990**, *67*, 6633–6642. [CrossRef]
17. Greve, H.; Woltermann, E.; Quenzer, H.-J.; Wagner, B.; Quandt, E. Giant magnetoelectric coefficients in (Fe90Co10)78Si12B10-AlN thin film composites. *J. Appl. Phys. Lett.* **2010**, *96*, 182501. [CrossRef]
18. Yun, X.; Lin, W.; Hu, R.; Liu, Y.; Wang, X.; Yu, G.; Zhang, B. Bandwidth-enhanced magnetoelectric antenna based on composite bulk acoustic resonators. *Appl. Phys. Lett.* **2022**, *121*, 033501. [CrossRef]
19. Liu, Y.; Cai, Y.; Zhang, Y.; Tovstopyat, A.; Liu, S.; Sun, C. Materials, Design, and Characteristics of Bulk Acoustic Wave Resonator: A Review. *Micromachines* **2020**, *11*, 630. [CrossRef]
20. Yao, Z.; Wang, Y.E. 3D modeling of BAW-based multiferroic antennas. In Proceedings of the 2017 IEEE International Symposium on Antennas and Propagation & USNC/URSI National Radio Science Meeting, San Diego, CA, USA, 9–14 July 2017; pp. 1125–1126.
21. Yao, Z.; Wang, Y.E. 3D ADI-FDTD modeling of platform reduction with thin film ferromagnetic material. In Proceedings of the 2016 IEEE International Symposium on Antennas and Propagation & USNC/URSI National Radio Science Meeting, Fajardo, PR, USA, 26 June–1 July 2016; pp. 2019–2020.
22. Lin, H.; Page, M.R.; Mcconney, M.; Jones, J.; Howe, B.; Sun, N.X. Integrated ME devices: Filters, pico-TesIa magnetometers, and ultracompact acoustic antennas. *MRS Bull.* **2018**, *43*, 841–847. [CrossRef]
23. Schneider, J.D.; Domann, J.P.; Panduranga, M.; Tiwari, S.; Shirazi, P.; Yao, Z.; Sennott, C.; Shahan, D.; Selvin, S.; McKnight, G. Experimental demonstration and operating principles of a multiferroic antenna. *J. Appl. Phys.* **2019**, *126*, 224104. [CrossRef]
24. Zaeimbashi, M.; Lin, H.; Dong, C.; Liang, X.; Nasrollahpour, M.; Chen, H.; Sun, N.; Matyushov, A.; He, Y.; Wang, X.; et al. NanoNeuroRFID: A Wireless Implantable Device Based on Magnetoelectric Antennas. *IEEE J. Electromagn. RF Microw. Med. Biol.* **2019**, *3*, 206–215. [CrossRef]
25. Dong, C.; He, Y.; Li, M.; Tu, C.; Chu, Z.; Liang, X.; Chen, H.; Wei, Y.; Zaeimbashi, M.; Wang, X. A Portable Very Low Frequency (VLF) Communication System Based on Acoustically Actuated Magnetoelectric Antennas. *IEEE Antennas Wirel. Propag. Lett.* **2020**, *19*, 398–402. [CrossRef]
26. Niu, Y.; Ren, H. A miniaturized low frequency (LF) magnetoelectric receiving antenna with an integrated DC magnetic bias. *J. Appl. Phys. Lett.* **2021**, *118*, 264104. [CrossRef]
27. Luong, K.Q.T.; Wang, Y.E. Analysis of Dynamic Magnetoelastic Coupling in Mechanically Driven Magnetoelectric Antennas. *Sensors* **2022**, *22*, 455. [CrossRef]
28. Chen, S.; Li, J.; Gao, Y.; Li, J.; Dong, H.; Gu, Z.; Ren, W. A Micromechanical Transmitter with Only One BAW Magneto-Electric Antenna. *Micromachines* **2022**, *13*, 272. [CrossRef]
29. Shuxiang, D.; Jie-Fang, L.; Dwight, V. Longitudinal and transverse magnetoelectric voltage coefficients of magnetostrictive/piezoelectric laminate composite: Theory. *IEEE Trans. Ultrason. Ferroelectr. Freq. Control* **2003**, *50*, 1253–1261. [CrossRef]
30. Wang, Y.; Hu, J.; Lin, Y.; Nan, C.-W. Multiferroic magnetoelectric composite nanostructures. *NPG Asia Mater.* **2010**, *2*, 61–68. [CrossRef]
31. Xie, Z.; Jiao, J.; Yang, K.; He, T.; Chen, R.; Zhu, W. Experimental and numerical exploration on the nonlinear dynamic behaviors of a novel bearing lubricated by low viscosity lubricant. *Mech. Syst. Signal Process.* **2023**, *182*, 109349. [CrossRef]

micromachines

MDPI

Article

Magnetic Interconnects Based on Composite Multiferroics

Alexander Khitun

Electrical Engineering Department, University of California Riverside, Riverside, CA 92521, USA; akhitun@engr.ucr.edu

Abstract: The development of magnetic logic devices dictates a need for a novel type of interconnect for magnetic signal transmission. Fast signal damping is one of the problems which drastically differs from conventional electric technology. Here, we describe a magnetic interconnect based on a composite multiferroic comprising piezoelectric and magnetostrictive materials. Internal signal amplification is the main reason for using multiferroic material, where a portion of energy can be transferred from electric to magnetic domains via stress-mediated coupling. The utilization of composite multiferroics consisting of piezoelectric and magnetostrictive materials offers flexibility for the separate adjustment of electric and magnetic characteristics. The structure of the proposed interconnect resembles a parallel plate capacitor filled with a piezoelectric, where one of the plates comprises a magnetoelastic material. An electric field applied across the plates of the capacitor produces stress, which, in turn, affects the magnetic properties of the magnetostrictive material. The charging of the capacitor from one edge results in the charge diffusion accompanied by the magnetization change in the magnetostrictive layer. This enables the amplitude of the magnetic signal to remain constant during the propagation. The operation of the proposed interconnects is illustrated by numerical modeling. The model is based on the Landau–Lifshitz–Gilbert equation with the electric field-dependent anisotropy term included. A variety of magnetic logic devices and architectures can benefit from the proposed interconnects, as they provide reliable and low-energy-consuming data transmission. According to the estimates, the group velocity of magnetic signals may be up to 10^5 m/s with energy dissipation less than 10^{-18} J per bit per 100 nm. The physical limits and practical challenges of the proposed approach are also discussed.

Keywords: synthetic multiferroic; interconnects; magnetic logic devices

Citation: Khitun, A. Magnetic Interconnects Based on Composite Multiferroics. *Micromachines* **2022**, *13*, 1991. https://doi.org/10.3390/mi13111991

Academic Editors: Viktor Sverdlov, Seung-bok Choi and Jayne C. Garno

Received: 6 October 2022
Accepted: 12 November 2022
Published: 17 November 2022

Copyright: © 2022 by the author. Licensee MDPI, Basel, Switzerland. This article is an open access article distributed under the terms and conditions of the Creative Commons Attribution (CC BY) license (https://creativecommons.org/licenses/by/4.0/).

1. Introduction

The development of novel computational devices is well stimulated by the technological challenges and physical limits of the current complimentary metal–oxide–semiconductor (CMOS) technology [1]. Magnetic logic circuits are among the most promising approaches offering a significant reduction in consumed power by utilizing the inherent non-volatility of magnetic elements. In magnetic logic circuitry, logics 0 and 1 are encoded into the magnetization state of a nano-magnet, which may be kept for a long time without any power consumption, while the external energy is required only to perform computation (i.e., switching between the magnetization states). Though magnetic memory became a widely used commercial product a long time ago, magnetic logic is largely in its infancy. The development of energetically efficient and reliable magnetic interconnects is one of the main challenges to be overcome. Similar to electronic transistor-based circuits, where one transistor drives the next stage transistors by electric signals, magnetic logic circuits require one magnet to drive the next stage magnets by sending magnetic signals. There is a variety of possible mechanisms for magnetic signal transmission between the input and the output magnets (i.e., by making an array of nano-magnets sequentially switched in a domino fashion [2], by sending a spin-polarized current [3], by sending a spin wave [4], or by moving a domain wall [5]). There is always a tradeoff between the speed, the energy per bit, and the reliability of magnetic signal transmission. It takes either a large amount

of energy for error-prone signal transmission, or the error probability increases with the distance due to the thermal noise, defects, and signal dispersion. The lack of amplification is one of the key issues inherent to the above-mentioned approaches. In this work, we consider composite multiferroics for magnetic interconnects, which may provide magnetic signal amplification by transferring energy between the electric and magnetic domains.

Composite multiferroics (or two-phase multiferroics) comprise piezoelectric and magnetoelastic materials, where an electric field applied across the piezoelectric produces stress, which, in turn, affects the magnetization of the magnetoelastic material. Although the study of composite multiferroics started in the 1970s [6], they have been in the shadow of the single-phase multiferroics (i.e., $BiFeO_3$ and its derivatives [7]) for a long time. Currently, there is a resurgence of interest in composite multiferroics due to the technological flexibility in the independent variation of piezoelectric or magnetostrictive layers. The most important advantage of composite multiferroics over the single-phase ones (e.g., $BiFeO_3$) is the larger strength of the electro-magnetic coupling, which can significantly exceed the limits of their single-phase counterparts [8]. Magnetization rotation in two-phase multiferroics was observed as a function of the applied voltage in several experimental works [9,10]. For instance, a reversible and permanent magnetic anisotropy reorientation was reported in a magnetoelectric polycrystalline Ni thin film and (011)-oriented $[Pb(Mg_{1/3}Nb_{2/3})O_3](1 - x)$–$[PbTiO_3]$ x (PMN-PT) heterostructure [9]. The application of a 0.2 MV/m electric field induces 1200 ppm strain, which, in turn, affects the magnetization of Ni film. According to our preceding work on a similar sample [11], a 0.8 MV/m electric field produces a linear response with in-plain anisotropic strains of $\varepsilon x = 350$ μm/m and $\varepsilon y = -1200$ μm/m. It is also important to note that the changes in magnetization states are stable without the application of an electric field and can be reversibly switched by an electric field near a critical value (i.e., 0.6 MV/m for Ni/PMN-PT). An ultra-low energy consumption required for magnetization rotation is possible because of this relatively small electric field [12]. The idea of using a stress-mediated mechanism for nano-magnet switching is currently under extensive study [13,14]. The development of multiferroics provides a new approach to spin-wave control. For instance, strain reconfigurable spin-wave transport in the lateral system of magnonic stripes was achieved [15]. It was also observed that the properties of spin-wave propagation in magnonic crystal in contact with a piezoelectric layer can be controlled by an external electric field [16]. Recently, spin-wave propagation and interaction were demonstrated in the double-branched Mach–Zehnder interferometer scheme. The use of a piezoelectric plate connected to each branch of the interferometer leads to the tunable interference of the spin-wave signal at the output section [17]. Here, we propose to utilize multiferroics in magnetic interconnects and exploit the strain-mediated electro-magnetic coupling for magnetic signal amplification. The rest of the paper is organized as follows. In Section 2, we describe the material structure and the principle of operation of the composite multiferroic interconnects. The results of numerical modeling illustrating signal propagation are presented in Section 3. The Discussion and Conclusions are given in Sections 4 and 5, respectively.

2. Material Structure and Principle of Operation

The schematics of the proposed interconnect on top of a silicon wafer are shown in Figure 1A. It consists of the bottom to the top of a conducting layer (e.g., Pt), a layer of piezoelectric material (e.g., PMN-PT), and a layer of magnetoelastic material (e.g., Ni). The whole structure represents a parallel plate capacitor filled with a piezoelectric, where one plane (the bottom) comprises a non-magnetic metal and the top plate comprises a magnetoelastic metal. The top layer is the medium for magnetic signal propagation between the nano-magnets to be placed on the top of the layer. For simplicity, we have shown just two nano-magnets, which are marked as A and B in Figure 1A. The nano-magnet market A is the input element to send a magnetic signal to the receiver nano-magnet B. The spins of the nano-magnets are coupled to the spins of the ferromagnetic magnetostrictive layer via the exchange interaction. The nano-magnets are assumed to be of a special

shape to ensure the two thermally stable states of magnetization. Hereafter, we assume the magnetoelastic layer to be polarized along the *x*-axis, and the nano-magnets to have two states of magnetization along or opposite the *y*-axis. Each of the nano-magnets has an electric contact where a control voltage is applied. The bottom layer, comprising a nonmagnetic metal, serves as a common ground plate.

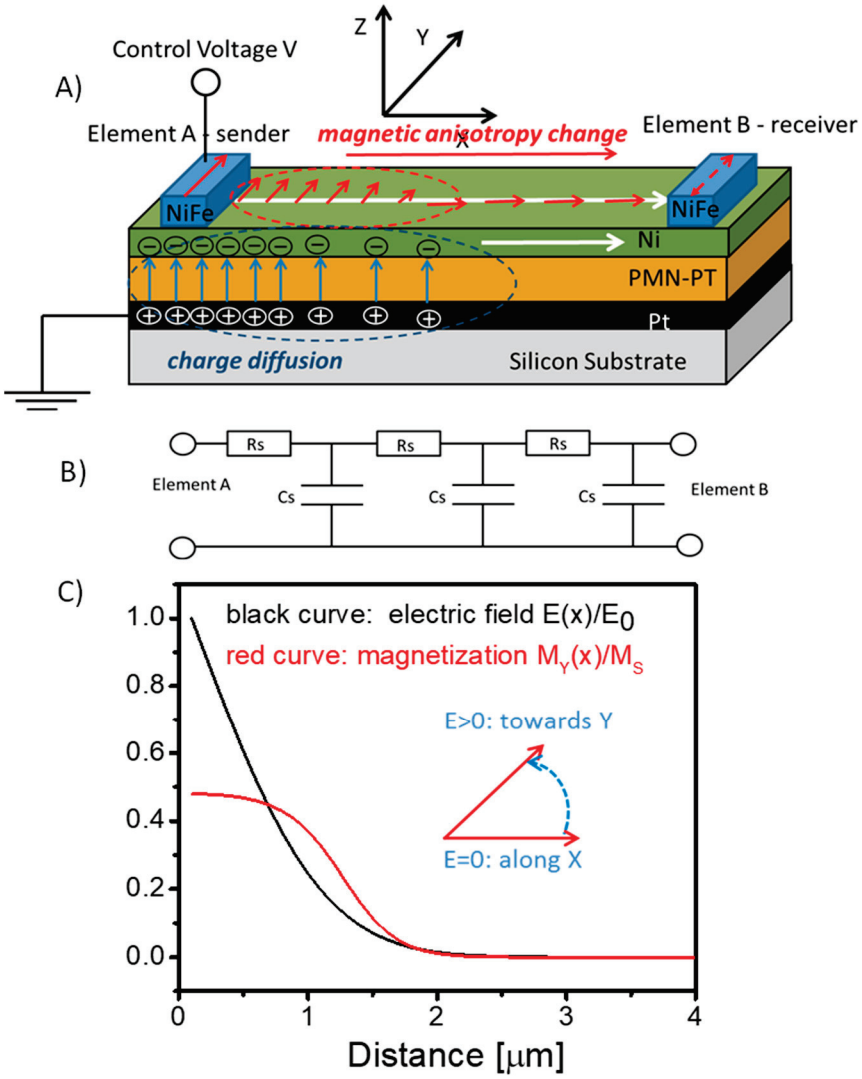

Figure 1. (**A**) Schematics of the synthetic multiferroic interconnect comprising a piezoelectric layer (PMN-PT) and a magnetostrictive layer (Ni). The structure resembles a parallel plate capacitor. An application of voltage at point A results in charge diffusion through the plates. In turn, an electric field applied across the piezoelectric produces stress, which rotates the easy axis of the magnetoelastic material. (**B**) The equivalent electric circuit—RC line, which is used in numerical simulations. (**C**) Results of numerical simulations showing the distribution of the electric field and the magnetization along the interconnect. The change of magnetization in the magnetoelastic layer follows charge diffusion.

The principle of operation is the following. In order to send a signal from A to B, a control voltage V is applied to the nano-magnet A. The application of voltage starts the charge diffusion through the conducting plates. The equivalent circuit is shown in Figure 1B. The charge diffusion through the capacitor plates is well described by the RC model, where the resistance R and the capacitance C are defined by the geometric size and the material properties of the conducting plates and the piezoelectric layer. An electric field appears across the piezoelectric produces stress, which affects the anisotropy of the magnetostrictive

material by rotating its easy axis. It is assumed that the application of voltage rotates the easy axis from the *x*-axis towards the *y*-axis. The change of the anisotropy field caused by the applied voltage affects the magnetization of the magnetoelastic layer. There are two possible trajectories for the magnetization to follow: along or opposite the *y*-axis. The particular trajectory is defined by the magnetization state of the sender nano-magnet A (i.e., the magnetization of the ferromagnetic layer copies the magnetization of the sender nano-magnet).

In Figure 1C, we present the results of numerical modeling, showing the snapshot of the distribution of the electric field E(x) and the magnetization component My(x) through the interconnect. The details of numerical modeling are presented in the next section. Here, we wish to illustrate the main idea of using composite multiferroics as a magnetic interconnect: magnetic signals (i.e., the local change of magnetization) can be sent through large distances without degradation, as the angle of magnetization rotation is controlled by the applied voltage. The direction of signal propagation (e.g., from A to B, or vice versa) is also controlled by the applied voltages. The charging of the capacitor eventually leads to the uniform electric field distribution among the plates and the static distribution of magnetization through the magnetoelastic layer. There are several possible ways to switch output nano-magnet B. For example, it can be preset in a metastable state prior to computation (e.g., magnetization along the *z*-axis), so the magnetic signal sent by A triggers the relaxation towards one of the thermally stable states along or opposite to the *y*-axis. There may also be possible scenarios where the receiver nano-magnet is connected to two or more nano-magnets, so the final state is defined by the interplay of several incoming signals (e.g., MAJ operation). In this work, we focus on the mechanism of signal transmission only, though the utilization of composite multiferroic interconnects may further evolve the design of magnetic logic circuits similar to the ones presented in [3,4,18].

3. Numerical Modeling

The model for signal propagation in the composite multiferroic combines electric and magnetic parts. The electric part aims to find the distribution of an electric field through the piezoelectric, and the magnetic part describes the change of magnetization in the magnetoelastic layer. The charge distribution is modeled via the following equation [19]:

$$R_s C_s \frac{d^2 V(x,t)}{dx^2} = \frac{dV(x,t)}{dt} \quad (1)$$

where R_s and C_s are the resistance and capacitance per unit length, and $V(x,t)$ is the voltage distribution over the distance. The simulations start with $V(0,0) = V\text{in}$, and $V(x,0) = 0$ everywhere else through the plates.

The process of magnetization rotation is modeled via the Landau–Lifshitz equation [20]:

$$\frac{d\vec{m}}{dt} = -\frac{\gamma}{1+\eta^2}\vec{m} \times [\vec{H}_{eff} + \eta\vec{m} \times \vec{H}_{eff}] \quad (2)$$

where $\vec{m} = \vec{M}/M_s$ is the unit magnetization vector, M_s is the saturation magnetization, γ is the gyro-magnetic ratio, and η is the phenomenological Gilbert damping coefficient. The effective magnetic field $\vec{H}_{eff}$ is the sum of the following:

$$\vec{H}_{eff} = \vec{H}_d + \vec{H}_{ex} + \vec{H}_a + \vec{H}_b \quad (3)$$

where H_d is the magnetostatic field, H_{ex} is the exchange field, H_a is the anisotropy field $\vec{H}_a = (2K/M_s)(\vec{m}\cdot\vec{c})\vec{c}$ (K is the uniaxial anisotropy constant, and $\vec{c}$ is the unit vector

along the uniaxial direction), and H_b is the external bias magnetic field. The two parts are connected via the voltage-dependent anisotropy term as follows:

$$c_x = \cos(\theta),\ c_y = \sin(\theta),\ c_z = 0 \tag{4}$$

$$\theta = \frac{\pi}{2}\left(\frac{V(x)}{V_\pi}\right)$$

where V_π is the voltage resulting in a 90-degree easy axis rotation in the X-Y plane.

The introduction of the voltage-dependent anisotropy field (Equation (4)) significantly simplifies simulations, as it presumes an immediate anisotropy response on the applied electric field without considering the stress-mediated mechanism of the electro-magnetic coupling. Such a model can be taken as a first-order approximation. Nevertheless, this model is useful in capturing the general trends of signal propagation and can provide estimates of the maximum speed of signal propagation and energy losses. In our numerical simulations, we use the following material parameters: the dielectric constant ε of the piezoelectric is 2000; the electrical resistivity of the magnetoelastic material is 7.0×10^{-8} Ω·m, the gyro-magnetic ratio is $\gamma = 2 \times 107$ rad/s, the saturation magnetization is M_s = 10 kG/4π; 2 K/Ms = 100 Oe, external magnetic field H_b = 100 Oe is along the x-axis, and the Gilbert damping coefficient is η = 0.1 for the magnetostrictive material. For simplicity, we also assumed the same resistance for the bottom and the top conducting plates. The strength of the electro-magnetic coupling (i.e., V_π) is calculated based on the available experimental data for PMN-PT/Ni (i.e., 0.6 MV/m for 90-degree rotation [9]). More details on the simulation procedure can be found in [21].

The results of the numerical simulations shown in Figure 1C are obtained for the interconnect comprising 40 nm of piezoelectric and 4 nm of magnetoelastic materials. The two curves in Figure 1C depict the distribution of the electric field $E(x)$ and the projection of magnetization My(x) along the interconnect after the voltage has been applied through the nano-magnet A. The curves are plotted in the normalized units E/E_0 and My/Ms, where $E_0 = V_\pi/d$, where d is the thickness of the multiferroic layer (40 nm). The distribution of the electric field was found by solving Equation (1). Then, the anisotropy field was found via Equation (4), and, finally, magnetization change was simulated via Equations (2) and (3). The results in Figure 1C show a snapshot taken at 0.4 ns after the voltage has been applied. In these simulations, we assumed the nano-magnet A to be polarized along the y-axis, and the magnetization of the interconnect beyond the nano-magnet My(0) = $0.1M_s$ due to the exchange coupling with the spins of the nano-magnet. The spins of the magnetoelastic material tend to rotate in the same direction as the spins of the sender nano-magnet A. Eventually, the Y-component of the magnetization of the interconnect saturates along the constant value, which is defined by the interplay of the anisotropy and the bias magnetic fields.

In Figure 2, we show the results of numerical modeling illustrating the dynamics of magnetization rotation in the interconnect. The curves in Figure 2 depict the evolution of local magnetization in the interconnect located 1.5 μm, 1.7 μm, and 2.0 μm away from the excitation point. The insets in Figure 2 show the initial state of magnetization of the sender nano-magnet A. In all cases, the magnetization trajectory in the interconnect repeats the initial magnetization of the nano-magnet A (e.g., the magnetization component My is positive if nano-magnet A is polarized along the y-axis, and the My is negative if nano-magnet A is polarized opposite to the y-axis). The absolute value of the final steady state is the same (about 0.5 Ms) for all six curves. These results illustrate the main idea of implementing electric field-driven multiferroic interconnects, allowing us to keep the amplitude of the magnetic signal constant regardless of the propagation distance.

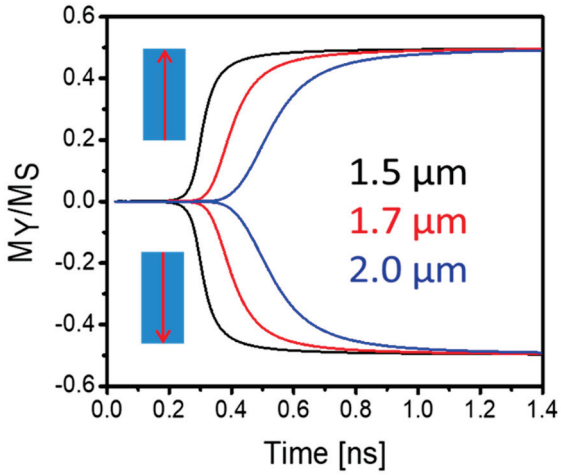

Figure 2. Results of numerical modeling showing the normalized magnetization M_Y/M_S as a function of time. The two sets of curves show magnetization trajectories following the initial state of the sender nano-magnet A (e.g., along or opposite to axis *y*). The black, red, and blue curves show magnetization at 1.0 μm, 2.0 μm, and 3.0 μm distance away from the starting point A.

4. Discussion

The ability to pump energy into the magnetic signal during its propagation is the most appealing property of the described interconnects. The pumping occurs via the magneto-electric coupling in the multiferroic, where some portion of the electric energy provided to the capacitor is transferred to the energy of the magnetic signal. The amplitude of the magnetic signal (i.e., the angle of magnetization rotation) is controlled by the applied voltage and saturates to a certain value as the electric field across the piezoelectric reaches its steady-state distribution. This property is critically important for logic circuit construction, allowing us to minimize the effect of structure imperfections and make logic circuits immune to thermal noise. It should be also noted that the absolute value of magnetization change in the interconnect may exceed the initial magnetization state of the sender nano-magnet. For instance, the Y component of the magnetization of the nano-magnet A may be 0.1 Ms, while the Y magnetization of the magnetic signal in the interconnect may saturate around 0.5 Ms, as illustrated by numerical modeling in the previous section. In other words, the proposed interconnects may serve as an amplifier for magnetic signals, similar to the multiferroic spin-wave amplifier described in [21]. Another important property of the proposed interconnect is the ability to control the direction of signal propagation by the applied voltage. Similar to the "All Spin Logic" approach [3], where the direction of magnetic signal is defined by the direction of spin-polarized current flow, the change of magnetization in the multiferroic interconnect follows the charge diffusion. This property resolves the problem of input–output isolation and provides an additional degree of freedom for logic circuit construction.

Energy dissipation in a two-phase magnetoelastic/piezoelectric multiferroic has been studied in [14,22,23]. According to the estimates, a single two-phase magnetoelastic/piezoelectric multiferroic single-domain shape-anisotropic nano-magnet can be switched, consuming as low as 45 kT for a delay of 100 ns at room temperature, where the main contribution to the dissipated energy comes from the losses during the charging/discharging ($\approx CV^2$) [23]. The capacitance of one-micrometer-long multiferroic interconnects comprising 40 nm of PZT and 4 nm of Ni with the width of 40 nm is about 15 fF, and the control voltage required for 90-degree anisotropy easy-axis change is 0.6 MV/m × 40 nm = 24 mV. Thus, assuming all the electric energy dissipated during signal propagation, one has 9 aJ per signal per 1 μm transmitted. It is important to note that, according to the theoretical estimates [23], the energy dissipation increases sub-linearly with the switching speed. For example, in order to increase the switching speed by a factor of 10, the dissipation needs to increase by a factor of 1.6.

The propagation of the magnetization signal involves several physical processes: charge diffusion, the mechanical response of the piezoelectric to the applied electric field, change of the anisotropy field caused by the stress, and magnetization relaxation. Thus, the total delay time τ_t is the sum of the following:

$$\tau_t = \tau_e + \tau_{mech} + \tau_{mag} \quad (5)$$

where τ_e is the time delay due to the charge diffusion τ_e = RC, τmech is the delay time of the mechanical response $\tau_{mech} \approx d/v_a$, where d is the thickness of the piezoelectric layer, v_a is the speed of sound in the piezoelectric, and τ_{mag} is the time required for the spins of magnetostrictive material to follow the changing anisotropy field. In the theoretical model presented in the previous section, we introduced a direct coupling among the electric field and the anisotropy field (i.e., Equation (4)), presuming an immediate anisotropy field response on the applied electric field. The latter may be valid for the thin piezoelectric layers (e.g., taking d = 40 nm, $v_a = 1 \times 10^3$ m/s, τ_{mech} is about 40 ps). We also introduced a high damping coefficient η, which minimizes the magnetic relaxation time $\tau_{meag} < 50$ ps. In this approximation, the speed of signal propagation is mainly defined by the charge diffusion rate. The smaller RC, the faster the charge diffusion and the lower the energy losses for interconnect charging/discharging.

In Figure 3, we show the results of numerical modeling on the speed of signal propagation for different thicknesses of the piezoelectric layer. The four curves correspond to the signal propagation in the interconnects with different PMN-PT thicknesses (e.g., 20 nm, 40 nm, 80 nm, and 200 nm), respectively. The thickness of the nickel layer is 4 nm for all cases. We also plotted a reference line corresponding to the magnetostatic spin wave with a typical group velocity of 3.1×10^4 m/s. According to these estimates, one may observe that the magnetic signal in the multiferroic interconnect may propagate faster than the spin wave at short distances (<500 nm) and slower than the spin wave at longer distances. The latter leads to an interesting question of whether or not it is possible to transmit magnetic signals faster than the spin wave in the magnetoelastic material. Although magnetic coupling does not define the speed of signal propagation, it should determine the trajectory of spin relaxation. Exceeding the speed of spin wave in ferromagnetic material may lead to a chaotic magnetic reorientation along the ferromagnetic layer. At the same time, it will limit the propagation length. Would it be possible to cascade multiferroic interconnects? This is one of many questions to be answered with further study.

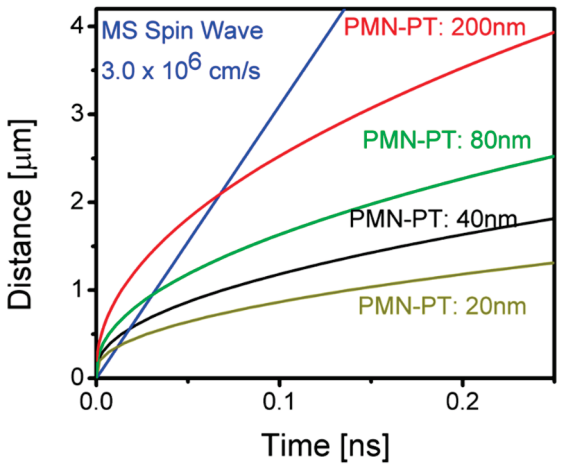

Figure 3. Results of numerical modeling illustrating the speed of signal propagation in the synthetic multiferroic interconnect. Shown are several curves corresponding to different thicknesses of the PMN-PT layer (20 nm, 40 nm, 80 nm, and 200 nm). The blue line is the reference data for the Magnetostatic Surface Spin Wave (MSSW) with a group velocity of 3.0×10^4 m/s.

Finally, we wish to compare the main characteristics of different magnetic interconnects and discuss their advantages and shortcomings. Moving a domain wall is a reliable and experimentally proven method for magnetic signal transmission [24]. A domain wall propagates through a magnetic wire, as long as an electric current or an external magnetic field is applied, and remains at a constant position if the driving force is absent. This property is extremely useful for building magnetic memory (e.g., the "racetrack" memory [25]). The speed of domain motion may exceed hundreds of meters per second if the driving electric current has a sufficiently large density (e.g., 250 m/s at 1.5×10^8 A/cm^2 from [25]). Slow propagation speed and high energy per bit are the main disadvantages of the logic circuits' exploding domain wall motion.

The interconnects made from the sequence of nano-magnets are relatively faster and less power consuming, where the nearest neighbor nano-magnets are coupled via the dipole–dipole interaction (the so-called Nano-Magnetic Logic (NML) [2]). Experimentally realized wires formed from a line of anti-ferromagnetically ordered nano-magnets show a signal propagation speed up to 10^3 m/s with an internal (without the losses in the magnetic field generating contours) power dissipation per bit of approximately tens of atto Joules [18]. There is a tradeoff between the speed of signal propagation and the dissipated energy. The slower the speed of propagation, the lower the energy dissipated within the interconnect. The main shortcoming of the nano-magnet interconnect is associated with reliability, as the thermal noise and fabrication-related imperfections can cause errors in signal transmission and the overall logic functionality of the NML circuits [26].

Interconnects exploiting spin waves may provide signal propagation with the speed of 10^4 m/s–10^5 m/s. At the same time, the amplitude of the spin-wave signal is limited by the several degrees of magnetization rotation, in contrast to the complete magnetization reversal provided by the domain wall motion or NML. The amplitude of the spin wave decreases during propagation (e.g., the attenuation time for magnetostatic surface spin waves in NiFe is 0.8 ns at room temperature [27]). The unique advantage of the spin-wave approach is that the interconnects themselves can be used as passive logic elements exploiting spin-wave interference. The latter offers an additional degree of freedom for logic gate construction and makes it possible to minimize the number of nano-magnets per logic circuit [4].

The All-Spin Logic (ASL) proposal suggests the use of spin-polarized currents for nano-magnet coupling [3]. This approach allows for much greater defect tolerance, as the variations in the size and position of input/output nano-magnets are of minor importance. It is also scalable, since shorter distances between the input/output cells would require less spin-polarized currents for switching. According to theoretical estimates [28],

ASL can potentially reduce the switching energy-delay product. The major constraint is associated with the need for the spin-coherent channel, where the length of the interconnects exploiting spin-polarized currents is limited by the spin diffusion length.

The described magnetic interconnects based on composite multiferroics combine high transmission speed (as fast as the spin waves) with the possibility of transmitting large amplitude signals (up to 90 degrees of the magnetization rotation). As we stated above, the main appealing property of the proposed interconnect is the ability to keep constant the amplitude of the magnetization signal. All these advantages are the result of using the electro-magnetic coupling in multiferroics, allowing us to pump energy from the electric to the magnetic domain. Based on the presented estimates, the energy per transmitted bit may be as low as several atto Joules per 100 nm of transmitted distance. From a practical point of view, the implementation of composite multiferroic interconnects is feasible, as it relies on the integration of well-known materials (e.g., PMN-PT and Ni) and can be integrated on a silicon platform. However, the dynamics of the electro-mechanical-magnetic coupling in composite multiferroics remain mainly unexplored. The expected challenges are associated with the limited scalability, as the thickness of the piezoelectric should be sufficient to generate the stress required for anisotropy change. The quality of the interface between the piezoelectric and magnetostrictive layers is another important factor to be considered. The

inevitable structure imperfections should be below the magnetization reversal threshold (e.g., as defined by Equation (4)). In Table 1, we have summarized the estimates on the main characteristics of different magnetic interconnects and outlined their major advantages and shortcomings.

Table 1. The estimates on the main characteristics of different magnetic.

	Domain Wall	MCA	Spin Wave	ASL	Multiferroics
Mechanism of coupling	Domain wall motion	Dipole–dipole coupling	Spin waves	Spin polarized current	Magnetization signal
Speed of propagation	10^2 m/s	10^3 m/s	10^4 m/s–10^5 m/s	* 10^5 m/s	* 10^5 m/s
Energy dissipated per bit transmitted	>1000 aJ	** 1 aJ	0.1 aJ	N/A	1 aJ
Main advantage	Non-volatile, can be stopped at any time and preserve its position	Internal dissipated energy approaches zero at the adiabatic switching	Computation in wires—additional functionality via wave interference	Scalable, defect tolerant	Fast signal propagation, signal amplification
Main disadvantage	Slow and energy consuming	Effect of thermal noise increases with the propagation distance	Propagation distance is limited due to the spin-wave damping	Propagation distance is limited by the spin diffusion length	Limited scalability

* Signal propagation speed is determined by the charge diffusion and decreases with the distance. ** The estimates for 10^3 m/s propagation speed and include only for the energy dissipated inside the magnetic interconnect (without considering the energy losses in the magnetic field generating contours).

5. Conclusions

In summary, we considered a novel type of magnetic interconnect exploiting electromagnetic coupling in two-phase composite multiferroics. According to the presented estimates, composite multiferroic interconnects combine the advantages of fast signal propagation (up to 10^5 m/s) and low power dissipation (less than 1 aJ per 100 nm). The most appealing property of the multiferroic interconnects is the ability to pump energy into the magnetic signal and amplify it during propagation. A voltage-driven magnetic interconnect may be utilized in nano-magnetic logic circuitry and provide an efficient tool for logic gate construction. The fundamental limits and practical constraints inherent to two-phase multiferroics are associated with the efficiency of stress-mediated coupling at high frequencies. There are many questions related to the dynamic of the stress-mediated signal propagation, which will be clarified with a further theoretical and experimental study.

Funding: The National Science Foundation (NSF) under Award # 2006290, Program Officer Dr. S. Basu.

Institutional Review Board Statement: Not applicable.

Informed Consent Statement: Not applicable.

Data Availability Statement: All data generated or analyzed during this study are included in this published article.

Acknowledgments: This work was supported in part by the National Science Foundation (NSF) under Award # 2006290, Program Officer S. Basu.

Conflicts of Interest: The authors declare no conflict of interest.

References

1. Semiconductors, I.T.R. Chapter PIDS. 2011. Available online: http://www.itrs.net (accessed on 7 January 2011).
2. Cowburn, R.P.; Welland, M.E. Room temperature magnetic quantum cellular automata. *Science* **2000**, *287*, 1466–1468. [CrossRef] [PubMed]
3. Behin-Aein, B.; Datta, D.; Salahuddin, S.; Datta, S. Proposal for an all-spin logic device with built-in memory. *Nat. Nanotechnol.* **2010**, *5*, 266–270. [CrossRef] [PubMed]
4. Khitun, A.; Wang, K.L. Non-Volatile Magnonic Logic Circuits Engineering. *J. Appl. Phys.* **2011**, *110*, 034306–034310. [CrossRef]
5. Nikonov, D.E.; Bourianoff, G.I.; Ghani, T. Proposal of a Spin Torque Majority Gate Logic. *IEEE Electron Device Lett.* **2011**, *32*, 1128–1130. [CrossRef]
6. Vanrun, A.; Terrell, D.R.; Scholing, J.H. Insitu Grown Eutectic Magnetoelectric Composite-Material. 2. Physical-Properties. *J. Mater. Sci.* **1974**, *9*, 1710–1714. [CrossRef]

7. Wang, J.; Neaton, J.B.; Zheng, H.; Nagarajan, V.; Ogale, S.B.; Liu, B.; Viehland, D.; Vaithyanathan, V.; Schlom, D.G.; Waghmare, U.V.; et al. Epitaxial BiFeO3 multiferroic thin film heterostructures. *Science* **2003**, *299*, 1719–1722. [CrossRef]
8. Eerenstein, W.; Mathur, N.D.; Scott, J.F. Multiferroic and magnetoelectric materials. *Nature* **2006**, *442*, 759–765. [CrossRef]
9. Wu, T.; Bur, A.; Zhao, P.; Mohanchandra, K.P.; Wong, K.; Wang, K.L.; Lynch, C.S.; Carman, G.P. Giant electric-field-induced reversible and permanent magnetization reorientation on magnetoelectric Ni/(011) $[Pb(Mg_{1/3}Nb_{2/3})O_3]_{(1-x)}$–$[PbTiO_3]_x$ heterostructure. *Appl. Phys. Lett.* **2011**, *98*, 012504–012507.
10. Shabadi, P.; Khitun, A.; Wong, K.; Amiri, P.K.; Wang, K.L.; Andras, C.A. Spin wave functions nanofabric update. In Proceedings of the IEEE/ACM International Symposium on Nanoscale Architectures (NANOARCH-11), San Diego, CA, USA, 8–9 June 2011; pp. 107–113.
11. Balinskiy, M.; Chavez, A.C.; Barra, A.; Chiang, H.; Carman, G.P.; Khitun, A. Magnetoelectric Spin Wave Modulator Based On Synthetic Multiferroic Structure. *Sci. Rep.* **2018**, *8*, 1–10. [CrossRef]
12. Shabadi, P.; Khitun, A.; Narayanan, P.; Mingqiang, B.; Koren, I.; Wang, K.L.; Moritz, C.A. Towards logic functions as the device. In Proceedings of the 2010 IEEE/ACM International Symposium on Nanoscale Architectures (NANOARCH 2010), Anaheim, CA, USA, 17–18 June 2010. [CrossRef]
13. D'Souza, N.; Atulasimha, J.; Bandyopadhyay, S. An Ultrafast Image Recovery and Recognition System Implemented With Nanomagnets Possessing Biaxial Magnetocrystalline Anisotropy. *IEEE Trans. Nanotechnol.* **2012**, *11*, 896–901. [CrossRef]
14. Roy, K.; Bandyopadhyay, S.; Atulasimha, J. Energy dissipation and switching delay in stress-induced switching of multiferroic nanomagnets in the presence of thermal fluctuations. *J. Appl. Phys.* **2012**, *112*, 023914. [CrossRef]
15. Grachev, A.A.; Sheshukova, S.E.; Nikitov, S.A.; Sadovnikov, A.V. Strain reconfigurable spin-wave transport in the lateral system of magnonic stripes. *J. Magn. Magn. Mater.* **2020**, *515*, 167302. [CrossRef]
16. Grachev, A.A.; Matveev, O.V.; Mruczkiewicz, M.; Morozova, M.A.; Beginin, E.N.; Sheshukova, S.E.; Sadovnikov, A.V. Strain-mediated tunability of spin-wave spectra in the adjacent magnonic crystal stripes with piezoelectric layer. *Appl. Phys. Lett.* **2021**, *118*, 262405. [CrossRef]
17. Grachev, A.A.; Sadovnikov, A.V.; Nikitov, S.A. Strain-Tuned Spin-Wave Interference in Micro- and Nanoscale Magnonic Interferometers. *Nanomaterials* **2022**, *12*, 1520. [CrossRef]
18. Niemier, M.T.; Bernstein, G.H.; Csaba, G.; Dingler, A.; Hu, X.S.; Kurtz, S.; Liu, S.; Nahas, J.; Porod, W.; Siddiq, M.; et al. Nanomagnet logic: Progress toward system-level integration. *J. Phys. Condens. Matter* **2011**, *23*, 493202. [CrossRef]
19. Solin, P. Equations of Electromagnetics. 2006; 269–318.
20. Landau, L.; Lifshitz, E. Theory of the dispersion of magnetic permeability in ferromagnetic bodies. *Phys. Z. Sowjetunion* **1935**, *8*, 153–169.
21. Khitun, A.; Nikonov, D.E.; Wang, K.L. Magnetoelectric spin wave amplifier for spin wave logic circuits. *J. Appl. Phys.* **2009**, *106*, 123909. [CrossRef]
22. Fashami, M.S.; Roy, K.; Atulasimha, J.; Bandyopadhyay, S.; Markwitz, A. Magnetization dynamics, Bennett clocking and associated energy dissipation in multiferroic logic. *Nanotechnology* **2011**, *22*, 155201, Erratum in *Nanotechnology* **2011**, *22*, 309501. [CrossRef]
23. Roy, K.; Bandyopadhyay, S.; Atulasimha, J. Hybrid spintronics and straintronics: A magnetic technology for ultra low energy computing and signal processing. *Appl. Phys. Lett.* **2011**, *99*, 063108. [CrossRef]
24. Allwood, D.A.; Xiong, G.; Faullkner, C.C.; Atkinson, D.; Petit, D.; Cowburn, R.P. Magnetic domain-wall logic. *Science* **2005**, *309*, 1688–1692. [CrossRef]
25. Parkin, S.S.P.; Hayashi, M.; Thomas, L. Magnetic domain-wall racetrack memory. *Science* **2008**, *320*, 190–194. [CrossRef] [PubMed]
26. Spedalieri, F.M.; Jacob, A.P.; Nikonov, D.E.; Roychowdhury, V.P. Performance of Magnetic Quantum Cellular Automata and Limitations Due to Thermal Noise. *IEEE Trans. Nanotechnol.* **2011**, *10*, 537–546. [CrossRef]
27. Covington, M.; Crawford, T.M.; Parker, G.J. Time-resolved measurement of propagating spin waves in ferromagnetic thin films. *Phys. Rev. Lett.* **2002**, *89*, 237202. [CrossRef] [PubMed]
28. Behin-Aein, B.; Sarkar, A.; Srinivasan, S.; Datta, S. Switching energy-delay of all spin logic devices. *Appl. Phys. Lett.* **2011**, *98*, 123510. [CrossRef]

micromachines

MDPI

Article

Magnetostriction Enhancement in Midrange Modulus Magnetorheological Elastomers for Sensor Applications

Muhammad Asyraf Tasin [1], Siti Aishah Abdul Aziz [2], Saiful Amri Mazlan [1,*], Mohd Aidy Faizal Johari [1], Nur Azmah Nordin [1], Shahir Yasin Mohd Yusuf [1], Seung-Bok Choi [3,4,*] and Irfan Bahiuddin [5]

[1] Engineering Materials and Structures (eMast) iKohza, Malaysia-Japan International Institute of Technology (MJIIT), Universiti Teknologi Malaysia, Kuala Lumpur 54100, Malaysia
[2] Faculty of Applied Sciences, Universiti Teknologi MARA (UiTM) Cawangan Pahang, Jengka 26400, Malaysia
[3] Department of Mechanical Engineering, The State University of New York, Korea (SUNY Korea), Incheon 21985, Republic of Korea
[4] Department of Mechanical Engineering, Industrial University of Ho Chi Minh (IUH), Ho Chi Minh City 70000, Vietnam
[5] Department of Mechanical Engineering, Vocational College, Universitas Gadjah Mada, Yogyakarta 55281, Indonesia
* Correspondence: amri.kl@utm.my (S.A.M.); seungbok.choi@sunykorea.ac.kr (S.-B.C.)

Abstract: Magnetorheological elastomer (MRE), which is capable of exhibiting magnetostriction in the presence of a magnetic field, has a great potential to be used for the development of sensor devices. Unfortunately, to date, many works focused on studying low modulus of MRE (less than 100 kPa) which can hamper their potential application in sensors due to short lifespan and low durability. Thus, in this work, MRE with storage modulus above 300 kPa is to be developed to enhance magnetostriction magnitude and reaction force (normal force). To achieve this goal, MREs are prepared with various compositions of carbonyl iron particles (CIPs), in particular, MRE with 60, 70 and 80 wt.% of CIP. It is shown that both the magnetostriction percentage and normal force increment are achieved as the concentration of CIPs increases. The highest magnetostriction magnitude of 0.075% is obtained with 80 wt.% of CIP, and this increment is higher than that of moderate stiffness MRE developed in the previous works. Therefore, the midrange range modulus MRE developed in this work can copiously produce the required magnetostriction value and potentially be implemented for the design of forefront sensor technology.

Keywords: magnetostriction; magneto-deformation; magnetoactive elastomer; normal force; hysteresis; magnetorheological elastomer

Citation: Tasin, M.A.; Aziz, S.A.A.; Mazlan, S.A.; Johari, M.A.F.; Nordin, N.A.; Yusuf, S.Y.M.; Choi, S.-B.; Bahiuddin, I. Magnetostriction Enhancement in Midrange Modulus Magnetorheological Elastomers for Sensor Applications. *Micromachines* **2023**, *14*, 767. https://doi.org/10.3390/mi14040767

Academic Editor: Behrad Khamesee

Received: 20 February 2023
Revised: 23 March 2023
Accepted: 23 March 2023
Published: 29 March 2023

Copyright: © 2023 by the authors. Licensee MDPI, Basel, Switzerland. This article is an open access article distributed under the terms and conditions of the Creative Commons Attribution (CC BY) license (https://creativecommons.org/licenses/by/4.0/).

1. Introduction

In recent years, there is a constant demand for soft sensors which innately possess desirable features such as high durability and flexibility yet being resilient and robust. The design and development of these soft sensors will therefore warrant searching for appropriate smart materials to overcome some of the limitations of the constituent materials of solid sensors. Among the types of smart materials available to date, magnetorheological elastomer (MRE) has the potential to be implemented in soft sensors due to its ability to adapt to multiscale and dynamic deformations, mechanical compliance and the exceptional magnetostriction phenomenon that is sensitive to the strength of a magnetic field. Magnetostriction phenomenon, or commonly denoted in the literature as magnetostriction [1,2] can be defined as a change in physical dimensions in the presence of a magnetic field. This alteration in dimensions includes a contraction or an elongation, a process within the materials which involves converting the electromagnetic energy into mechanical energy. Both MRE and crystalline ferromagnets display a magnetostriction effect when subjected to a magnetic field. However, the underlying process of such length-changing behavior defers

between both materials. In crystalline ferromagnets, the magneto-strain coupling is caused by the quantum spin–orbit interaction [3]. On the other hand, the basis of such effect in MRE is the restructuring or rearrangement of the particles embedded within the matrix to align in the direction of the magnetic field. The degree of elongations and deformations of MRE is largely depending upon the stiffness characteristics of the elastomeric matrix and the magnetic properties of the embedded particles.

Taking into account the variation of probable matrix-particles combinations, previous works on MRE's composition such as the compliance of the elastomer matrix, volume fraction and distribution of the particles have been conducted in order to fine-tune its magnetostriction response. Among all possible material compositions, a combination of Terfenol-D (TD) particles and Epoxy matrix accounted for the majority of research work on the magnetostriction effect in MRE [4–8]. Such material combination was reported to produce a magnetostriction value up to 0.15% [8]. However, this value was lower than the monolithic form of TD (0.3%) [9]. Other studies have combined polyurethane (PU) elastomers with TD [10] due to better degradation stability than natural rubber and obtained a maximum saturation magnetostriction value of 0.0813% at an applied magnetic field of 0.5 T [11]. Despite the MRE based on TD producing a massive magnetostriction value, some works have combined Galfenol (Fe–Ga) with epoxy and PU matrix [12–14] due to lower cost than TD and showed that the value of saturation magnetostriction could reach above 0.03% [15]. Most recently, a combination of iron, cobalt and vanadium (FeCo–2V) was used as the particles to fabricate MRE and obtained magnetostriction value of 0.3731% [16]. In addition to the aforementioned MRE composition, some works have crosslinked micron-sized iron particles with silicone rubbers and produced varying magnetostriction strain. Iron particles are commonly used for MRE and known for their high permeability [17], high saturation magnetization [18] and low remanent [19], while silicone rubber possesses excellent aging properties [20], good thermal and processability [21,22], as well as their low modulus that manages to facilitate the magneto-mechanical interaction [23]. One kind of silicone rubber, which has been every so often adopted as the matrix of MREs in the recent works is polydimethylsiloxane (PDMS). This is due to the excellent adhesive property with iron and low viscosity of its precursor and thus promoting homogeneous particles distribution and ease of MRE fabrication, while also avoiding the possibility of particle agglomeration [24–27].

Research works pertaining to magnetostriction of MRE based on iron particles and silicone rubber (SRFE) can be found in the literature, and the trend over the year suggests utilizing low-modulus elastomer in order to augment the magnetostriction magnitude, while lowering the magnetic field imposed. As far as particle distribution is concerned, orientation of chain-like structure (anisotropic) produces higher magnetostriction than random isotropic. Bednarek [28] was the earliest pioneer to study MRE based on SRFE more than 20 years ago and reported a relative magnetostriction of about 1% in magnetic fields up to 8 T using silicone rubber with elastic modulus of 0.25 MPa. Afterward, a similar author [29] incorporated pores in the MRE (foam-like) and obtained the maximum magnetostriction of 4.81%. In another study, Guan et al. [1] studied the magnetostriction on isotropic and anisotropic MRE based on SRFE with three different particle volume fractions (15, 20 and 27 vol%) and observed a maximum magnetostriction of 0.0184% for the anisotropic MRE and 0.0134% for the isotropic MRE. From this point onwards, many studies on magnetostriction of MRE seem to employ low stiffness in their samples. This was demonstrated by Abramchuk et al. [30], at which higher magnetostriction magnitude (11.6%) was achieved than previous studies in a MRE based on SRFE with storage modulus of 13.5 kPa. Later on, Diguet et al. [31] also used low storage modulus silicone rubber (47 kPa) to fabricate an isotropic MRE, and were able to produce a magnetostriction magnitude of 9.2%. The trend of using low stiffness MRE was continued by Saveliev et al. [2], in which they obtained the largest measured magnetostriction in MRE based on SRFE (approximately 20%). Such large magnetostriction value is made possible due to the low modulus of MRE. The MRE, which is made of PDMS matrix along with other additives

such as plasticizer, has a storage modulus of 30 kPa. They also investigated the effect of the MRE storage modulus on the magnetostriction by fabricating three samples varying in modulus (30, 40 and 50 kPa) and concluded that magnetostriction increased with decreasing modulus of MRE, where the particles' orientation in a chain-like structure influenced the magnetostriction considerably.

All of the aforementioned works on low-modulus MRE are known to use some form of additives to reduce the stiffness of the matrix. In fact, the fabricated MRE samples have disproportionately lower modulus than the bare silicon rubber. As an example, the low storage modulus of MRE obtained in the work of Saveliev et al. [2] is actually significantly lower than the bare PDMS. Lötters et al. [32] reported that the storage modulus of PDMS fabricated with the standardized ratio of 10:1 with its curing agent was 250 kPa. Such value of storage modulus is expected to increase when magnetic particles are added to the PDMS to fabricate the MRE without using any form of additives such as plasticizer or chain extender modifier. Indeed, it has become apparent that the nature of magnetostriction behavior of MRE is significantly affected based on the constituent materials, particles' concentrations, distribution and sample shape as well as the elastic modulus of the polymer matrix. Although the use of the low modulus of MRE can produce higher magnetostriction value [2], problems such as short lifespan and low durability should arise when integrating the MRE in some high-performance sensor application [33]. As an example, for a multi-fingered sensor hand of a robot which is required to dexterously grasp and manipulate an object, the use of low modulus of elastomer may cause handling problems and be unable to bear a larger load due to unstable structure, and thus limiting the application to relatively light and soft objects only [34,35]. Additionally, the majority of works on magnetostriction of MRE based on SRFE focuses on the study of a low stiffness elastomer. The popularity of utilizing soft silicon rubber has limited the investigation of MRE with storage modulus higher than 300 kPa. In fact, reported storage modulus values of MRE based on SRFE in the literature range from 13.5 kPa [30] to 200 kPa [1,36] while Young's modulus takes values from 0.25 [29] to 1100 MPa [7] in magnetostriction studies.

A higher storage modulus indicates that the material can store more energy. As an example, at very low frequencies, the rate of shear is very low, and hence, the capacity to retain the original strength of the media is very high. The rate of shear increases as the frequency and amount of energy input to the polymer matrix chains are increased. Because the storage modulus determines a polymer matrix's solid-like character, the higher the storage modulus, the more difficult it is to break down the polymer matrix and prolong its durability performance. After removing the applied force, material flow recovery will be greater than a smaller storage modulus value. Taking these points into consideration, the magnetostriction of MRE based on SRFE with storage modulus above 300 kPa is an important matter worthy of investigation. Therefore, this paper presents a set of experiments to study the magnetostriction of MREs with storage modulus above 300 kPa. In order to achieve this target, MRE samples are made utilizing polydimethylsiloxane (PDMS) silicone rubber with different weight fraction of the CIPs, followed by the morphology investigation to show the microstructure characterization. Then, the field-dependent magnetostriction and normal force of MRE samples are evaluated and the results are discussed in the sense sensor applications.

2. Materials and Methods

2.1. Material and Preparation of MRE

The matrix material used to fabricate the MRE samples was polydimethylsiloxane (PDMS) silicone rubber from SYLGARD™184 (The Dow Chemical Company, Midland, MI, USA). The base matrix consisted of two parts, a curing agent and a low viscosity of liquid silicone rubber (base agent) which smoothen its fabrication process and handling. The density of PMDS-based matrix is 1.1 g/cm^3. The particles that used the MRE were carbonyl iron particles (CIPs) type OM from BASF (Ludwigshafen, Germany). The CIPs had an average diameter of 5 μm with a spherical shape and were a type of soft magnetic particle.

The CIPs' density was approximately 7.874 g/cm^3 and the purity of iron in the CIPs was high (99.9%). This type of CIPs was reported to have high saturation magnetization, high permeability and low remanent magnetization [37–39]. The experimental procedure for fabricating the PDMS-based MRE is as follows. Firstly, the base agent and hardener of PDMS at a weight ratio 10:1 was firstly mixed evenly using a mechanical stirrer at room temperature for about 10 min. Then, the CIP was added to the mixture and stirred sufficiently for another 10 min. The final mixture was poured into a mold to ensure a 1 mm thickness of samples. The mold then was placed into a vacuum chamber for 30 min to eliminate the unwanted bubbles. The curing process was carried out in an oven at 100 °C for approximately 35 min without the presence of a magnetic field and the mold was left to cool down before removing the MRE sheet from the mold. Afterward, the MRE sheet was cut using a hole puncher into a circular shape with a diameter of 20 mm and thickness of 1 mm for magnetostriction measurements. In this research, three different samples varying in CIPs weight concentrations (60, 70 and 80 wt.%) were prepared. The CIPs concentrations was measured in weight percentages relative to the total weight of the sample. In an effort to meet the selection criteria (storage modulus of MRE above 300 kPa), initial tests were performed on the prepared samples to determine the storage modulus. The range of storage modulus varies from 350 up to 743 kPa depending on the CIP content in the MRE sample. Table 1 summarizes CIP and PDMS compositions of the fabricated MREs and their respective storage modulus.

Table 1. Details on the proportions of components and storage modulus of MRE samples.

Samples	Particle's Weight (%)	Sylgard 84 (10:1 wt%)	Storage Modulus (kPa)
MRE 60 wt.%	60	40	350
MRE 70 wt.%	70	30	680
MRE 80 wt.%	80	20	743

2.2. Microstructure Observation and Magnetostriction Measurements

Field-emission scanning electron microscopy (FESEM) (JEOL JSM 7800F, Tokyo, Japan) was used to observe the microstructure of PDMS-based MREs. For FESEM, the samples were sliced into extremely small pieces (5 × 1 mm) and coated with a thin layer of gold prior to perform the analysis in order to prevent charging of the surface and to provide a homogeneous surface for analysis and imaging. The cross-section of the samples was examined at an acceleration voltage of 2 kV under magnifications up to 1200×. Magnetostriction measurements were conducted using a commercial rheometer (Modal: Physica MCR302, Anton Paar, Graz, Austria equipped with a MR device (MRD 170/1 T). The intensity of the magnetic field was controlled by adjusting the current applied to the electromagnetic coil. The MRE samples were placed between a parallel base plate and the pedestal. The magnetic field was generated perpendicular to the disk plane and going through the samples. In order to ensure a homogeneous magnetic field is being applied on the MRE sample, the two-part metal cover was used to close the magnetic generator (MRD 170 controller). Figure 1a,b show the schematic of the rheometer (MCR302) and the two-part metal cover (MRD 170 controller). It is noted that the H vector arrows representing the flow of magnetic field shown in Figure 1 are an idealized concept of magnetic flow within the rheometer and do not indicate field concentration areas. This kind of ideal working condition to illustrate the magnetic flow within the rheometer is normally provided by the rheometer manufacturing company (Anton Paar in this work). In addition, it is remarked that the research on the simulation of actual field flow is beyond the scope of this work.

The magnetostriction measurement was carried out as follows. The current (I) was set using the computer and supplied to the electromagnet coil to generate a uniform magnetic field, H on the MRE. The current between 0 to 3 A was varied to achieve magnetic field excitations in the range of 0 to 0.6 T during the tests. Table 2 describes the current magnitude relative to the magnetic field. The change in length (Δl) of the sample (magnetostriction) was detected by the parallel base plate and determined from the difference between the

initial (l) and the final length of the sample as given in Figure 1c. In comparison with the most commonly used strain gauge method, magnetostriction measurements via rheometer method are tailored toward samples having extremely thin thickness (approximately 1 mm) and being small in diameter. In such cases, attachment of a conventional strain gauge to a soft and small MRE can possibly alter its deformation and magnetostriction measurement. Conversely, the existing strain gauge method may work well for classical magnetostrictive materials which are usually relatively rigid (the elastic modulus is in range of 10^{11} Pa).

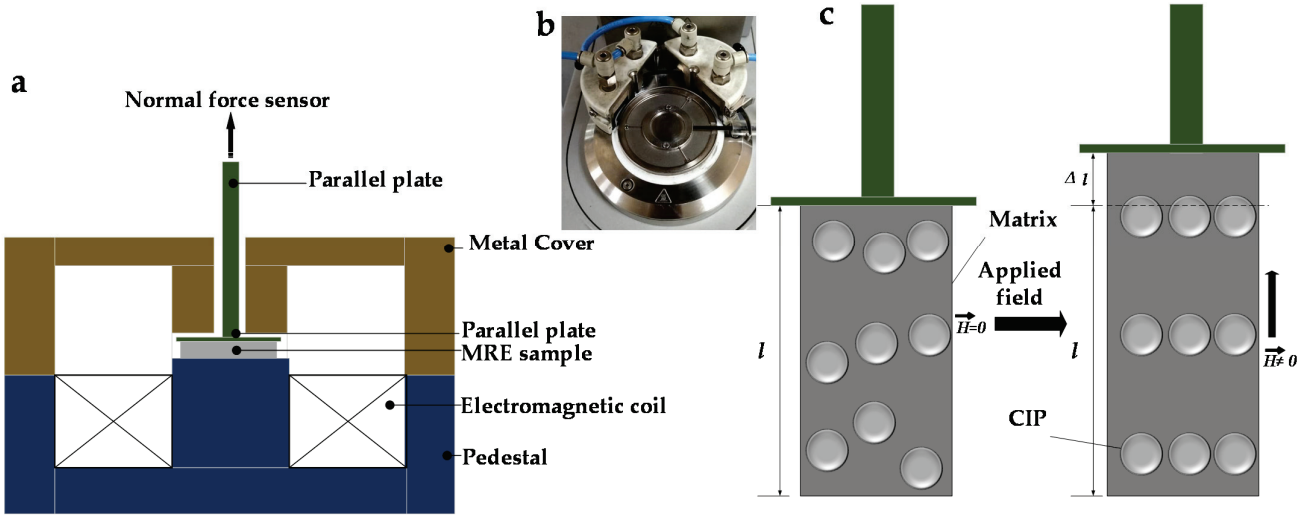

Figure 1. Experimental set-up of magnetostriction measurement (**a**) Schematic illustration of rheometer, (**b**) the two-part metal cover (MRD 170 controller) and (**c**) schematic illustration of the MRE under a magnetic field: *H* is the magnetic field intensity, *l* is the length of sample.

Table 2. The current magnitude relative to the magnetic field.

Current (A)	Magnetic Field (T)
0	0
1	0.21
2	0.39
3	0.61

3. Results and Discussion

3.1. Morphology Characteristic

Figure 2 shows the cross-section surface imaging for all three microstructures of the MRE samples. A random distribution of CIPs which forms an isotropic structure was observed homogenously distributed and well embedded within the elastomer matrix. However, some voids seemed to appear as well. Figure 2a represents the MRE with 60 wt.% with a little agglomeration of CIPs, though the level of agglomeration as well as voids increase with higher CIP concentration. The same observation is noticeable in Figure 2b,c for samples with 70 and 80 wt.% CIPs, respectively. Furthermore, the higher concentration of CIPs in MRE, the denser the matrix was occupied with CIPs, indicative of lesser space and closer distance between CIPs.

3.2. Effects of Particles' Weight Percentage on Magnetostriction of MRE

In general, a particular feature of the material employed in sensors is the ability to produce a reaction force in order to interact with the external stimulus and to generate movement. In this study, when the MRE sample was under the presence of magnetic field, the CIPs embedded within the matrix rubber become magnetized. Concurrently, the magnetic moments of the CIPs tended to rearrange themselves to be realigned in the direction of the applied magnetic field. This resulted in interaction between the CIPs and the

forming of a chainlike structure, which consequently led to deformation or magnetostriction of MRE. An induced/reaction force, which is also called a normal force, was generated at the same time. Thus, to better understand the reaction force of the material, the normal force was studied alongside the magnetostriction under various strengths of magnetic field (from 0 to 0.6 T). The graphs of magnetostriction and normal force as functions of magnetic fields are presented in Figure 3.

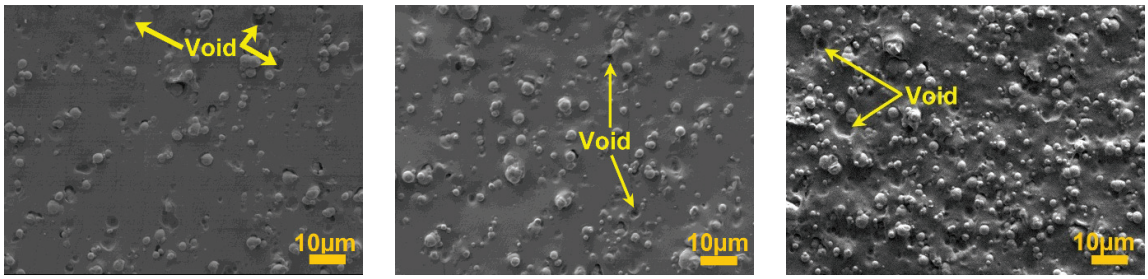

(**a**) (**b**) (**c**)

Figure 2. Microstructure of PDMS MREs under magnifications of 1200× with CIPs of (**a**) 60, (**b**) 70, and (**c**) 80 wt.%.

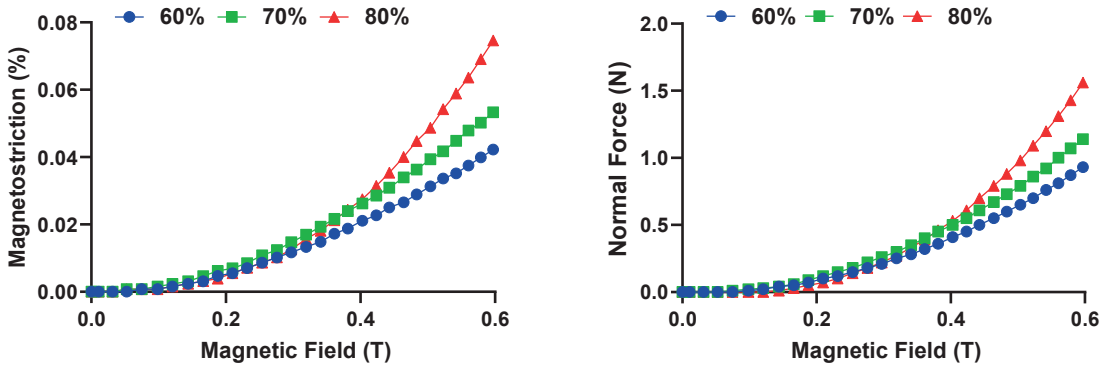

(**a**) (**b**)

Figure 3. The curves of (**a**) magnetostriction and (**b**) normal force versus the magnetic field with various concentrations of CIPs.

The curves of magnetostriction as shown in Figure 3a show that all MRE samples are experiencing an increase in magnetostriction under the influence of a magnetic field, indicative of the fact that the samples were elongated. The general behavior of such an increase in magnetostriction can be divided into three main stages. In the initial state, all MRE samples have not exhibited magnetostriction when a magnetic field was first imposed until up to approximately 0.1 T. A similar occurrence has been reported in the past work [2] and such benign effects may be attributed to the higher constraining force of the elastomer matrix than the magnetized CIP in MRE, which prevents magnetostriction from occurring at a low magnetic field. From 0.1 until 0.3 T, there was a slight increase in magnetostriction for all MRE samples, and at this range of magnetic field, the magnetostriction curves almost coincided, which was the indication of similar increasing rate. A magnetic field of 0.3 T marked the onset of diverging curves of magnetostriction, where after that point, MRE 80 wt.% displayed a steeper increase in magnetostriction than MRE 70 and 60 wt.%. The magnetostriction curves culminated at a magnetic field of 0.6 T with MRE 80 wt.% exhibiting the highest magnetostriction value (0.075%), followed by the MRE 70 wt.% (0.05%) and MRE 60 wt.% (0.04%). By comparison, the magnetostriction value obtained in this study has shown an improvement of 4.5-fold compared to the previous study [1] for similar CIPs structure (isotropic) and 3-fold for the aligned CIPs (anisotropic), while applying 25% less maximum magnetic field.

On the other hand, Figure 3b shows the change of normal force as a function of a magnetic field. Overall, all MRE samples with various CIPs weight concertation demonstrated a gradual increase in the normal force as the magnetic field was increased. Such an increasing trend was interestingly analogous to the increase in magnetostriction value as increasing the magnetic field. The rate of increase, as well as the curves' steepness of the normal force, were qualitatively similar to the magnetostriction curves. The MRE with 80 wt.% of CIPs generated the highest maximum normal force, which was larger than 1.5 N at 0.6 T. Such force was approximately 40 and 70% higher than the MRE sample with 70 and 60 wt.%, respectively. In terms of sensitivity of the MRE material, the sample with 60 wt.% CIP demonstrated a high sensitivity towards the normal force, which was capable of detecting as low as 0.01 N at 0.072 T and thereby making it suitable for sensor applications, since high sensitivity is required during usage. Table 3 summarizes the relative magnetic field required of all samples to detect a normal force of 0.01 N.

Table 3. Summary of the sensitivity of the MRE material to detect 0.01 N.

Samples	Magnetic Field (T)
MRE 60 wt.%	0.72
MRE 70 wt.%	0.74
MRE 80 wt.%	0.78

The different rates of increase in magnetostriction and normal force at different intensities of magnetic field could be attributed to the critical value of the magnetic field strength [40,41]. At the initial state, the elastic interactions of the matrix were more dominant than the magnetic interactions (between the magnetized CIPs) due to the magnetic field strength being lower than the critical value. This led to restrictive movement of CIPs. This phenomenon has been observed in [40] and was explained by the fact that the magnetically-induced CIPs were insufficient to overcome the elastic energy barrier of the elastomer matrix in order to elongate. At a certain critical value of the magnetic field strength, the elastic interactions were comparable with magnetic interactions. As the magnetic field exceeded a particular threshold of magnetic field (higher than the critical value), the magnetic interaction was prevailing over the elastic interactions, which accelerated the movement of CIPs for realignment process. As a result, the rate of increase in magnetostriction and normal force became faster. Figure 4 presents a comparison of the magnetostriction magnitude with other previous studies regarding the storage and Young's modulus of MRE. To some extent, the difference in the constituent materials, particles' concentrations, distribution and the imposed magnetic field on the MRE made fair and direct comparison between results difficult. However, a superficial analysis of the orders of magnitude of the magnetostriction and the respective modulus of the MRE revealed appealing results. As shown in Figure 3, the magnetostriction values in the present work are nearly 0.08% with storage modulus of 743 kPa, which well eclipses the previous results. Thus, it indicated that the aspect ratio of a sample could affect the magnetostriction of MRE to a certain degree. Additionally, the range of storage modulus from 300 to 750 kPa was an ideal range for potential applications in force sensors [42,43] and actuators [44–46], since moderate stiffness could ensure high durability of the sensor device, while maintaining sufficient magnetostriction magnitude.

It is remarked here that the distribution of the CIP would affect the magnetostriction. A couple of the previous works have reported that pre-aligning the CIPs along the direction of magnetic field would increase the magnetostriction value, whereas pre-aligning the CIPs in the transverse direction would decrease the magnetostriction value. However, this phenomenon has not always been the case, since other works demonstrated lower magnetostriction value compared to random distribution. This is attributed to the increase in MRE stiffness, which inhibits elongation.

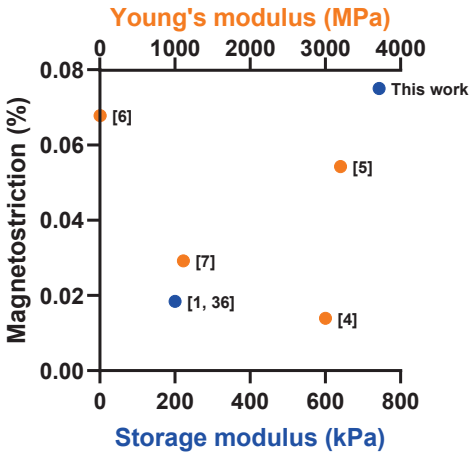

Figure 4. Comparison of magnetostriction obtained versus the storage/Young's modulus [1,4–7,36].

3.3. Normal Force under Cyclic Magnetic Loading at Different Strains

The following sets of experiments were designed from the viewpoint of practical sensor applications. Such experiments could be used to evaluate the reusability and reproducibility of the generated normal force of the MRE. In order to simulate the material used under real settings, the MRE was subjected to continuous cyclic increase and decrease in the magnetic field between the maximum field amplitude (H = 0.6 T) and zero magnitude. The stepwise increase and decrease in the magnetic field were consecutively repeated several times (10 cycles of stepwise increase and decrease) at shear strain of 0.01%, 0.1% and 1%. In addition, previous works have reported that hysteresis phenomena such as storage and loss modulus and magnetostriction were evident in MRE [40,41,47,48]. Therefore, it should be expected that there would be hysteresis in the normal force as well. In this section, the MRE of 80 wt% was chosen for a further hysteresis analysis since it showed the highest normal force value. Figure 5 shows the change in normal force of MRE with 80 wt.% CIP as function of stepwise magnetic fields between zero field and 0.6 T. The color transition from light to dark blue of curves denoted the stages of the cyclic experiment, where the light and the dark colors indicated the initial and final stage of the magnetic cycle, respectively. In Figure 5a, the relative curve of increase and decrease in normal force as a result of the imposing and removing of a magnetic field is evidently nonlinear. The path corresponding to the ascending and descending of normal force as a function of magnetic field at strain amplitude of 0.01% differs, indicative of hysteresis behavior in the MRE material. It is observed that the descending branch of normal force was larger than the ascending branch. Qualitative comparison between the initial and each subsequent cycle of magnetic field loading showed the curves shifted upward and tended to reach saturation in the last few cycles. At strain amplitude of 0.1%, the change in normal force as a function of magnetic load has similar characteristics to the strain of 0.01% as given in Figure 5b. It is seen that the normal force at strain amplitude of 0.1% increases with the increasing magnetic field intensity and decreases with decreasing magnetic field intensity. Overall, all curves' shapes of ascending and descending of normal force were reproduced very well for the three-shear strain imposed. A quantitative comparison between every cycle of magnetic field showed little variations in patterns of ascending and descending of normal force. The maximum normal force, however, decreases with increment of shear strain, and this was due to the shear stress on the MRE material. With increasing shear strain, the inter-CIPs distance decreases and under the influence of a magnetic field, the magnetic moment in every CIP was induced and rotated. As a result, CIPs tended to align in the direction of the external magnetic field and induced an attraction force within each CIP. The closer distance between CIPs led to a greater force of attraction between the CIPs. However, at a larger shear strain, the structure formed between the magnetized CIPs might break and consequently reduce the elastic energy boundary. Previous works [49,50] have reported that the elastic modulus of MRE decreases with increasing shear strain, and this caused the normal force to decrease as well.

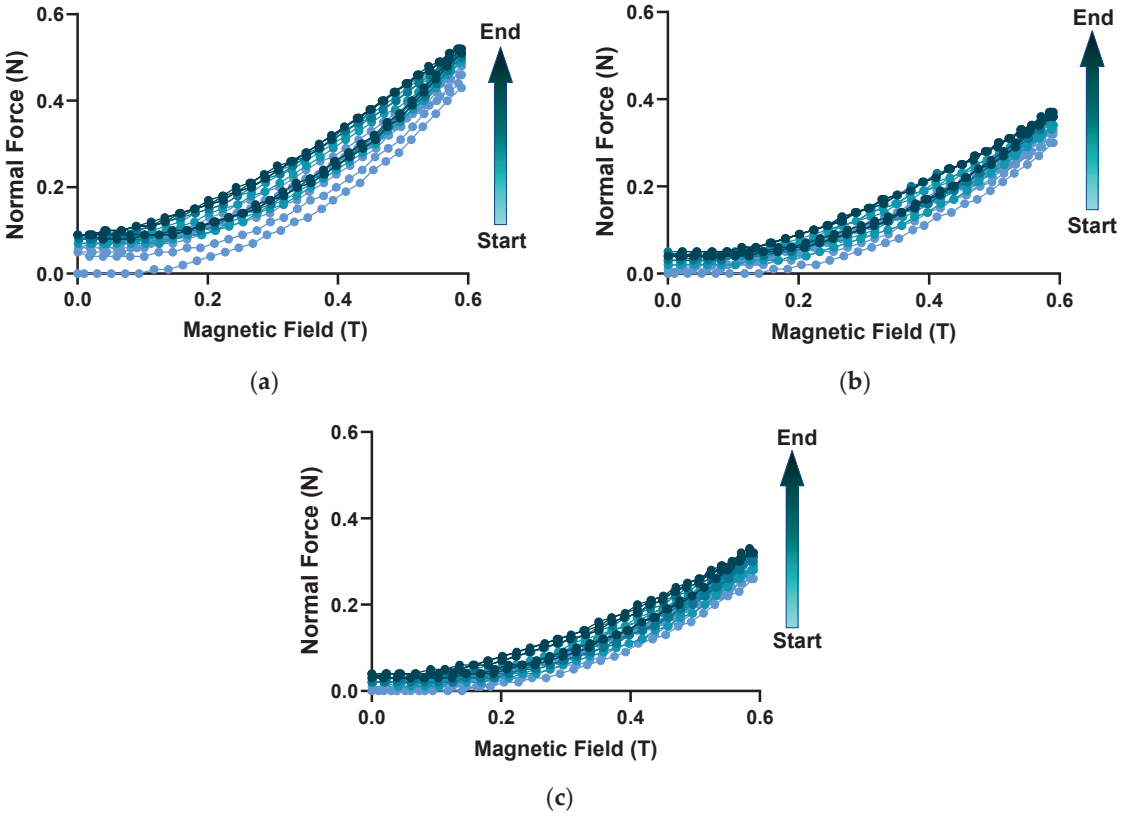

Figure 5. Comparison of normal force at shear strain of (**a**) 0.01%, (**b**) 0.1% and (**c**) 1% versus the magnetic field.

Similar phenomenon such as the descending branch of normal force above the ascending branch could also be seen, as well as the upward shift of normal force curves as the number of loading cycles increases, though the maximum normal force value decreases to nearly 0.4 N when imposing higher shear strain (0.1%) than previous shear strain amplitude (0.01%). In addition, increasing the shear strain amplitude to 1% hardly affected the curve of normal force as given in Figure 5c. Regardless of whether the comparative basis was the nonlinear shape of the ascending and descending of normal force or the pronounced upward shift of normal force curves with the increase in loading cycles, the MRE material nonetheless exhibited hysteresis phenomenon at a strain amplitude of 1%. The increase in strain amplitude from 0.1% to 1% resulted in lower magnitude of maximum normal force (slightly above 0.3 N at 1% strain), and while this figure was considered the lowest maximum normal force among all shear strain amplitudes, the highest maximum normal force was evidently produced at strain amplitude of 0.01% (slightly above 0.5 N). In order to quantify the hysteresis phenomenon in MRE, the employment of the changes of the maximum normal force (λ) during the course of increasing/decreasing in the magnetic cycles was examined. In particular, the shift, λ, is calculated by subtracting the relative maximum normal force in the nth (F_n) from the maximum normal force (F_1) in the initial cycle. The total subtraction value (ΔF) is then divided by F_1. The constitutive equation to determine λ is given by:

$$\lambda = (F_n - F_1)/F_1, \quad (1)$$

Figure 6 shows the curves of parameter λ, which commendably reflects the changes of the maximum normal force of MRE in the magnetic cycles for the three different strain amplitudes imposed. For all three data sets, the parameter λ tended to grow with the continuous increase in number of cycles until a saturation point was reached. At shear strain of 0.01%, the increases of parameter λ were measured on the order of 18% and saturated at the 7th cycle. Meanwhile, under the shear strain of 0.1%, the curves of

parameter λ demonstrated an almost similar growth trend to the strain of 0.01%, though the former marginally instigated a larger shift of normal force magnitude (about 5% higher).

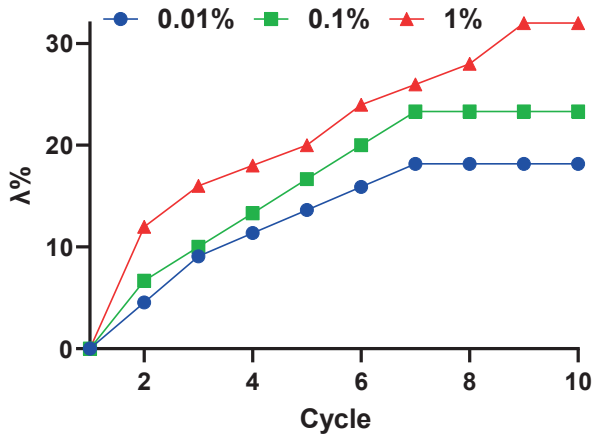

Figure 6. Dependence of the parameter λ on the number of cycles loading.

Significant changes could be seen within the first cycle and only moderate changes (3%) for the following cycles. A linear increase in parameter λ could also be observed with the corresponding rates of its growth per cycle, which was approximately 3% from the second cycle up to the saturation point (7th cycle). The hysteresis nature of the MRE was more prevalent under shear strain of 1%, with parameter λ measuring a larger value than its counterpart (about 8% higher than 0.1% strain and 14% higher than 0.01% strain). Furthermore, at 1% shear strain, the parameter λ continued to grow after the 7th cycle and saturated much later at the 9th cycle. The high magnitude of λ indicated that the displacement of interfacial slipping between the CIP and the matrix was large enough to warrant shifting of maximum normal force, and that the relative shift of maximum normal force accumulated with the increases of cyclic loading. A comparison between the first cycle and second cycle has a significant increase in parameter λ for all values of shear strain and such behavior was more predominant with higher shear strain. A considerable change of λ in between the first cycle and second cycle were congruent with the initial (increasing/decreasing magnetic field) curve of normal force from the subsequent cycles as depicted in Figure 6. Similar phenomena have been reported for magnetic hysteresis behavior [51], dynamic modulus [40], normal force [40,48] and dielectric permittivity [52]. A large change of λ between the first and second cycle implied that principal restructuring of the CIPs occurred during the first cycle, which resulted in major shift of maximum normal force, but minor in the subsequent cycle. The underlying reason for the hysteretic behavior in MRE could be attributed to the dependence of CIPs restructuring/restructuring on the history of magnetic loading-unloading.

An examination on the CIP's state of motion might reveal what likely transpires on the microscale level and possibly explain the working mechanism behind the MRE hysteresis phenomenon. Theoretically, the MRE hysteresis phenomenon was related to the transition of phases of the continuous loading cycle. At zero magnetic field, the CIP and matrix of the MRE were in equilibrium, and when exposed to a magnetic field, the CIP tended to move along the direction of the magnetic field from its initial position, while being pushed by the attraction from the nearest neighboring CIP. The distance between the CIP and its origin position grew, while the distance between CIPs closes and the CIPs interacted. As a result, the elastomer molecular chain stretched longer, producing a magnetostriction effect in the MRE sample. Correspondingly, as the magnetic field was gradually decreased to zero from its maximum value with a constant shear, the CIP was inclined to return back to its initial position driven by the elastic force of the elastomer matrix. The CIP, however, has not immediately returned to its initial position, but relocated to a new position, which led to some remanent appearing. This caused the initial value of normal force to shift as compared

to the previous cycle. Over the course of continuous cyclic ascending and descending of the magnetic field, the remanent along with the stretching of the elastomer molecular chain grew, thus shifting the maximum normal force to a higher value until a state of saturation was achieved. Additionally, larger shear strain caused larger bond rupture between the CIP and the polymer matrix, which was an interesting corollary to the increase in distance between the CIP and its initial positions. Consequently, the displacement of interfacial slipping between the CIP and the matrix was also increased with larger shear strain, and hence, a larger shift of maximum normal force taken place.

Table 4 summarized the field-dependent magnetostriction of MRE currently available in the literature along with the storage modulus value. A direct and shallow comparison between the studies demonstrates a disproportionately higher magnetostriction magnitude for the low modulus of MRE than the midrange modulus of MRE. In spite of this, an assessment on other factors such as the costs of the manufacturing of such materials, the durability performance and the types of sensor application may reveal an interesting outcome.

Figure 7 is a representation of the state-of-the-art robotic gripper utilizing MREs as a force sensor. The robotic gripper, which has a simple structure, can grasp diverse arbitrary objects, while the force sensor attached to the end effector of the gripper can measure the reaction forces. When assigned to repetitive tasks and prolonged use of the robotic gripper, several issues which are often associated with the durability of MRE such as elastic stretching, cross-link disengagement, inelastic deformation, structural shift by phase transformation, microplasticity and microphase separation can arise [53,54]. In particular, the implementation of low-modulus MRE on the robotic gripper can theoretically accelerate these processes within a finite interval of time, and consequently, permanent deformation or a non-reversible change in shape of the MRE may ensue. Such phenomena can be further explained by the fundamental principle of storing energy performance in MRE. A material with a higher storage modulus has the potency to store more energy. For example, the rate of shear is low at very low frequencies, hence, the capability to retain the original strength of the media is high. As the rate of shear increases with frequency, the amount of energy stored to the polymer matrix chains also increases. The storage modulus, which primarily determines the elastomer matrix's solid-like character, also plays an important role in the strength and rigidity of the material. A midrange modulus MRE possesses better strength and is harder to break down its elastomer matrix than the low-modulus MRE. Shape-retaining and recovering after removing the applied force will be better with a midrange modulus MRE than that of a low-storage modulus. Therefore, the implementation of a midrange modulus MRE as a sensor can improve its durability performance and prolong its life cycle.

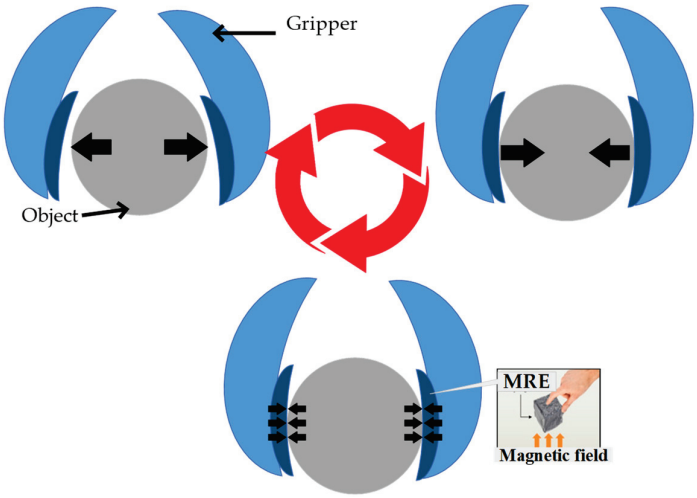

Figure 7. The cycle of use of soft robotic gripper with MREs.

Table 4. Selected studies investigating the magnetostriction of MRE along with the storage modulus value.

Modulus (kPa)	Magnetostriction	Reference
13.5	11.6%	Abramchuk [30]
47	9.2%	Diguet [31]
47	20%	Saveliev [2]
47	0.0134%	Guan [1]
350–743	0.04–0.075%	This work

4. Conclusions

The current work presented comprehensive investigation of magnetostriction in MRE with moderate modulus by imposing the homogeneous magnetic field. Apart from magnetostriction, the MRE has the capability to produce a reaction force called the normal force. The MRE samples with different concentrations of CIPs ranging from 60 to 80 wt%. were successfully prepared. The highest magnetostriction achieved by the MRE of 80 wt% CIP was 0.075% and the normal force produced was 1.56 N at 0.6 T. The measured magnetostriction was considered as an improvement over the MRE with similar range of modulus found in the literature. Nevertheless, the magnetostriction improvement is regarded as not outstanding (approximately 3-fold higher than the previous work [1] for the aligned CIPs and 4.5-fold for similar CIPs structure). This would certainly depend upon the comparison of the relevant fabrication and experimental parameters such as the intensity of magnetic field (25% less maximum magnetic field than [1]), stiffer MRE samples (nearly three-fold higher storage modulus than [1]) and the structure of the embedded CIPs in MRE. As such, the trivial enhancement of magnetostriction achieved can still be particularly valuable in soft sensor design that requires a corresponding increase in the magnitude. Meanwhile, the results demonstrated that the MRE with 60, 70 and 80 wt% showed a trend of increase in the magnetostriction percentage and normal force that was parallel with the increased concentration of CIPs. With regard to the sensitivity of the MRE material, as low as 0.01 N of normal force can be detected while employing a small amount of magnetic field (0.072 T). In general, high sensitivity with change in magnetic field is sought after in soft sensor applications. In particular, a soft robotic gripper with an MRE will be able to have an infinitesimal deformation upon being triggered by a magnetic field and thus easier to predict the response of closing patterns accurately upon contact or touch with the object. Additionally, such a trait is exceptionally useful for selecting grasping patterns according to the object nature.

On the other hand, the hysteresis analysis showed that the maximum normal force produced by the MRE with 80 wt% CIP increases with the number of cycle loads of magnetic field until a saturation point was reached. The change of maximum normal force was dependent on the shear strain amplitude. In other words, higher amplitude of shear strain resulted in greater change of maximum normal force. Based on the presented results, the midrange modulus MRE herein could be considered as a viable candidate for specific sensor applications, namely, force sensors [42,43], since moderate stiffness could ensure high durability of the sensor device, while maintaining sufficient magnetostriction magnitude. Characterization of various temperature effects on the magnetostriction performance will be a beneficial starting point for future work given that the utilization of MRE in sensor will not be restricted to a particular scenario, yet able to function even in extreme conditions. It is finally noted that manufacturing of a specific MRE-based sensor device and its experimental performances such as accuracy and signal producing remain as future works.

Author Contributions: M.A.T.: Writing—original draft preparation, methodology, investigation, validation; S.A.M., M.A.F.J. and S.-B.C.: supervision, conceptualization, writing—reviewing and editing, funding acquisition; N.A.N.: supervision, writing—reviewing and editing; S.A.A.A.: writing—reviewing and editing; I.B.: writing—reviewing and editing; S.Y.M.Y.: writing—reviewing and editing; S.-B.C.: reviewing and editing. All authors participated in writing the manuscript. All authors have read and agreed to the published version of the manuscript.

Funding: This research work is supported and funded by Universiti Teknologi Malaysia (UTM) under Fundamental Research (Vot. No. 22H14) and Professional Development Research University (PDRU) (Vot. No.06E29).

Data Availability Statement: The raw/processed data required to reproduce these findings cannot be shared at this time as the data also form part of an ongoing study. In future, however, the raw data required to reproduce these findings will be available from the corresponding authors.

Conflicts of Interest: The authors declare no conflict of interest. The authors also declare that they have no known competing financial interests or personal relationships that could have appeared to influence the work reported in this paper.

References

1. Guan, X.; Dong, X.; Ou, J. Magnetostrictive Effect of Magnetorheological Elastomer. *J. Magn. Magn. Mater.* **2008**, *320*, 158–163. [CrossRef]
2. Saveliev, D.V.; Belyaeva, I.A.; Chashin, D.V.; Fetisov, L.Y.; Romeis, D.; Kettl, W.; Kramarenko, E.Y.; Saphiannikova, M.; Stepanov, G.V.; Shamonin, M. Giant Extensional Strain of Magnetoactive Elastomeric Cylinders in Uniform Magnetic Fields. *Materials* **2020**, *13*, 3297. [CrossRef] [PubMed]
3. Dapino, M.J. On Magnetostrictive Materials and Their Use in Adaptive Structures. *Struct. Eng. Mech.* **2004**, *17*, 303–329. [CrossRef]
4. Nersessian, N.; Or, S.W.; Carman, G.P.; Choe, W.; Radousky, H.B. Hollow and Solid Spherical Magnetostrictive Particulate Composites. *J. Appl. Phys.* **2004**, *96*, 3362–3365. [CrossRef]
5. Liu, J.J.; Pan, Z.B.; Song, X.H.; Zhang, Z.R.; Ren, W.J. Enhanced Magnetostrictive Effect in Epoxy-Bonded Tb x Dy 0.9−x Nd 0.1 ($Fe_{0.8}Co_{0.2}$) 1.93 Pseudo 1–3 Particulate Composites. *J. Appl. Phys.* **2015**, *117*. [CrossRef]
6. Kaleta, J.; Lewandowski, D.; Mech, R. Magnetostriction of Field-Structural Composite with Terfenol-D Particles. *Arch. Civ. Mech. Eng.* **2015**, *15*, 897–902. [CrossRef]
7. Gonçalves, R.; Larrea, A.; Sebastian, M.S.; Sebastian, V.; Martins, P.; Lanceros-Mendez, S. Synthesis and Size Dependent Magnetostrictive Response of Ferrite Nanoparticles and Their Application in Magnetoelectric Polymer-Based Multiferroic Sensors. *J. Mater. Chem. C* **2016**, *4*, 10701–10706. [CrossRef]
8. Altin, G.; Ho, K.K.; Henry, C.P.; Carman, G.P. Static Properties of Crystallographically Aligned Terfenol-D/polymer Composites. *J. Appl. Phys.* **2007**, *101*, 033537. [CrossRef]
9. Rhyne, J.J.; Legvold, S. Magnetostriction of Tb Single Crystals. *Phys. Rev.* **1965**, *138*, A507–A514. [CrossRef]
10. Dobrzanski, L.; Tomiczek, A.; Nabiałek, A.; Zuberek, R. Structure and Magnetic Properties of Magnetostrictive Tb0.3Dy0.7Fe1.9/Polyurethane Composite Materials. *J. Achiev. Mater. Manuf. Eng.* **2010**, *43*, 527–532.
11. Rodríguez, C.; Barrio, A.; Orue, I.; Vilas, J.L.; León, L.M.; Barandiarán, J.M.; Ruiz, M.F.-G. High Magnetostriction Polymer-Bonded Terfenol-D Composites. *Sens. Actuators A Phys.* **2008**, *142*, 538–541. [CrossRef]
12. Yoo, B.; Na, S.M.; Pines, D.J. Influence of Particle Size and Filling Factor of Galfenol Flakes on Sensing Performance of Magnetostrictive Composite Transducers. *IEEE Trans. Magn.* **2015**, *51*, 2503204. [CrossRef]
13. Hong, J.I.; Solomon, V.C.; Smith, D.J.; Parker, F.T.; Summers, E.M.; Berkowitz, A.E. One-Step Production of Optimized Fe–Ga Particles by Spark Erosion. *Appl. Phys. Lett.* **2006**, *89*, 142506. [CrossRef]
14. Li, J.; Gao, X.; Zhu, J.; Jia, J.; Zhang, M. The Microstructure of Fe–Ga Powders and Magnetostriction of Bonded Composites. *Scr. Mater.* **2009**, *61*, 557–560. [CrossRef]
15. Walters, K.; Busbridge, S.; Walters, S. Magnetic Properties of Epoxy-Bonded Iron–Gallium Particulate Composites. *Smart Mater. Struct.* **2013**, *22*, 025009. [CrossRef]
16. Silva, J.A.; Gouveia, C.; Dinis, G.; Pinto, A.M.; Pereira, A.M. Giant Magnetostriction in Low-Concentration Magnetorheological Elastomers. *Compos. Part B Eng.* **2022**, *243*, 110125. [CrossRef]
17. Carlson, J.D.; Jolly, M.R. MR Fluid, Foam and Elastomer Devices. *Mechatronics* **2000**, *10*, 555–569. [CrossRef]
18. Lokander, M.; Stenberg, B. Performance of Isotropic Magnetorheological Rubber Materials. *Polym. Test.* **2003**, *22*, 245–251. [CrossRef]
19. Zhu, J.T.; Xu, Z.D.; Guo, Y.Q. Experimental and Modeling Study on Magnetorheological Elastomers with Different Matrices. *J. Mater. Civ. Eng.* **2013**, *25*, 1762–1771. [CrossRef]
20. Oldfield, D.; Symes, T. Long Term Natural Ageing of Silicone Elastomers. *Polym. Test.* **1996**, *15*, 115–128. [CrossRef]
21. Yu, Z.R.; Li, S.N.; Zang, J.; Zhang, M.; Gong, L.X.; Song, P.; Zhao, L.; Zhang, G.D.; Tang, L.C. Enhanced Mechanical Property and Flame Resistance of Graphene Oxide Nanocomposite Paper Modified with Functionalized Silica Nanoparticles. *Compos. Part B Eng.* **2019**, *177*, 107347. [CrossRef]
22. Song, P.; Song, J.; Zhang, Y. Stretchable Conductor Based on Carbon Nanotube/Carbon Black Silicone Rubber Nanocomposites with Highly Mechanical, Electrical Properties and Strain Sensitivity. *Compos. Part B Eng.* **2020**, *191*, 107979. [CrossRef]
23. Kostrov, S.A.; Gorodov, V.V.; Sokolov, B.O.; Muzafarov, A.M.; Kramarenko, E.Y. Low-Modulus Elastomeric Matrices for Magnetoactive Composites with a High Magnetic Field Response. *Polym. Sci.-Ser. A* **2020**, *62*, 383–391. [CrossRef]
24. Wei, B.; Gong, X.; Jiang, W. Influence of Polyurethane Properties on Mechanical Performances of Magnetorheological Elastomers. *J. Appl. Polym. Sci.* **2010**, *116*, 771–778. [CrossRef]

25. Ioppolo, T.; Otügen, M.V. Magnetorheological Polydimethylsiloxane Micro-Optical Resonator. *Opt. Lett.* **2010**, *35*, 2037–2039. [CrossRef]
26. Zhang, X.; Peng, S.; Wen, W.; Li, W. Analysis and Fabrication of Patterned Magnetorheological Elastomers. *Smart Mater. Struct.* **2008**, *17*, 045001. [CrossRef]
27. Xu, Z.; Wu, H.; Wang, Q.; Jiang, S.; Yi, L.; Wang, J. Study on Movement Mechanism of Magnetic Particles in Silicone Rubber-Based Magnetorheological Elastomers with Viscosity Change. *J. Magn. Magn. Mater.* **2020**, *494*, 165793. [CrossRef]
28. Bednarek, S. The Giant Volumetric Magnetostriction of Ferromagnetic Composites with Elastomer Matrix. *Mod. Phys. Lett. B* **1999**, *13*, 865–878. [CrossRef]
29. Bednarek, S. The Giant Linear Magnetostriction in Elastic Ferromagnetic Composites within a Porous Matrix. *J. Magn. Magn. Mater.* **2006**, *301*, 200–207. [CrossRef]
30. Abramchuk, S.; Kramarenko, E.; Grishin, D.; Stepanov, G.; Nikitin, L.V.; Filipcsei, G.; Khokhlov, A.R.; Zrínyi, M. Novel Highly Elastic Magnetic Materials for Dampers and Seals: Part, I.I. Material Behavior in a Magnetic Field. *Polym. Adv. Technol.* **2007**, *18*, 513–518. [CrossRef]
31. Diguet, G.; Beaugnon, E.; Cavaillé, J.Y. Shape Effect in the Magnetostriction of Ferromagnetic Composite. *J. Magn. Magn. Mater.* **2010**, *322*, 3337–3341. [CrossRef]
32. Lötters, J.C.; Olthuis, W.; Veltink, P.H.; Bergveld, P. The Mechanical Properties of the Rubber Elastic Polymer Polydimethylsiloxane for Sensor Applications. *J. Micromechanics Microeng.* **1997**, *7*, 145–147. [CrossRef]
33. Ahn, J.; Gu, J.; Choi, J.; Han, C.; Jeong, Y.; Park, J.; Cho, S.; Oh, Y.S.; Jeong, J.H.; Amjadi, M.; et al. A Review of Recent Advances in Electrically Driven Polymer-Based Flexible Actuators: Smart Materials, Structures, and Their Applications. *Adv. Mater. Technol.* **2022**, *7*, 2200041. [CrossRef]
34. Tsujio, S.; Chaen, T.; Yu, Y. High-Stiffness and High-Sensitivity 3-Axis Force Sensor Using Strain-Deformation Expansion Mechanism. In Proceedings of the 2006 IEEE/RSJ International Conference on Intelligent Robots and Systems, Beijing, China, 9–13 October 2006; pp. 4417–4422.
35. Jeong, Y.; Gu, J.; Byun, J.; Ahn, J.; Byun, J.; Kim, K.; Park, J.; Ko, J.; Jeong, J.; Amjadi, M.; et al. Ultra-Wide Range Pressure Sensor Based on a Microstructured Conductive Nanocomposite for Wearable Workout Monitoring. *Adv. Healthc. Mater.* **2021**, *10*, 2001461. [CrossRef]
36. Dong, X.; Ma, N.; Qi, M.; Li, J.; Chen, R.; Ou, J. The Pressure-Dependent MR Effect of Magnetorheological Elastomers. *Smart Mater. Struct.* **2012**, *21*, 075014. [CrossRef]
37. Tian, T.; Nakano, M. Fabrication and Characterisation of Anisotropic Magnetorheological Elastomer with 45° Iron Particle Alignment at Various Silicone Oil Concentrations. *J. Intell. Mater. Syst. Struct.* **2018**, *29*, 151–159. [CrossRef]
38. Cantera, M.A.; Behrooz, M.; Gibson, R.F.; Gordaninejad, F. Modeling of Magneto-Mechanical Response of Magnetorheological Elastomers (MRE) and MRE-Based Systems: A Review. *Smart Mater. Struct.* **2017**, *26*, 023001. [CrossRef]
39. Lee, C.J.; Kwon, S.H.; Choi, H.J.; Chung, K.H.; Jung, J.H. Enhanced Magnetorheological Performance of Carbonyl Iron/Natural Rubber Composite Elastomer with Gamma-Ferrite Additive. *Colloid Polym. Sci.* **2018**, *296*, 1609–1613. [CrossRef]
40. Sorokin, V.V.; Stepanov, G.V.; Shamonin, M.; Monkman, G.J.; Khokhlov, A.R.; Kramarenko, E.Y. Hysteresis of the Viscoelastic Properties and the Normal Force in Magnetically and Mechanically Soft Magnetoactive Elastomers: Effects of Filler Composition, Strain Amplitude and Magnetic Field. *Polymer* **2015**, *76*, 191–202. [CrossRef]
41. Zhang, Y.; Fang, F.; Huang, W.; Chen, Y.; Qi, S.; Yu, M. Dynamic Mechanical Hysteresis of Magnetorheological Elastomers Subjected to the Cyclic Loading and Periodic Magnetic Field. *Front. Mater.* **2019**, *6*, 292. [CrossRef]
42. Zhang, S.; Ge, C.; Liu, R. Mechanical Characterization of the Stress-Strain Behavior of the Polydimethylsiloxane (PDMS) Substate of Wearable Strain Sensors under Uniaxial Loading Conditions. *Sens. Actuators A Phys.* **2022**, *341*, 113580. [CrossRef]
43. Shintake, J.; Cacucciolo, V.; Floreano, D.; Shea, H. Soft Robotic Grippers. *Adv. Mater.* **2018**, *30*, 1707035. [CrossRef] [PubMed]
44. Santaniello, T.; Migliorini, L.; Locatelli, E.; Monaco, I.; Yan, Y.; Lenardi, C.; Franchini, M.C.; Milani, P. Hybrid Nanocomposites Based on Electroactive Hydrogels and Cellulose Nanocrystals for High-Sensitivity Electro–Mechanical Underwater Actuation. *Smart Mater. Struct.* **2017**, *26*, 085030. [CrossRef]
45. Piazzoni, M.; Piccoli, E.; Migliorini, L.; Milana, E.; Iberite, F.; Vannozzi, L.; Ricotti, L.; Gerges, I.; Milani, P.; Marano, C.; et al. Monolithic Three-Dimensional Functionally Graded Hydrogels for Bioinspired Soft Robots Fabrication. *Soft Robot.* **2022**, *9*, 224–232. [CrossRef]
46. Jing, X.; Chen, S.; Zhang, C.; Xie, F. Increasing Bending Performance of Soft Actuator by Silicon Rubbers of Multiple Hardness. *Machines* **2022**, *10*, 272. [CrossRef]
47. Yoon, J.H.; Lee, S.W.; Bae, S.H.; Kim, N.I.; Yun, J.H.; Jung, J.H.; Kim, Y.-G. Effect of Cyclic Shear Fatigue under Magnetic Field on Natural Rubber Composite as Anisotropic Magnetorheological Elastomers. *Polymers* **2022**, *14*, 1927. [CrossRef]
48. Molchanov, V.S.; Stepanov, G.V.; Vasiliev, V.G.; Kramarenko, E.Y.; Khokhlov, A.R.; Xu, Z.D.; Guo, Y.Q. Viscoelastic Properties of Magnetorheological Elastomers for Damping Applications. *Macromol. Mater. Eng.* **2014**, *299*, 1116–1125. [CrossRef]
49. Guo, F.; Du, C.; Yu, G. The Normal Force Characteristic of a Novel Magnetorheological Elastomer Based on Butadiene Rubber Matrix Compounded with the Self-Fabricated Silly Putty. *Adv. Mater. Sci. Eng.* **2021**, *2021*, 5831721. [CrossRef]
50. Liao, G.; Gong, X.; Xuan, S. Influence of Shear Deformation on the Normal Force of Magnetorheological Elastomer. *Mater. Lett.* **2013**, *106*, 270–272. [CrossRef]

51. Linke, J.M.; Borin, D.Y.; Odenbach, S. First-Order Reversal Curve Analysis of Magnetoactive Elastomers. *RSC Adv.* **2016**, *6*, 100407–100416. [CrossRef]
52. Belyaeva, I.A.; Kramarenko, E.Y.; Shamonin, M. Magnetodielectric Effect in Magnetoactive Elastomers: Transient Response and Hysteresis. *Polymer* **2017**, *127*, 119–128. [CrossRef]
53. Johari, M.A.F.; Mazlan, S.A.; Nasef, M.M.; Ubaidillah, U.; Nordin, N.A.; Aziz, S.A.A.; Johari, N.; Nazmi, N. Microstructural Behavior of Magnetorheological Elastomer Undergoing Durability Evaluation by Stress Relaxation. *Sci. Rep.* **2021**, *11*, 10936. [CrossRef]
54. Johari, M.A.F.; Mazlan, S.A.; Nordin, N.A.; Ubaidillah, U.; Aziz, S.A.A.; Nazmi, N.; Johari, N.; Choi, S.-B. The Effect of Microparticles on the Storage Modulus and Durability Behavior of Magnetorheological Elastomer. *Micromachines* **2021**, *12*, 948. [CrossRef]

Disclaimer/Publisher's Note: The statements, opinions and data contained in all publications are solely those of the individual author(s) and contributor(s) and not of MDPI and/or the editor(s). MDPI and/or the editor(s) disclaim responsibility for any injury to people or property resulting from any ideas, methods, instructions or products referred to in the content.

MDPI

MDPI

Article

High Sensitivity Planar Hall Effect Magnetic Field Gradiometer for Measurements in Millimeter Scale Environments

Hariharan Nhalil [1], Moty Schultz [1], Shai Amrusi [2], Asaf Grosz [2] and Lior Klein [1,*]

[1] Department of Physics, Institute of Nanotechnology and Advanced Materials, Bar-Ilan University, Ramat-Gan 52900, Israel
[2] Department of Electrical and Computer Engineering, Ben-Gurion University of the Negev, P.O. Box 653, Beer-Sheva 84105, Israel
* Correspondence: Lior.Klein@biu.ac.il

Abstract: We report a specially designed magnetic field gradiometer based on a single elliptical planar Hall effect (PHE) sensor, which allows measuring magnetic field at nine different positions in a 4 mm length scale. The gradiometer detects magnetic field gradients with equivalent gradient magnetic noises of ∼958, ∼192, ∼51, and ∼26 nT/m$\sqrt{\text{Hz}}$ (pT/mm$\sqrt{\text{Hz}}$) at 0.1, 1, 10, and 50 Hz, respectively. The performance of the gradiometer is tested in ambient conditions by measuring the field gradient induced by electric currents driven in a long straight wire. This gradiometer is expected to be highly useful for the measurement of magnetic field gradients in confined areas for its small footprint, low noise, scalability, simple design, and low costs.

Keywords: planar hall effect; gradiometer; magnetic sensor

Citation: Nhalil, H.; Schultz, M.; Amrusi, S.; Grosz, A.; Klein, L. High Sensitivity Planar Hall Effect Magnetic Field Gradiometer for Measurements in Millimeter Scale Environments. *Micromachines* **2022**, *13*, 1898. https://doi.org/10.3390/mi13111898

Academic Editors: Viktor Sverdlov and Seung-bok Choi

Received: 15 September 2022
Accepted: 27 October 2022
Published: 2 November 2022

Copyright: © 2022 by the authors. Licensee MDPI, Basel, Switzerland. This article is an open access article distributed under the terms and conditions of the Creative Commons Attribution (CC BY) license (https://creativecommons.org/licenses/by/4.0/).

1. Introduction

The detection of magnetic field gradients is important for many applications, including geomagnetic mapping [1,2], magnetic navigation [3,4], current sensing [5,6], medical diagnosis [7,8], etc. To perform detections in confined spaces, especially where the compact form factor is highly important (e.g., any portable [9] or wearable electronic devices [10–12], body implants [13], etc.), the sensors should have low equivalent magnetic noise and a small footprint as the minimum baseline (the distance between two sensors) of the gradiometer is decided by its footprint. Although there are gradiometers that can quantify the field gradient by measuring the magnetic field only at a single point [14], commonly, the determination of the magnetic field gradient requires magnetic field measurements at two or more locations.

Planer Hall effect sensors have the features required for confined space gradiometry: small footprint and high field resolution. Compared to other magnetoresistive sensors, they exhibit very low equivalent magnetic noise (EMN or resolution), especially at very low frequencies [15–17]. Previously, EMNs of ∼5 pT/$\sqrt{\text{Hz}}$ at 10 Hz and less than 25 pT/$\sqrt{\text{Hz}}$ at 50 Hz were reported for elliptical PHE sensors with and without magnetic flux concentrators (MFCs), respectively [16,17]. Here, the area of the magnetic ellipse with a major axis length of 5 mm (aspect ratio of 1/6) without MFCs is only ∼5 mm^2, whereas for high-resolution sensors such as superconducting quantum interference device (SQUID) magnetometers [18] or conventional fluxgate magnetometers [19], they have at least a one-order higher footprint, which makes them unsuitable for many confined space measurements. Moreover, some of these high-resolution magnetometers are operated at cryogenic temperatures and require bulky instrumentation. PHE sensors on the other hand are known for their room temperature operation, low temperature dependence [20], simple design and fabrication, linearity, and portability. These important characteristics make them ideal for gradiometer applications in confined spaces.

Here, we discuss the fabrication and testing of a specially designed elliptical planar Hall effect gradiometer (EPHEG) with nine sensing positions in a 4 mm length scale and a footprint less than 5 mm^2. Since the excitation current is shared by all sensing positions, the power consumption is 9 times smaller than the power needed to operate nine separate sensors. Moreover, the EPHEG can be used in smaller volumes than nine separate elliptical sensors and has redundancy in case one voltage pair fails during a measurement. Our EPHEG presents low equivalent gradient magnetic noises of ∼958, ∼192, ∼51, and ∼26 nT/m$\sqrt{}$Hz at 0.1, 1, 10, and 50 Hz. We also demonstrate the gradiometer performance by measuring the field gradient induced from a current-carrying long straight wire in ambient (outside the magnetic shield) conditions.

2. Experimental Techniques

Al_2O_3(60 nm)/Ta(5 nm)/Permalloy ($Ni_{80}Fe_{20}$, Py)(50 nm)/Ta(5 nm) films are sputter deposited on Si/SiO_2(naturally oxidized) wafers by ion beam sputtering (Intelvac Nanoquest I, Ontario, Canada). Elliptical shapes with a major axis (a) length of 5 mm and minor axis (b) length of 0.833 mm are patterned via photo-lithography, ion milling, and wet etch processes. Gold electrical contact pads of ∼1.5 times the thickness of Py are deposited and patterned via photo-lithography and lift-off processes in a second stage. Figure 1 shows a schematic diagram of an EPHEG including the configuration and dimensions of its electrical contacts. Sensitivity is measured in zero dc field by measuring the PHE signal with an ac magnetic field (100–200 nT) generated by a home-built, calibrated solenoid kept inside a magnetic shield (AMUNEAL MFG CORP, Philadelphia, PA, USA). For noise characterization and sensitivity measurements, the sensor is excited along the magnetic easy axis (long axis of the ellipse) with an ac current (1210 Hz) of different amplitudes employing a PXI-5421 function generator. Using an ultra-low noise transformer-matched amplifier (TMA, home built) [21], the transverse PHE voltage is amplified and digitized using a 24-bit sigma-delta analog to digital converter model PXIe 4464, from National Instruments. Noise measurements are performed inside a 3-layer Mu-metal magnetic shield to mitigate the effect of the ambient field and electromagnetic interferences. Gradient sensitivity and equivalent gradient magnetic noise are calculated from the measured sensitivity and voltage noise spectral densities of different voltage pairs, respectively. For testing and demonstration, the magnetic field from a long thin straight wire (length ∼1.5 m, radius ∼0.1 mm) carrying an ac current (5 Hz) is measured using the same instruments and electronics used for noise measurements in an open environment (outside the magnetic shield) and compared to the theoretical values calculated by Ampere's law. All measurements are performed at room temperature.

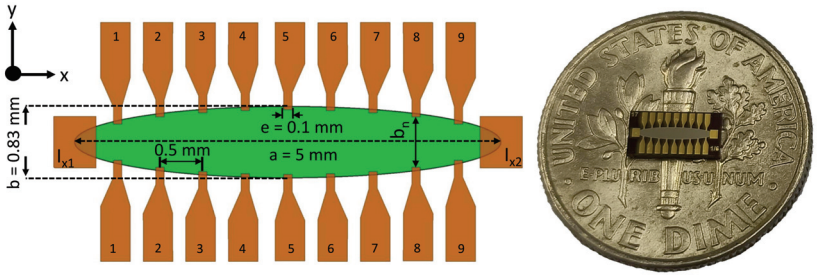

Figure 1. (**left**) Schematics of EPHEG geometry (not to scale). The orange regions are gold electrical contact pads. The long and short axes of the ellipse are labeled as a and b, respectively. The sensor is excited between I_{x1} and I_{x2}, and the transverse signal is measured across any of the parallel 9 voltage pairs (marked from 1 to 9). b_n is the distance between voltage pairs n. (**right**) Photograph of a sensor on a dime as a size reference.

3. Equivalent Magnetic Noise Characterizations

Our EPHEG consists of nine parallel voltage pairs that are equally spaced along the x-axis with a separation of 0.5 mm between each pair (Figure 1). To explore the position dependence of EMN, we measured the sensitivity (S_y) and noise at all voltage pairs.

The S_y of the EPHEG is defined as the ratio between the transverse voltage V_y (voltage across the parallel voltage pairs 1 to 9 in Figure 1) and the in-plane magnetic field B applied along the short axis of the ellipse given a current I_x flowing between I_{x1} and I_{x2} (Figure 1). For magnetic fields much smaller than the magnetic anisotropy field, S_y in V/T is given by [22]:

$$S_y = \frac{V_y}{B} = I_x \cdot \frac{\Delta\rho}{t} \cdot \frac{1}{H_{eff}} = I_x \cdot \Delta R \cdot \frac{1}{H_{eff}} \quad (1)$$

where $\Delta\rho$ is $(\rho_{\parallel} - \rho_{\perp})$, $\rho_{\parallel}$ and $\rho_{\perp}$ are the resistivities when the magnetization is parallel and perpendicular to the current, t is the film thickness, ΔR is $\frac{\Delta\rho}{t}$, and H_{eff} is the effective anisotropy field, which is the sum of the shape-induced anisotropy and growth-induced anisotropy [23].

S_y for all the nine parallel voltage pairs is measured for several excitation currents and is found to be linear with the excitation (FIG. S1 in the supporting information (SI)). S_y for I_x ~130 mA (peak) and different voltage pairs is listed in Table 1. We note a systematic change in S_y; S_y is maximum for the middle voltage pairs, and it decreases towards edge pairs. Based on Equation (1), S_y depends inversely on H_{eff}. H_{eff} is lowest at the middle voltage pair (pair 5) and increases gradually towards the edge pairs. The reduction in S_y (~21% reduction from the middle to edge pair), however, is mostly due to the reduction in ΔR rather than the nominal increase in H_{eff} (only ~ 6%).

R_y (transverse resistance) is at a maximal value at the middle voltage pair and decreases towards the edges due to the increase in the transverse distance (b_n) between the parallel voltage pairs (see the schematic in Figure 1). R_y, H_{eff}, ΔR, and b_n for different voltage pairs are also tabulated in Table 1. The two-probe longitudinal resistance (R_x) and AMR ratio of the film are ~38 Ω and ~1.9 %, respectively.

Equivalent magnetic noise (EMN or B_{eq}) is defined as follows [21,22]:

$$B_{eq}(f) = \frac{e_{\Sigma}(f)}{S_y} \quad (2)$$

where S_y and e_{Σ} are the sensitivity (given by Equation (1)) and total noise spectral density, respectively. e_{Σ} has different contributions from $1/f$, Johnson (thermal), and preamplifier noises and can be expressed as follows [21]:

$$e_{\Sigma}(f) = \sqrt{I_x^2 R_x^2 \frac{\delta_H}{N_{\dot{c}} Vol \cdot f^{\alpha}} + 4k_B T R_y + e_{amp}^2} \quad (3)$$

where δ_H is the Hooge parameter [24]. N_C is Permalloy's free electron density of $(1.7 \times 10^{29}/\mathrm{m}^3)$. Vol is the sensor's effective volume, where the electrons contribute to the conduction process in a homogeneous sample. f is the frequency. α is a constant. k_B is the Boltzmann constant. T is the temperature of the sensor. R_y is the resistance across the voltage terminals, and e_{amp} is the total noise of the TMA [21]. B_{eq} is obtained by measuring S_y and e_{Σ} separately [22].

Each EMN vs. frequency data between 0.1 and 100 Hz is fitted with $B_{eq}(f) = \sqrt{c_0^2 + \left(\frac{c_1}{f^{\beta}}\right)^2}$ (where c_0, c_1, and β are fit parameters [17]). From the fit, EMN at a specific frequency is extracted. EMN for different voltage pairs with an excitation current of ~ 130 mA is shown in Figure 2 for four different frequencies. It can be seen that the best EMNs are in the middle voltage pairs and can be attributed to the observed high sensitivities and comparatively larger effective volumes (due to larger b_n). Similar changes in EMN with voltage-pair positions are also seen for lower excitation (Table S1 in the SI). The best EMNs measured are ~29 pT/$\sqrt{\text{Hz}}$, ~62 pT/$\sqrt{\text{Hz}}$, ~279 pT/$\sqrt{\text{Hz}}$, and ~1322 pT/$\sqrt{\text{Hz}}$ at 50, 10,

1, and 0.1 Hz, respectively, for voltage pair number 5. The obtained EMNs closely resemble those in our previous study with respect to similar thickness (50 nm) elliptical PHE sensors where we explored the thickness dependence of EMNs [17].

Table 1. Typical values of R_y, H_{eff}, S_y (for I_x = ~130 mA (peak)), ΔR, and b_n for different parallel voltage-pairs of EPHEG.

V-Pair No:	R_y (Ω)	H_{eff} (Oe)	S_y (V/T)	ΔR (Ω)	b_n (m)
1	10.05	5.68	17.83	0.0778	4.200×10^{-4}
2	11.14	5.44	22.43	0.0938	5.866×10^{-4}
3	11.53	5.43	23.06	0.0964	6.837×10^{-4}
4	11.57	5.35	23.62	0.0973	7.365×10^{-4}
5	11.79	5.35	23.68	0.0975	7.533×10^{-4}
6	11.61	5.43	23.39	0.0974	7.365×10^{-4}
7	11.49	5.46	23.02	0.0966	6.837×10^{-4}
8	11.07	5.52	22.70	0.0966	5.866×10^{-4}
9	10.12	5.66	18.01	0.0781	4.200×10^{-4}

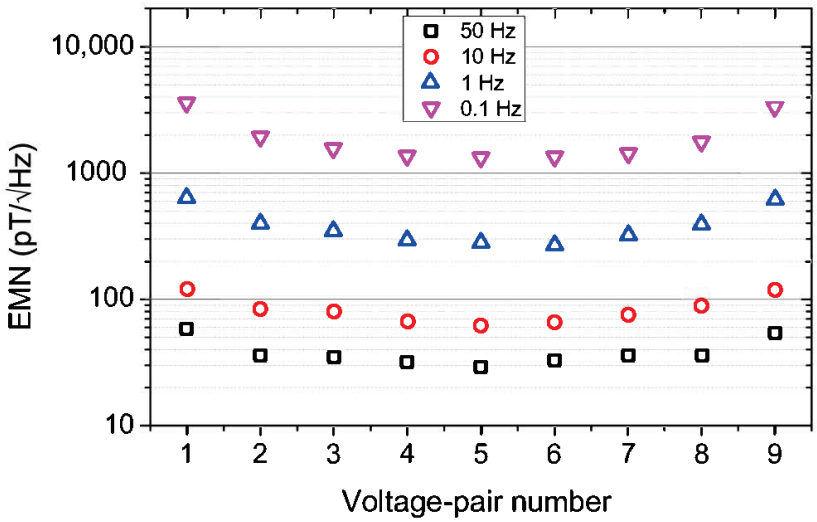

Figure 2. Plot showing the variation of EMN with the position of the voltage pairs for 50, 10, 1, and 0.1 Hz frequencies and for the highest excitation current of ~130 mA.

4. Equivalent Gradient Magnetic Noise

Our EPHEG with nine voltage pairs can be treated as an array of nine sensors that are placed linearly at 0.5 mm separation between each pair. Considering that the noise measurements are performed in a three-layer magnetically shielded environment, and by employing extremely low noise TMA, the noise sources of any two voltage pairs can be approximated to be completely uncorrelated. The equivalent gradient magnetic noise (gradient resolution, EGMN, or $grad\_B_{eq}$) of two sensors with noise sources that are uncorrelated can be defined as follows.

$$grad\_B_{eq} = \frac{Total\ voltage\ spectral\ noise\ density(f)}{Gradient\ sensitivity} \quad (4)$$

Here, the total voltage spectral noise density (TVSND) can be calculated from individual voltage spectral noise densities (VSNDs) of the two separate sensors as follows:

$$TVSND(f) = \sqrt{{VSND_1}^2(f) + {VSND_2}^2(f)} \quad (5)$$

where $VSND_1$ and $VSND_2$ are the voltage spectral noise densities of sensors 1 and 2, respectively, in $V/\sqrt{Hz}$. The denominator gradient sensitivity (GS) in Equation (4) is the sensitivity towards the gradient field and is defined as follows:

$$GS = \left| \frac{B_1 \cdot S_{y1} - B_2 \cdot S_{y2}}{gradB} \right| \tag{6}$$

where B_1 and B_2 are the magnetic field acting on sensors 1 and 2, and S_{y1} and S_{y2} are their respective sensitivities in V/T. $gradB$ is the magnetic field gradient in T/m.

Equation (6) can be rewritten as follows:

$$GS = \left| \Delta d \cdot S_{y1} + \frac{B_2(S_{y1} - S_{y2})}{gradB} \right| \tag{7}$$

where Δd is the distance between the sensors. Equation (7) shows that GS depends both on the strength of the magnetic field and the gradient field. GS does not depends on the field strength only when both sensors have the same sensitivity: $S_{y1} = S_{y2}$. Selecting a pair of leads with a larger distance will result in higher gradiometer sensitivity. On the contrary, as this distance increases, the capability of the gradiometer to reject interferences generated by other sources of field decreases. This is an important parameter, for example, in real-world scenarios where many sources of interference are present [25]. The multi-lead approach applied with this sensor allows the user to select an optimal sensitivity/rejection configuration that is most applicable to his specific use case. In the case of EPHEG, for obtaining a better GS, we choose two voltage pairs that are farther apart as possible and have the same or very similar S_y. From Table 1, it is clear that S_y of voltage pairs that are relatively at the same positions from the middle of the sensor have similar sensitivities; i.e., voltage pairs 1–9, 2–8, 3–7, and 4–6 have similar sensitivities. Out of these 4 voltage pairs, 1–9 are the farthest pairs and are expected to provide the highest GS and subsequently the best EGMN.

From the S_y of each voltage pair measured for the same excitation, GS is calculated for two voltage pairs having similar sensitivities for an arbitrary constant ΔB of 1 nT ($\Delta B = B_1 - B_2$, B_1 and B_2 are the magnetic field at positions 1 and 2, respectively). TVSND is calculated from the respective VSNDs according to Equation (5) and EGMN is calculated. The calculated frequency dependence of EGMN is fitted with the following:

$$grad\_B_{eq}(f) = \sqrt{a_0^2 + \left(\frac{a_1}{f^{\gamma}}\right)^2} \tag{8}$$

where a_0, a_1, and γ are fit parameters. Figure 3 shows the EGMN vs. frequency for four different dual voltage pairs. For clarity, data and fit together are shown only for the 1–9 dual voltage pairs, and for all others, only the fit according to Equation (8) is shown. As expected, the best EGMN is obtained when measurement voltage pairs are the farthest apart. The EGMN obtained are ∼958, ∼192, ∼51, ∼26, and ∼25 $\mathrm{nT/m}\sqrt{\mathrm{Hz}}$ ($\mathrm{pT/mm}\ \sqrt{\mathrm{Hz}}$) at 0.1, 1, 10, 50, and 100 Hz, respectively, with fit parameters a_0, a_1, and γ as 3.76×10^{-9}, 4.43×10^{-8}, and 0.69, respectively.

In comparison with other gradiometers, SQUID-based gradiometers have the best reported gradient field resolution $<$100 $\mathrm{fT/m}\sqrt{\mathrm{Hz}}$ followed by atomic magnetometers with $<$10 $\mathrm{pT/m}\sqrt{\mathrm{Hz}}$ [26–28]. Fluxgate and magnetoelectric gradiometers reported gradient resolutions $<$1 $\mathrm{nT/m}\sqrt{\mathrm{Hz}}$ [29–31]. If we compare the EGMN of a fluxgate gradiometer with baselines of 100 mm [29] and 600 mm [30], they have 0.52 $\mathrm{nT/m}/\sqrt{\mathrm{Hz}}$ and 0.03 $\mathrm{nT/m}/\sqrt{\mathrm{Hz}}$ gradient resolutions, respectively, and they are at least two orders higher than our EPHEG's EGMN. However, the reported baselines of these sensors are several times higher than that of our EPHEG sensor, which has a maximum baseline of 4 mm and a minimum baseline of 0.5 mm. The EMN of our EPHEG 's middle pair is 29 $\mathrm{pT}/\sqrt{\mathrm{Hz}}$, which is better than or within the range of many high-end MEMS fluxgate sensors of smaller size [32,33]. However, the very small baseline of EPHEG has a negative impact on the overall EGMN.

To demonstrate the performance of the EPHEG, the field gradient from an ac current (1 mA, 5 Hz) carrying a long thin straight wire (length ∼1.5 m) is measured in the ambient conditions (outside the magnetic shield) and compared with the theoretical values. For measurements, a calibrated EPHEG is placed near the wire such that the field lines from the wire are in-plane and perpendicular to the long axis of the sensor, as shown schematically in the inset of Figure 4. Starting from a position very close to the wire, the EPHEG is moved (in 4 mm steps) radially outwards on a rail that has precision control on the lateral movements. At each position, the magnetic field is measured by the five different voltage pairs (five alternate pairs covering a total distance of 4 mm) separately with a bandwidth of 0.1 Hz. After measuring all five pairs at a position, the sensor is moved radially outwards 4 mm to a new position and all five pairs are measured again. This procedure is repeated to obtain the field vs. distance plot shown in Figure 4. The error bar on each measurement point represents the standard deviation of ten measurements, and the experimentally measured magnetic fields agree well with the theoretical field values. The lowest gradient field calculated from this measurement is ∼100 nT/m at ∼40 mm.

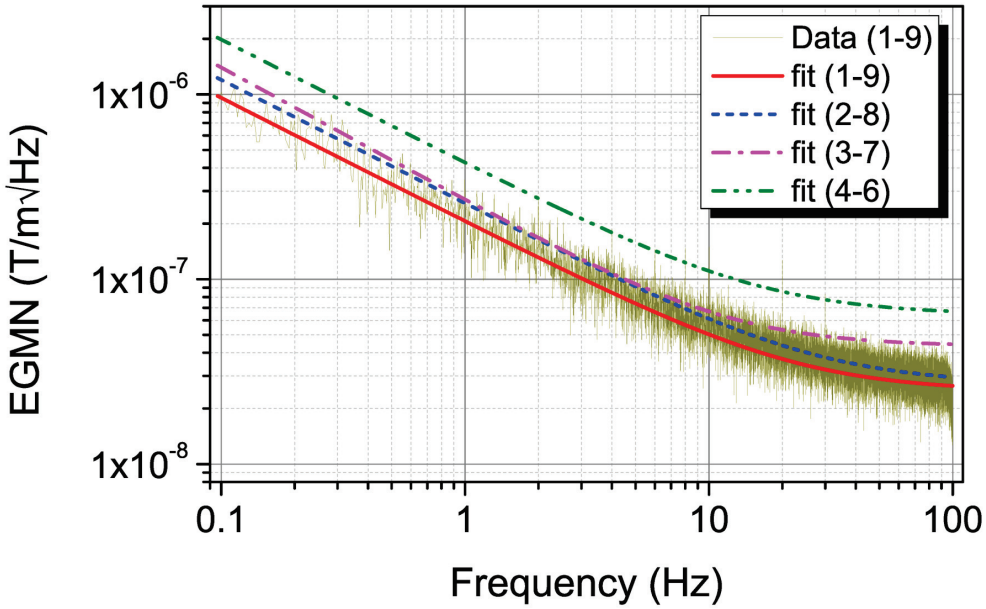

Figure 3. Frequency– dependence of EGMN of 4 voltage pairs 1–9, 2–8, 3–7 and 4–6. Data and fit according to Equation (8) are shown only for the 1-9 voltage pairs. For clarity, only the fit is shown for remaining pairs.

The gradient field resolution improves with the increase in the baseline, and in applications where the gradient field is relatively homogeneous in the sensor's volume, measurement errors can be reduced by averaging the output of several sensor pairs [34,35]. To find out the performance limit of EPHEG, the magnetic field is measured by five different voltage pairs (averaging 20 measurements at each voltage pair) that are separated 1 mm apart (i.e., alternate voltage pairs) covering a total length of 4 mm at a distance of ∼ 40 mm from the wire. At this distance, the magnetic field variation with radial distance from the wire can be approximated to be linear and the slope will give the field gradient. Figure 5 shows the magnetic field from a wire carrying 0.2 mA and 0.4 mA measured along with linear fits. We define the limit of the measurement when the slope of the experimental curve deviates ±10% from the slope of the theoretical one. Accordingly, the lowest magnetic field gradient measured is ∼20 nT/m (slope = −0.0254 nT/mm) for 0.2 mA and ∼40 nT/m (slope = −0.045 nT/mm) for 0.4 mA. In terms of linear fit errors, measuring five pairs has a nominal advantage over measuring two pairs. These values are higher than the EGMN determined for two voltage pairs inside the magnetic shield and the difference could be attributed to the harsh measurement environment. Below 0.2 mA, even though the sensor was able to sense the magnetic field, the gradient field

calculation is erroneous, and for excitations below 0.1 mA, the signal was below the noise floor. Lower bandwidth measurements utilizing all nine voltage pairs are expected to improve these results.

A comparison of gradient field detectivity of several different types of gradiometers by converting a uniform field sensor to a gradiometer of baseline of 1 cm is reported by J. Javor et al. [14]. Notably, the detectivity of the EPHEG is within the range of the microelectromechanical system (MEMS)[14], Hall effect [36], Fluxgate [19,37], and the majority of magnetoresistive gradiometers [14]. Since our EPHEG can sense the magnetic field at different positions simultaneously, it can find applications in bio-magnetic sensing [38,39], drug delivery [40,41], and other fields where the speed and flow rate of the bio-magnetic particles need to be determined.

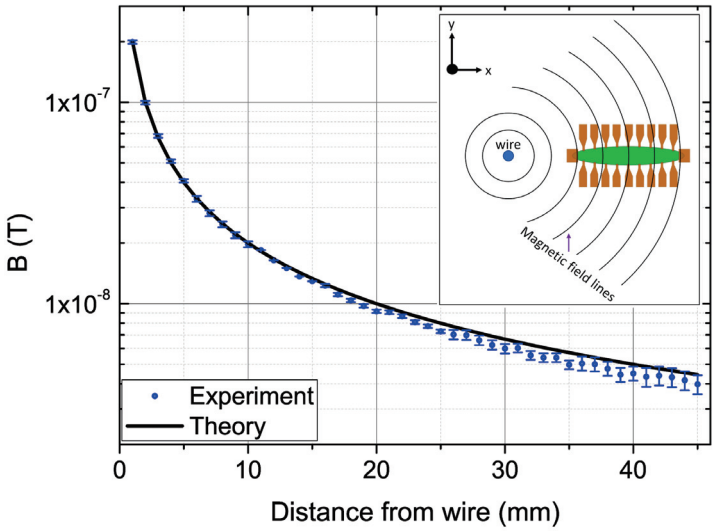

Figure 4. The variation of the magnetic field from a current-carrying wire with a distance from the wire (measured outside the magnetic shield) with an EPHEG along with the calculated magnetic field. The standard deviation of 10 measurements is presented as the error at each point. The inset depicts the schematics of the measurement setup. The current-carrying wire is in the z-direction perpendicular to the plane of the figure.

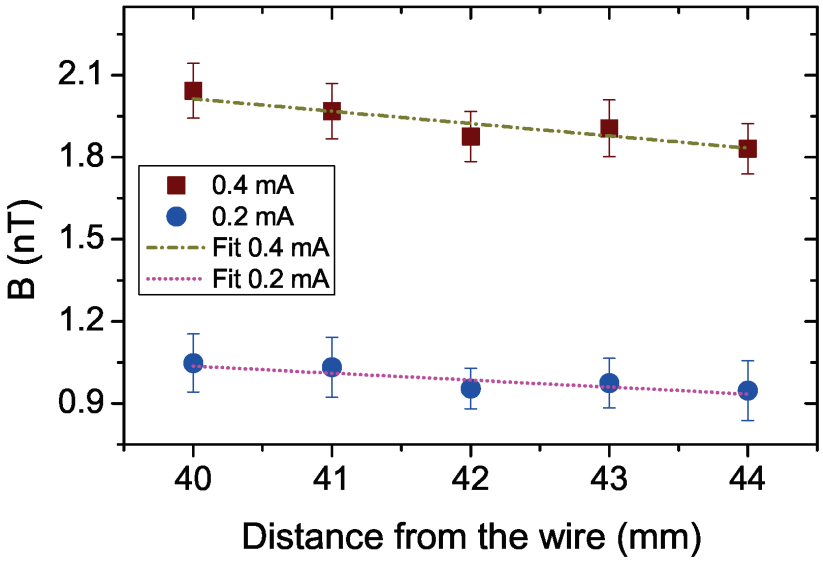

Figure 5. The magnetic field from a wire carrying 0.2 mA and 0.4 mA measured at a distance of ~40 mm using five voltage pairs. The error bar shown for each data point represents the standard deviation of 20 measurements.

5. Summary

In summary, we report the fabrication and performance of a permalloy-based elliptical planar Hall effect magnetic field gradiometer with nine field-sensing positions. Using two field sensing positions with a baseline of 4 mm, it can measure the magnetic field gradients with equivalent gradient magnetic noises of ∼958, ∼192, ∼51, and ∼26 nT/m$\sqrt{\text{Hz}}$ (pT/mm$\sqrt{\text{Hz}}$) at 0.1, 1, 10, and 50 Hz, respectively. We demonstrate the performance of the EPHEG by measuring the field gradient from a current-carrying wire using five voltage pairs with a minimum detectivity of ∼20 nT/m in ambient conditions outside the magnetic shield. Our simple, low-cost, high-resolution, and small-footprint gradiometer is expected to be highly useful in measuring gradient fields in confined spaces.

Supplementary Materials: The following supporting information can be downloaded at: https://www.mdpi.com/article/10.3390/mi13111898/s1. Figure S1: Excitation current vs Sensitivity (S_y) plot for different excitation currents for all the 9-voltage pairs showing linear dependency. For clarity, only one linear fit is shown (for pair number 9). Table S1: EMNs for 2 different excitation currents for the 9-voltage pairs for 50, 10, 1 and 0.1 Hz frequencies.

Author Contributions: Conceptualization, H.N., L.K., A.G. and M.S.; methodology, H.N. and M.S.; software, H.N., S.A. and M.S.; validation, H.N. and M.S.; investigation, H.N. and M.S.; data curation, H.N.; writing—original draft preparation, H.N.; writing—review and editing, H.N., L.K., A.G., S.A. and M.S.; visualization, H.N.; supervision, L.K.; project administration, L.K. All authors have read and agreed to the published version of the manuscript.

Funding: This research received no external funding.

Data Availability Statement: Not applicable.

Conflicts of Interest: The authors declare no conflict of interest.

References

1. Kim, H.; Golynsky, A.; Golynsky, D.; Yu, H.; von Frese, R.; Hong, J. New Magnetic Anomaly Constraints on the Antarctic Crust. *J. Geophys. Res. Solid Earth* **2022**, *127*, e2021JB023329. [CrossRef]
2. Chen, C.H.; Chen, P.W.; Chen, P.J.; Liu, T.H. Indoor Positioning Using Magnetic Fingerprint Map Captured by Magnetic Sensor Array. *Sensors* **2021**, *21*, 5707. [CrossRef]
3. Včelák, J.; Ripka, P.; Kubik, J.; Platil, A.; Kašpar, P. AMR navigation systems and methods of their calibration. *Sens. Actuator A* **2005**, *123*, 122–128. [CrossRef]
4. Ausserlechner, U. The optimum layout for giant magneto-resistive angle sensors. *IEEE Sens. J.* **2010**, *10*, 1571–1582. [CrossRef]
5. Musuroi, C.; Oproiu, M.; Volmer, M.; Neamtu, J.; Avram, M.; Helerea, E. Low field optimization of a non-contacting high-sensitivity GMR-based DC/AC current sensor. *Sensors* **2021**, *21*, 2564. [CrossRef]
6. Ripka, P.; Mlejnek, P.; Hejda, P.; Chirtsov, A.; Vyhnánek, J. Rectangular array electric current transducer with integrated fluxgate sensors. *Sensors* **2019**, *19*, 4964. [CrossRef]
7. Barroso, T.G.; Martins, R.C.; Fernandes, E.; Cardoso, S.; Rivas, J.; Freitas, P.P. Detection of BCG bacteria using a magnetoresistive biosensor: A step towards a fully electronic platform for tuberculosis point-of-care detection. *Biosens. Bioelectron.* **2018**, *100*, 259–265. [CrossRef]
8. Li, Y.; Cheng, H.; Alhalili, Z.; Xu, G.; Gao, G. The progress of magnetic sensor applied in biomedicine: A review of non-invasive techniques and sensors. *J. Chin. Chem. Soc.* **2021**, *68*, 216–227. [CrossRef]
9. Mooney, J.W.; Ghasemi-Roudsari, S.; Banham, E.R.; Symonds, C.; Pawlowski, N.; Varcoe, B.T. A portable diagnostic device for cardiac magnetic field mapping. *Biomed. Phys. Eng. Express* **2017**, *3*, 015008. [CrossRef]
10. Kim, J.; Kumar, R.; Bandodkar, A.J.; Wang, J. Advanced materials for printed wearable electrochemical devices: A review. *Adv. Elect. Mater.* **2017**, *3*, 1600260. [CrossRef]
11. Melzer, M.; Mönch, J.I.; Makarov, D.; Zabila, Y.; Cañón Bermúdez, G.S.; Karnaushenko, D.; Baunack, S.; Bahr, F.; Yan, C.; Kaltenbrunner, M.; et al. Wearable magnetic field sensors for flexible electronics. *Adv. Mater.* **2015**, *27*, 1274–1280. [CrossRef]
12. Jucevičius, M.; Ožiūnas, R.; Narvydas, G.; Jegelevičius, D. Permanent magnet tracking method resistant to background magnetic field for assessing jaw movement in wearable devices. *Sensors* **2022**, *22*, 971. [CrossRef]
13. Feiner, R.; Dvir, T. Tissue–electronics interfaces: from implantable devices to engineered tissues. *Nat. Rev. Mater.* **2017**, *3*, 17076. [CrossRef]
14. Javor, J.; Stange, A.; Pollock, C.; Fuhr, N.; Bishop, D.J. 100 pT/cm single-point MEMS magnetic gradiometer from a commercial accelerometer. *Microsyst. Nanoeng.* **2020**, *6*, 71. [CrossRef]

15. Lim, B.; Mahfoud, M.; Das, P.T.; Jeon, T.; Jeon, C.; Kim, M.; Nguyen, T.K.; Tran, Q.H.; Terki, F.; Kim, C. Advances and key technologies in magnetoresistive sensors with high thermal stabilities and low field detectivities. *APL Mater.* **2022**, *10*, 051108. [CrossRef]
16. Nhalil, H.; Givon, T.; Das, P.T.; Hasidim, N.; Mor, V.; Schultz, M.; Amrusi, S.; Klein, L.; Grosz, A. Planar Hall Effect Magnetometer With 5 pT Resolution. *IEEE Sens. Lett.* **2019**, *3*, 2501904. [CrossRef]
17. Nhalil, H.; Das, P.T.; Schultz, M.; Amrusi, S.; Grosz, A.; Klein, L. Thickness dependence of elliptical planar Hall effect magnetometers. *Appl. Phys. Lett.* **2020**, *117*, 262403. [CrossRef]
18. Tsukamoto, A.; Adachi, S.; Hato, T.; Oshikubo, Y.; Tanabe, K. Design and Fabrication of HTS-SQUID Gradiometer With Imbalance of 10–4 Using a Gradiometric SQUID Structure. *IEEE Trans. Appl. Supercond.* **2022**, *32*, 1600309. [CrossRef]
19. Sui, Y.; Miao, H.; Zhou, Z.; Luan, H.; Wang, Y. Correction and compensation of an airborne fluxgate magnetic tensor gradiometer. *Explor. Geophys.* **2018**, *49*, 726–734. [CrossRef]
20. Mahfoud, M.; Tran, Q.H.; Wane, S.; Ngo, D.T.; Belarbi, E.H.; Boukra, A.; Kim, M.; Elzwawy, A.; Kim, C.; Reiss, G.; et al. Reduced thermal dependence of the sensitivity of a planar Hall sensor. *Appl. Phys. Lett.* **2019**, *115*, 072402. [CrossRef]
21. Grosz, A.; Mor, V.; Amrusi, S.; Faivinov, I.; Paperno, E.; Klein, L. A high-resolution planar Hall effect magnetometer for ultra-low frequencies. *IEEE Sens. J.* **2016**, *16*, 3224–3230. [CrossRef]
22. Grosz, A.; Mor, V.; Paperno, E.; Amrusi, S.; Faivinov, I.; Schultz, M.; Klein, L. Planar hall effect sensors with subnanotesla resolution. *IEEE Mag. Lett.* **2013**, *4*, 6500104. [CrossRef]
23. Mor, V.; Schultz, M.; Sinwani, O.; Grosz, A.; Paperno, E.; Klein, L. Planar Hall effect sensors with shape-induced effective single domain behavior. *J. Appl. Phys.* **2012**, *111*, 07E519. [CrossRef]
24. Gijs, M.; Giesbers, J.; Beliën, P.; Van Est, J.; Briaire, J.; Vandamme, L. 1/f noise in magnetic Ni80Fe20 single layers and Ni80Fe20/Cu multilayers. *J. Magn. Magn. Mater.* **1997**, *165*, 360–362. [CrossRef]
25. McKenna, S.P.; Parkman, K.B.; Perren, L.J.; McKenna, J.R. Response of an electromagnetic gradiometer to a subsurface wire. *IEEE Trans. Geosci. Remote Sens.* **2011**, *49*, 4944–4953. [CrossRef]
26. Song, Z.; Dai, H.; Rong, L.; Dong, H.; Wu, J.; Qiu, L.; Zhang, G.; Wang, Y.; Tao, Q.; Pei, Y.; et al. Noise compensation of a mobile LTS SQUID planar gradiometer for aeromagnetic detection. *IEEE Trans. Appl. Supercond.* **2019**, *29*, 1600205. [CrossRef]
27. Perry, A.; Bulatowicz, M.; Larsen, M.; Walker, T.; Wyllie, R. All-optical intrinsic atomic gradiometer with sub-20 fT/cm/sqrt Hz sensitivity in a 22 μT earth-scale magnetic field. *Opt. Express* **2020**, *28*, 36696–36705. [CrossRef]
28. Limes, M.; Foley, E.; Kornack, T.; Caliga, S.; McBride, S.; Braun, A.; Lee, W.; Lucivero, V.; Romalis, M. Total-field atomic gradiometer for unshielded portable magnetoencephalography. *arXiv* **2020**, arXiv:2001.03534. [CrossRef]
29. Sui, Y.; Li, G.; Wang, S.; Lin, J. Compact fluxgate magnetic full-tensor gradiometer with spherical feedback coil. *Rev. Sci. Instr.* **2014**, *85*, 014701. [CrossRef]
30. Merayo, J.M.; Brauer, P.; Primdahl, F. Triaxial fluxgate gradiometer of high stability and linearity. *Sens. Actuators A* **2005**, *120*, 71–77. [CrossRef]
31. Zhang, M.; Or, S.W. Magnetoelectric transverse gradient sensor with high detection sensitivity and low gradient noise. *Sensors* **2017**, *17*, 2446. [CrossRef]
32. Shen, X.; Teng, Y.; Hu, X. Design of a low-cost small-size fluxgate sensor. *Sensors* **2021**, *21*, 6598. [CrossRef]
33. Wang, Z.; Shen, Y.; Lei, C.; Wang, J.; Zhao, S.; Chen, J.; Chu, Z.; Gao, J. Highly-Sensitive MEMS Micro-Fluxgate Magnetometer. *IEEE Elec. Dev. Lett.* **2022**, *43*, 1327–1330. [CrossRef]
34. Shen, Y.; McLaughlin, K.L.; Gao, J.; Li, M.; Li, J.; Viehland, D. Effective optimization of magnetic noise for a Metglas/Pb (Zr, Ti) O3 magnetoelectric sensor array in an open environment. *Mater. Lett.* **2013**, *91*, 307–310. [CrossRef]
35. Leach, W.M. Fundamentals of low-noise analog circuit design. *Proc. IEEE* **1994**, *82*, 1515–1538. [CrossRef]
36. Jung, G.; Ocio, M.; Paltiel, Y.; Shtrikman, H.; Zeldov, E. Magnetic noise measurements using cross-correlated Hall sensor arrays. *Appl. Phys. Lett.* **2001**, *78*, 359–361.
37. Sui, Y.; Miao, H.; Wang, Y.; Luan, H.; Lin, J. Correction of a towed airborne fluxgate magnetic tensor gradiometer. *IEEE Geosci. Remote. Sens. Lett.* **2016**, *13*, 1837–1841. [CrossRef]
38. Klein, T.; Wang, W.; Yu, L.; Wu, K.; Boylan, K.L.; Vogel, R.I.; Skubitz, A.P.; Wang, J.P. Development of a multiplexed giant magnetoresistive biosensor array prototype to quantify ovarian cancer biomarkers. *Biosens. Bioelectron.* **2019**, *126*, 301–307. [CrossRef]
39. Schutt, J.; Illing, R.; Volkov, O.; Kosub, T.; Granell, P.N.; Nhalil, H.; Fassbender, J.; Klein, L.; Grosz, A.; Makarov, D. Two Orders of Magnitude Boost in the Detection Limit of Droplet-Based Micro-Magnetofluidics with Planar Hall Effect Sensors. *ACS Omega* **2020**, *5*, 20609–20617. [CrossRef] [PubMed]
40. Gul, A.; Tzirtzilakis, E.E.; Makhanov, S.S. Simulation of targeted magnetic drug delivery: Two-way coupled biomagnetic fluid dynamics approach. *Phys. Fluids* **2022**, *34*, 021911. [CrossRef] [PubMed]
41. Shaw, S.; Shit, G.; Tripathi, D. Impact of drug carrier shape, size, porosity and blood rheology on magnetic nanoparticle-based drug delivery in a microvessel. *Colloids Surf. A* **2022**, *639*, 128370. [CrossRef]

MDPI
St. Alban-Anlage 66
4052 Basel
Switzerland
www.mdpi.com

Micromachines Editorial Office
E-mail: micromachines@mdpi.com
www.mdpi.com/journal/micromachines

Disclaimer/Publisher's Note: The statements, opinions and data contained in all publications are solely those of the individual author(s) and contributor(s) and not of MDPI and/or the editor(s). MDPI and/or the editor(s) disclaim responsibility for any injury to people or property resulting from any ideas, methods, instructions or products referred to in the content.

Academic Open
Access Publishing

mdpi.com

ISBN 978-3-0365-9891-8